Université de Lille – Faculté des Sciences et Technologies

Ecole doctorale Sciences de la Matière, du Rayonnement
et de l'Environnement (SMRE) - Ed. 104

HABILITATION A DIRIGER DES RECHERCHES

Anne Cécile GREGOIRE

Comportement des produits de fission en situation accidentelle grave d'un réacteur nucléaire à eau pressurisée – du relâchement combustible à la dispersion atmosphérique

Fission product behaviour in a severe accident situation of a NPP – from fuel release up to atmospheric dispersion

le 25 Mai 2022

Jury

M. Cote Gérard	Professeur émérite, Chimie Paristech	Rapporteur
M. Wortham Henri	Professeur, Université Aix Marseille	Rapporteur
M. Girard Luc	Enseignant Chercheur, ENSCM	Rapporteur
M. Gasnot Laurent	Professeur, Université de Lille	Examinateur
M Paul Jean-François	Professeur, Université de Lille	Examinateur
M. Cantrel Laurent	Dr-HDR, IRSN	Examinateur
M. Perron Hadrien	Dr, Ingénieur-Chercheur, EDF R&D	Membre Invité

RÉSUMÉ

Mots clés : Mémoire HDR, Accident Grave, Chimie Transport, Iode , Césium

Ce mémoire résume une vingtaine d'années de recherche expérimentale consacrées au comportement des produits de fission (PF) en lien avec les situations accidentelles graves de réacteurs nucléaires. Une attention particulière a été portée à l'iode et au césium, qui sont les deux contributeurs majeurs aux conséquences radiologiques, en cas de relâchement significatif à l'environnement. L'objectif est de comprendre aussi finement que possible leur comportement physico-chimique depuis le relâchement du combustible dégradé, jusqu'à leur émission potentielle à l'environnement et leur transport dans le compartiment atmosphérique. Le but final est d'améliorer les outils de simulation développés par l'IRSN qui permettent d'évaluer les rejets possibles à l'environnement. Les rejets extérieurs constituent ce que l'on appelle le terme source (TS), il est défini pour un isotope donné et une forme chimique.

Si les essais intégraux Phébus PF ont apporté de nombreux enseignements sur le relâchement des produits de fission et des matériaux des barres de commande, des questionnements subsistent, notamment sur la réactivité de ces matériaux durant leur transport dans le circuit primaire. Les expérimentations que j'ai dirigées depuis 2008 sur la ligne CHIP ont apporté des éléments de compréhension essentiels pour mieux simuler cette phase de l'accident. En effet, il a été confirmé qu'outre CsI, d'autres formes iodées (gazeuses/condensées) peuvent être transportées dans le circuit primaire. La persistance d'une fraction importante d'iode gazeux à la brèche en branche froide semble être fortement liée à la nature de l'atmosphère gazeuse et à la présence d'autres produits de fission (Mo et surtout le rapport Mo/Cs). Les éléments issus de la dégradation des barres de contrôle (B pour B_4C et Cd, Ag pour AIC) peuvent aussi jouer un rôle sur la chimie transport de ces PFs. Les efforts portent maintenant sur l'amélioration des outils de simulation pour mettre en cohérence les simulations avec les observables expérimentaux.

Les phénomènes de revaporisation depuis les dépôts dans l'installation peuvent contribuer à des rejets tardifs comme cela a été mis en lumière lors de l'accident de Fukushima Daiichi. Les premiers travaux expérimentaux que j'ai conduits sur cette thématique visaient à identifier les principaux paramètres qui régissent ce phénomène à une échelle analytique et à quantifier le rejet possible de formes iodées gazeuses. Les premiers essais avec l'iodure de césium et l'iodure d'argent ont mis en évidence le rôle du potentiel oxydant de l'atmosphère dans la formation d'iode gazeux, mais aussi le rôle de la réactivité hétérogène. En effet, la décomposition de CsI est observée dès 300-500°C – domaine de température bien inférieur à sa vaporisation – et est attribué à des réactions hétérogènes solide -gaz avec l'air ou à des interactions avec la surface d'acier oxydée. Les travaux expérimentaux sur cette thématique vont se poursuivre dans le cadre du programme OCDE ESTER associant essais à petite échelle mais aussi à une échelle intermédiaire dans la ligne expérimentale CHIP permettant de reproduire des compositions de dépôts plus complexes dans un gradient thermique maîtrisé.

Enfin, en raison des conséquences sanitaires résultant de l'exposition de la population et de la contamination des sols, le devenir des espèces radio-iodées après leur émission dans l'atmosphère est une préoccupation majeure. Afin d'améliorer les outils IRSN de prédiction de la dispersion des radio-contaminants, des études expérimentales à l'échelle du laboratoire ont été entreprises sur la réactivité de l'iode avec les aérosols atmosphériques. Ces études visent à compléter la connaissance du cycle atmosphérique de l'iode dont la réactivité hétérogène gaz/solide est encore peu documentée dans la littérature. Plus particulièrement, je me suis intéressée à l'interaction de CH_3I avec des solides modèles des principales classes atmosphériques d'aérosols (sels marins, aérosols inorganiques secondaires et organiques secondaires). Le résultat principal est que l'interaction de l'iodure de méthyle avec ces solides modèles est du second ordre par rapport à la chimie en phase gazeuse. On s'attend donc à ce que l'iodure de méthyle reste en phase gazeuse pendant son cycle de vie dans la troposphère et soit principalement impliqué dans les processus photochimiques, comme mentionné dans la littérature. Les futurs travaux seront consacrés à l'iode moléculaire – réputé plus réactif - afin d'évaluer les conséquences de ce type d'interaction sur son cycle de vie et donc sa dispersion. Ces travaux s'inscrivent dans un projet plus global au sein de l'institut dénommé SPECIOSA visant à mieux évaluer la dispersion, notamment en champs relativement proche.

Les avancées de ces recherches ont apporté des éléments de réponse pour compléter/valider les outils de simulation et ont suscité de nombreuses perspectives d'études sur le terme source (cas du Cr des combustibles innovants EATF), la revaporisation (programme OECD-ESTER) et enfin la dispersion atmosphérique des radio-nucléides (programme IRSN transverse SPECIOSA).

SUMMARY

Key-words: Research Summary, Severe Accident, FP chemistry, Iodine, Caesium

This brief summarizes 20 years of experimental research on the behaviour of fission products in relation to severe accidental nuclear reactor situations. Particular attention has been paid to iodine and caesium, which are the two major contributors to the short- and medium-term radiological consequences in the event of significant release to the environment. The aim is to understand as finely as possible their physico-chemical behaviour from the release of degraded fuel to their potential emission to the environment. The final goal is to improve the simulation tools developed by the IRSN, which make it possible to assess potential releases to the environment and predict their dispersion. External releases are the so-called source term (TS), defined for a given isotope and chemical form.

If numerous information on fission product and control rod material release could be gained from the integral PHébus FP tests, some important transport issues were pointed out - in particular concerning their reactivity during their transport in the reactor coolant system. The experiments which I conducted in the CHIP line since 2008, brought some key elements of understanding to better simulate this accident phase. It was indeed confirmed that beside CsI, other iodine forms (gaseous /condensed) can be transported in the RCS in severe accident conditions. The persistence of a significant gaseous iodine fraction in cold leg break conditions seems to be strongly linked to nature of gas atmosphere and the ratio of the other released elements – especially Mo/Cs ratio. Control rod elements (Boron for B_4C and Ag, Cd for SIC control rod) were highlighted as playing also a role on FPs transport. Efforts are now ongoing to improve modelling to be capable of reproducing the trends experimentally observed.

Revaporization phenomena from the reactor coolant system or containment vessel and their consequences in terms of late phase releases were highlighted by the Fukushima Daiichi accident. The first experiments I have led, were aimed at identifying the main parameters that governs this phenomena at an analytical scale and to quantify the possible release of iodine gaseous forms. The first tests with caesium iodide and silver iodide highlighted the role of the oxidative potential of the atmosphere in the release of gaseous iodine species but also the role of heterogeneous reactivity. Indeed, both reaction with oxidised stainless steel surface and heterogeneous reaction with air atmosphere resulted in CsI decomposition producing gaseous iodine species in a temperature range (from 300-500 °C) far much lower than expected from CsI vaporisation. this thematic will be further investigated in the framework of the OECD ESTER program. Experiments will be performed at analytical scale and at an intermediate scale allowing to consider complex deposit compositions as obtained in the CHIP Line.

After their emission into the environment following an accidental or an incidental situation, the fate of iodine species in the atmosphere is a strong issue for predicting human exposure and land contamination – given the health effects of exposition to radio-contaminants. In order to improve the relevance and accuracy of iodine modelling in the IRSN dispersion software, experimental studies at laboratory scale were undertaken with the objective of fulfilling the understanding of iodine atmospheric mechanism. Strong interest was brought on gaseous iodine interaction with atmospheric aerosols – as this field is still poorly documented in the literature. Interaction of methyl iodide with surrogates of the main atmospheric aerosol classes (sea salt, secondary inorganic and organic aerosols) was firstly considered. The main outcome is that interaction of methyl iodide with such solids seems to be of second order compared to gas phase chemistry. Methyl iodide is thus expected to remain in the gaseous phase during its lifecycle in the troposphere – and be mainly involved in photochemical gas phases processes as mentioned in the literature. Further work will be devoted to molecular iodine - expected to be more reactive – in order to evaluate the consequence of such interactions on its tropospheric lifecycle. This work is part of a more global project within the institute called SPECIOSA dedicated to better assess iodine dispersion.

The achievements of these research programmes have given rise to new questions and are extended into many experimental perspectives on source term issues (role of Cr from Accident Tolerant Fuel), on revaporisation issues (OECD –ESTER programme) and finally on atmospheric dispersion issues (IRSN SPECIOSA programme).

Remerciements

Je tiens tout d'abord à adresser mes remercicement les plus chaleureux aux membres du jury pour avoir bien voulu s'impliquer dans la relecture de ce mémoire et plus particulièrement aux rapporteurs , Messieurs Gérard Cote, Henri Wortham et Luc Girard.

Je tiens également à remercier tout particulièrement Jean François Paul pour s'être engagé à être le référent scientifique de ce mémoire et aussi pour notre collaboration engagée depuis le programme MIRE et nos dicussions toujours pertinentes tant sur les aspects expérimentaux que pour leur interprétation.

Mes remerciement vont bien entendu à tous les collègues que j'ai cotoyés depuis 2002 à l'IRSN et pour leur contribution à ses travaux. Tout d'abord, mes collègues du LEMRA sur les expérimentations Phébus et nos nombreuses discussions qui ont été fort utiles à la rédaction des rapports de synthèses expérimentaux . Puis mes collègues du LEA puis L2EC et notamment l'équipe CHIP dont la persévérence et la patience ont permis de mener à bien ces expérimentations parfois ardues.

Merci aussi aux stagiaires , doctorants, post doctorants dont l'enthousiame et le volontarisme sont des moteurs essentiels à la vie du laboratoire et des équipes.

CONTENTS

LIST OF FIGURES

LIST OF TABLES

1 INTRODUCTION

The shift towards production of carbon-free energy is the main challenge of XXI century that can meet the double objectives of limiting climate change (IPCC, 2021) and facing fossil energy shortage (oil, gaz, and coal). Such a shift at a world stage and within a very short time lapse (30-50 years) will result in a massive switch of energy production toward electricity. In France, even in a context of energy restraint, electricity demand is expected to increase strongly up to 750-900 TWh by 2050 given the retained energy shift scenario (RTE, 2021; Académie des Sciences, 2021 ; GrandJean *et al.*, 2014). Indeed, the applications of electricity are numerous and can meet almost all the industrial or individual needs of our advanced societies – including individual transport (battery and especially production of hydrogen by water electrolysis). To address this issue, the production of electricity by atomic fission (of ^{235}U and/or ^{239}Pu) has major advantages (Schlömer *et al.*, 2014; Guillaumont *et al.*, 2021): very low CO_2 emissions per kWh produced (6-12 g/kWh) comparable to wind energy, very high energy density of nuclear fuels compatible with sustainable source material and low land consumption for Nuclear Power plants construction. Availability of nuclear electricity production exceeds largely that of the intermittent renewable energy resources with a load factor for nuclear power energy generation of 0.85 compared to 0.1 to 0.25 for wind or solar energy production. The present world's uranium resources are sufficient for supplying nuclear fuel over a period of one hundred years up to several hundred years with the Fast Neutron Reactor technology (enabling the full energy potential of uranium to be exploited).

The energy guidelines decided in France in the 1970s following the first oil crisis (Messmer Plan, Gaïc Le Gros, 2016) enabled France to acquire a fleet of nuclear power plants in the following 30 years (currently 56 reactors in operation, all pressurized water technology) contributing to the production of more than 70% of electricity. Combined with hydro-electric production (10-14% of annual electricity production) and renewable energy resources (wind plus solar), French electricity production is thus more than 90% carbon-free (https://www.rte-france.com/eco2mix). Such electricity production mix allows France to limit very strongly the greenhouse gas emissions related to the production of electrical energy compared to our European neighbours (https://app.electricitymap.org/map).

If, in normal operations, the entire nuclear power plant (from the manufacture of the fuel, its use in power plants, then its reprocessing and the storage of wastes) leads only to very low radioactive discharges with no health impact, accidental situations can lead to significant releases of radionuclides to the atmosphere with important consequences for the environment and the surrounding populations. Taking into account the specificity of nuclear installations and the consequences of releases to the environment, from the design of installations, measures shall be taken to prevent accidental situations or limit their effects, in all phases of a nuclear facility's life – from construction to dismantling. This safety culture at a very high level is ensured by the operator and controlled in France by an independent authority (Nuclear Safety Authority) with the technical support of IRSN.

Although the probability of an accident with very advanced core melting or degradation remains very low (10^{-5} reactor/year, Cénérino, 2008), and the measures to reduce the occurrence of such accidents are constantly reassessed/improved, the deployment of large-scale nuclear power generation (442 reactors currently in operation and 57 under construction (from WNA, 2021) means that the occurrence of this type of accident cannot be excluded. Over the past four decades, three main accidents occurred:

• The severe accident on a pressurized water reactor at the Three Miles Island power plant (USA, 1979) which led to a very advanced meltdown of the core following technical and human failures (IRSN website, 2019). This accident resulted in only limited releases to the atmosphere (0.56 TBq for ^{131}I). Indeed, although significant quantities of radionuclides were released into the containment building during this accident, its integrity was maintained and it was thus able to act as a barrier to confine radioactive species. This event was ranked at Level 5 of the International Nuclear Event Scale (INES).

• The Chernobyl disaster in 1986 (IRSN website, 2021b) which is a reactivity accident on a RBMK-type reactor that caused the reactor to explode and a multi-day graphite fire that caused the massive dispersion of very large amounts of radioactivity into the atmosphere (up to 1800 PBq for ^{131}I). This accident was ranked at the maximum level 7 on the INES scale.

• The major accident at the Fukushima Daichii power plant in 2011 (IRSN website, 2021a), which was caused by the combination of two major natural events: an earthquake of very high intensity followed by a tsunami that flooded the entire plant and caused the loss of conventional cooling sources as well as total power losses for the 4 reactors located at the bottom of the plant. The shutdown of cooling led to the melting of the cores of reactors 1 to 3 over three days (the n°4 being in maintenance and thus discharged) and loss of containment integrity following explosions resulting in massive releases of radionuclides to the environment (100-200 pBq iodine-131). This accident was classified as INES Level 7.

The last two accidents resulted in massive releases of radionuclides to the environment and forced large-scale population evacuations. Remediation (total or partial) of the sites requires considerable effort spanning several decades. The consequences of such accidents in terms of economical and societal costs (IRSN website, 2013) make it a major issue in the acceptability of this energy by the public and has for more than forty years motivated major research efforts by operators and safety institutes of the major nuclear countries (France, United Kingdom, USA, Japan, Canada…). In France, the main research programmes on nuclear reactor accidents were initiated in the early 1980s following the TMI accident and were carried out by the main operators in the nuclear industry (IRSN, CEA, EDF, Framatome, Orano). This work has focused on both reactivity accidents (RIA) resulting from a local or extended loss of fission reaction control, and severe core melting (SA) accidents whose residual core heat cannot be evacuated at reactor shut down.

The remainder of this manuscript will focus on researches into severe pressurized water reactor accidents. The aim is to understand as precisely as possible the physical and chemical phenomena involved, to quantify/model them and to reduce their uncertainties. The ultimate goal is to develop simulation tools that can be applied to reactor cases in order to be able to predict the progression of a large panel of severe accident situations and to assess the possible releases to the environment based on accidental scenarios and be able to define suitable post-accident management strategies. Modelling cannot do without experimentation useful to guide and validate models development. The experiments were carried out on the one hand by considering the different phenomena separately and on the other by carrying out more general tests (but on a very small scale compared to the reactor case) in order to evaluate the interactions between these phenomena. The research was carried out on experimental installations on a technically (and financially) accessible scale, while remaining sufficiently representative to allow extrapolation to the reactor case.

In a typical scenario of a nuclear severe accident (Cenerino, 2008; Jacquemain *et al.*, 2015), the initiating event(s) can be a series of failures in the circuit ensuring the cooling of the core (Reactor Coolant System, Secondary loop or even Reactor residual heat removal circuit) which can lead to partial or even total loss of cooling systems. Indeed, even after core shut down, the residual heat (representing up to 7% of the nominal thermal power of a core and mainly due to fission products decay heat) has to be constantly removed (Jacquemain *et al.*, 2015). Failure of cooling systems results in a dewatering of the core and subsequent overheating. Severe accidents are characterized by extended core degradation i.e., by losing its geometrical integrity induced by melting and debris formation when the non-submerged parts of the core undergo significant temperature rise (more than 1200°C). At this stage of core degradation, significant material releases occur in vapour form (volatile fission products and control rod material), which are then transported through the reactor coolant system and partially released into the containment building. During a severe accident, chemical reactivity in the containment building must take into account the released fission products, the presence of steam, water, organic material, metal and concrete surfaces, high temperatures and radiation effects.

Moreover, different physical phenomena are liable to occur progressively with core degradation such as vessel rupture inducing the escape of the degraded core (named corium) in the lower part of the containment and then molten core/concrete interaction in the reactor pit, or steam explosion when the molten core encounters water accumulated in the sump. In the containment atmosphere, hydrogen combustion can cause direct containment heating and finally, containment rupture, and leakages. This mode of containment failure is very important as it can allow radioactive species to be released earlier directly to the environment.

The main radiological significant fission products to be released into the environment in case of severe nuclear accident are iodine, caesium and tellurium. Strontium, ruthenium, barium, molybdenum and the lanthanides are less released. Fuel material and minor actinides are not usually considered to be released in such accident scenario. Behaviour of iodine is of main concern given its volatility and the potential short-term radiological

consequences of releases of radioactive iodine to the environment. The amount, the nature and isotopic composition of the released radioactive material released from the core is called "Source Term", and its quantification is the main objective of the international research programs in severe accident as it is taken into consideration when defining corrective actions that have to be taken to protect people under these conditions. The source term is defined as a specific type of release characteristic to a family of reactors and representative of the accident type, i.e., in general a containment failure mode following complete core melt (Cenerino, 2008).

In the objective of better predicting the consequence of such an accident and evaluate the radiological consequences to the population and the environment, the French expert in nuclear safety has developed, over the past 25 years, several computational tools dedicated to simulate an accidental sequence of a PWR and predict fission products source term and in particular, the radioiodine source term. The integral Accident Source Term Evaluation Code (ASTEC) (Chatelard *et al.*, 2016) code is designed to simulate the entire core melt accident from the initiating event up to radioactive release outside the containment vessel – including thermahydraulic aspects, core degradation, material release and transport in the RCS up to the containment, and physico-chemical evolution of the main FPs. This code is mainly dedicated to safety analyses. The atmospheric dispersion of the radionuclides and especially that of iodine, is then modelled by C^3X operational tool (Saunier *et al.*, 2020) also developed by IRSN, further dispersion in the terrestrial, and biogenic compartment is then taken into account in SYMBIOSE tool (Gonze *et al.*, 2002).

Development of such simulation tools must rely on large experimental data sets – needed both for the development of the physical and chemical models implemented in the code and for the final validation process. Code validation ensures that the outputs give a reliable representation of all physical and chemical phenomena that can be encountered in a given severe accident scenario. In this view, several experimental research program were launched at IRSN over the past decades dedicated to study the phenomenology of a severe accident from core degradation up to iodine chemistry in the containment vessel. Concerning the specific point of material release, transport and their long term behaviour in the containment building, several experimental programs were conducted by IRSN or performed in collaboration with other national (CEA) or international partners. These programmes involved separate effect tests (ISTP-EPICUR, STEM-EPICUR for iodine behaviour in conditions of the containment, STEM-START dedicated to Ru transport and revaporisation in the RCS; Clément and Zeyen, 2005; STEM&STEM2 on OECD web site), coupled effect tests (as VERCORS and VERDON for FP release from actual small fuel samples, CHIP-CHIP+ dedicated to study physical chemical behaviour of complex chemical systems involving several FPs and CR material in the RCS; Pontillon and Ducros, 2010; Gallais-During *et al.*, 2012; Clément and Zeyen, 2005) and large scale integral tests featuring a whole degradation sequence and performed on large fuel samples (Phébus FP programme, 1990-2012; Clément and Zeyen, 2013). Besides, major efforts have been made to better assess or complete the thermo-chemical properties of the material in SA conditions (fuel, cladding and control rod alloys, expected released species based on literature review, experimental studies at analytical scale (High temperature mass spectrometry for instance) or l chemistry simulations (theoretical approaches via DFT and molecular dynamics, thermochemical computations …).

In this view, my contribution over the past 20 years at IRSN in the field of research on severe accident was to develop and conduct experiments dedicated to better understand the behaviour of fission products from their release from the degraded fuel, their transport in the RCS up to the containment and finally in the atmospheric compartment. A special attention was brought on caesium and iodine chemistry as these volatile FPs are the most concerned with possible environmental consequences. Within the Department of Studies and Experimental Research from the Nuclear Safety division, I took part to several international or national experimental programmes, some of them still going on.

From 2002 up to 2006, my first contribution was the follow-up of the post-test chemical analyses on samples collected during FPT2 and FPT4 tests of the Phébus FP programme. In this view, I managed an international working group on radio analytical chemistry. Within the experimental IRSN team specialized in γ spectrometric characterizations, I realised then the synthesis on material release and transport of these two tests and participated as a main contributor to the drafting of the corresponding test reports and to the final synthesis of the Phébus FP programme. Some main features of this work will be presented in chapter 2.

From 2007 up to now, within the Environment and Chemistry Experimental Research Laboratory, I carry on the experimental research on FP physico-chemical behaviour in conditions of severe accident. In the framework of

the international CHIP programme (2004-2012) and its bipartite CHIP+ programmes (2012-2019) in collaboration with EDF, I worked on main FPs (I, Cs, Mo) and Control material (B, In, Ag, Cd) transport in conditions of a RCS on small scale lines and the CHIP phenomenological line at IRSN. The main aim was to identify the conditions enhancing the transport of gaseous form of iodine as was observed in some Phébus FP tests. Tight collaboration with academic partners helped to progress on this problematic by performing analytical experiments on simplified chemical systems (flame studies in collaboration with the PC2A laboratory of the University of Lille through the common laboratory C3R) and by allowing a fine characterization of the deposits collected after tests performed with complex system in the CHIP PL line (multi techniques surface characterization in collaboration with the UCCS and LASIR laboratories of Lille university and the ISM-GSM group of Bordeaux university). Some important development of the CHIP PL line and relevant results concerning the reactivity of the main FPs in SA conditions will be presented in Chapter 3.

More recently, I have focused my research on the mid-term behaviour of FPs inducing late phase release as observed in the aftermath of the FD accident. Within the MIRE program (PIA - ANR-11-RSNR-0013-01), the revaporization behaviour of caesium iodide was considered – the experimental work was performed though a Ph-D work (2014-2017) under shared supervision with our partners of the UCCS. In the framework of this study, the development of on-line instrumentation dedicated to molecular iodine monitoring was finalised (post-doctoral position under my supervision) and allowed to complement the capabilities of the experimental lines. Main instrumental development and results of this study will be presented in Chapter 4.

In continuation to the studies performed on iodine source term evaluation, the last issue in which I am involved concerns the fate of radio-iodine in the atmospheric compartment after accidental/ incidental releases. In order to improve the relevance and accuracy of iodine modelling in the IRSN dispersion software, experimental studies at laboratory scale were undertaken since 2017 with the objective of fulfilling the understanding of iodine atmospheric mechanism in particular its interaction with atmospheric aerosols. We considered first the reactivity of methyl iodine with surrogates of aerosols most representative of the atmosphere (inorganic and organic). The new thematic needed the development of dedicated reactors. Main outcomes of this first study – undertaken in collaboration with the ISM-GSM group of Bordeaux University – will be presented in Chapter 5.

Finally I made a short synthesis of all these research works and provided some perspectives for the nexr 5-years.

Iin the appendix part, I present some of my most relevant publications in peer reviewed international publications.

2 PHEBUS TEST –EXPERIMENTAL CIRCUIT DATA

The Phébus Fission Product (FP) project was an international reactor safety project initiated in 1988 and supported by the European Commission, with NRC, JNES, JAEA, KAERI, COG, PSI and HSK [1]and managed by the Institut de Radioprotection et de Sûreté Nucléaire (IRSN) in the Phébus reactor operated by CEA (Cadarache). The aim of this programme was to perform integral experiments (scale 1/5000th) simulating phenomena involved in a severe accident of a nuclear power plant, starting from the fuel degradation, the release of fission products (FPs), control rod material and structure material and their transport through the reactor coolant system (RCS) to the containment building of a Light Water Reator (LWR) (Schwarz *et al.*, 1999; Clément and Zeyen, 2013). A special attention was focused on the iodine radiochemical behaviour as it can directly impacts the consequences of potential radioactivity release to the environment.

Such integral experiments are seen as a necessary addition to one-by-one qualification of physical and chemical models using the results of separate effect experiments. Indeed, separate effect studies have the drawback of making strong hypothesis related in particular to the additivity of the different phenomena or on the nature of involved species not allowing the assurance that some important phenomena have not been omitted. For Integral experiments contribute also to the validation of models and computer codes to be used for the calculation of the source term in case of a severe accident with core meltdown in a LWR as the IRSN ASTEC code (Chatelard *et al.*, 2016).

The Phébus test matrix included five in-pile experiments successfully performed from 1993 to 2004. The first two tests, FPT0 and FPT1, were dedicated to studying fuel bundle degradation and material release and transport in a model primary circuit and containment building under steam rich (steam flow rate of 2~g/s) and low pressure (about 0.2~MPa) conditions. The first test (FPT0, Girault *et al.*, 1999) was performed in December 1993 using a bundle of fresh fuel rods. The second one (FPT1, Jacquemain *et al.*, 2000) was conducted in July 1996 under similar conditions, but with a bundle of irradiated fuel rods(23~GWd/tU). The FPT2 test (Grégoire *et al.*, 2008), conducted with 32~GWd/tU fuels rods in October 2000, aimed at studying the same phenomena but in a steam poor environment (steam flow of 0.5~g/s) and with an injection of boric acid (with a boron mass concentration of 1000 ppm). The FPT3 experiment (Payot *et al.*, 2010), performed in November 2004, must be considered as a continuation of FPT0, FPT1 and FPT2 series except that the absorber material was boron carbide instead of silver-indium-cadmium. The objective of the specific FPT4 test (Chapelot *et al.*, 2004), performed earlier in July 1999, was to study core degradation and release from a debris bed.

My task within the experimental Phébus FP team (2002-2006), was the follow up of the post-test chemical analyses performed on sampling from the experimental circuit (FPT4 and FPT2 tests). The main objective of such chemical analyses was to collect information on the release and transport behaviour of the poorly or non γ-active material (fuel material, some fission products, control rod and structural material). In continuation to this work, I achieved the synthesis on material release and transport in the model primary circuit of the Phébus FP facility as reported in the final experimental reports of the FPT4 (Chapelot *et al.*, 2004) and FPT2 (Grégoire *et al.*, 2008) tests as well as contributing to the final synthesis of the Phébus FP programme (Haste *et al.*, 2012; Grégoire and Haste, 2013). This section will be focused on some relevant results of material release and transport during the FPT2 test concerning main FPs (Cs, I, Mo, Ru, Ba..), control rod (In, Cd, Ag), fuel (U) and structure elements (Zr). A special section will be devoted to iodine behaviour in the circuit. The Phébus facility and FPT2 test scenario in connection with the main bundle degradation events will be presented first to provide a global overview of such integral experiments.

[1] HSK- NRC Nuclear Regulatory Commission, NUPEC Nuclear Power Engineering Corporation, JNES Japan Nuclear Safety Organization, JAEA Japan Atomic Energy Agency, KAERI Korean Atomic Energy Research Institute, COG Candu Owners Group, PSI Paul Scherrer Institute, HSK Swiss Federal Nuclear Safety Inspectorate, CEA Commissariat à l'Energie Atomique.

2.1 Description of the Phébus FPT2 experiment

The Phébus FP facility was operated by the French ''Commissariat à l'Energie Atomique'' (CEA) at Cadarache and is implemented in the Phébus reactor (pool type driver core with a central cavity). An overall description of the Phébus FP facility is given by March and Simondi Teisseire (2013). The detailed design, material data and test scenario of the FPT2 test are reported in the FPT2 final report (Grégoire *et al.*, 2008).

2.1.1 The Phébus FPT2 test experimental facility

The Phébus FP facility was designed to be representative of a French 900 MWe PWR scaled down 1:5000 in the frame of a low-pressure cold-leg break scenario as illustrated in Figure 2.1. The objectives were to investigate:

- The degradation of a fuel bundle with a fuel mass of about 10kg. The test assembly was composed of twenty Zircaloy-cladded UO_2 fuel-rods (2 fresh fuel rods and 18 pre-irradiated at an average burn-up of 32 GWd/tU with 1-metre-long fissile length (initial enrichment was 6.85%)),together with a central stainless-steel-cladded SIC (Silver Indium Cadmium) control rod[2]. The fuel bundle including two Zircaloy-4 spacer grids was surrounded by insulating shrouds (several concentric high density thoria sleeves) and housed in a pressure tube of inconel placed in the central cavity of the Phébus reactor, which provides neutron flux heating for the degradation of the test bundle (1). An upward flow was continuously sustained in between rods (steam injection flow rate 0.5 g/s, with boric acid at a boron mass concentration of 1000ppm), during the bundle degradation. A fraction of the injected steam was converted into hydrogen ($Zr + H_2O \rightarrow ZrO_2 + H_2$) during the oxidation phases;
- The FPs release, deposition and transport from the test bundle to the containment via an upper-plenum and a vertical line (directly located above the test bundle) connected to an experimental circuit that simulates the RCS (reactor coolant system) and includes a model steam generator. The latter, which consisted of one 4-metre-high inverted U-tube (3), ensured temperature transition between the circuit hot leg (2), regulated at 700°C, and the circuit cold leg (4), regulated at 150°C. The temperature regulation transition is located at the steam-generator inlet. The released materials conveyed with the fluid flow through the fuel bundle and the experimental circuit, ended up in a $10m^3$ vessel simulating the containment building (5);
- The material behaviour in this containment vessel on the long term, with a special attention to iodine source-term issue. The containment is equipped with a water-filled sump (120L buffered at pH=9) at the lower part (6) and dry and wet painted surfaces (named condensers) suspended at the vessel top (7). The steam condensation occured throughout the degradation phase on the condensers. The sump is overhung by an elliptic floor, dedicated to recover most of the settled aerosol injected in the containment.

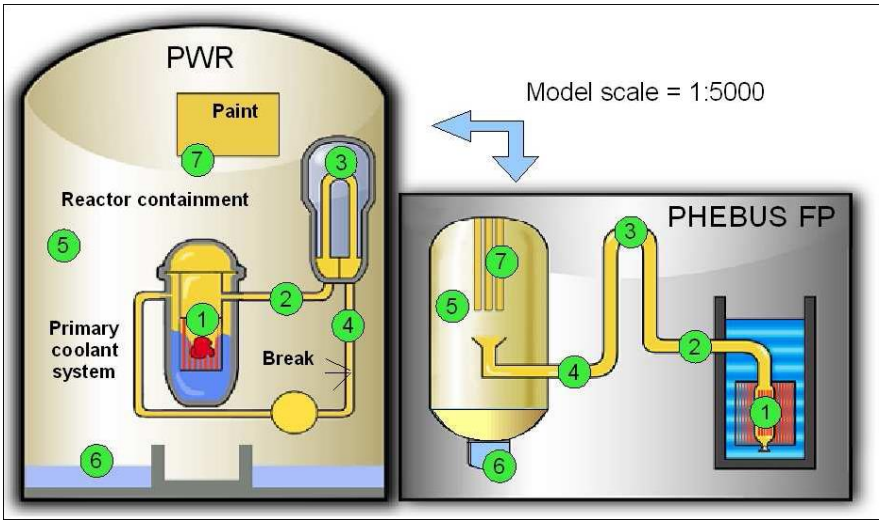

Figure 2.1 : The Phébus FP facility as compared to a PWR.

[2] The control rod was held in a fixed fully-inserted position. It was not actually used as a control rod, but rather as source of prototypic material to allow reactor-representative material interactions to take place during and after the degradation process.

2.1.2 Experimental circuit instrumentation

The test bundle (1), the experimental circuit (2), (3), (4) and the containment vessel (5) are well instrumented (Grégoire *et al.*, 2008) to analyze the key phenomena occurring through the test by means of several techniques:

- the fuel bundle degradation kinetics was mainly followed by thermocouple measurements. The final state of the bundle is characterized both by X-ray imaging techniques (radiography and transmission tomograms that allow to establish a general view of the post-test fuel bundle degradation) and by γ-spectroscopy examinations (providing a quantitative profile of γ -emitters of various nuclides present in the test device after the test);
- the thermal hydraulic conditions were also followed on-line throughout the test thanks to thermocouples, pressure probes, flow meters placed along the circuit and in the containment. In addition, hydrogen production (as a result of the zircaloy cladding oxidation) was measured on-line both in the experimental circuit and in the containment vessel;
- the material released from the fuel bundle, its transport through the circuit and its accumulation in the containment vessel were characterized by means of γ-spectrometers targeted at key positions of the hot leg, steam generator and containment vessel. In addition, sampling devices located in furnaces along the circuit hot-leg, the circuit cold-leg, and in the containment vessel were operated during the test (50-60 sampling operations). They were aimed at collecting both aerosols conveyed in the experimental circuit and released into the containment atmosphere (by filters and impactor devices) and liquid samples from the sump or the condensers (liquid capsules). All these samples were post-test analysed by γ-spectrometry for quantitative determination of the collected nuclide mass. Complementary destructive chemical analyses were performed on a selection of samples;
- the amount of material deposited between the fuel bundle and the containment was also evaluated on several zones namely on the plenum, on the vertical line, on the circuit hot leg (on-line and post-test γ-scannings), on the steam generator inner surface (post-test cut in 24 sections for γ-scanning and chemical analyses) and on the cold leg inner surface (post-test γ-scanning);
- some specific devices implemented in the experimental circuit (hot leg and cold leg) were specifically designed to discriminate the various iodine species transiting through the circuit. In the circuit hot leg, four sampling channels (composed of filters at 700°C and 150°C connected by the so called "Transition Line") allow to discriminate the iodine forms transiting at 700°C i.e. aerosol (condensed iodine species), vapour (iodine species condensing between 700°C and 150°C) and gas (iodine species transiting at 150°C and thus condensing at temperature lower than 150°C such as I_2 and HI). In complement, thermally controlled sampling tubes (so-called Thermal Gradient Tube) allowed to characterize vapour condensation in the 700-150°C range. In the cold leg (150°C), successive filtering stages were used to distinguish between condensed iodine species (trapped in stainless steel or quartz filters), gaseous inorganic iodine (trapped in silver knitmesh filters) and gaseous organic iodide (trapped in silver zeolite filters). These sequential samplings were post-test γ-measured.

In the framework of the Post Test Analyses plan, ~30 samples devoted to aerosol collection were sent to external laboratories for destructive chemical analyses: mainly aerosol filters and impactor samples from the hot leg, cold leg and containment vessel as well as 3 sections of the steam generator model. The objectives of these chemical analyses were to assess a reliable nuclide distribution in the experimental circuit for the stable or poorly γ-active elements. Indeed γ-spectrometric measurements allowed to determine the nuclide distribution only for ^{140}Ba/^{140}La, ^{137}Cs, ^{131}I, ^{129m}Te, ^{110m}Ag and ^{114m}In. The main analytical technique was Inductively Coupled Plasma – Mass spectrometry after solubilisation of deposits in appropriate aqueous media (alkaline and concentrated nitric acid solutions). Direct and indirect information on aerosols characteristics (size, morphology and composition) were obtained by Scanning Electron Microscopy coupled to Energy Dispersive X-ray Spectrometry (impactor samples). The main issue of these chemical analyses was the handling of high radioactive samples which required to work in the hot cell facilities of the partner laboratories of the Phébus programme: ITU, CEA Cadarache and Saclay, AEA-T, PSI. The PTA campaign of FPT tests lasted three years (2002 -2005).

2.1.3 Experimental scenario and main bundle/FP release events

The first phase concerned the fuel re-irradiation period (8 days) to generate a representative short lived FPs inventory. Then, a transition period (37 hours) occurred both to deplete the reactor xenon poisoning and to adjust the circuit thermal hydraulic conditions. The experimental phase itself comprised two main parts namely the degradation phase (or transient phase) and a long term phase.

The degradation phase corresponded to a 5-hours transient[3] during which the steam flow through the bundle was set to 0.5 g/s, while the driver core power was progressively increased by successive plateaus and ramps from 0.48 up to 7.9 MW to heat-up the experimental bundle (Figure 2.2). This phase lasted 19740 s. The temperature reached during the transient, as a result of both the nuclear power increase and the Zircaloy oxidation, led to the successive thermo-mechanical failure of the fuel clad and the absorber rod, followed by the melting and relocation of fuel and structural materials. This degradation phase resulted in an extensive release of hydrogen, fission products, fuel elements and structural materials into the circuit and the containment vessel.

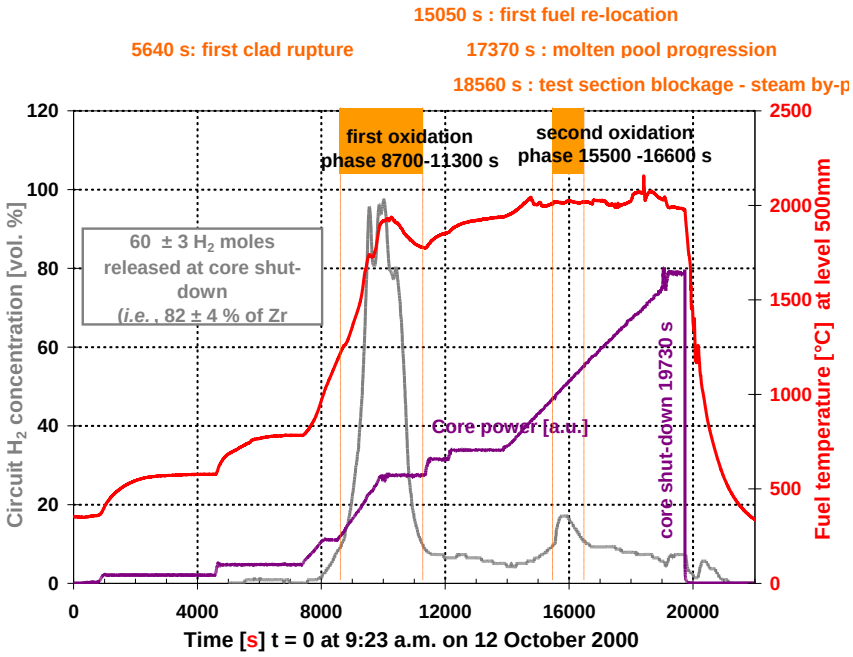

Figure 2.2 : Phébus FPT2 test General chronology of the transient.

The first indication of Zircaloy cladding failure was identified at the beginning of the second temperature plateau by the detection of aerosols released in the circuit (5630 s) at a temperature of fresh fuel of ~760°C. Later, the release of noble gases was measured in the containment by γ-spectrometry. The SIC control rod rupture is evidenced at 8730 s and for a temperature of ~730°C, before the oxidation runaway (9204 s). Due to the lower steam injection rate, about 0.5 g/s in FPT2 instead of 2 g/s in FPT0 and FPT1, the progression of the Zircaloy cladding oxidation front was slower in FPT2 than in FPT0 and FPT1. The first oxidation phase lasted about 43 minutes (from 8700 up to 11300 s with a steam poor period (H_2 > 75 vol%) of 18 minutes and a maximum hydrogen concentration of 97 vol%.

As in FPT0 and FPT1, a second less-intense oxidation phase was observed at a later stage of the degradation, correlated with re-location of hot material in the lower part of the degraded test bundle (from 15500 up to 16600 s). This late oxidation phase lasted about 18 minutes (H_2 > 10 vol%), with a 3-to-4-minute-long plateau corresponding to a maximum hydrogen concentration of 17%. A total production of about 60 moles of hydrogen was measured throughout the transient. Assuming that hydrogen was essentially produced by the oxidation of Zr about 82% of the Zr was oxidised during the bundle degradation.

During the degradation, some progressive fuel relocation occurred from the middle to the bottom of the bundle. It started at 15050 s with fuel departing from the hottest plane and arriving on to the lower Zircaloy spacer grid

[3] In the following, times are specified relative to the time origin of the transient: t = 0 at 9:23 a.m. on October 12th, 2000 (start of the power increase).

(see Figure 2.3) . In the end, the stacking area extended to the whole cross section of the test bundle. A as result of the constant temperature increase in the degraded bundle, molten pool formation in the fuel relocation zone is observed starting from 17370 s. A chimney was formed still allowing the steam to flow through the molten pool but was later blocked at 18560 s as the molten pool extended over all this zone. This plugging of the test section caused the steam to bypass the bundle through the gaps in the shroud. The pool that formed in the lower part of the test bundle finally filled the entire cross-section and led to the experiment shutdown at 19740 s, due to the rapid temperature increase inside the shroud. The relatively low liquefaction and relocation temperatures (2200-2300°C) of the fuel rods already observed in the previous FPT0 and FPT1 tests were confirmed.

The experimental circuit sequential samplings (hot leg and cold leg aerosol filters and iodine specific instrumentation) were operated during the key phases of the transient (first clad rupture, main and late oxidation phases) so as to obtain a kinetic of material release and transport in the circuit.

The transient was ended by the reactor power shutdown and was followed by the cooling of the bundle by steam and then by the containment vessel isolation. The experimental phase went then on with a 4-day long-term phase consisting of: an aerosol phase (2 days) dedicated to the analysis of aerosol deposition mechanisms in the containment (gravitational settling and wall deposition), a washing phase (20 min) which aimed at collecting aerosols into the sump, and a chemistry phase (2 days) devoted to the analysis of iodine chemistry under conditions representative of a severe LWR accident. The description of the fission product behaviour in the containment vessel both during the transient and the long term phase is reported in the FPT2-final report (Grégoire *et al.*, 2008).

2.2 FPT 2 test - Final state of the bundle

The degradation objective which consisted in reaching at least an instantaneous 2 kg of molten fuel was successfully fulfilled as post-test non-destructive analyses indicate that the mass of material in the molten-pool zone (100 to 263 mm BCF) was ~5.2 kg, i.e., ~2.9 kg (resulting from fuel relocation) added to the initial ~2.3 kg mass.

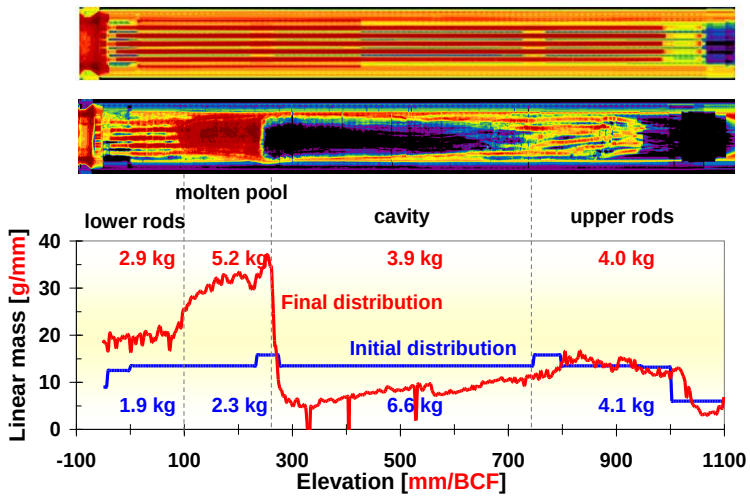

Figure 2.3 : Phébus FPT2 test –Initial and final state of the fuel bundle : X-ray tomography and mass distribution. Elevation reference is the "bottom pof the fissile column.

Four zones can be distinguished in the degraded bundle (Figure 2.3), characterised by different fuel degradation states:

- bottom of the degraded bundle from -50 to 100 mm/BFC: at the location of the lower support plate some materials are visible between the rods. The aggregates are made of corium, or of control rod materials. Above the support plate, fuel rods are still in place and surrounded with materials coming from upper levels;

- the molten pool zone from 100 to 263 mm/BFC: it is quite extended compared to the previous Phébus tests. Post test analyses showed that the corium composition (U_2O and Zr-oxide rich with low contents of iron, chromium and absorber material) is quite comparable with those obtained in the FPT0 and FPT1;
- the cavity from 263 to 766 mm/BFC. The cavity is a crust of molten materials with no remnant of fuel rods. The upper part of the cavity contains rod remnants at the periphery;
- the upper fuel rods from 766 up to 1027 mm/BFC. At the lower level of this zone, there are only peripheral rods and at the upper level of this zone, all the rods are visible.

2.3 Fission product and material transport/deposition in the experimental circuit

The release of FPs, control rod and structure materials through the primary circuit during the FPT2 transient were strongly correlated with bundle degradation events. Three main release phases could be identified: the first large release event was observed during the first oxidation phase (first phase), followed by a period of fairly steady release (for volatile fission products and control rod material) until approximately the late oxidation phase (second phase). Then, a second large material release occurred (less volatile material), at the time when oxidation happened in the lower part of the fuel bundle, accompanied important fuel liquefaction and relocation (third phase). At 17150 s, aerosol concentration in the containment atmosphere peaked then it started to decrease suggesting that materials was transported to the containment only in small quantities that could not compensate for losses associated with deposition processes. After 17500 s, i.e. after the formation of the molten pool, fission product transport to the containment almost stopped; this did not mean that material were not released from fuel anymore since circuit deposits could account for differences between containment measurements and integral fuel release.

2.3.1 Transport in the cold leg of the experimental circuit

Mass flow rate of material transported in the experimental circuit could be determined for the cold leg only. Two independent sources of data were used to establish material transport kinetics:

- The post test γ-spectrometric and chemical analyses performed on the aerosols filters operated in the cold leg during the transient (6 sequential samplings operated at key period of the transient). The single activities or nuclide mass determined for each sample were converted in mass flow rate given the thermal hydraulic data of each sampling. Assuming a linear law between two successive samplings, an average mass transport kinetic could be then build up for most of released FPs, control rod, fuel and structural material. An integral filter operated during all the transient completed this data set.
- The on-line γ-activity evolution in the containement atmosphere which was determined by a dedicated on-line γ-station. These on-line data allowed to determine quantitatively the material accumulation in the containement vessel during the whole transient but only for a reduced set of nuclides (^{137}Cs, ^{131}I, ^{132}Te, ^{99}Mo and ^{116m}In). Its derivative correspond to the mass flow rate in the cold leg assuming that all material transported in the cold leg is released into the containement vessel.

When considering the cumulated masses, comparison of the two data sets are rather satisfactory for I (Figure 2.4), Cs (Figure 2.5), and Te, less for Mo (Figure 2.6). After rescaling with cold leg integral filter data, In transport data matches also with a good degree the containement vessel measurements (Figure 2.7). The discrepencies between the derivative of containment atmosphere activity measurements and the mass flow rate curves determined in the cold leg (Figure 2.4 and Figure 2.5 for I and Cs respectively) may account for a better time resolution of on-line measurement able to catch the short duration release events which was not the case of the sequential samplings – especially for In. Nevertheless, larger uncertainties for on-line measurements may also account for these discrepencies. For the poorly γ-active and stable elements, transport in the cold leg (and subsequent cumulated mass injection into the containement vessel) is only determined from cold leg aerosol samplings (as displayed in Figure 2.7 for Ru, Ag and Cd).

The elements may be classified depending on their release/ transport kinetics from the degraded fuel bundle to the containment vessel :

- Noble gas release started during the first oxidation runaway. The released noble gases exhibited a faster initial accumulation kinetics in the containment vessel than volatile fission products (not shown here);
- Volatile and semi volatile FPs release to the containment occurred at a fairly steady rate between the end of the first oxidation peak and the end of the second oxidation peak (Cs, I, Rb and Te, Mo with some delay) in qualitative agreement with the fact that bundle degradation was progressive in FPT2.;
- Low volatile FPs (Ru, Ba, La, Y, Sr,) were mostly released during the late phase of the transient starting at high temperatures in the bundle (late oxidation phase and final heat up) as shown in Figure 2.7 for Ru. This is also the case of structure (Sn, Zr), instrumentation material (W) and fuel (U) though there are considered almost as non volatile;
- Control rod material (Cd, In, Ag) release/ transport is dependent of the type of control failure (Haste and Plumecoq, 2003; Dubourg *et al.*, 2010). In the case of FPT2 test, a large burst of Cd is observed at the beginning of the first oxidation phase (Figure 2.7) – accordingly to a large control rod failure. More refractive, significant In and Ag releases started at higher bundle temperatures, after the first oxidation phase for In (followed by a fairly steady release up to the second oxidation peak) and during the late oxidation phase for Ag.

Due to experimental difficulties (failure of thermal hydraulic measurements for the hot leg samplings), no mass flow rate curves could be established in the hot leg of the circuit during the transient.

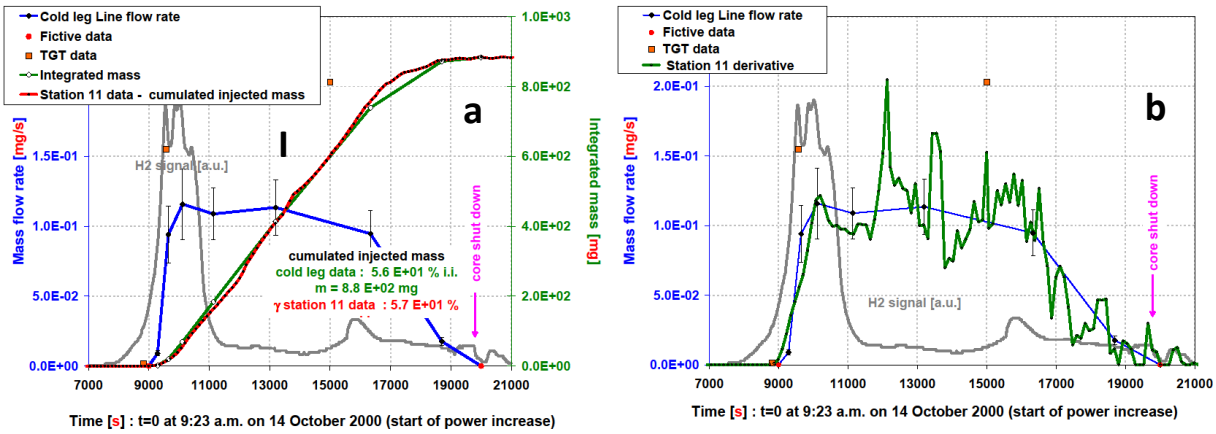

Figure 2.4 : Phébus FPT2 test - Iodine cold leg transport determined from cold leg samplings. Comparison with on-line containtement atmospheric γ-measurements a) cumulated mass, b) derivative.

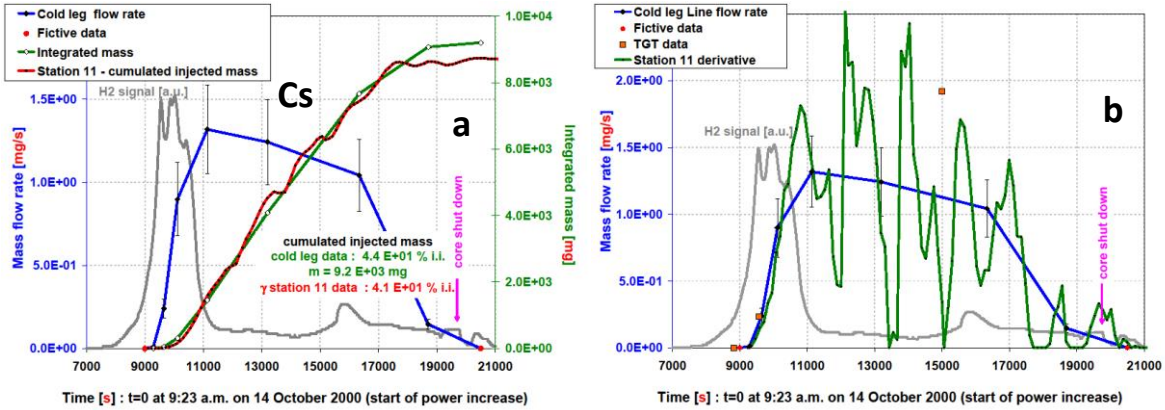

Figure 2.5 : Phébus FPT2 test - Caesium cold leg transport determined from cold leg samplings. Comparison with on-line containtement atmospheric γ-measurements a) cumulated mass, b) derivative.

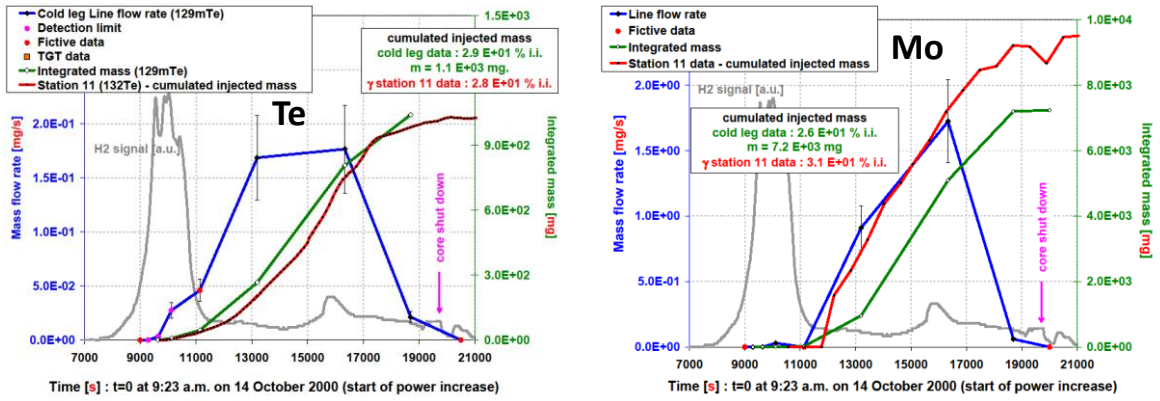

Figure 2.6: Phébus FPT2 test – Te and Mo cold leg transport determined from cold leg samplings. Comparison with on-line containtement atmospheric γ-measurements (cumulated mass).

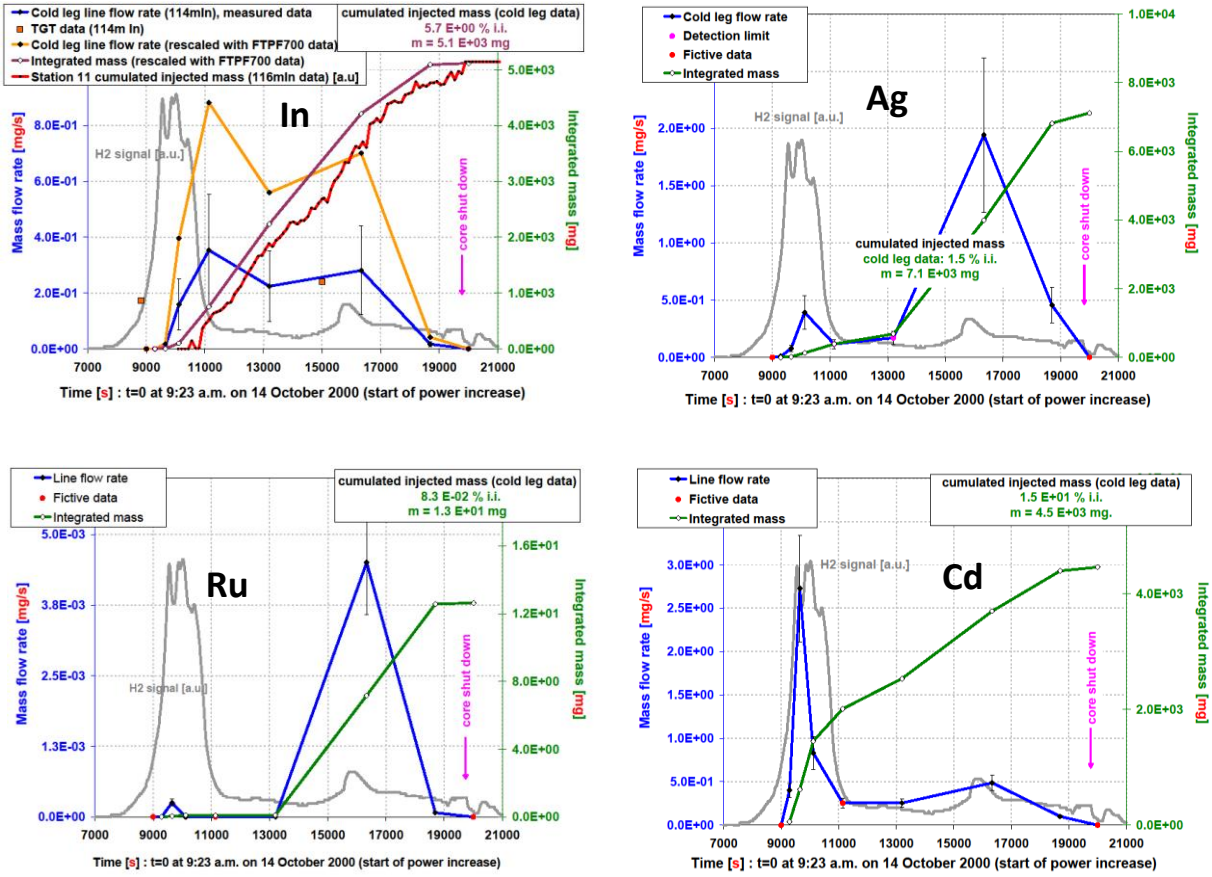

Figure 2.7: Phébus FPT2 test – In, Ru, Ag and Cd cold leg transport determined from cold leg samplings. Comparison with on-line containtement atmospheric γ-measurements (cumulated mass) only for In after rescaling with cold leg integral filter.

2.3.2 Material retention in the circuit

On the circuit wall – from the upper plenum down to the cold leg, deposition processes probably involved i) vapour condensation on cooler surfaces, possibly followed by chemical interactions with the surfaces or with the deposited elements, ii) thermophoresis, iii) aerosol impaction, and iv) aerosol settling processes. Vapour condensation and thermophoresis are most expected in the strong temperature transition zone of the upper plenum (> 1500 -700°C) and steam generator model inlet sections (700-150°C), whereas aerosol impaction and settling are most expected in the colder zone of the experimental circuit (150°C). During the FPT2 test, the low steam injection rate (0.5 g/s) resulted in a significant deposition of volatile fission products (Cs, I, Te and Mo) in the upper section of the degraded test bundle (above the upper grid at the level of the remaining upper fuel

rods, see Figure 2.3). Deposits were also significant for all species (except noble gases) both in the hot leg and in the cold leg of the circuit (as reported in Table 2.1 in section 2.4.3).

In the cold leg, deposit could be determined only for caesium, barium and silver. Nevertheless, compared to the mass injected into the containment, a generic behaviour could be identified for volatile (Cs) and low volatile material deposit (Ag, Ba) allowing to estimate the cold leg deposits for the unmeasured elements: cold leg deposition is estimated up to 11% and 43% of containment injected mass for volatile elements and low volatile elements respectively. In the hot leg, material deposition could be determined experimentally for a larger set of elements (Cs, I, Te, Ba, Ag) ; for the unmeasured elements, hot leg deposition was calculated with similar approach using hot leg deposit/cold leg transport ratio for low volatile elements (0.33 of the mass transiting through the cold leg) and for volatile elements (0.016).

In the steam generator model (SG) inlet section, deposition profile indicates that all material entered into the steam generator in a condensed form (simple exponential decay, involving a single deposition process assumed to be aerosol deposition process lead by thermophoresis), even the elements which were identified to be partly in a vapour form in the hot leg. For iodine and cadmium, this observation contrast to the previous FPT1 test (Jacquemain *et al.*, 1999), where those elements were identified as a mix of vapour and condensed species at the SG model inlet. A lower fluid/wall temperature at the SG model inlet than the target value (700°C) may explain this early vapour condensation. Deposits in the hot leg of the steam generator represented about 84% and 94% of the total mass deposited in the steam generator respectively for low volatile and volatile elements.

After the core shutdown, a large increase of caesium activity was observed on the steam generator, indicating re-volatilization of upstream caesium deposits (upper plenum and vertical line), caesium was next swept along with the carrier gas and deposited mainly in the steam generator. A similar observation was made for iodine : at the end of the degradation phase, both ^{131}I and ^{132}I activity kept on increasing on the steam generator tube till end of steam injection. This increase is shown to correspond to iodine creation by decay of respectively, ^{131}Te and ^{132}Te, which are deposited in large quantities along the circuit hot-leg. This fact suggests that tellurium deposits decay to volatile forms of iodine that are not retained in the circuit hot-leg, contrarily to earlier iodine deposits but that these volatile forms of iodine condense (at least partly) in the steam generator.

2.3.3 Aerosol characterisation

Condensed material was transported in the cold leg as mixed aerosols. The structure of the aerosol particles was predominantly ball shaped, with an AMMD (average mass median diameter) of about 2µm. Very fine particles may have been agglomerated to form larger particles.

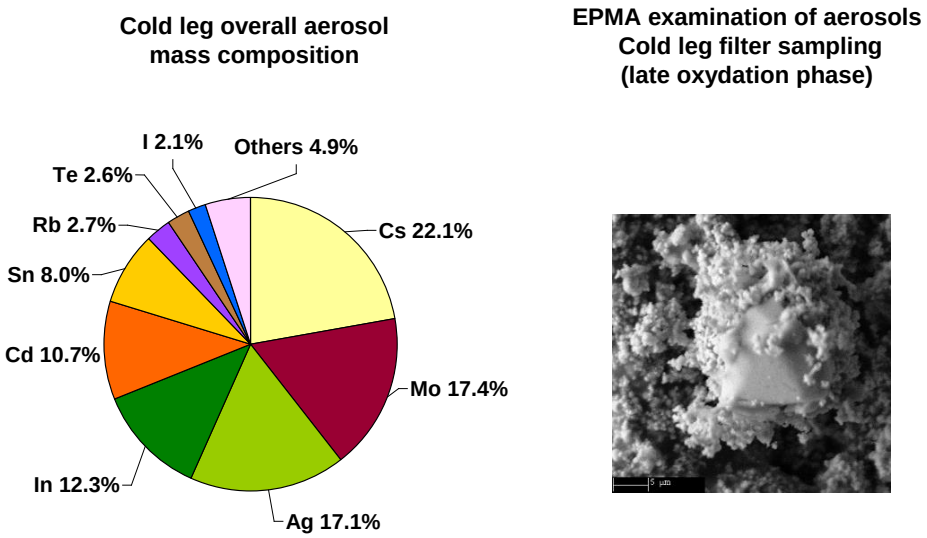

Figure 2.8 : Phébus FPT2 test – Aerosol release in the Containment vessel; Average morphology and mass composition.

The composition of the aerosols transiting through the cold leg (Figure 2.8) was dominated by fission products (Cs, Mo), control rod materials (Ag, Cd , In) and cladding material (Sn). The total material mass flowing through the circuit, determined from elements measured in the circuit either by γ-spectrometry or by chemical analyses, amounted to about 60~g in the circuit hot leg (vapour and condensed material) and about 42~g in the circuit cold leg. Based on speciation data gained from the previous FPT0 and FPT1 tests, oxidation of material could have increased the total aerosol masses to about 50 g in the circuit cold leg. The aerosol mass composition was dependent on the bundle degradation events:

- large control rod material (almost exclusively Cd) contributions during the first main oxidation phase;
- large volatile FP (Cs, Mo) and significant control rod (Ag) and structure material (Sn) contributions during the phase leading to the melt initiation and propagation;
- dominant Ag and significant volatile FPs (Cs, Mo), control rod (Cd) and structural material (Sn) contributions during the late oxidation and the final heat-up.

The aerosol mass concentration was at its highest level during the late oxidation phase: about 12% of the aerosol mass transited through the circuit during the main oxidation phase, 17% during the phase leading to the melt initiation and progression in the fuel bundle and 71% during the second oxidation phase.

2.4 Mass balance in the experimental circuit

Based on the quantitative analyses of the degraded fuel bundle (post-test γ-scannings), and the main sections of the experimental circuit (γ-spectrometry and ICP-MS analyses) one may build up an overall distribution and an integral release for most of nuclides of interest, taking into account:

- The initial bundle material inventory for the fuel, the fission products, the control rod and the structural materials;
- The amount of material remaining in the test bundle zone or re-deposited in the upper plenum and the vertical line at the exit of the test bundle at the end of the degradation phase;
- The amount of material deposited in the circuit experimental lines (horizontal hot leg, model steam generator and horizontal cold leg) at the end of the transient;
- The amount of material (mainly aerosol and a small fraction of gaseous species) which transited through the circuit cold leg and was finally released into the containment vessel during the degradation phase.

2.4.1 Initial bundle inventory

The fission product and the heavy nuclide inventories of the initial bundle were calculated with the PEPIN2 code of the DARWIN package (Tsilanizara *et al.*, 2000). It relies on the specification of the power/burn up history experienced by the irradiated fuel, including the prior in-reactor irradiation (the BR3 reactor for FPT1, FPT2 and FPT3 irradiated rods and the Gravelines 5 plant for the FPT4 fuel), the Phébus re-irradiation phase (except for FPT4) and the Phébus transient phase.

The validation of the APOLLO2/PEPIN2 calculated inventories by comparison with experimental data is discussed in (Jacquemain *et al.*, 2000) for FPT1, (Chapelot *et al.*, 2004) for FPT4, (Grégoire *et al.*, 2008) for FPT2 and (Payot *et al.*, 2011) for FPT3. For a large number of fission products and for some heavy nuclides (the inventory of which could be experimentally measured only for FPT4) a good consistency between the experimental and calculated inventories was obtained. Thus for those nuclides, the data gained from the APOLLO2/PEPIN2 calculation were retained as the reference initial bundle inventory (with a relative uncertainty comprised between +/- 5 and 15%). The determination of the activation product inventory (mainly ^{134}Cs and the activation products of the control rod material: ^{110m}Ag and ^{114m}In) by APOLLO2/PEPIN2 is known to be less accurate (Grégoire *et al.*, 2008); so those inventories were either considered with a large uncertainty (up to +/-50%) or indirectly determined by comparison with post-test chemical analyses performed on a selection of samples (FPT2 test, nevertheless with still a large uncertainty ~ +/- 30%).

The inventory of natural element present in the fuelled part of the test section (cladding, structure and control rod material) was deduced from its description.

2.4.2 Methodology for the determination of the integral release

For the elements detected by -scanning in the in-pile test section (including the degraded bundle, upper plenum and vertical line), the integral release was directly determined assuming that it corresponds to the difference between the initial inventory and the remaining part in the degraded bundle. For the other elements, as no data were available for the in-pile test section, the integral release was estimated assuming that it corresponds exactly to the sum of the inventory fraction deposited in the hot leg, the steam generator, the cold leg and released in the containment vessel. In this case, the calculated release is a minimum value, since the possible deposits in the upper plenum and vertical line were not accounted for and were thus considered as not released.

2.4.3 Establishment of a mass balance closure

For the well-detected γ-emitters, independent measurements were available for material remaining in the bundle, for deposit and transit in the experimental circuit and finally for release in the containment vessel. An overall check of the consistency of the data could thus be performed for the following elements: barium (γ-spectrometry data for ^{140}Ba/La), caesium (data for ^{137}Cs), iodine (data for ^{131}I), ruthenium (γ-spectrometry data for ^{103}Ru completed by chemical data for $^{101\text{-}102}$Ru), tellurium (^{129m}Te and ^{132}Te/I), molybdenum (^{99}Mo data completed by chemical analyses on the non-radioactive isotopes of Mo), silver (^{110m}Ag data).

For most of the detected elements, mass balance closure is consistent within the experimental errors between the degraded fuel bundle and the circuit and between circuit and containment vessel. Thus no correction or adjustment has to be applied on the experimental data. The uncertainties remain between +/-20% for all elements except for In and Ag. For the low volatile elements (such as Ba, Ru, Ce, Zr) the uncertainty is dominated by the amount remaining in the degraded bundle The uncertainty is close to +/-35% for Ag and to +/- 55% for In due to a bad evaluation of their initial fuel bundle inventory.

Circuit distribution and integral release from the degraded bundle is reported in Table 2.1 for the main FPs, control rod and structure material and fuel. Whenever possible, the data reported here were obtained from experimental determinations (black figures). Elsewhere, they were estimated either by deduction between several data sets or by the use of generic behaviours identified for the detected nuclides (blue figures).

Table 2.1 : Phébus FPT2 test – Main material distribution in the experimental circuit and integral release.

		In pile test section				hot leg (700°C)		SG (700-150°C)	cold leg (150°C°		Integral release	
		Test section	fuel area	upper plenum	vertical line	deposit	transit	deposit	deposit	transit	% of i.i.	mass [mg]
Noble gas	**Kr**	*4.00E+01*					**6.00E+01**			**6.00E+01**	6.00E+01	2.05E+03
	Xe	*2.10E+01*					**7.90E+01**			**7.90E+01**	7.90E+01	3.31E+04
Fission product	**I**	**3.3E+01** *3.2E+01*	**2.8E+01** *2.7E+01*	**4.1E+00**	**3.8E-01**	**4.4E-01**	6.8E+01	**5.8E+00**	5.6E+00	5.6E+01	7.3E+01	1.1E+03
	Cs	3.5E+01 *4.4E+01*	3.3E+01 *4.2E+01*	2.3E+00	2.0E-01	6.9E-01	5.5E+01	5.5E+00	5.1E+00	4.4E+01	5.8E+01	1.2E+04
	Mo	5.2E+01 *6.3E+01*	4.8E+01 *6.0E+01*	3.6E+00	3.3E-01	4.2E+00	3.2E+01	3.9E+00	2.9E+00	2.6E+01	4.0E+01	1.1E+04
	Te	3.1E+01 *5.5E+01*	1.9E+01 *4.3E+01*	1.0E+01	2.1E+00	9.5E+00	3.6E+01	2.9E+00	3.4E+00	2.9E+01	5.7E+01	2.1E+03
	Ba	8.7E+01 *9.9E+01*	8.7E+01	8.6E-02	1.3E-02	4.1E-01	6.2E-01	8.2E-02	1.7E-01	3.7E-01	1.1E+00	1.6E+02
	Ru	8.9E+01 *1.0E+02*	8.9E+01	0.0E+00	0.0E+00	2.6E-02	1.2E-01	1.5E-03	3.5E-02	8.3E-02	1.5E-01	2.2E+01
Control rod	**Ag**	8.6E+01 *9.7E+01*	8.6E+01 *9.7E+01*	2.2E-01	0.0E+00	6.6E-01	1.9E+00	3.1E-01	5.2E-01	1.5E+00	3.2E+00	1.5E+04
	In	9.2E+01				6.7E-01	7.8E+00	1.4E+00	6.5E-01	5.7E+00	8.4E+00	7.6E+03
	Cd	7.4E+01				2.3E-01	2.5E+01	8.7E+00	1.7E+00	1.5E+01	2.6E+01	7.7E+03
Structure	**Sn**	9.1E+01				1.1E-01	8.9E+00	1.3E+00	7.8E-01	6.8E+00	9.0E+00	4.4E+03
	Zr	1.0E+02				2.5E-03	1.2E-02	8.0E-04	3.2E-03	7.6E-03	1.4E-02	5.0E+02
	W	9.1E+01				1.8E-02	8.2E-02	2.8E-03	2.3E-02	2.1E-02	6.7E+00	1.2E+03
Fuel	**U**	1.0E+02				9.2E-04	5.5E-03	1.5E-03	1.2E-03	2.8E-03	6.4E-03	5.7E+02

The experimental data in Table 2.1 are presented for the four zones of the experimental circuit:

- "test bundle zone" divided into the "fuel zone" which corresponds to the zone where the test bundle was initially placed and the "upper plenum and vertical line zone" corresponding to the zones placed directly above the initial locations of the test fuel bundle. For the elements not detected by the γ-scannings of the in-pile test section, the inventory fraction which remained in the in-pile test section (including the degraded fuel bundle, the upper plenum and the vertical line) could be roughly estimated assuming that it complements exactly the inventory fraction which deposited in the hot-leg, the steam generator and the cold leg plus the fraction transiting through the cold leg. Those data are presented in a single column "test section" ;
- the "circuit hot leg zone" divided into material deposits and transit ;since no quantitative mass flow rates could be determined from hot leg aerosol sampling devices, the estimation of the integral amount flowing through hot leg was made using results obtained in other parts of the circuit: transit through cold leg plus deposits in the steam generator and in the cold leg;
- the "circuit cold leg zone" divided into material deposits and transit; The amount of material flowing through the circuit cold leg is obtained by integration of the mass flow rate curves (as reported in section);
- the steam generator model U-tube which connects the circuit hot leg and the circuit cold leg and is therefore placed in between the "circuit hot leg zone" and the "circuit cold leg zone".

The noble gases (Xe and Kr) are almost totally released from the fuel as observed in the previous severe accident fuel tests, and entirely transported into the containment vessel. The volatile FPs (I, Cs, Te, Mo, Rb) are characterized by a fraction of 45-85% of initial bundle inventory released from the fuel bundle. The amounts reaching the containment vessel are however lower (30-60% of initial bundle inventory) since these elements deposited partially on the circuit surfaces. These elements consequently have a low contribution to residual power in a reactor case. However, FPT2 results indicate that released volatile FPs can deposit in the upper fuel zone. These deposits thus potentially affect the decay-heat distribution in the damaged core, in a reactor case. On the other hand, they make the considered FPs available for delayed re-vaporisation as the fuel heat-up progresses upwards through the degradation phase.

Deposits in the circuit are significant for all species (except for noble gases) both in the hot leg and in the cold leg of the circuit. For instance, a marked tellurium deposition process was observed in the hot leg of the circuit with almost 9% of its bundle inventory remaining deposited there after the degradation phase. On the other hand, it was observed from cold leg decontamination solutions that about 5% of initial bundle inventory of caesium have deposited along the circuit cold leg. Important deposits were also measured for barium and silver.

Low-volatile elements remain almost entirely in the fuel zone, where they contribute to the residual power. These include fuel material (U), fission products (Ba, Sr, Ru, Tc, La, Ce) and control rod material (Ag).

Intermediate between volatile and low-volatile elements, semi-volatile species are identified with 8-25% of initial bundle inventory released from the fuel bundle. But due to deposition in the circuit line, the fraction reaching the containment vessel is lower: 5-15% of initial inventory. These include control-rod material (In, Cd), structure material (Sn) and material associated with bundle instrumentation (W).

2.5 Iodine behaviour in the experimental circuit

During the test a particular attention is given to the iodine radiochemistry. With regard to the iodine source-term issue, measurements performed on-line and off-line on the sequential samplings located both in the circuit hot leg and in the circuit cold leg provide data for the description of the iodine Iodine behaviour in the circuit.

Iodine released from the fuel area is mainly transported from the upper plenum to the circuit hot leg as final deposits were relatively low: 4.5% of i.i in the upper plenum and vertical line area and 0.44 %i.i. from on-line γ-measurements of station located along the hot leg (see Table 2.1).

Results of the four sampling channels located in the hot leg of the circuit (Table 2.2) and trigerred during the main release phases (oxidation runaway, first oxidation phase, P4 power plateau and last heat up) reveal that iodine was essentially transported in vapour form, which fraction ranged between 55.7% and 88.9% of the total

iodine sampled in each channel, the remainder being aerosols. The gaseous iodine fraction was measured to be lower than 0.3% of total iodine whatever the sampling.

Table 2.2:- FPT2 test transient - Iodine form detected in the circuit hot leg.

	oxidation runaway (9126-9311s)[1]	First oxidation (9955-10144s)	P4 power plateau (13180-13309s)	Late heat-up (18676-18806 s)
Aerosol	30.2	21.0	11.0	44.2
Vapor	69.7	78.7	88.9	55.7
gaz	0.1	0.3	0.1	~0.0

[1] sampling duration ~175-200 s

Post-test γ-scannings of the Transition Line (of the hot leg sampling channels) and TGT samplings provided information about iodine and caesium vapour species transported though the hot leg. Indeed, iodine (^{131}I) and Cs (^{137}Cs) deposition profile (the only measured isotopes here) showed several peaks as the temperature decreases, denoting vapour condensation. This deposition profile evolved with transient progress (Grégoire *et al.*, 2008). As an example, Figure 2.9 displays iodine and caesium deposition profile for the transition line and the TGT operated between the two oxidation phases (P4 power plateau, oxidising conditions). For the transition line, one caesium condensation peak overlapping one of the iodine peaks can be observed (Figure 2.9 a). This may be explained by the presence of CsI or Cs_2I_2. The presence of two additional iodine deposition peaks (not linked to caesium) points the presence of other iodide species in such conditions. Similar feature were also observed on the TGT device operated at the same period (Figure 2.9 b). The nature of the other iodide vapour species could not be identified, even if silver and cadmium were found deposited in significant amount on this TGT device (global chemical analyses of the TGT device).

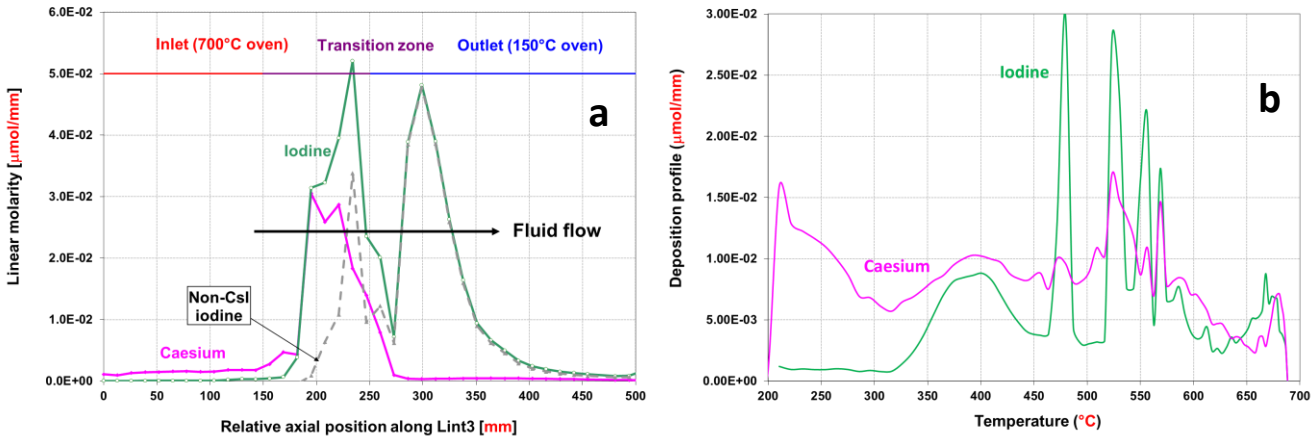

Figure 2.9 : Phébus FPT2 test –Iodine and caesium deposition profile in 750-150°C temperature gradient, sampling during the P4 power plateau a) transition line b) TGT device.

Iodine deposits measured in the steam generator sections were evaluated at 4.3%i.i. The post-test γ- scanning of first six steam generator sections showed that the iodine deposition profile is similar to that of caesium suggesting that, as caesium, iodine is deposited by aerosol thermophoresis process in this zone. Nevertheless, when one compares the iodine fraction released from the fuel bundle (72%i.i.) with the fraction conveyed through the circuit cold leg (56%i.i.), it can be assumed that some iodide vapour fraction could be deposited in the non-analysed upstream part of the steam generator.

In the circuit cold leg, most of iodine was transported in an aerosol form towards the containment vessel (56.7%i.i.). Each sampling only indicated a negligible fraction of gaseous iodine throughout the transient phase, which does not exclude the possibility that gaseous iodine fractions may have been temporarily much higher [4] .

Additionally, these results proved that most of the iodine species that are not condensed in the hot leg had time to condense on the aerosols before reaching the containment and (or) also to deposit on the steam-generator inner surface.

2.6 Main outcomes of the FPT2 test& Phébus programme – Fission product release and transport

The fission product integral releases observed in Phébus FP and more particularly FPT2 test are globally consistent with those observed on separate-effect experiments such as VERCORS (Ducros *et al.*, 2001) and HI/VI (Lorenz and Osborne, 1995). The VERCORS classification of FPs behaviour can be applied for the volatile (Kr, Xe, Cs, I, Rb, Te..), low volatile (Ru, Ce, Eu, La..) and non-volatile (Nd, Pr) observed in the Phébus test. As observed in the Vercors test, fuel (U, Pu) is also non-volatile. In the semi volatile group, only Mo results are in agreement with separate effect tests, the others falling into the low-volatile class. A notable case is Ba, weakly released in Phébus bundle experiment, strongly in Vercors, HI/VI tests and even in the Phébus debris bed configuration (Grégoire *et al.*, 2004). Up to now, there is no clear explanation for such different behaviour: strong interaction between fuel and structural material (Zr and Fe) or high temperature/ mild oxidative conditions in the Phébus tests may have contributed to enhance the formation of low volatile Ba forms – in contrast to separate effect tests.

In addition, the large scale Phébus test allowed to show the role of fuel degradation progress on fission products/ material release kinetics, particularly in the FPT2 test. Indeed, the formation of an extended molten pool resulted in a strong reduction of material release as already observed during previous studies on releases from a molten pool (Bechta *et al.*, 2010). Such behaviour can be related to element vapour pressure which is strongly dependent on their physical state: solid phase or dissolved in a liquid phase as in a molten pool.

While no direct measurement of the chemical species transiting in the experimental circuit could be done, major outcomes concerned the nature of some important fission products (Cs, I) transported in the RCS. Indeed, contrarily to what was previously assumed on Iodine speciation in the RCS (expected to be mainly transported as CsI), the presence of metallic iodide other than CsI has been evidenced – based on Cs and I vapour deposition profile in thermal gradient zone. Formation of CdI_2 is put forward. In addition, Cs transport in the hot leg mainly in condensed form involved less volatile species than the previously expected CsOH form. Cs_2MoO_4 (depending on Mo release kinetics) was put forward as a less volatile candidate. The other important factor concerning iodine transport was the presence of gaseous iodine in the RCS which was then released in the model containment vessel. Indeed, measurable gaseous iodine amounts were detected in the containment vessel, strongly dependant of the test conditions: with gaseous fractions (relative to containment inventory) ranging from 0.6% (FPT2 test) up to 80% (FPT3 test) (Simondi Teisseire *et al.*, 2013). Such behaviour could not be explained by the current version of the severe accident simulation code.

In order to improve the comprehension of the phenomena observed during the Phébus FP test, additional separate-effect experiments were conducted by IRSN in the framework of the International Source Term Programme (ISTP) (Clément and Zeyen, 2008). The aim of those experiments was to investigate individual phenomena (which was not possible with the integral Phébus FP tests), with a special attention on iodine radiochemistry both in the RCS (CHIP and CHIP+ programmes, see section 3) and containment building (EPICUR-STEM and STEM2 OECD program and its follow up STEM2).

[4] According to FPT3 results, it can be assumed that some gaseous iodine amount was trapped in the aerosol filter upstream the filter dedicated to gaseous iodine trapping

3 FPS CHEMISTRY IN THE RCS IN SEVERE ACCIDENT CONDITIONS

In order to better understand the main chemical formation/decomposition/deposition processes in which released FPs and control rod elements are involved in the Reactor coolant system (RCS) during a SA and also to build an experimental database allowing the validation process for models, the ISTP-CHIP (2005-2012) and its follow up CHIP+ (2012-2018) programmes were launched at IRSN. Over the past 14 years, the work (Grégoire, 2021) was focused on the reactivity of fission products (I, Cs, Mo) and control rod elements (B, Ag, In, Cd) transported in open flow reactors reproducing as close as possible the thermalhydraulic conditions prevailing in the RCS in the case of a large cold leg break (Jacquemain et al., 2015) : high thermal gradient (1600-150°C), short residence time (a few second) and steam or even steam/hydrogen atmospheres. A special attention was brought on the possible release of gaseous iodine in such conditions.

3.1 State of the art and programmes objectives

Little information is available in the literature concerning the chemical speciation inside the RCS (Clément *et al.*, 2007). The phenomena occurring in the RCS during a SA are very complex involving strong thermal gradients, rapid atmosphere changes from reducing to oxidizing conditions, complex chemical systems involving some more or less volatile FPs and control rod (CR) materials. The chemical form of iodine and its behaviour after entering containment from the RCS were previously documented in NUREG/CR-5732 (Beahm *et al.*, 1992). Based on thermodynamic computations, it was considered that iodine entering the containment was at least 95 % under CsI form with the remaining 5% as I and HI under gaseous form. After extensive experimental research and modelling on fission product release and transport in severe accident conditions over the past thirty years, the situation appears much more complex. The large scale Phébus FP test series showed that in addition to CsI, other condensable iodide forms may exist in the RCS (Girault *et al.*, 2013). Moreover, the fractions of aerosol/gaseous iodine transported into the Phébus containment vessel (150°C) were variable and strongly dependent on the test scenario (Girault *et al.*, 2010, Girault *et al.*, 2012), suggesting a complex chemistry during the transit though the experimental circuits. The small-scale Falcon ISP1/2 tests performed with simulant fuel pellets (Williams, 1994) and VERCORS HT2/3 tests performed with actual spent fuel pellets (Pontillon and Ducros 2010) supported also the assumption of iodine being transported in others forms than CsI.

Linked to its high thermodynamic stability, CsI formation is favoured under the conditions prevailing in the RCS during a SA, as caesium is always present in excess relative to iodine. Cs initial inventory in the irradiated fuel is about a factor ten higher than that of iodine, it also behaves as a volatile FPs, with similar kinetic of releases as iodine. Nevertheless, it is not the only possible metallic iodide which can be formed in the RCS. Indeed - in presence of Silver-Indium-Cadmium (SIC) control rods as was the case for the FPT0/1/2 tests - strong release of cadmium (early degradation phase), indium (after the main oxidation phase) and later of silver are expected with the progress of bundle degradation. Even if those elements are not as volatile as iodine or caesium (Grégoire and Haste, 2013), their high initial inventories contribute to a transport in the RCS in excess relative to iodine, resulting in the possible formation of other metallic iodide (AgI, CdI_2, possibly InI_x) than CsI.

Molybdenum has been identified so far as a potential caesium trap by the formation of caesium molybdates (Smith et al, 2021; Hoekstra, 1973; MacFarlane *et al.*, 2002). In the fuel, molybdenum is present in a slight excess relative to caesium and can be released in significant amounts particularly under RCS oxidising conditions as was observed during the Phébus FP tests (Grégoire and Haste, 2013). Indeed, during the FPT2 test, integral releases of Mo up to 40% i.i were observed with a kinetics of transport strongly accelerated in steam atmosphere (see Figure 2.6) so that excess of Mo relative to Cs in the RCS is not excluded. Molybdenum is transported in vapour form in the hottest part of RCS (1500-700 °C zone) where it can react with Cs species in the gas phase. Below 700°C, it is then mainly present in aerosols form (Haste *et al.*, 2013). As for boron strongly released following B_4C control rod degradation (Phébus FPT3 test, Payot *et al.*, 2010), it has been shown experimentally that it reacts with Cs to form caesium borates (Bowsher *et al.*, 1985, Bowsher *et al.*, 1986, Elrick *et al.*, 1987). Computed simulation indicates that the formation of caesium borate are favoured in gas phase at high temperature (>750°C) compared to that of CsI (Vandeputte *et al.*, 2019; Miwa *et al.*, 2016) with no kinetic limitations (Miyahara *et al.*, 2019). These elements may thus prevent the formation of CsI, promoting gaseous iodine

formation as Mo and B are not expected to form stable iodides in this temperature range (given their thermodynamic properties as reported by Cheynet *et al.* (1992) and Kaye *et al.* (2010).

The volatile tellurium fission product is also known to form caesium telluride species (McFarlane and Leblanc, 1996; De Boer and Cordfunke, 1995). Tellurium production in the spent UO_2 pellets is nevertheless lower than that of caesium, resulting in total Te amounts about 5 times lower than Cs amounts in the fuel bundle (Jacquemain *et al.*, 2000; Grégoire *et al.*, 2008), so that is not expected - in a first approach - to have a major influence on caesium reactivity with the afore mentioned FP and CR elements.

Improved understanding of the RCS iodine chemistry must take into consideration complex chemical systems, featuring the main elements which can interfere with iodine chemistry (directly or indirectly) - and representative of the concentrations and ratio prevailing in such scenarios. It relies mostly on computer simulations which need reliable thermodynamic and thermokinetic data for chemistry of FPs and CR material at high temperature. Even if recent studies contributed to improve these data (Grégoire *et al.*, 2017; Miyahara *et al.*, 2019) – researches are still ongoing on this.

At IRSN, the CHIP experimental set-up (CHemistry of Iodine in the Primary Circuit) and its small scale homolog named GAEC (Generation of Aerosols in the primary Circuit) have been developed over the past decade within the framework of the ISTP- CHIP (2005-2012) (Alpy *et al.*, 2004; Clément and Zeyen, 2005) and the CHIP+ (2012-2018) programmes. In order to provide a better understanding of the conditions allowing to the possible release of volatile iodine at the RCS break, these laboratory scale experiments were aimed at:

i/ collecting or reassessing fundamental data of the main species playing a role in the RCS chemistry on thermodynamic and also some possible kinetic limitations impacting iodine transport;

ii/ building an experimental database allowing the extension/validation of models in conditions as close as possible to SA.

Reduced chemical systems involving iodine and the main released FPs (Cs, Mo) and control rod material (B, Cd, Ag and In) were considered with increasing complexity under thermal hydraulic conditions close of a RCS during a SA (strong temperature gradient, short residence time, steam and/or hydrogen atmosphere). The elements retained are the most relevant with respect to iodine chemistry and were identified following the integral Phébus test series. One of the main issues was to achieve element injections with targeted concentration and element ratios as close as possible to reactor case (Cantrel and Cousin, 2007) and relevant of the Phébus tests.

My contribution to the CHIP and CHIP+ program was the follow up of the entire program in the lines operated at the L2EC laboratory including the continuous development of the experimental capabilities of the lines (element injection; sampling devices). Meanwhile, tight collaboration with academic partners allowed to study some specific aspect of this program: work on the thermokinetic properties of the I-O-H system was partly performed at Lille university within the framework of the C3R common laboratory between IRSN- PC2A laboratory of Lille University. Molecular analyses of deposits collected in the CHIP PL line was facilitated thank to the expertise of the LASIR laboratory (University of Lille) and thenafter of the GSM group (ISM - university of Bordeaux). Validation of the modelling approach of the SOPHAEROS simulations tool was performed with the support of the IRSN – LETR laboratory. In the following sections, I will focus on some relevant results concerning the IOH system, the role of Mo as Cs scavenger, the role of Indium, silver and cadmium separately in the former MoCsI system.

3.2 EXPERIMENTAL FACILITIES AT IRSN

The chemical systems were studied in the CHIP phenomenological line and/or in the GAEC small-scale test line. Studies dedicated to collect fundamental data on thermodynamic and/or thermokinetic properties were performed on specific facilities in collaboration with academic partners: high temperature mass spectrometer (Roki, 2009, SIMAP university of Grenoble) and flat flame burner (Délicat, 2012- University of Lille) and will be not presented here.

3.2.1 CHIP and GAEC lines

The CHIP line is dedicated to the study of complex systems involving up to 7 elements (Grégoire and Mutelle, 2012; Grégoire *et al.*, 2018) and the small-scale GAEC line is limited to a reduced set of elements but allows parametric studies (Lacoué-Nègre, 2010; Gouello, 2012; Grégoire *et al.*, 2015). Both are designed as open flow reactors in which the reagents are continuously injected, mixed at high temperature (1600°C) and then transported with a residence time of a few seconds into a controlled thermal profile and an atmosphere (steam or steam/H_2) reproducing the conditions of the RCS of a Light Water Reactor (LWR) in an accident scenario featuring a break in the cold leg (150°C) (Jacquemain *et al.*, 2015). FPs natural simulant (Cs, I, Mo) and constituent of the control rod (B, Cd, In, Ag) were injected in concentrations and ratios representative of their release in case of a SA (Haste et *al.*, 2013). At 1600°C, all the species are supposed to be under gaseous form at thermodynamic chemical equilibrium. Downstream the fluid is cooled in the reaction zone where chemical reactions take place producing aerosols and gases. Material deposited in the thermal gradient, as well as aerosols and gases transported at 150°C are collected for off-line characterisations with a focus on the detection of gaseous iodine.

The CHIP test line (3.5 m long and 60 mm in internal diameter) is composed of two tubes assembled by a specific junction (Figure 3.1): an alumina tube (2 m) located in the high temperature zone and a stainless steel tube (1.5 m) in the transport zone - to be representative of the RCS. The thermal profile is obtained by mean of several furnaces and is composed of three zones (injection zone, reaction zone and aerosol/ deposit and gas collection zone). Thermal profile is obtained after ~20-24 h slow heating before element injections. Carrier gas is mainly composed of steam with, for some experiments, the addition of a low amount of hydrogen to allow for a sligthly reducing atmosphere. Inert gas (He or Ar) is added to adjust the residence time from the high temperature zone to the outlet (10-12 s) .

A quartz plate is inserted in the main line for deposits and aerosols collection in the 850-350°C temperature range. The line is terminated by an integral quartz aerosol filter followed by gas scrubbers filled with an alkaline solution dedicated to trap the gaseous iodine species. Different sampling lines which can be sequentially operated, are also implemented either at 500°C (corresponding to a hot leg break of a RCS) or at 150°C (cold leg break). Depending on their design, these lines are devoted to the:

- collection of the transported aerosols: filters or cascade impactor device;
- quantification of the transported gaseous iodine fraction: gas scrubbers filled with alkaline media placed downstream the filtering device ; these lines are noted "Igas&aerosol line"
- molecular iodine detection and gaseous iodine speciation: specific lines featuring gas scrubbers filled with toluene/diluted nitric solution and designed to limit as much as possible interaction between collected molecular iodine and transported aerosols (see also next section). These lines are noted "I_2 line" and "I_g speciation line" respectively and their principle is detailed in section 3.2.2.

Most of the reagents of interest are injected by the mean of external generators connected to the inlet flange. Gaseous iodine is obtained by sublimation of molecular iodine pellets. Caesium, molybdenum and cadmium vapours are produced by vaporization of respectively caesium hydroxide, molybdenum trioxide and metallic cadmium. Boron is delivered by a steam generator producing either a mixture of steam/carrier gas or a mixture of steam/H_3BO_3/carrier gas by vaporization of a boric acid aqueous solution. One major issue to be addressed was the achievement of a controlled injection of cadmium (as Cd metal), indium (as In_2O_3 powder) and silver (as Ag metal). Several years of development were necessary to succeed injecting those refractive and poorly soluble elements in a controlled way. Indium oxide vapours are obtained by the injection of dry indium oxide aerosols produced at room temperature and then gradually vaporised in the pre-heating zone. Being more refractive than the other elements, silver is directly vaporised in the main line from silver powder deposited in crucible. At the

steady state, these generators produce a stable mass flow rate of each reagent. Separate element injection allows achieving a wide range of experimental conditions, in terms of chemical system, reagent concentrations and ratios.

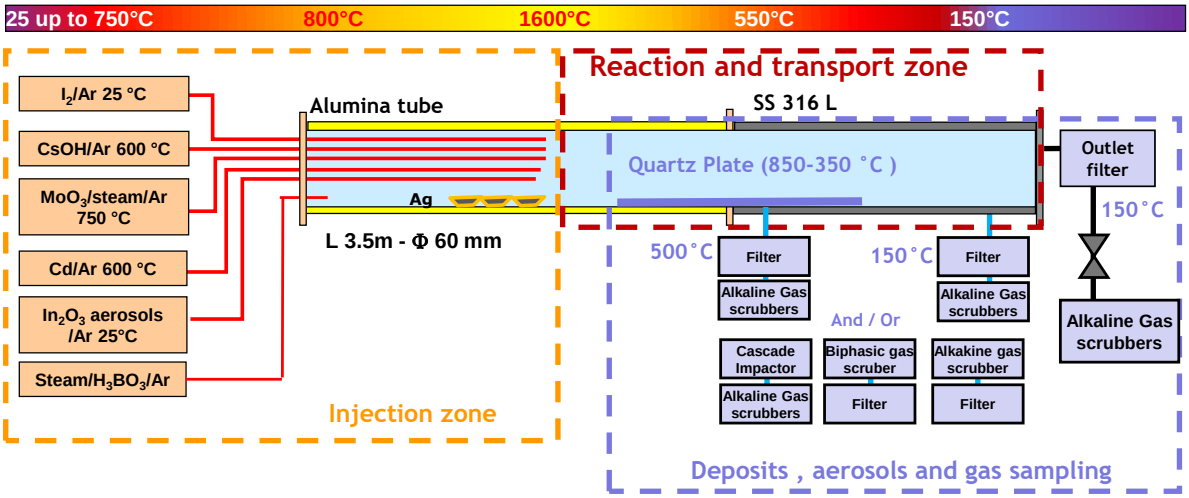

Figure 3.1: Scheme of the CHIP line.

Figure 3.2: Overview of the CHIP Line.

The GAEC line is composed of a single alumina tube (up to 2 metres long and 30 mm internal diameter) in which a stainless steel tube can be inserted. As for the CHIP line, the thermal profile is obtained by the mean of several heating elements. The inlet is provided with separate lines allowing injection of a mixture of steam/H_3BO_3/argon and gaseous molecular iodine. Residence time in the range of 4-8 s can be achieved in this line. CsOH and/or MoO_3 vapours are directly generated in the main line from powders placed in crucibles. Aerosols and gas sampling are only performed at the main line outlet (cold leg break conditions) with a similar design as for the CHIP set-up.

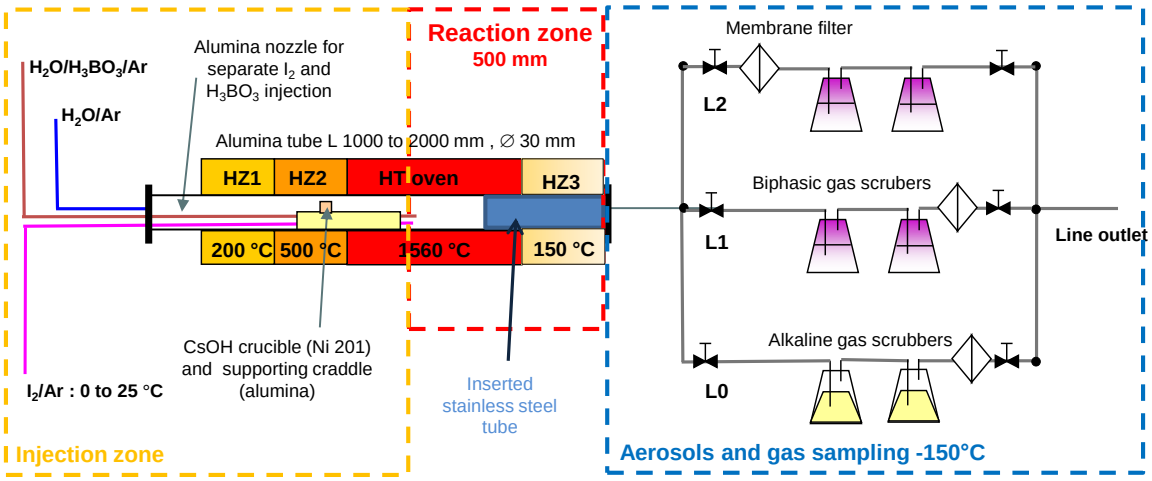

Figure 3.3: GAEC scheme configured for I, Cs and B injection.

Relevance of CHIP-CHIP+ test conditions compared to Phébus experiments and reactor case are summarized in Table 3.1.

Post test, each part of the line was leached in appropriate aqueous solutions in order to solubilize the deposits. Multi-elemental analysis techniques such as Inductively Coupled Plasma Mass-Spectrometry or Optical-Spectrometry allowed establishing a reliable element distribution over the entire line (with an uncertainty of +/- 8% at 95% confidence level). Element distribution is reported in terms of high/low temperature deposition, aerosol/gas transport at 500°C (condition of a hot leg break) or at 150°C (conditions of a cold leg break). Finally, the element mean mass flow rate or mean concentration in the high temperature zone was determined from the total injected element mass and the injection duration assuming a steady injection rate.

A selection of samplings (sequential filters and quartz plate sections) was preserved for deposit and aerosol characterization. Scanning Electron Microscopy coupled to an Energy dispersive X-ray detector (SEM-EDX) used in low vacuum mode allowed to determined size, morphology and elemental composition of deposited material and aerosols. Complementary to SEM-EDX, X-ray photoelectron spectroscopy (XPS), Raman microspectroscopy (RMS) and X-ray diffraction (XRD) allowed to identify the condensed species. Few analyses involved Time of flight Secondary Ion mass spectrometry (Grégoire, 2021) - but they supported the relevance of this technique to identify species in trace amount as metallic borates – whose detection by others spectroscopic techniques is an issue (Gouello, 2012). Deposit characterization was performed in collaboration with academic partners from the university of Lille (LASIR and UCCS), and the university of Bordeaux (GSM group of ISM).

Table 3.1 : Comparison of CHIP test actual conditions with Phébus experimental circuit conditions and SA scenarii.

Tests	**CHIP Phenomenological line**	**Relevance of PHEBUS FP conditions – circuit data** Jacquemain *et al.*, 2000; Grégoire *et al.*, 2008 ; Payot *et al.*, 2010	**SA scenarii**
Objective	Confirm the hypothesis that volatile iodine occurs in the primary circuit for reaction systems illustrative of the reactor sequence – measure amounts and chemical forms of the volatile iodine involved	/	/
Reaction system (homogeneous and/or heterogeneous reactions)	**Reduced** but illustrative of the most reactant elements with respect to iodine (except Rb and Te but 2nd order) Carrier gas (O, H)[5] + 7 elements With: I, Cs, Ag, Cd, In, Mo, B Stainless Steel Surfaces prototypic of reactor sequences High surface/volume ratio	**+** **+** **+**	**+** **+** **-**
Temperature T	$T_{high\ temperature}$ uniform at 1900 K $T_{hot\ leg}$ uniform from 1000 to 1300 K $T_{cold\ leg}$ uniform at 400 K For T > 1900 K no potential kinetic effect	**+**	**+**
Carrier gas composition	Inert gas (Ar or He)/Steam/Hydrogen/ Low hydrogen contents (less than 3%)but allowing H_2/H_2O molar ratio from 0 up to 1. High hydrogen contents are not expected to favour gaseous iodine transport Inert gas to ajust residence time in the lines	**Relevant for main release phase – not for main oxidation phase (e.g. featuring highly reducing atmospheres**	**+ (except fuel cladding oxidation phase)**
Residence time in the reaction zone (between high temperature zone and measurement point)	4-10 s	~5 s for PHEBUS FPT1	Illustrative of reactor sequence depending on the break size (~1 s for a 12'' hot leg break)
Concentration in the high temperature injection zone [mol/L]	I : 5 10^{-8} up to 1 10^{-7} Cs: 2 10^{-7} up to 3 10^{-7} Mo : 4 10^{-7} up to 1.4 10^{-6} B : 3 10^{-6} up to 8 10^{-6} Cd : 8 10^{-7} up to 1 10^{-5} In ~4 10^{-7} Ag : 1.5 10^{-6} up to 3.6 10^{-6}	Illustrative for lower bound concentrations of most elements in the Phébus circuit (hot or cold leg) Less illustrative of the upper bound concentrations	Partly Illustrative **of reactor case concentration but only lower bound values**
Molar Ratios	 Cs/I ~1 to 5 Mo/Cs ~2 to 5 In/I ~4.5 Cd/I~10-125 Ag/I ~25-50 B/Cs ~18-24	Illustrative for some Phébus sequences in the circuit: Low Cs/I ratio (Phébus case ranging from 5 to 20) High Mo/Cs ratio (Phébus case ranging from 0 to 3.5) Low In/I (Phébus case ranging from 2 to 8) Cd/I and Ag/I are higher than observed in Phébus sequences featuring significant I releases B/Cs illustrative of boric acid transport consecutive to vaporisation of RCS water (FPT-2 test)	REP900* Cs/I ~10 0 ≤ Mo/Cs ≤ ~1.5 ~3 ≤ In/I ≤ ~5 ~4 ≤ Cd/I ≤ ~6 ~10 ≤ Ag/I ≤ ~30 ~15 ≤ B/Cs ≤ ~20 (for REP1300 the higher ratio can reach 30)

(*) mean values based on bundle inventory and assumptions made on fraction released.

3.2.2 Analytical development

Given the complexity of the chemical systems and the large amount of material injected in the CHIP line (up to several grams of each elements, except iodine with only 200-500 mg), a special care was brought to the identification and quantification of gaseous iodine species and metallic iodide.

[5] This potentially means other components of the carrier gas (N,C).

Gaseous iodine sampling

In presence of Cs, Cd and Ag able to form metallic iodides, the aerosol/gas separation based on filters/liquid gas scrubbers proved sometimes to be inefficient due to strong interaction between gaseous iodine and aerosols trapped on the inlet filter inducing an unwanted gaseous iodine retention on the aerosol stage of the line and thus an underestimation of the iodine gaseous fraction. Such difficulties were already reported for the Phébus tests (Girault *et al.*, 2013). The sampling approaches based on gas sampling by denuder device (Huang and Hoffmann, 2009; Chance *et al.*, 2009) or optical on-line measurements (Johannson *et al.*, 2012) did not work with the high aerosols concentration levels encountered in the CHIP experiments. The retained strategy was a direct injection of the gas/aerosol flow into gas scrubbers filled with specific media able to trap selectively gaseous iodine species and allow an efficient separation from the other transported species (gas, aerosols).

In presence of caesium and cadmium, gas scrubbers filled with a biphasic mix composed of toluene and diluted nitric acid allowed to trap selectively and quantitatively molecular iodine in the organic phase while the other iodinated gaseous species and aerosols transported in the flow are trapped in the aqueous phase (nitric acid solution). In this configuration, the total gaseous iodine cannot be determined since both the other expected iodinated species (HI, HOI) and transported aerosols (CsI, CsOH and caesium borates) are all trapped in the aqueous phase, so that such line configuration is called "I_2 line". In toluene, molecular iodine is stable and absorbs at 309 nm and ~498 nm allowing quantification by UV-visible spectrometry with a good sensitivity (molar absorption coefficient of ~8700 $l.mol^{-1}.cm^{-1}$ at 309 nm). In a second configuration, such line displays an inlet aerosol filter so that aerosols can be separated from the gas flow and allowing to separate molecular iodine from the other inorganic gaseous forms (HI, HOI). This second line configuration called "$I_{g\ speciation}$ line" works only in the absence of gas/aerosol interactions.

Nevertheless, in presence of silver, the biphasic traps turned out to be inefficient to trap molecular iodine (if any) as was observed during the test with Ag-MoCsIOH chemical system ([Ag+MoCsI] test). Indeed, we experimentally checked that silver particles react readily and quantitatively with molecular iodine dissolved in toluene to form a silver iodide precipitate. In order to overcome this difficulty, we choose to direct the gas/aerosol flow into a liquid scrubber filled with an alkaline solution. There, soluble iodine gaseous species (HI, HOI, I_2) are quantitatively trapped resulting in the formation of iodide and iodate ions which are stable for several days even in presence of a large excess of silver powder (Thomas *et al.*, 1980). Contrarily to iodide ions which can come from gaseous iodine species and from soluble metallic iodide, iodate originates only from gaseous molecular iodine (resulting from the disproportionation reaction of I_2 in alkaline media); its detection can be unambiguously assigned to I_{2g}. Ionic chromatography (IC) allows to quantify IO_3^- with a good level of sensitivity (~20 ppb). Such lines were implemented for the integral tests only.

Metallic iodide quantification

Given the fact that iodine will be injected as the minor reagent, the metal iodide (if formed) will represent only a low fraction of the formed deposits/aerosols making their detection difficult.

Raman lines of metallic iodide are rather weak and below 200 cm^{-1} (Agrawa *et al.*, 1975; Delanay *et al.*, 1976; Cingolani *et al.*, 1984). X-ray diffraction is not enough sensitive. X-ray photoelectron spectroscopy not enough resolved to allow for an unambiguous identification of CsI, AgI or CdI_2 when mixed together. Indeed bonding energies of iodine (3d5/2) is at 619.9 eV for I_2, at 618.2 for CsI, 619.0 for AgI and 619.2 to 619.4 for CdI_2- (NIST data base) - not taking into account for charging effect which causes displacement of the bonding energies of the same order of magnitude neither for line interference from other elements (as for Cd 3p line at 618.4 eV). In addition, working on Cs, Ag or Cd spectrum will not help much as I bonding contribution to their spectra will be only very weak compared to X-O bonding.

As it is insoluble even in strong acid, silver iodide could be isolated from the other species which were leached in acidic media (except for silver iodide, silver species are leached in 5 M nitric acid). The silver iodide residue was finally quantified after its decomposition by hot aqua regia leading to the formation of AgCl precipitates and the formation of the stable soluble dichlorite iodide ICl_2^- (Spies, 1936; Wan *et al.*, 1989). The solubilised form of iodine could be then quantified by ICPMS. No equivalent approach could be developed for CdI_2 and CsI due to their strong solubility in aqueous media. Formation of such species was then deduced by default of other species.

3.2.3 Modelling with ASTEC/SOPHAEROS

Modelling of the open flow reactor experiments (GAEC and CHIP lines) was performed with the SOPHAEROS module (Cousin *et al.*, 2008; Cousin *et al.*, 2013) of the ASTEC code (Accident Source Term Evaluation Code) developed by IRSN (Chatelard P. *et al. 2016*). The basic I-O-H, Cs-IOH and Mo-CsIOH systems were thus interpreted and compared with experimental results (as reported in the following sections) with the support of the IRSN/LETR laboratory.

For the more complex systems involving the former Mo-CsIOH system plus one or several control rod elements (In, Ag, Cd and B), no reliable modelling is proposed so far (Souvi, 2017), as experimental observations pointed out important lack in the thermodynamic database and potential kinetics effect are not excluded. An important work is currently underway at IRSN to complete the thermodynamic database in gas phase - based both on an extensive literature review and chemical theoretical calculations.

ASTEC/SOPHAEROS computes chemistry and transport of the fission products in the PWR primary circuit during a severe accident. Geometry is nodalised with different 1D control volumes assembled by junctions with a fixed temperature for each control volume. The modelling is based on a set of mass balance equations where the main vapour and aerosol phase phenomena are represented. The mass-balance equation resulting from the intra-volume phenomena combined with inter-volume transport produced a nonlinear system solved by the Newton-Raphson method.

In the vapour phase, SOPHAEROS computes chemical speciation, vapour condensation, the aerosol physics and in a less extent vapour/surface reactions (sorption approach based on few available literature data). It considers aerosol nucleation, coagulation processes, deposition mechanisms and aerosol resuspension. A sectional approach is adopted to model the aerosol distribution. The same species composition is considered in all the aerosol size classes. Only gas phase reactivity and congruent condensation is accounted for in SOPHAEROS (figure 8). Non-congruent condensation and gas/solid phase reactivity are not modelled in the current version.

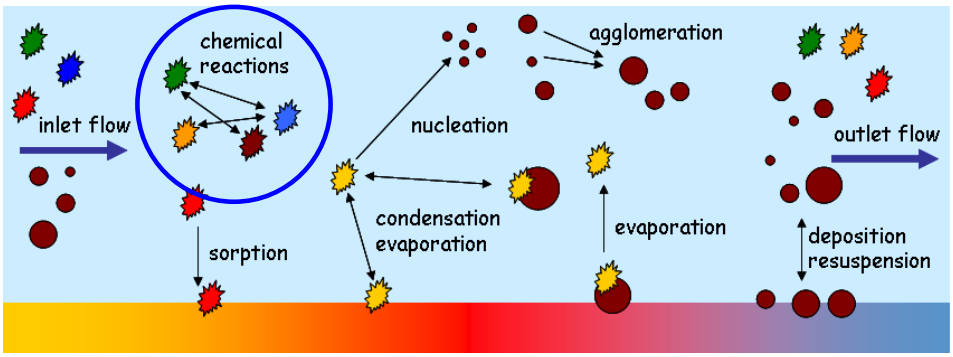

Figure 3.4: SOPHAEROS modelling - main phenomena taken into account (F. Cousin, 2017).

Calculations presented here were performed with the V2 version of the SOPHAEROS code described in detail in Cousin *et al.* (2013). The fission product (FP) speciation in the vapour phase is computed assuming a thermodynamic equilibrium. It depends on the element inventory, on the species involved in equilibrium and on the associated free energy functions at the given temperature. Chemistry-related data are stored in the Material Data Base (MDB) of the ASTEC code. This database contains around 800 vapours species potentially stable in reactor accident conditions (Kaye *et al.*, 2010). The list of species of interest for the CHIP PL and GAEC modelling and stored in the MBD are reported in Table 3.2.

The thermodynamic equilibrium assumption is usually true at high temperature (T> ~1500 K) but not necessarily verified at lower temperature (Kissane and Drosik, 2006; Cousin *et al.*, 2013). In ASTEC/SOPHAEROS V2, kinetic iodine reactions can also be used to compute FP speciation. FP species involved only in kinetic reactions are not implied obviously in thermodynamic equilibrium.

A kinetic scheme describing the reactivity of iodine in the gas phase with O and H was developed by a combined approach associating literature data and theoretical studies (Canneaux *et al.*, 2010; Hammaecher *et al.*, 2011;

Xerri *et al.*, 2012; Cantrel *et al.*, 2013). A set of 35 elementary reactions was established and is reported in Table 3.3 and Table 3.4. Part of this mechanism was recently taken up by Miyahara *et al.* (2019).

Input data for SOPHAEROS modelling are the composition and mass flow rate of the considered chemical system (including the carrier gas) and the thermal profile, see Figure 3.5. The CHIP PL and GAEC lines have been nodalised with ASTEC/SOPHAEROS, to represent the temperature gradient between the high temperature zone and the cold leg part of the lines: 40 volumes are used for CHIP and up to 50 modules for GAEC. Input data were deduced from the experiments and from qualification tests. The chemical elements were injected into the first volume with their respective experimental mass flow rates. Standard models and recommended parameters were used for the different physical and chemical phenomena so as to be representative of plant simulations.

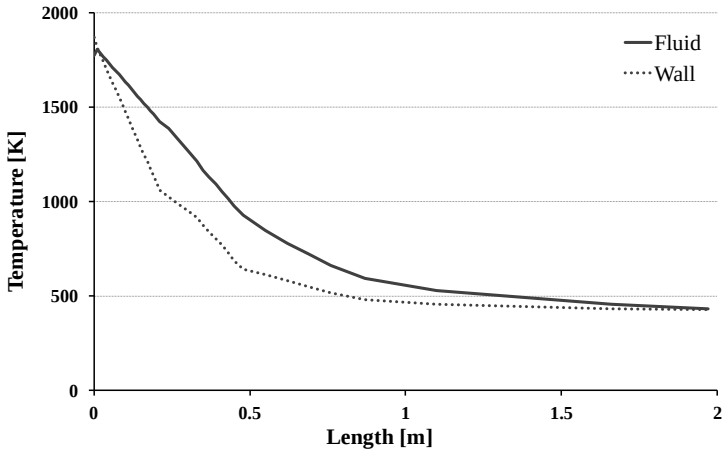

Figure 3.5: Wall and fluid temperature profiles of the CHIP line (from the high temperature zone to the line outlet) modelled by ASTEC/SOPHAEROS.

Table 3.2: Species present in the MDB data base and involving : O, H, I, Cs, Mo, B, Ag, In, Cd) b(as of Nov. 2019).

O-H	I-O-H	Cs-IOH	Mo-OH	BMo-CsIOH	AgInCd-MoCsIOH
H (g)	HI (g)	Cs (g, s)	Mo (g, s)	I_2Mo (g, s)	AgI (g, l, s)
H_2 (g)	I (g)	Cs_2 (g)	MoO (g)	I_2MoO_2 (g)	CdI (g)
H_2O (g)	I_2 (g)	Cs_2O (g, s)	MoO_2 (g, s)	BI (g)	CdI_2 (g, l, s)
O (g, s)	IO (g)	Cs_2O_2 (g, s)	MoO_3 (g, s)	BI_2 (g)	InI(g, l, s)
O_2 (g)		CsO (g)	Mo_2O_6 (g)	Cs_2MoO_4 (g, l, s)	InI_2 (g, l, s)
		CsH (g, s)	Mo_3O_9 (g)		InI_3 (g, l, s)
		CsOH (g, s)	Mo_4O_{12} (g)		
		$Cs_2H_2O_2$(g)	Mo_5O_{15} (g)		
		CsI (g, l,s)	HMoO (g)		
		Cs_2I_2 (g, s)	$HMoO_2$ (g)		
			H_2MoO_2 (g)		
			H_2MoO_4 (g)		

Table 3.3: IOH thermo-kinetic system - Elementary reactions involving oxygen, hydrogen and M (molecules for collision) from Cantrel *et al.* (2013).

Reaction	$k_{direct}(T)$ ($m^3.mol^{-1}.s^{-1}$ or $m^6.mol^{-2}.s^{-1}$)	Origin
$OH + OH \leftrightarrows H_2O + O$	$1.5\ x10^3\ T^{1.14}\ exp(-420/RT)$	Literature review
$OH + H_2 \leftrightarrows H_2O + H$	$1.8\ x10^3\ T^{1.21}\ exp(-19710/RT)$	Theoretical chemistry
$O + H_2 \leftrightarrows OH + H$	$5.1\ x10^{-2}\ T^{2.67}\ exp(-26270/RT)$	Literature review
$O + OH \leftrightarrows O_2 + H$	$2.8\ x10^5\ T^{0.40}\ exp(3090/RT)$	Theoretical chemistry
$H_2O + M \leftrightarrows H + OH + M$	$3.5\ x10^9\ exp(-440000/RT)$	Literature review
$OH + M \leftrightarrows O + H + M$	$2.4\ x10^9\ exp(-416000/RT)$	Literature review
$H_2 + M \leftrightarrows H + H + M$	$4.6\ x10^{13}\ T^{-1.40}\ exp(-437000/RT)$	Literature review
$O_2 + M \leftrightarrows O + O + M$	$1.6\ x0^{12}\ T^{-1.0}\ exp(-494000/RT)$	Experimental
$HO_2 + H \leftrightarrows H_2 + O_2$	$6.7\ x10^1\ T^{1.77}\ exp(2380/RT)$	Theoretical chemistry
$HO_2 + H \leftrightarrows H_2O + O$	$9.1\ x10^2\ T^{1.47}\ exp(-58100/RT)$	Theoretical chemistry
$HO_2 + H \leftrightarrows OH + OH$	$2.2\ x10^5\ T^{0.88}\ exp(270/RT)$	Theoretical chemistry
$HO_2 + OH \leftrightarrows H_2O + O_2$	$2.9\ x10^7\ exp(2080/RT)$	Literature review
$HO_2 + O \leftrightarrows OH + O_2$	$2.0\ x10^7$	Literature review
$O_2 + H + M \leftrightarrows HO_2 + M$	$5.7\ x10^{14}\ T^{-1.80}$	Literature review

Table 3.4 : IOH thermo-kinetic system - Elementary reactions involving iodine, oxygen, hydrogen and M (molecules for collision)from Canneaux *et al.* (2010); Hammaecher *et al.* (2011), Xerri *et al.* (2012) and Cantrel *et al.* (2013).

Reaction	$k_{direct}(T)$ ($m^3.mol^{-1}.s^{-1}$ or $m^6.mol^{-2}.s^{-1}$)	Origin
$I + H_2 \leftrightarrows HI + H$	$241\ T^{1.93}\ exp(-137300/RT)$	Theoretical chemistry
$I + H_2O \leftrightarrows HI + OH$	$30.7\ T^{2.26}\ exp(-184700/RT)$	Theoretical chemistry
$I + HI \leftrightarrows H + I_2$	$577.9\ T^{1.72}\ exp(-164200/RT)$	Theoretical chemistry
$I + OH \leftrightarrows HI + O$	$282.9\ T^{1.70}\ exp(-127700/RT)$	Theoretical chemistry
$I_2 + OH \leftrightarrows HOI + I$	$12.0\ T^{1.90}\ exp(12000/RT)$	Theoretical chemistry
$H_2 + IO \leftrightarrows HOI + H$	$7.2\ x10^{-7}\ T^{3.98}\ exp(-44400/RT)$	Theoretical chemistry
$OH + I \leftrightarrows IO + H$	$1.5\ x\ 10^8\ exp(-267500/RT)$	Chlorine analogy
$HO_2 + I \leftrightarrows HI + O_2$	$9.0\ x10^6\ exp(-9060/RT)$	Literature review
$HO_2 + I \leftrightarrows OH + IO$	$2.5\ x\ 10^7\ exp(-3700/RT)$	Literature review
$I + HOI \leftrightarrows HI + IO$	$2.2\ T^{2.29}\ exp(-119400/RT)$	Theoretical chemistry
$O + IO \leftrightarrows I + O_2$	$8.4\ x10^7$	Literature review
$HO_2 + IO \leftrightarrows HOI + O_2$	$8.4x\ 10^6\ exp(4490/RT)$	Literature review
$OH + IO \leftrightarrows HOI + O$	$7.2\ x10^{-12}\ T^{5.18}\ exp(-11900/RT)$	Theoretical chemistry
$OH + HI \leftrightarrows HOI + H$	$9.0\ x10^{-1}\ T^{2.28}\ exp(-103600/RT)$	Theoretical chemistry
$OH + HOI \leftrightarrows IO + H_2O$	$2.2x\ 10^{-9}\ T^{4.41}\ exp(19900/RT)$	Theoretical chemistry
$O + I_2 \leftrightarrows I + IO$	$8.4x\ 10^7$	Literature review
$I_2 + H_2 \leftrightarrows HI + HI$	$1.9x\ 10^8\ exp(-171000/RT)$	Literature review
$HOI + H \leftrightarrows I + H_2O$	$6.0\ x10^2\ T^{1.55}\ exp(-13100/RT)$	Theoretical chemistry
$I + I + M \leftrightarrows I_2 + M$	$200\ exp(4780/RT)$	Literature review
$I + H + M \leftrightarrows HI + M$	$2\ x\ 10^9\ T^{-1.87}$	Literature review
$I + OH + M \leftrightarrows HOI + M$	10^3	Estimation

For each reaction, only the direct rate constant is reported here. The reverse one is deduced from the direct rate constant and the Gibbs free energy of the reaction which is based on thermodynamic data of the reactants and products (Canneaux *et al.*, 2010; Cantrel *et al.*, 2013, Xerri *et al.*, 2012, Hammaecher *et al.*, 2011).

3.3 Test matrix

The overall test matrix is reported in Table 3.5. The I-O-H and Cs-I-O-H systems (see) were firstly considered with the objective to collect fundamental data on thermodynamic and/or thermokinetic properties of the main species identified as playing a role in the iodine chemistry (i.e. inorganic gaseous iodine species, caesium iodide and caesium hydroxide). To quantify the influence of Mo and B elements on gaseous iodine release, two series of tests were performed - each one featuring the former CsIOH system (with Cs still in excess relative to I) plus Mo or B in excess relative to Cs: the Mo-CsIOH and B-CsIOH systems. Both oxidising and reducing conditions were considered. Finally, the combined role of Mo and B was investigated. The study of the extended system considered the separate effect of each component of the SIC control rod (Silver or Indium or Cadmium) on the persistence of gaseous iodine - compared to the reference test performed in presence of molybdenum. The CHIP+ programme was ended with "integral tests" aimed at studying the global phenomenology of complex system involving both FPs (I, Cs and Mo) and several control rod elements (Cd, Ag and B).

Table 3.5 : CHIP and CHIP+ programmes - summary of the studied chemical systems.

	Chemical systems	**Line - year**	**Objectives and main parameters**
Basic systems	**I-O-H (CHIP)**	Flame studies 2009-2012 **GAEC line 2012-2014**	**Quantify kinetic limitations under oxidising and reducing conditions**
	Cs-IOH (CHIP)	GAEC line 2010-2011	Search for kinetic limitations of CsI formation both under oxidising and reducing conditions. Cs/I ≅ 2 -4
Study of Cs sink	**Mo-CsIOH (CHIP)**	GAEC line 2010-2012 **CHIP Line 2011-2017**	Role of Mo under oxidising conditions Mo/Cs ~1 - 6, Cs/I=1 **Role of Mo under reducing & oxidising conditions, Mo/Cs > 2, Cs/I > 2**
	B-CsIOH (CHIP &CHIP+)	GAEC line 2011-2014 CHIP Line 2011	Role of boron under oxidising conditions, B/Cs ~20, Cs>I
	BMo-CsIOH (CHIP+)	CHIP Line 2017	Combined Role of B and Mo on gaseous iodine release under reducing conditions (B>Cs, Mo>Cs and Cs>I)
Extended systems	**Cd-MoCsIOH (CHIP+)**	**CHIP Line 2013**	**Role of Cd under oxidising conditions (Cd>I)**
	In-MoCsIOH (CHIP+)	**CHIP Line 2015**	**Role of In under oxidising conditions (In>I)**
	Ag-MoCsIOH (CHIP+)	**CHIP Line 2016**	**Role of Ag under slightly reducing conditions (Ag>I)**
Integral system	AgCd-MoCsIOH BAgCd-MoCsIOH	CHIP Line 2018 CHIP Line 2018	Study of systems involving mains FPs(I, Cs, Mo) and control rod material (Ag, Cd, B) under oxidising conditions (steam).

3.4 Basic systems – the I-O-H system

The objective of this experimental study was to assess the capabilities of the kinetic scheme describing the I-O-H system in the gas phase to predict the reactivity of iodine obtained from two independent experimental series: flame technique and open flow reactor. Flame study was performed at the PC2A laboratory and open flow reactor tests were realized at IRSN. IOH experimental study was initiated in the framework of a pH-D (Délicat, 2012) supervised by L. Gasnot and myself.

The main interest of the flame technique (Hirschfelder *et al.*, 1953) is to get key species (HI, H_2O, and OH) concentration profiles for kinetic validation. The high temperature gradient in the studied flames (1600 – 300 K) is close to the temperature gradient which may occur in a RCS of a PWR in SA. However high iodine concentrations have to be used (about 10 000 time higher than in the open flow reactor tests), not representative of SA conditions and stable flames cannot afford high steam content. The experimental results obtained by the flame study were then simulated by the CHEMKIN II-PREMIX software. The profile of the key chemical species (HI, H_2O and OH radical) in the flames can be quite satisfactorily simulated within the uncertainty ranges of kinetic rate constant (Délicat, 2012; Grégoire *et al.*, 2017).

The study was completed by open flow reactor experiments in the GAEC line in which molecular iodine was injected at high temperature (> 1440 K) in a reducing or oxidizing atmosphere. The aim of these global tests was to determine the iodine gas speciation at 423 K in conditions more representative of a severe accident. Even if the experimental data gained from the open flow reactor tests are less detailed than for the flame study, this experimental device is well suited for both low iodine concentration and high steam concentrations. The data obtained in the open flow reactor device were interpreted with ASTEC/SOPHAEROS software. Experimental results and ASTEC/SOPHAEROS modelling test will be discussed in the following paragraphs.

3.4.1 Open flow reactor tests (GAEC line)

The iodine gas speciation was determined at 150°C (423K) after high temperature (>1160°C -1450 K) decomposition of the injected reagents (molecular iodine, steam and di-hydrogen) and their recombination in a strong temperature gradient down to 150°C. At this temperature and in the absence of any other elements, iodine species are expected to be all in vapour form (molecular or inorganic) so that sampling lines were equipped with toluene/nitric acid gas scrubbers without aerosol filter (see previous section). The influence of the atmosphere composition (oxidative with injection of steam or reducing with injection of di-hydrogen) and the iodine concentration levels were the main parameters taken into consideration.

Due to significant iodine deposition in the main line, only five tests of the initial study were retained. For these tests, iodine deposition was below 40% of the total injected so that iodine speciation in the sampling lines is expected to be representative of the actual one at 150°C. The test conditions and main results are displayed in Table 3.6.

- Three tests ([IOH-1], [IOH-2], [IOH-3]) were performed under a reducing atmosphere composed of argon and a low fraction of di-hydrogen (below 2.7% volume). The main parameters are the elemental iodine and hydrogen concentrations in the injection zone, so that a reducer over iodine ratio (H/I) between 3200 and 26000 could be obtained for those tests.

In the absence of oxygen, the iodine detected in the aqueous phase of the gas scrubbers is attributed to HI (as I_2 is trapped in the organic phase). Detectable amounts of molecular iodine (in the organic phase) were still observed at 423 K (150°C), showing that the IOH system undergoes some kinetic limitations. The maximum temperature seems to have no significant influence on the kinetic limitations ([IOH-3] test) indicating that a temperature of 1450 K (1160°C) seems to be sufficient to obtain a total decomposition of molecular iodine. The H/I molar ratio seems to be the main parameter that governs the kinetic limitations– as the other thermal hydraulic parameters were very close from one test to another (temperature profile, pressure and residence time as reported in Table 3.6). As this ratio increases, the I_2 fraction at 423 K decreases so that the system tends to reach thermodynamic equilibrium.

- Two tests ([IOH-4] and [IOH-5]) were performed under an oxidising atmosphere composed of a mixture of steam and argon (50/50). Two iodine concentration levels were considered with an iodine concentration about 5 times lower for the [IOH-4] test compared to the [IOH-5] test so that an oxidiser over iodine ratio (H_2O/I) up to 79 000 could be obtained.

Under oxidising conditions, the iodine species which could be present in the aqueous phase are HI and HOI. Large amount of HOI are nevertheless excluded because it is an intermediate species and in acidic conditions HOI will react quickly and quantitatively with HI ($HOI + I^- + H^+ \rightarrow I_2 + H_2O$) and the I_2 formed will be then transferred in the organic phase. Therefore we consider that the amount of iodine detected in the aqueous phase is attributed to HI.

For both tests, the gaseous iodine flow at 423 K is mainly composed of molecular iodine (between 90 and 96 %). The remaining iodine fraction detected in the aqueous phase (9.1% for the [IOH-5] test and 3.8% for [IOH-4]) is attributed to HI. The presence of measurable amounts of HI species indicates that the IOH system in oxidising conditions is also kinetically limited, although less marked than in reducing conditions. The amount of HI species decreases with increasing H_2O/I ratio as reported in Table 3.6.

Table 3.6: IOH test series performed in the GAEC line - main results (Grégoire *et al.*, 2017).

Test name	**[IOH-1]**	**[IOH-2]**	**[IOH-3]**	**[IOH-4]**	**[IOH-5]**
Thermal hydraulic conditions					
Pressure (MPa)	0.106	0.105	0.120	0.106	0.106
HT Zone max.temp (°C)	1550	1550	1160	1550	1550
Carrier gas flow ($l.min^{-1}$ – NPT) and composition	1.0 Ar/H_2 97.3/2.7	1.0 Ar/H_2 99/1	1.4 Ar/H_2 98/2	1.0 H_2O/Ar 50/50	1.0 H_2O/Ar 50/50
Residence time (s)	7.5	7.5	6.9	7.5	7.5
Element injection in the HT zone : iodine concentration and element molar ratio					
Iodine concentration (mol/l)	$3.8\ 10^{-8}$	$3.9\ 10^{-8}$	$1.7\ 10^{-8}$	$4.4\ 10^{-8}$	$2.3\ 10^{-7}$
Reducer H/I ratio $x10^3$	9.9 ±0.7	3.2 ±0.2	26 ±1.8		
Oxidiser (H_2O)/I ratio $x10^3$				79 ±4	15 ±0.7
I Deposited in the main line (1550 -150°C temperature zone)					
I	(36±3)%	(26±2)%	(42±3)%	(18±1.5) %	(33±3)%
Iodine released at 150°C	(64±4)%	(74±5)%	(58±5)%	(82±5)%	(67±4)%
I as I_2	**(14±2)%**	**(20±1) %**	**(4±0.4)%**	**(96±1)%**	**(91 ±6)%**
I as HI (possibly I or HOI)	**(86±2)%**	**(80±1)%**	**(96±13)%**	**(4±1)%**	**(9.0±6)%**

NPT conditions: 0°C, 0.101325 MPa; ‡ Element injection based on the final mass distribution in the line and assuming a steady injection rate (relative uncertainties below ⍰5%). Values rounded to two significant figures.

SOPHAEROS calculations were applied on the IOH GAEC tests with the IOH kinetic network. In the simulation, no iodine deposition on the line was modelled due to the lack of data describing the iodine loss with temperature and concentration. As observed in table 6, for tests with a large excess of I_2 ([IOH-5]) or HI ([IOH-1]) at the outlet, the deposited iodine amount is very close. We can think that the deposition process is similar for I_2 and HI and thus has a weak impact on iodine speciation at 423 K. Therefore we consider that the simulated fractions of I_2 and HI can be compared to the measured ones.

3.4.2 ASTEC/SOPHAEROS simulation of Tests performed under reducing conditions

[IOH-1] to [IOH-3] tests have been conducted under hydrogen (H_2) conditions with argon. The SOPHAEROS calculation assuming a thermodynamic equilibrium provides only HI at the outlet. If kinetic system is activated, taking into account the adjustment on the rates constant of: ($H + H + M \rightarrow H_2 + M$) and ($O_2 + H + M \rightarrow HO_2 + M$) to better fit the flame data, around 74 to 89% of iodine at the outlet is under I_2 which is totally in disagreement with experimental values.

A complete analysis of chemical reaction path has been done to understand iodine behaviour under hydrogen (H_2) (Grégoire *et al.*, 2017). At high temperature, I_2 is immediately decomposed in I radical. In stationary regime, I_2 and HI are actually produced when the temperature is lower than 1000K. At the outlet, HI is mainly produced by reaction between I_2 and H and I and H_2. There is no global loss rate of HI during the transport. I_2 is only produced by I+I and consumed by reaction with H radical to form HI.

A first hypothesis is that the reactions leading to the production of HI are too slow to correctly account for the experimental observations. In order to enhance HI production, several reactions leading to HI formation were accelerated by increasing the kinetic reaction constant by a factor 5 (within the uncertainty range of kinetic constant): $H + I + M \rightarrow HI + M$, $H + I_2 \rightarrow I + HI$ and $I + H_2 \rightarrow HI + H$ (listed in Table 3.4). In this case, HI fraction at the outlet is increased and reaches ~28% (for [IOH-1]). Even if this percentage significantly increases, it is not enough to explain the experimental values.

A second hypothesis is that H radical amount is underestimated with the kinetic reactions - limiting thus the production of HI. It is therefore assumed that H_2 is in equilibrium with H radical. In this context only reactions including iodine are activated. In this case, 90% of HI is computed at the end of the facility. Results are summarized in Table 3.7 for the [IOH-1] (similar trends is observed for [IOH-2] and [IOH-3] tests, see Grégoire *et al.*, 2017). The computation performed with the carrier gas assumed to be in thermodynamic equilibrium has a higher impact on the nature of the iodine released at the line outlet than the modification of the kinetic reaction

rate directly involved in HI production or loss. Indeed, when H_2 and H are supposed to be in thermodynamic equilibrium, the global balance between HI production and loss has been modified. HI production occurs at higher temperature (>1000K). This is more realistic because, even if HI is the more stable species at lower temperature, its production is very low at these temperatures. Because H_2 and H are in equilibrium, if H radical is consumed to form HI, it is necessary to also consume H_2. The main reaction which produces HI is in this case I + H_2 → HI + H. It allows respecting H_2 and H equilibrium, producing H radical with H_2. HI production is thus enhanced.

Table 3.7: I_g composition at the GAEC line outlet in reducing conditions ([IOH-1]), modelling results.

	HI (%)	I_2 (%)	I (%)
Measurement- IOH 1 test	86	14	
Thermodynamic equilibrium	100	0	0
Kinetic reaction	5.2	87.2	7.60
Modified reactions	27.7	66.5	5.8
H_2 and H computed at equilibrium	90.5	5.7	3.8

3.4.3 ASTEC simulation of tests performed under oxidising conditions

Assuming a thermodynamic equilibrium for all species, SOPHAEROS predicts only molecular iodine at the main line outlet which is close to the experimental results. With all the kinetic systems, SOPHAEROS predicts 65% of iodine released as molecular iodine, 19% as HI, the rest as HOI and I. A third computation is done assuming carrier gas at equilibrium, similarly to reducing conditions. In this case, I_2 represents around 92% of total iodine at the outlet. Only 3.3% of HI are formed and 4.2% are in I radical, see Table 3.8.

An analysis of the chemical reaction pathway was performed in both cases. It shows that HO_2 and IO are enhanced with kinetic system. These radicals are involved in the HI (HO_2 + I → HI + O_2) and HOI production (IO + H_2O → IH +HOI). With the carrier gas at thermodynamic equilibrium, reduced production of these species also reduces the HI and HOI production. I_2 is the main produced species below 1000 K (I+ I+ M → I_2 + M) and because I radical concentration is higher (no production of IO radical nor HI), there is more molecular iodine in this case. OH radical concentration is enhanced at high temperature with equilibrium assumption. But at these temperatures, only HI production can occur and because OH radical is involved in both HI and HOI losses, it explains also the reason why HI and HOI are not promoted with carrier gas at equilibrium.

Table 3.8: Ig composition at the GAEC line outlet in oxidising conditions ([IOH-4]), modelling results.

	HI (%)	**I_2 (%)**	**I (%)**	**HOI (%)**
Measurement ([IOH-4] test)	3.8	96.2		
Thermodynamic equilibrium	0	99.99	0.01	0.0
Kinetic reaction	18.9	65.0	4.0	12.1
Carrier gas at thermodynamic equilibrium	3.3	92.4	4.2	0.1

Regarding all GAEC tests, it appears that thermodynamic equilibrium computation is close to experimental results but cannot explain all the speciation found in the sampling lines. If all species of the IOH system, including carrier gas, are computed with the kinetic systems, computation trends are not satisfying. **Assuming a thermodynamic equilibrium only for the carrier gas allows catching general experimental trends**.

3.4.4 Conclusion: I-O-H system - experimental and modelling works

The IOH thermo-kinetic scheme, describing iodine reactivity at high temperature, is able to reproduce quite well the two sets of experimental data gained in the open flow reactor test series.

A good agreement is obtained for iodine by the adjustment of the kinetic rate constant of only two reactions involving H radicals (H + H + M → H_2 + M) and (O_2 + H + M → HO_2 + M) within the uncertainty range of such constant. The HI and I_2 amounts measured in the open flow reactor tests are quite well predicted by ASTEC/SOPHAEROS modelling.

At high temperature (above 1440K, 1170°C), the main identified iodine form is atomic iodine. Recombination occurs at lower temperatures leading to the formation of more stable species: molecular iodine prevails in the presence of steam (oxidizing conditions) and hydrogen iodide in presence of di-hydrogen (reducing conditions). Kinetic limitations allow the persistence of HI or HOI in oxidizing conditions and I_2 in reducing conditions but seem more pronounced in reducing conditions compared to oxidizing conditions.

3.5 Influence of a Cs sink: Molybdenum

As observed from the tests performed with the Cs-IOH chemical system (Grégoire *et al.*, 2015), as soon as Cs is added in excess with respect to iodine, iodine reacts quickly and completely to form caesium iodide in a large temperature range (high thermal stability) whatever the atmosphere conditions (reducing or oxidative). Modelling at thermo-dynamical equilibrium correctly simulates the experimental results, indicating no kinetic limitation for gaseous caesium chemistry.

The influence of Mo on gaseous iodine release was studied firstly with in the GAEC line with concomitant injection of CsI and MoO_3 vapours in pure steam conditions (Lacoué-Nègre, 2010; Gouello, 2012; Gouello *et al.*, 2013) achieving Mo/Cs ranging from 0.2 to 5. It has been observed that the presence of molybdenum increases the fraction of gaseous iodine at low temperature: 60 - 100% of the injected iodine was released in gaseous form at 150°C as soon as Mo is in excess relative to Cs (Gouello *et al.*, 2013). Molecular iodine dominates the gaseous form (80-90%). Caesium molybdates identified as Cs_2MoO_4, $Cs_2Mo_2O_7$, $Cs_2Mo_3O_{10}$, $Cs_2Mo_4O_{13}$, $Cs_2Mo_5O_{16}$ and $Cs_2Mo_7O_{22}$ on the basis of the reference spectra (Hoekstra, 1973) were identified in the deposited species (aerosols or condensed vapours) collected in the 1000-270°C temperature range as well as the aerosols collected at the outlet (micro-Raman spectrometry). The Mo stoichiometry in these molybdates increases with decreasing temperature and with the Mo/Cs ratio in the HT zone. For the tests featuring an excess of Mo relative to Cs, MoO_3 is also found from 600°C down to the outlet filters. XPS characterisations support these observations.

3.5.1 Mo-CsIOH chemical system – CHIP Tests

Several tests were performed in the CHIP line featuring I_2, CsOH and MoO_3 separate injection in oxidising or reducing atmospheric conditions (Grégoire al., 2015). Two tests will be discussed here: the [PL-MoCsI_3] test performed in steam/argon atmosphere, and the [PL-MoCsI_2] test featuring a reducing atmosphere by the addition of hydrogen. Hydrogen level in the line was limited to 2.8% of the carrier gas for safety consideration. Nevertheless, by reducing steam injection to its lower limit (at least 40 g/h mandatory for MoO_3 vaporisation), quite reducing atmosphere composition can be achieved for the PL_MoCsI_2 test. Both tests were performed with an excess of Cs relative to I (ranging from 3.3 to 4.1) and with an excess of Mo relative to Cs (Mo/Cs ratio between 2 and 3) in the range of ratios observed during the Phébus FP test sequences (Haste *et al.*, 2013, see also Table 3.1).

Test conditions and results are displayed in Table 3.9 in terms of main line deposition and aerosol/gas transport at 150°C (conditions of a cold leg break). Distributions are expressed in % relative to the total mass injected in the high temperature (HT) zone for each element. Element distribution in the CHIP "main line" is too coarse to allow for the identification of species condensation peak as the CHIP line was divided only into two parts: the alumina tube for a temperature range of 1600-600°C and the stainless steel tube for 600-150°C. Except for iodine, the other elements (Cs, Mo) found at the line outlet (at 150°C) are attributed to transport in aerosol form owing to their low volatility. In order to get information on deposit speciation, SEM-EDX, XPS, Raman spectrometry and XRD characterizations were undertaken.

Table 3.9: [PL_MoCsI_2]and [PL_MoCsI_3] tests in the CHIP line- Main results (Grégoire *et al.,* 2015).

Test name	**[PL_MoCsI_2]**	**[PL_MoCsI_3]**
Thermal hydraulic conditions		
Pressure (Mpa)	0.2	
Carrier gas flow (l/min – NPT)	34.7	34.3
Max. temperature in the HT zone (°C)	1600	1600
Residence time in the transport zone (s)	11-12	11-12
Carrier Gas composition	$Ar/H_2O/H_2$	$H_2O/He/Ar$
	94.8/2.4/2.8	50.8/44.1/5.1
H_2/H_2O molar ratio	**1.2**	**0**
Element injection in the HT zone : iodine concentration and element molar ratio		
Iodine concentration (mol/l)	$5.8\ 10^{-8}$	$7.6\ 10^{-8}$
Cs/I	4.2 ±0.4	4.0 ±0.4
Mo/Cs	3.7 ±0.4	3.2 ±0.3
Deposition in the main line	1600 -600 °C (alumina tube) and *600-150 °C (stainless steel tube)*	
I	(1.5±0.1)%	0 %
	(36.5±3.0)%	*(0.2±0.02)%*
Cs	(34±2.7)%	(11±0.9)%
	(18± 1.5)%	*(16±1.3)%*
Mo	(57± 4.5)%	(4.0±0.3)%
	(10±1)%	*(21±1.7)%*
Sampling line data: iodine Transport at 150°C		
I gas fraction	**(1 ±1)%[a,b]**	**(88±6.4)%[a,b]**
Iodine gas identification		
I as I_2	0[c]	~ 2/3[b,c]
I as HI	1 (assumption)	~ 1/3[b,c]
I aerosol fraction	**(61 ±3)%[a,b]**	**(11.8±6.4)%[a,b]**
Iodine aerosol identification	Not determined assumed to be CsI	
Sampling line data: Transport of other elements at 150°C		
Cs (aerosol)	(48 ±3)%	(73 ±1.6)%
Mo (aerosol)	(33 ±5)%	(75 ±1.7)%

Flow rate are given for NPT (Normal Pressure and Temperature) conditions: 0°C (273 K), 0.101325 MPa; ‡ Element injection based on the final mass distribution in the line and assuming a steady injection rate (relative uncertainties below +/-7%). data rounded to two significant figures**. a** : '$I_{aerosol\&gas}$ line' data; **b**: 'I_g speciation line' data ; **c**: 'I_2 line' data.

Tests performed in pure steam atmosphere:

As already observed in the small-scale test line, a significant release of gaseous iodine is observed as soon as molybdenum is in excess relative to caesium: at 150°C, an average gaseous iodine fraction of 88% could be observed during the [PL_MoCsI_3] test. The gaseous iodine flow is mainly composed of molecular iodine (~ 2/3); the remaining gaseous iodine fraction detected in the aqueous phase (~ 1/3) can be reasonably attributed to HI[6]. The results are consistent with GAEC tests (Gouello *et al.*, 2013) and the [PL_MoCsI_1] test also performed in oxidising conditions (Grégoire *et al.*, 2015).

Consistently with the observations done for the GAEC tests, SEM-EDX analyses of the deposits collected on the quartz plates at 750°C, 660°C and 500°C revealed the presence of dendritic deposits which size decreases with the temperature to finally form fine large parallepipedic-like particles (see Figure 3.6), Mo and Cs being the main components of those deposits. The molybdenum to caesium ratios determined on the plate at 750°C (Mo/Cs~1-2) and at 660°C ($1 \leq Mo/Cs \leq 3$) are homogeneous, though a slight enrichment in Mo is observed as the deposition temperature is decreasing. The deposits collected on the plate at 510°C presents in-homogeneities with long crystallised parallepipedic particles containing almost only Mo ($18 \leq Mo/Cs \leq 43$) and expected to be MoO_3 and smaller particles containing both Mo and Cs ($3.4 \leq Mo/Cs \leq 8$) indicating that the deposits undergoes a strong enrichment in Mo at this temperature (figure 18). Raman characterisations of those deposits indicate the presence of a mixture of caesium polymolybdates of the $Cs_2Mo_xO_y$ type with x and y increasing as the

[6] Indeed, the other possible gaseous iodinated specie HOI is much less volatile than I_2 at 150 °C (Lin *et al.*, 1981) and may be thus collected on the inlet filtering device. Amounts of I at this level of temperature is also very low as this species is recombined into I_2 which is a more stable species in this range of temperature.

temperature decreases: $Cs_2Mo_2O_7$, $Cs_2Mo_3O_{10}$ clearly identified on the plate at 750°C, $Cs_2MoO_3O_{10}$ and $Cs_2MoO_5O_{16}$ for the plate at 670°C and $Cs_2MoO_5O_{16}$, $Cs_2MoO_7O_{22}$ with pure α-MoO_3 on the plate at 500°C, with the Mo enrichment of the deposits as predicted by the Cs-molybdate – Mo oxide binary diagram (Hoekstra, 1973, Smith *et al.*, 2021).

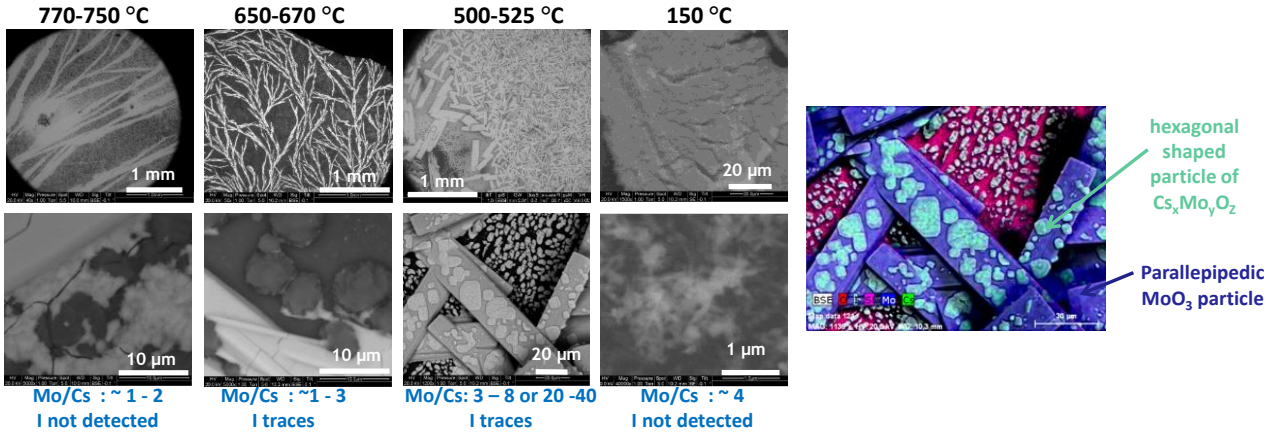

Figure 3.6: [PL_MoCsI_3] test - BSE imaging of aerosols deposited on quartz plates (Grégoire *et al.*, 2015). 500-525°C.

The aerosols collected on the filters appear as agglomerates of submicronic needle-like particles as observed by BSE imaging whatever the collecting zone (CL or HL), see Figure 3.6. Mo and Cs are the main components, I being detected in only very low amounts (EDX analyses). Mo is identified at its +VI oxidation state only given the binding energy of the Mo 3d peak (XPS analyses, binding energy at 232.7 eV) – in full agreement with (Gouello *et al.*, 2013); iodine is hardly detected by XPS on those samples. Though very sensitive to the laser beam (532 nm) used in Raman spectroscopy, the aerosols collected on the main line outlet filter (150°C) featured the presence of α-MoO_3, $Cs_2MoO_5O_{16}$ and $Cs_2Mo_7O_{22}$ compounds. The Raman spectra of aerosols collected in the HL or CL lines could not be clearly identified, even if some spectral bands may indicate the presence of $Cs_2Mo_4O_{13}$ and/or $Cs_2Mo_7O_{22}$ compared to reference spectra (Hoekstra, 1973).

Tests performed in steam/hydrogen atmosphere

Under more reducing conditions (steam/hydrogen, with H_2/H_2O ~1), only very low amounts of gaseous iodine (1 % of iodine injected in the test loop) have been evidenced at 150°C, even in presence of an excess of molybdenum relative to caesium (Mo/Cs ~3.3). As no I_2 was evidenced in the organic lines, this low amount of gaseous iodine may be assumed to be hydrogen iodide.

The deposits collected at ~590°C during the [PL_MoCsI_2] test present a mixture of easily distinguishable particles: submicronic needle-like particles and some larger ball-shaped particles. EDX analyses on the larger particles indicate the presence of Mo, Cs and I but with an enrichment of Cs and I relative to Mo – indicating the presence of CsI particles, the submicronic needle-like particles are molybdenum-rich (Figure 3.7). The aerosols collected at 150°C are fine needle-like particles mixed with larger particles (BSE examination, Figure 3.7). Consistently with the low gaseous iodine release in this test, I is easily detected (as are Mo and Cs) by EDX. Though the resolution of EDX analyses (> 1 µm[3]) does not allow analysis of single particles, the inhomogeneity of the Mo/Cs and Cs/I ratio determined over different agglomerates indicates a mixture of compounds for instance, some aggregates present a strong enrichment of Cs/I indicating probably the presence of CsI particles. It is recalled that caesium iodide is not active for Raman spectrometry (Lacoué -Nègre, 2010) and not present in sufficient amount to be detected by X-Ray diffraction[7].

The samples were sensitive to the Raman laser beam and underwent rapid degradation during the analyses. Nevertheless analyses by multivariate curve resolution of the Raman spectra allow to extract the spectrum of MoO_2, pure α-MoO_3 and besides several caesium polymolybdates ($Cs_2Mo_3O_{10}$, $Cs_2Mo_5O_{16}$, $Cs_2Mo_7O_{22}$) for the

[7] X-ray diffraction is not sensitive as only species with fraction higher than 5% of a mix can be detected - besides the fact that species must be under crystallized forms.

aerosols sampled both at 150°C and 590°C. The presence of MoO_2 was confirmed by both XRD and XPS analyses. Indeed, the Mo 3d spectrum obtained by XPS analyses (Figure 3.8) shows that the injected Mo(+VI) underwent a partial reduction in the steam/hydrogen flow. Three different oxidation states could be identified with a similar distribution on all samples: Mo(VI) ~50% - Mo(V) ~25% -Mo(IV) ~25%. Under reducing conditions, Mo is mainly found in the high temperature zone (57% of injected Mo is found deposited in the alumina tube above 600°C) consistently with the more refractive behaviour of its lower oxide[8] and is less transported up to the line outlet (33% in aerosol form). On the contrary, under oxidative conditions, Mo is less deposited (mainly below 600°C as reported in Table 3.9) and much more transported (70-75% in aerosol form). Similarly to molybdenum, caesium deposition pattern is dependant of the reducing/oxidative conditions.

At 150°C, iodine can be detected in small amounts at the sample surface and is bonded to Cs only, ($I(3d^{5/2})$ spectrum presents a peak at 618.8 keV typical of the I–Cs bond (Dillard, 1984). At ~590°C, a minor fraction of I is also detected as I_2 adsorbed on the aerosols surface as the $I(3d^{5/2})$ spectrum presents a second peak at 620.8 keV which is typical of the I–I bond.

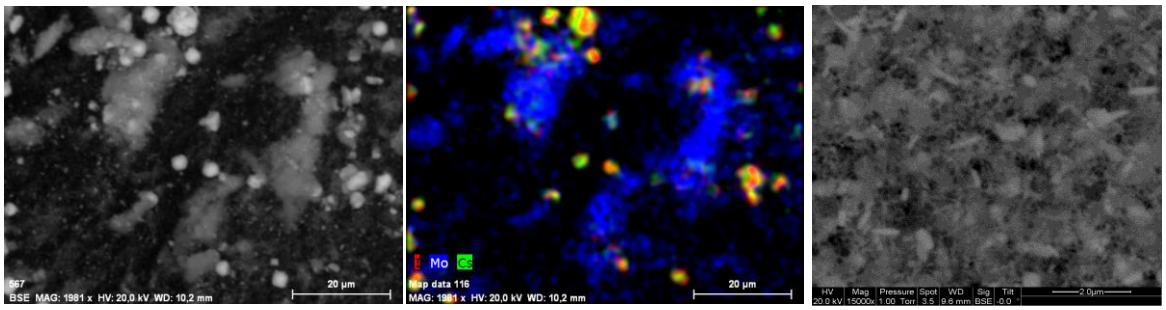

Figure 3.7: [PL_MoCsI_2 test] - left : SEM-EDX imaging of aerosol collected at 590°C –x 1981 - color code : I in red, Mo in blue, Cs in green. (Grégoire *et al.*, 2015).

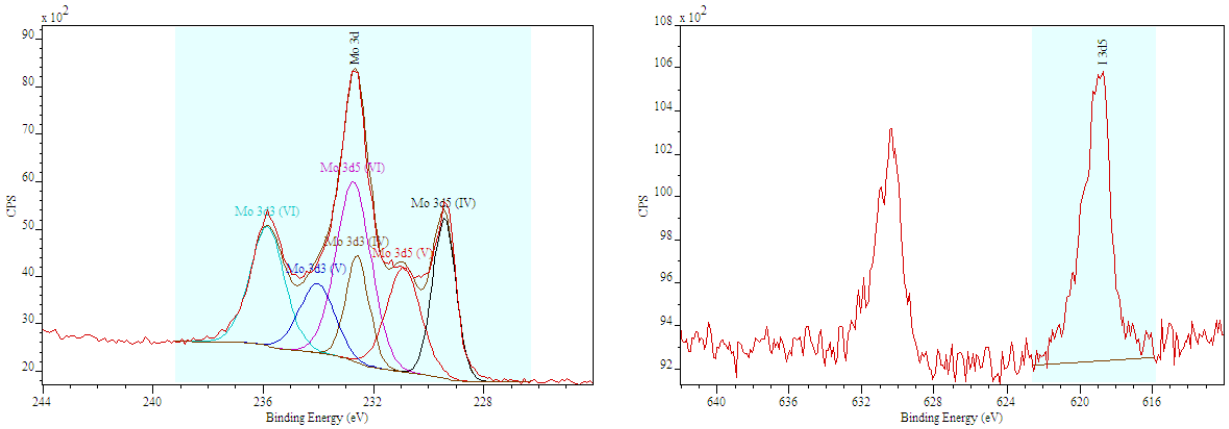

Figure 3.8: [PL_MoCsI_2 test] - XPS Spectra of aerosols collected on sequential aerosol filter of the cold leg sampling line (150 °C) (Grégoire *et al.*, 2015).

Left: binding energy zone of Mo3d: Mo3d5(+VI) at 232.7 eV, Mo3d5(+V) at 230.9 eV and Mo3d5(+IV) at 229.4 eV.
Right: binding energy zone of I3d (I3d3/2 and I3d5/2 doublet) - binding energy of I3d5/2 at 618.8 eV typical of I-Cs bond.

3.5.2 ASTEC/SOPHAEROS modelling

The [PL_MoCsI_3] and [PL_MoCsI_2] tests were simulated (Grégoire *et al.*, 2015) by ASTEC SOPHEAROS. Input data were the CHIP thermal profile and the initial test conditions (Table 3.9). Two kinds of computation were done assuming firstly thermodynamic equilibrium in the gas phase and then taking into account kinetic of the IOH system. In the first case, vapour speciation depends only on species involved, associated Gibbs fee energy and element inventory.

[8] MoO_2 melting point is at 2300°C whereas MoO_3 melting point is at 795°C.

Vapour concentration profiles of main species involving Cs and I and element ratios are represented in Figure 3.9 for the [PL_MoCsI_3] test. With temperature decrease, CsOH disappears to form mainly Cs_2MoO_4 and CsI. As for the GAEC simulation, due to condensation of Cs_2MoO_4 (at ~700-800°C) and CsI (at ~500-600°C), Cs inventory in the gas phase decreases faster than iodine inventory. In the gas phase, no other element can interact with iodine leading to molecular iodine formation at low temperature by equilibrium calculations contrarily to GAEC simulation for which HI is the main released gaseous iodine species.

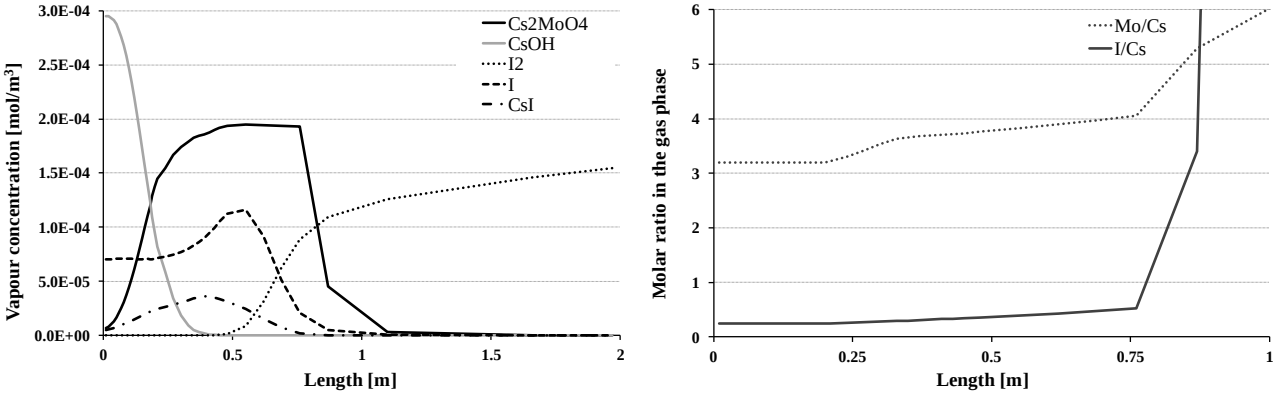

Figure 3.9: [PL_MoCsI_3] test, vapour concentration and element ratio profile calculated with thermodynamic equilibrium (only Cs I species are reported) (Grégoire *et al.*, 2015).

Results of the simulation are reported in Table 3.10. The amount of gaseous iodine released is around 95 % with respect to the initial inventory. It is quite satisfactory compared to experimental results. Iodine is only in molecular iodine form consistent with the dominant form experimentally detected. Cs and Mo are computed under aerosol form in agreement with experimental results. Nevertheless, condensation along the tube is overestimated for Cs and Mo. This discrepancy may partially result from uncertainties on temperature gradient which influences condensation process but also from absence of kinetic condensation processes. Possible remobilisation of some deposits, which are not modelled at this stage, can also account for this difference (remobilisation resulting from chemical transformation of the deposits by interaction with surfaces).

This computation shows that gaseous iodine is formed due to Cs interaction with Mo and Cs-Mo condensation or nucleation. Because these phenomena occur just downstream of the high temperature zone, the thermodynamic equilibrium assumption leads to good agreement on iodine behaviour.

Table 3.10: [PL_MoCsI_3] test, element repartition (gas release, aerosol release, deposited) in % of element mass injected. Results calculated with thermodynamic equilibrium and kinetic reactions (in parenthesis) (Grégoire *et al.*, 2015).

% ii	I model	I exp.	Cs model	Cs exp.	Mo model	Mo exp.
Gas released	94.3 (76.3)	88.3 ±6.4	0 (0)	0	0 (0)	0
Aerosol released	0.55 (16.3)	11.5 ±6.4	40 (43.4)	73	50.8 (54.1)	75
Deposited	5.15 (7.4)	0	60 (56.6)	27	49.2 (45.9)	25

A possible improvement is to consider kinetic reactions for iodine behaviour. In this case the gaseous release is slightly modified (values in parenthesis in Table 3.10). Gaseous iodine still remains in molecular form with very low amounts of HI and I at 150°C. On the contrary, the fraction of iodine aerosol (CsI) increases (16.3 % of element mas injected) in better agreement with experimental results (11.5 ±6.4%).

In steam and hydrogen (H_2/H_2O ~1) atmosphere ([PL_MoCsI_2] test), Cs_2MoO_4 concentration is lower. CsI is formed at higher temperature than in the calculation discussed above and there is no atomic iodine at low temperature (Figure 3.10). CsI and Cs_2MoO_4 retentions are important all along the tube. The molar ratio of I/Cs is lower than 1 after CsI condensation (Figure 3.10). It means that some Cs remains in the gas phase. A small amount of HI is formed at high temperature but due to the relative stabilities of CsI and Cs molybdates under these conditions, no significant amount of gaseous iodine can be formed.

Cs, I and Mo are released in aerosol form, which is in agreement with experiment for Cs and I. As for of Mo, experiment shows dominant line deposition (

Table 3.11). Mo is mainly in the MoO_3 form (and associated polymer). No Mo(IV) oxidation state is calculated, whereas the presence of condensed Mo(IV) has been experimentally established. This fact may account for the differences between calculation and experiment in terms of Mo distribution between aerosol/deposited forms. The Cs release modelled is mainly in the Cs_2MoO_4 and CsI forms. This last point agrees with experiment where CsI was observed.

The same simulation was performed in activating iodine kinetic reactions, values in parenthesis in

Table 3.11) The vapour concentration profile is quite similar to the one obtained with thermodynamic equilibrium computation. The main difference is the amount of HI, which remains at low temperature due to kinetic limitations. Therefore, a small fraction of gaseous iodine (HI) is modelled at the outlet (3.4%) in accordance with experimental observation featuring a very low gaseous iodine release - but not as molecular iodine.

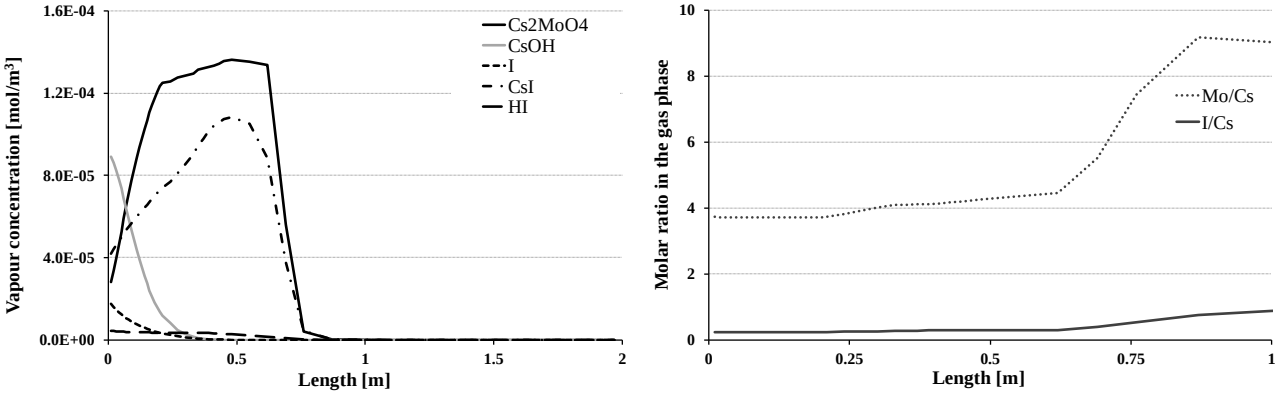

Figure 3.10: [PL_MoCsI_2] test, vapour concentration (left) and element ratio profile (right) for main species calculated with thermodynamic equilibrium (Grégoire *et al.*, 2015).

Table 3.11: [PL_MoCsI_2] test, iodine repartition (gas and aerosol release and deposited iodine) in % of iodine injected calculated with thermodynamic equilibrium and kinetic reactions (in parenthesis), (Grégoire *et al.*, 2015).

% ii	I model	I exp.	Cs model	Cs exp.	Mo model	Mo exp.
Gas released	0 (3.4)	~1	0 (0)	0	0 (0)	0
Aerosol released	68.9 (66.1)	61	54 (53.9)	48	64.8 (64.6)	33.4
Deposited	31.1 (30.6)	38	46 (46.1)	52	35.2 (35.4)	66.6

3.5.3 Conclusion: Mo reactivity on the Cs-IOH system

The GAEC and CHIP LP experiments showed significant gaseous iodine releases under oxidising conditions for $H_2/H_2O \leq 0.1$. Experiments in CHIP with element ratio close to a reactor case (Cs/I ~2-5 and Mo/Cs ~2-5) revealed a gaseous iodine release at the line outlet up to 90% of the initially injected flow, identified as a mixture of I_2 and HI. The deposits and aerosols collected in the line were composed of molybdenum oxides and of various forms of caesium molybdates ($Cs_2Mo_nO_{3n+1}$, $n \geq 2$). No CsI particles were detected. Under oxidising conditions ($H_2/H_2O \leq 0.1$), which enhance Mo(VI) formation and, with an excess of Mo (Mo>Cs), Cs is confined by the formation of Cs-molybdates inducing strong gaseous iodine release in both hot and cold leg break conditions. Molecular iodine is the main detected species.

On the contrary, a slightly reducing atmosphere (addition of a few % of H_2) is sufficient to promote the formation of CsI and thus strongly decreases the release of gaseous iodine even in presence of an excess of Mo relative to Cs. It was shown that molybdenum was significantly reduced to the (+V) and (+IV) oxidation states inhibiting caesium molybdates formation. A good consistency between simulation and experiments was obtained with the current Mo-CsIOH models in ASTEC/SOPHAEROS. In more reducing conditions ($H_2/H_2O = 1.2$), both the decrease of Mo release from the degraded fuel and the transport of the less reactive reduced form of Mo (Mo(IV) and Mo(V)) contribute to maintain Cs species available to react with iodine to lead to CsI formation.

3.6 Extended systems: influence of Silver-Indium-Cadmium (SIC)

The study of the extended systems addressed separately the effect of each element of the SIC control rod on the persistence of gaseous iodine compared to tests performed with the Mo-CsIOH system in pure steam conditions. As stated previously, steam conditions enhance the formation of the stable caesium molybdates, thus partially preventing CsI recombination and promoting the release of gaseous iodine. On the contrary, silver, cadmium and to a lesser extent indium are expected to react with iodine to form metallic iodide (AgI, CdI_2 and possibly InI_x species). Nevertheless, the formation of metal-molybdates is not excluded, competing either with metal iodide or caesium molybdates generation.

In this view, three tests were carried out with similar element mass flow rates (Mo, Cs, I) as for the former [PL_MoCsI_3] test **plus** one additional injection of a control rod element (cadmium, indium or silver) (Grégoire *et al.*, 2021, Grégoire 2021). The [In+MoCsI] test, featured only a moderate indium (injected as In_2O_3) excess relative to iodine (In/I~4.4), this excess corresponds to the lower bound of the expected transport in the RCS in a severe accident (Haste *et al.*, 2013, see also Table 3.1). For the [Cd+MoCsI] test, metallic cadmium vapours were generated in a very large excess relative to iodine (Cd/I ~125). A third test featured silver, the [Ag+MoCsI] test. To better assess reactivity with iodine in severe accident conditions, the test was performed with a very large excess of silver relative to iodine (Ag/I~55). Similar thermal gradient and residence time were applied compared to the [PL_MoCsI_3] test. As for the carrier gas composition, a mix of steam/inert gas was injected for the [In+MoCsI] and [Cd+MoCsI] tests as it was observed that those CR elements were also released during the Phébus test main release phase of Cs, I and Mo (in steam atmosphere). A low amount of hydrogen (1.8% of the total atmosphere) was added for the test featuring silver, as this element was released later when low amounts of H_2 were measured in the Phébus circuit (Grégoire and Haste, 2013).

The main objective was to assess the influence of each additional element (Ag, In, Cd) on the nature of deposited and transported species compared to the Mo-CsIOH chemical system alone. A special attention was brought on the formation of metallic iodide and metallic molybdates which may play a key role on gaseous iodine persistence at 150 °C.

3.6.1 Iodine transport and Element mass distribution in the CHIP line

Test conditions and element distributions are reported in Table 3.12 in terms of high/low temperature deposition, aerosol/gas transport at 150°C (conditions of a cold leg break). Distributions are expressed in % relative to the total mass injected in the high temperature (HT) zone for each element.

3.6.1.1 Nature of iodine released at 150°C

The sampling lines allowed to evaluate the level and nature of iodine release at 150°C for each test. Results are presented in the Table 3.12.
For the [In+MoCsI] test, almost only gaseous iodine was released at 150 °C, with average fraction close to 90% at 150°C (relative to the initial iodine mass injected in the HT zone). Roughly one half of the gaseous iodine is identified as molecular iodine, the rest being attributed to an inorganic form, assumed to be mostly HI because the formation of HOI is less probable in such conditions (Grégoire *et al.*, 2017). Results are comparable to the [PL_MoCsI_3] test, indicating that the presence of indium does not significantly alter the chemical Mo-CsIOH system in steam atmosphere. As a consequence, it is confirmed that aerosols composed of InI_x species are not formed in these experimental conditions.

For the [Cd+MoCsI] test, for both "$I_{aerosol\&gas}$ line" and "I_{gas} speciation line", the gaseous iodine fraction detected downstream of the aerosol filter is very low (< ~1%). On the contrary, a significant amount of gaseous molecular iodine is observed in the "I_2 line" (without inlet filter), representing 28% of initially injected gaseous iodine. The fact that a measurable gaseous iodine fraction could be detected only in the "I_2 line" can be accounted for by a significant retention of gaseous iodine species on aerosols collected on the inlet filter of the other sampling lines. Such retention was not observed during the [In+MoCsI] and [PL_MoCsI_3] tests, and may be due to presence of cadmium species in the case of the [Cd+MoCsI] test. We thus retain the value gained from the "I_2 line" (28% of initially injected iodine) for the gaseous iodine fraction. This value is considered as a minimum as only I_2 fraction could be quantified in this line. The gaseous iodine fraction is nevertheless almost three times lower than that

observed during the [PL_MoCsI_3] test (88.3%), indicating that cadmium species contribute to reduce the transport of gaseous iodine compared to the Mo-Cs-I-O-H system in steam. Nevertheless, such cadmium effect is observed for a very large Cd/I ratio.

For the [Ag+MoCsI] test, the "I_2 line" turned out to be inefficient to trap molecular iodine (if any) in presence of metallic silver particles (see section 3.2.2.). As a result, we retain only the data gained from the "$I_{aerosol\&gas}$ line" which shows a very low gaseous iodine fraction (<2%). One should keep in mind that this gaseous iodine fraction may be underestimated owing to possible gaseous iodine retention on the particles trapped on the inlet filter of the sampling line (similarly to the [Cd+MoCsI] test). Iodine-containing particles (expected to be AgI or CsI) was found predominantly soluble in aqueous media suggesting that formation of (insoluble) AgI is not the main reaction pathway leading to the release of iodine as aerosols. Indeed, only 10%-25% of iodine collected in the sampling lines could be identified as AgI that is not consistent with thermochemical simulations predicting most that 75%. As a consequence, the most probable iodine form to be released at 150°C is CsI.

Although the iodine nature at 150°C (cold leg break conditions) cannot be fully described in presence of cadmium or silver, these control rod materials tend to lower the gaseous iodine fraction formed along the thermal gradient.

3.6.1.2 **Element line distribution – comparison with reference test [PL_MoCsI_3]**

As for the other CHIP tests, element distribution in the line is reported for the 1600-600°C temperature range , 600-150°C and transport at 150°C. Except for iodine, the other element found at the line outlet (at 150°C) are attributed to transport in aerosol form owing to their low volatility. The following statements can be put forward based on the experimental results and compared with the [PL_MoCsI_3] test:

For iodine, no deposition is observed above 600°C for all tests. Deposition below 600°C is very low when iodine is mainly transported at the line outlet in gaseous form as for the [In+MoCsI] test (0.1% of total injection iodine found in the 600-150°C temperature range) or the [PL_MoCsI_3] reference test. When iodine is found mainly transported in aerosol form at 150°C, a significant iodine deposition is observed but only below 600°C : 13% for the[Cd+MoCsI] test and 15% for the [Ag+MoCsI] test. Such iodine deposition in the CHIP line results from vapour condensation or aerosol deposition of iodine containing species as already observed when iodine is transported as CsI (Grégoire *et al.*, 2015).

Mo distribution in the CHIP line for the [In+MoCsI] test shows 7% deposited above 600°C, 21% deposited in the 600-150°C temperature range and 72% transported as aerosols. These values are comparable to that obtained for the reference test. On the contrary, in presence of Cd or Ag, Mo high temperature deposition is enhanced up to 31% ([Cd+MoCsI] test) and 47% ([Ag+MoCsI] test) simultaneously to a strong decrease of the deposition in the stainless steel tube (10% of Mo deposited below 600°C for both tests) and to a decrease of Mo found transported at 150°C (59% for the [Cd+MoCsI] test and 43% for the [Ag+MoCsI] test). This distribution is comparable to that observed for the MoCsI test in steam/hydrogen (Grégoire *et al.*, 2015), in which a significant reduction of Mo(VI) to the less volatile Mo(IV) and Mo(V) compounds was evidenced. Indeed reduction of Mo is not excluded as oxidation of Cd or Ag in the steam flow at high temperature results in the production of low amounts of hydrogen capable of reducing (even partly) the injected MoO_3 (in addition to the injected low hydrogen flow for the [Ag+MoCsI] test). As consequence Mo may be less reactive to form metallic molybdates and thus may contribute to the increased formation of metallic iodides (CsI, CdI_2 and to a less extent AgI).

Indium and silver are mainly found deposited in the high temperature zone above 600°C (alumina tube) consistently with their strong refractive properties. For the [In+MoCsI] test, 42% of In is found in this zone, whereas deposition below 600°C represents only 10% of initially injected In. For the [Ag+MoCsI] test, 57% of silver is found deposited above 600°C and 6% below. On the contrary, cadmium which is more volatile is mainly found in the 600-150°C temperature zone (41% for the [Cd+MoCsI] test and less at high temperature (3% above 600°C).

Only caesium deposition pattern does not show significant changes in this test series: high temperature deposition (above 600°C) represents 6-13% of initially injected caesium, deposition in the 600-150°C temperature range 13-16% so that for all test, Cs is mainly transported to the line outlet in aerosol form (73-80%).

Table 3.12: [In+MoCsI], [Cd+MoCsI] and [Ag+MoCsI] tests - main results (Grégoire *et al.*, 2021).

Test name	**[In+MoCsI]**	**[Cd+MoCsI]**	**[Ag+MoCsI]**
Thermal hydraulic conditions			
Pressure (Mpa)	0.2		
Carrier gas flow (l/min – NPT)	38.2	35.3	35.1
Temperature in the HT zone (°C)	1600		
Residence time in the transport zone (s)	10-12 s		
Carrier Gas composition	Ar/H_2O	$H_2O/He/Ar$	$H_2O/Ar/H_2$
	54.3/45.7	49.4/42.8/7.8	49.6/48.6/1.8
Element injection and molar ratio in the HT zone			
Iodine concentration (mol/l)	$8.2\ 10^{-8}$	$8.3\ 10^{-8}$	$7.5\ 10^{-8}$
Cs/I	2.5±0.2	3.1±0.2	3.6±1.8
Mo/Cs	5.0±0.4	3.7±0.2	3.7±0.3
In/I	4.5±0.3		
Cd/I		126±9	
Ag/I			48±24[a]
Deposition in the main line		1600 -600 (alumina tube) *600-150 °C (stainless steel tube)*	
I	0%	0%	0%
	(0.1±0.01)%	*(13±1.3)%*	*(15±7)%*
Cs	(13±1.2)%	(10±0.9)%	(6±0.6)%
	(13±1.2)%	*(16±1.5)%*	*(14±0.1)%*
Mo	(7.0±0.6)%	(31±2.8)%	(47±4.4)%
	(21±2)%	*(10±0.9)%*	*(10±0.9)%*
In	(42±3.8)%		
	(10±0.9)%		
Cd		(3±0.3)%	
		(41±3.8)%	
Ag			(57±5.4)%
			(6±0.6)%
Sampling line data: Iodine transport at 150°C			
I (gas)	**(89.9 ±6.5)%[b]**	**(28 ±6.3)%[d]**	**< (2±1)%[b]**
		Other lines< 1%	
Iodine gas identification			
I as I_2	~ 1/2	1	nd
I as HI	~ 1/2	-	nd
I (aerosol)	**(10 ±6.5)%[b]**	**(59 ±6.3)% [d]**	**>(83 ±8)% [b]**
		Other lines > 86%	
Iodine aerosol identification	nd	Traces of CdI_2[e]	AgI ~1/10 to 1/4 [b]
Sampling line data : transport of other elements at 150°C			
Cs (aerosol)	(74 ±2.0)%	(74 ±2.0)%	(80 ±1.5)%
Mo (aerosol)	(72 ±2.0)%	(59 ±3.0)%	(43 ±4.4)%
In (aerosol)	(48 ±4.0)%		
Cd (aerosol)		(56 ±4.0)%	
Ag (aerosol)			(37 ±5.4)%

Data rounded to two significant figures. Flow rates given for NPT (Normal Temperature and Pressure) conditions: 273 K or 0°C, 0.101325 MPa ; ‡ Element flow rate based on the final mass distribution in the line and assuming a steady injection rate (relative uncertainties below ± 5% except for iodine in the Ag+MoCsI test : ± 50%); **a**: maximum ratio as silver vaporization may also occur during the heating phase; **b** : '$I_{aerosol\&gas}$ line' data; **c**: 'I_g speciation line' data ; **d**: 'I_2 line' data ; max. value for I_g (resp. min value for I_{aer}); **e**: Cd and I detected on few particles (main line deposit -EDX examination).

3.6.2 Deposit characterisation: competition in metallic molybdate formation

A full understanding of iodine behaviour cannot be obtained alone from sampling line data and the element distribution in the line even if some first important information could be gained. In this view, a fine characterization of aerosol deposits and condensed vapours was undertaken. Both condensed deposits collected in the main line (in a temperature range from ~850°C down to 350°C) and aerosols collected at 150°C were considered. Coupled analyses by SEM EDX, Raman micro spectrometry (RMS), XPS and XRD allowed to describe particle morphology, element composition and to identify the main species (Grégoire *et al.*, 2021). In the following sections, analysis of deposits are summarized with decreasing deposit collection temperature. Detailed description is provided in Grégoire *et al.*, 2021 (Appendix 2).

3.6.2.1 Results for the [In+MoCsI] test:

Above 700°C, In_2O_3 is the main deposited species identified as the cubic like particles (Figure 3.11a, SEM examination at 800-765°C). The large amorphous structures observed in this temperature range corresponds to melted silica. RMS allow to identify $CsIn(MoO_4)_2$ at temperature close to 700°C (as illustrated in Figure 3.12 left). This mixed Cs-In polymolybdates become the main species at 700°C (Figure 3.11b) and appears as the large parallepipedic and spherical particles (10-30 µm). Literature data predict the condensation of this species below 650° (Maczka *et al.*, 1997) rather consistent with the observations. Some small parallepipedic (not shown here) particles are identified as caesium molybdates (as shown in Figure 3.12 , right).

At 500°C, three structures can be determined: micronic parallepipedic particles and very fine needles clustered around the larger ones, some larger plate like crystallites (~5-20 µm). The stick like particles size increases as temperature decreases (Figure 3.11c and b). $CsIn(MoO_4)_2$, $In(MoO_4)_3$ are identified as the main species in the clusters of fine particles. Given data of the MoO_3-In_2O_3 binary diagram (Fillipek *et al.*, 2012), indium polymolybdates should be observed at higher temperature (eutectic point at 780°C), indicating competition with the formation of the mixed Cs-In polymolybdates.

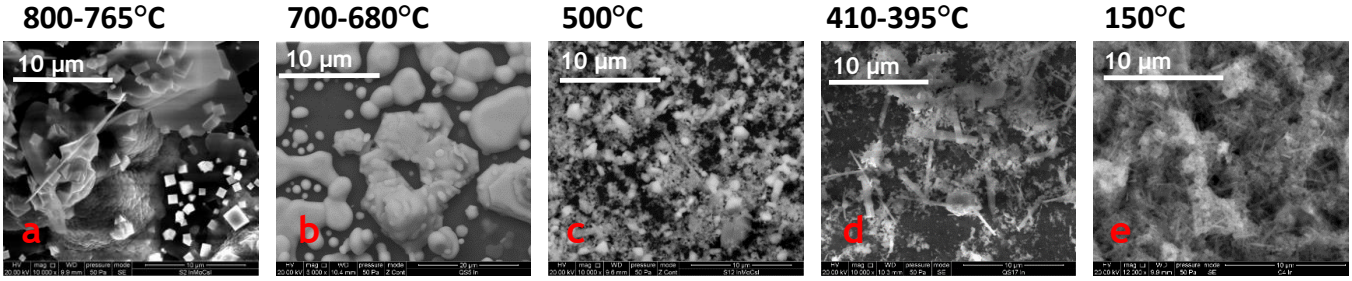

Figure 3.11: [In+MoCsI] test – SEM examination of deposits collected in the 800-150°C temperature range BSE imaging with magnification from 5000 up to 12200 (Grégoire *et al.*, 2021).

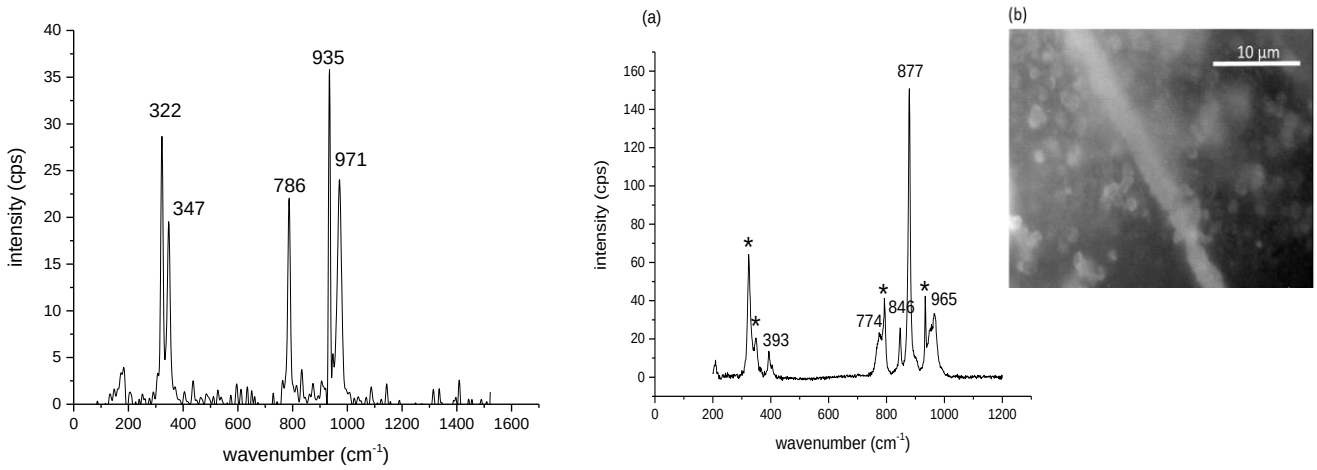

Figure 3.12 : [In+MoCsI] test – RMS analysis of condensed matter collected at 700°C on quartz plate (Grégoire *et al.*, 2021). Left : Typical Raman spectrum identified as $CsIn(MoO_4)_2$ by comparison with reference spectrum (Maczka *et al.*, 1997) . Right: (a) Typical Raman spectrum of needle like particles identified as $Cs_2Mo_7O_{22}$ by comparison with reference spectrum (Hoekstra *et al.*, 1973) (* typical Raman bands of $CsIn(MoO_4)_2$). (b) optical image of needle like particle together with particle of $CsIn(MoO_4)_2$.

In the 500-400°C temperature zone, the large sticks corresponds to α-MoO_3 (as seen in Figure 3.11c, d). This species dominate the deposit composition at 400°C and indicate that not all the molybdenum oxide was consumed by reaction with Cs or In. Some $Cs_2Mo_7O_{22}$ needles are observed. $In(Mo_4)_3$ is still observed (fine particles) but not as the main species.

The aerosols transported at 150°C (Figure 3.11e) are mainly composed of $CsIn(MoO_4)_2$ (DRX and Raman data) but the presence of $Cs_2Mo_5O_{16}$ cannot be excluded.

In the oxidative atmosphere of this test (injection of steam only and indium as indium oxide), only Mo(VI) species were transported in the line (XPS data, as shown in Figure 3.13). Similarly to the [PL_MoCsI_3] test, Mo main deposits are found below 600°C. Iodine was not detected in the solid sample consistently with a transport almost only under gaseous form.

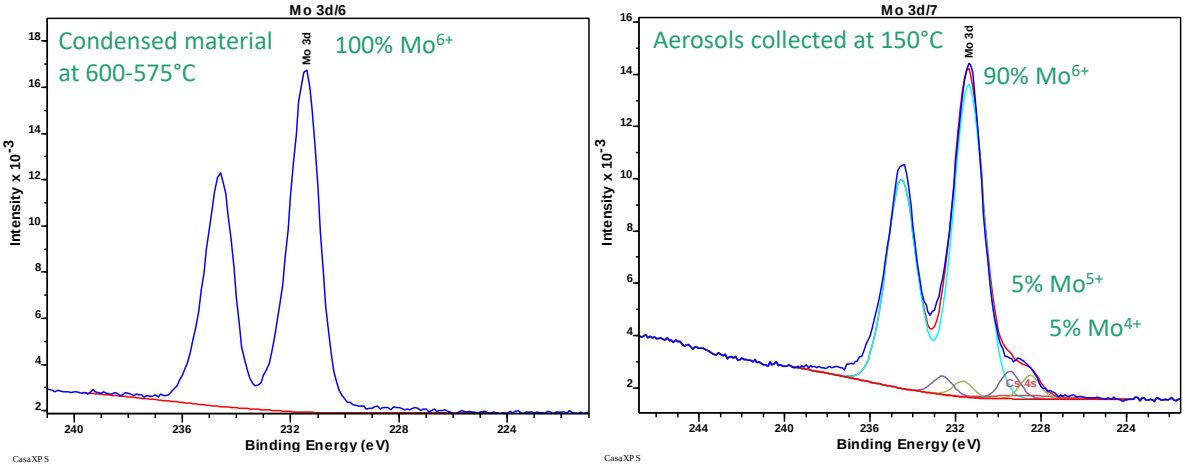

Figure 3.13: [In+MoCsI] test –Mo 3d XPS spectrum of condensed matter collected at 600-575°C on quartz plate and of aerosols collected at 150°C on quartz filter.

3.6.2.2 Results for the [Cd+MoCsI] test

Condensed species were analysed in the 670 -150°C temperature range as no collection devices were implemented for higher temperature. The size of the condensed material decreases with temperature featuring large octahedron particles and huge rods above 500°C, then submicronic needles and ball-shaped particles at lower temperatures (see Figure 3.14a to Figure 3.14e). By comparison with spectra referenced in the literature

or in data banks (Ozkan *et al.*, 1990; Phuruangrat *et al.*, 2011; Xing *et al.*, 2011; Tsyrenova *et al.*, 2011), several species involving cadmium are identified in the deposits.

Cadmium molybdates, mainly $CdMoO_4$, and mixed caesium-cadmium molybdates, $Cs_2Cd_2(MoO_4)_3$, are the main deposited species over all the 670-430°C temperature range. Additional particles composed of caesium-cadmium mixed compounds as $Cs_{2x}Cd_y(MoO_4)_{x+y}$ are hypothesized but these intermediates are not described in the literature. These metallic molybdates may result from the reactions at high temperature between $MoO_{3(g)}$ and $Cd(OH)_{2(g)}$ or $Cd_{(g)}$ and $CsOH_{(g)}$. Competitive reactions between Cd and Cs probably occur as $CdMoO_4$ is the main detected compound and as no pure caesium polymolybdates is detected. Above 600°C, the morphology of $CdMoO_4$ is octahedral (Shari *et al.*, 2013). With decreasing temperature, the overall particle size decreases and the particle shape changes to spherical (see Figure 3.14 a to Figure 3.14 d). Mixed Cs-Cd polymolybdates are localized in cement like deposits (SEM image at 640°C, Figure 3.14 b). Cadmium silicates are identified at lower temperatures (below 540°C) by EDX and XRD in plate shaped particles or rods (not shown here). Reaction between cadmium metal with quartz plate substrate may account for the formation of such species.

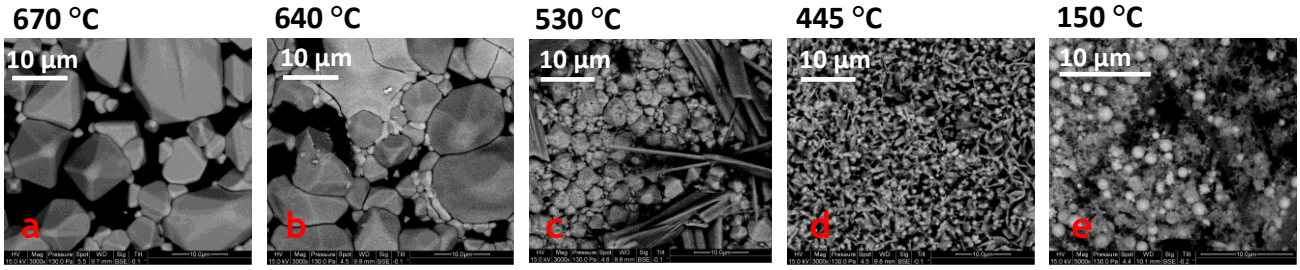

Figure 3.14: [Cd+MoCsI] test - SEM examination of deposits and aerosols collected in the 670-150°C temperature range (Grégoire *et al.*, 2021).

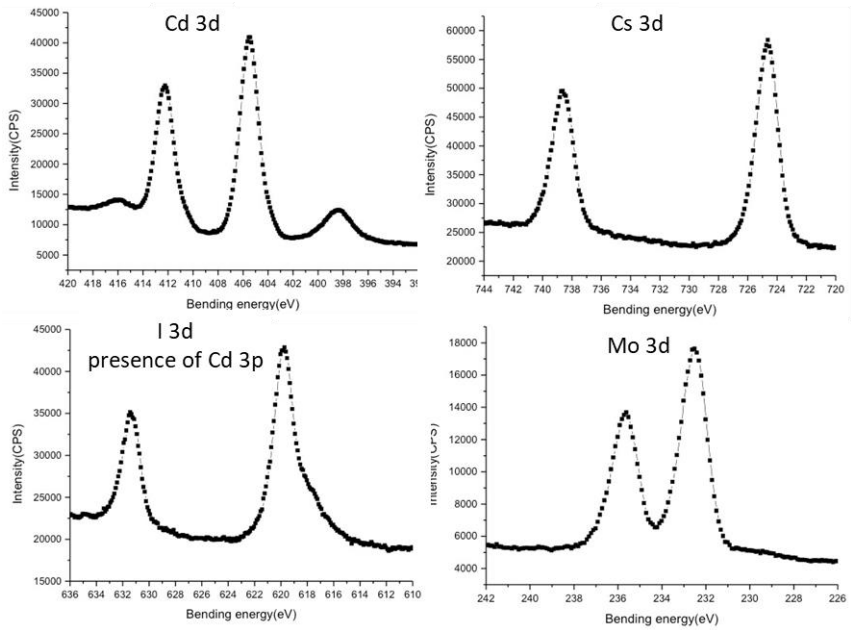

Figure 3.15: [Cd+MoCsI] test – Cd 3d, Cs 3d, Id 3d and Mo 3d XPS spectrum of aerosols collected at 150°C on quartz filter (Grégoire et al., 2021).

The aerosols collected at 150°C are composed of aggregates of submicron particles mixed with larger spherical particles (1-3 µm). $CdMoO_4$ and $Cs_2Cd_2(MoO_4)_3$ are the main compounds of the aggregates. Besides spherical particles of Cd metal, part of Cd may be also oxidized in the steam flow as $Cd(OH)_2$ and CdO forms are detected (Raman spectrometry and X-ray diffraction). Furthermore, traces of MoO_2 are also detected at 150°C, they may result from the reduction of MoO_3 by Cd metal at higher temperature. Although only evidenced at the line outlet, partial reduction of Mo(VI) to Mo(IV) is consistent with high amount of Mo found deposited in the high temperature zone (see Table 3.12) consecutively to the formation of the less volatile Mo (IV)-oxide.

No isolated caesium molybdates could be identified on any samples. The absence of such species in the deposits or in the transported aerosols may result from the competition between the caesium molybdate, cadmium molybdates and mixed cadmium-caesium molybdates formation which is in favour of the later one, since cadmium was injected in very large excess with respect to Cs and Mo.

As far as iodine is concerned, no metallic iodide (as CsI ou CdI_2) could be evidenced in the 670°C-430°C temperature range. Low amounts of iodine were detected at 150°C by XPS characterization (see Figure 3.15) with binding energies ($3d^{5/2}$ level, 619.9 eV) closer to I-I (Dillard, 1984) bonds than Cs-I bonds or Cd-I meaning that I is present as I_2 adsorbed on the particles, CsI and CdI_2 particles were not detected. Nevertheless, in presence of large amounts of Cd, the I3d5/2 XPS lines at 619 eV can be interfered by that of Cd3p3/2 (618.4 eV) so that chemical displacement interpretation should be considered with caution; the I 3d3/2 line (631.5 eV) remains free of interference but is less documented in the literature (NIST data base). The characterisation of the condensed material is consistent with the results gained from gaseous phase (organic line) strengthening the fact that interaction between iodine and cadmium seems to be weaker than expected from literature data (Girault and Payot, 2013), even for very large excess of Cd relative to I.

3.6.2.3 Results for the [Ag+MoCsI] test

Different particle morphologies have been identified by SEM (see Figure 3.16 and Figure 3.17) and are observed over almost all the temperature range of deposit collection (800-150°C) combination with RMS allows to identify most of the deposited species.

Large Ag-rich spherical particles (>10 µm) and partly coalesced at high temperature (>750°C) are observed (see Figure Figure 3.16 a) as the main component of the deposits and then more isolated with size decreasing along with sampling temperature down to submicronic particles (100 nm at 150°C);

Parallepipedic crystallites with size decreasing from ~10 µm to less than 1 µm and needle like particles below 700°C (initially 3-4 µm long then shorter as the collection temperature decreases, see Figures Figure 3.16 b, c, d) . EDX analyses reveal that these particles are Mo and Ag rich and micro-Raman characterisation of the deposits allow to identify molybdenum oxide and silver molybdates. In the 700-400°C temperature region, molybdenum(VI) and (IV) oxides are found as predominant species. The presence of reduced forms of Mo is also observed by XPS (Figure 3.18). The formation of MoO_2 is consistent with the injection of a low amount of hydrogen and the presence of important amount of silver metal which can be considered as a reducing agent. The presence of the less volatile Mo(IV) species is also consistent with enhanced Mo deposition at high temperature (see Table 3.12). Silver molybdates (Ag_2MoO_4 mainly and $Ag_2Mo_2O_7$, $Ag_2Mo_3O_{10}$) were identified by comparison with literature data (Beltran *et al.*, 2014).

The amorphous structures (aggregates of very fine particles?, see Figure Figure 3.16 b, c, d) detected below 700° C and in which Cs is detected (EDX) are identified as caesium molybdates (micro Raman analyses). Caesium molybdates become the dominant species only below 500°C. Competition between the formation of silver and caesium molybdates may explain the delayed deposition of caesium molybdates species, compared to tests featuring only the Mo-CsIOH chemical system (detection of caesium molybdate in the 900-1000°C temperature zone, Gouello, 2012).

Only few single particles featuring either CsI or AgI were found deposited between 350°C and 400°C (see Figure 3.17). Given the fact that iodine is injected with an elemental flow rate almost 50 times lower than silver, metallic iodide - if formed - remains a minor component of the deposits making its direct observation by surface analysis techniques most challenging.

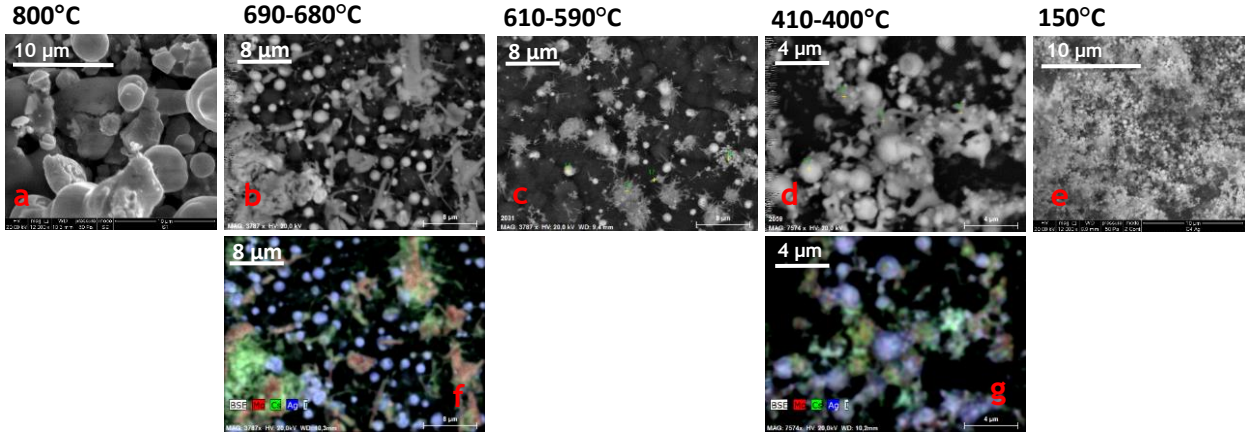

Figure 3.16: [Ag+MoCsI] test - SEM-BSE (a-e) and EDX (f,g) images of deposits and aerosols collected in the 800-150°C temperature range.
(on elemental images f and g: red is Mo, blue is Ag and green is Cs). (Grégoire *et al.*, 2021).

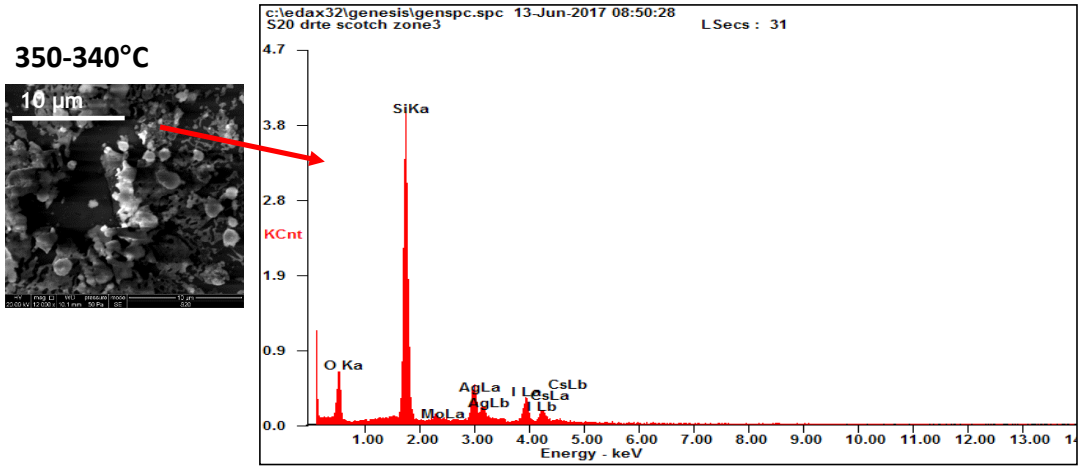

Figure 3.17: [Ag+MoCsI] test - SEM-EDX examination of deposits collected at~340-350°C (Grégoire *et al.*, 2021).

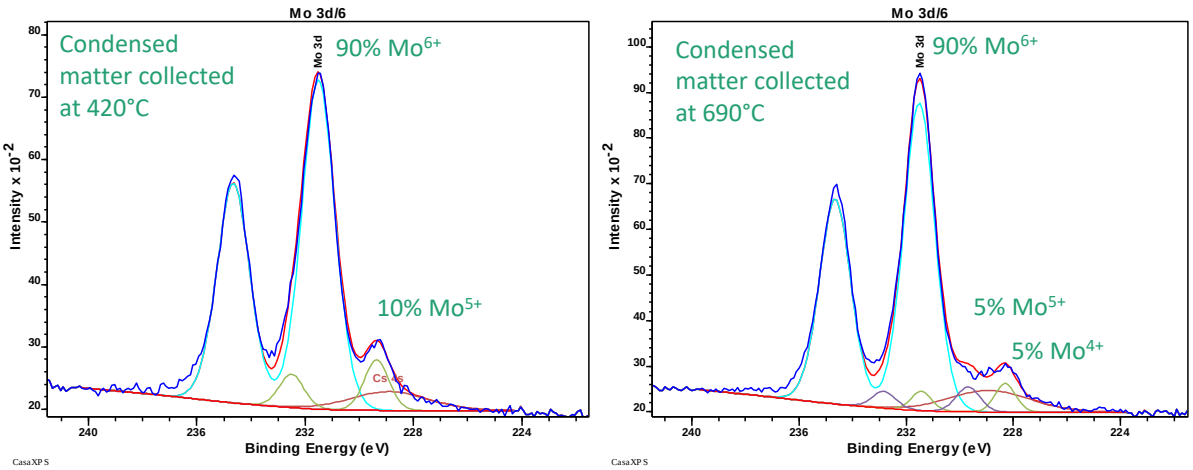

Figure 3.18: [Ag+MoCsI] test – Mo 3d XPS spectrum of condensed matter collected at 690 and 490 °C on quartz plate (Grégoire et al., 2021).

3.7 Discussion – Metallic iodide and metallic molybdate stability

to In the presence of elements of the SIC control rods, the behaviour of iodine may be contrasted. When indium is injected, the formation of InI_x species is not observed and iodine is still transported in the gaseous phase compared to the [PL_MoCsI_3] test. On the contrary, silver and cadmium injection in large excess with respect the other elements (I, Cs and Mo) induce the formation of iodide aerosols. AgI formation seems to be limited despite a large excess of silver, with a formation rate lower than 10% with respect to iodine ([Ag+MoCsI] test). This point confirms that AgI is less stable than CsI and CdI_2 consistently with thermodynamic data as reported in Table 3.13 . More specifically, the three tests exhibited some significant differences as for iodine behaviour:

- For the [In+MoCsI] test, a part of injected indium reacts preferentially with MoO_3 rather than iodine to form indium molybdates so that the formation of InI_x was not observed. As Mo was injected in excess relative to both In and Cs, molybdenum acts still as a Cs sink preventing CsI formation and thus allows the existence of gaseous iodine at 150°C. It is not excluded that injection of In_2O_3 in larger amounts (e.g. larger than Mo as for the tests with Cd and Ag) may result in enhanced consumption of MoO_3 to form In-molybdate competing with Cs-molybdate formation and thus favouring cesium iodide formation but anyway it is not very representative of SA case (In is still in lower amount than Mo).
- For the two other tests, despite the injection of a huge excess of cadmium or silver relative to all the other elements, the formation of metallic iodides such as CdI_2 or AgI, seems not to be the main reaction pathway for iodine. Two other reaction pathways can be hyptothetized. Firstly, reactivity of cadmium and silver with molybdenum oxides may contribute to reduce significantly the Cs-scavenging role of Mo preventing the formation of caesium molybdates with Mo(VI) oxidation state. Secondly, the oxidation of the injected metallic species (Cd, Ag) may promote indirectly the formation of less reactive MoO_2 oxide. This second reactional pathway is expected to remain limited as at most 10% of injected Mo(VI) could be reduced (XPS data, see section 3.6.2).

Table 3.13 : Standard Enthalpy of formation of metallic iodide of interest taken from literature.

Chemical species	**standard formation enthalpy for condensed species (kJ/mol)@298K**	**standard formation enthalpy for gaseous species (kJ/mol)@298K**
CsI	-348.1 (Cordfunke *et al.*, 1985)	-153.3 ± 1.8 (Roki *et al.*, 2014)
CdI_2	-205 (Konings *et al.*, 1993)	-58.8 ± 2.5 (Shugurov *et al.*, 2021)
AgI	-61.8 (Taylor *et al.*, 1921)	125.3 (Barin, 1989)
InI	-102 (Vasil'ev *et al.*, 1987)	26.4 (Gurvich *et al.* 1989)
InI_3	-223 (Vasil'ev *et al.*, 1987)	-105.4 (Gurvich *et al.* 1989)

Characterizations of the main compounds deposited in the CHIP line allowed to identify several metallic polymolybdates in addition to the caesium molybdates already characterized in similar thermal hydraulic conditions (Lacoué-Nègre, 2010; Gouello *et al.*, 2013; Grégoire *et al.*, 2015). Such species were not mentioned either for the VERCORS nor Phébus tests. Nevertheless, TGT deposition profile of In, Cs and Mo obtained for VERCORS HT tests (Pontillon *et al.*, 2010) showed concomitant deposition in the ~800°C (HT2 test), ~675-725°C (HT3 test) and ~640°C (HT2 test) temperature zones, so that deposition of metallic molybdates involving Cs and/or In cannot be excluded. Silver deposition is much more complex to discuss featuring a low homogeneous deposition detected below 700°C (HT3 test) and 600°C (HT2 test) and no data for Cd deposition is available. As only I and Cs deposition profiles were determined for the Phébus TGT during the FPT1 and FPT2 tests (Girault and Payot, 2013), it will be difficult to infer any comparison with our results.

The formation of various metallic polymolybdates entering in competition with the formation of caesium polymolybdates was clearly evidenced in the three tests. Indeed, deposits containing pure caesium molybdates were detected at a lower temperatures (below 600°C for the In-MoCsI and Ag-MoCsI tests) than observed when

only Mo oxide and Cs species are reacting together (1000°C, as reported in Gouello *et al.*, 2013). Cd and Ag were injected both in large excess relative to Mo and Cs, so that a direct comparison of the two tests in terms of molybdate formation can be put forward. Pure caesium molybdates were still observed in Ag-MoCsI test, as well as MoO_2 and MoO_3 species. On the contrary, cadmium containing molybdates were the dominant species in the Cd-MoCsI test featuring only mixed Cd-Cs molybdates and traces of MoO_2 (aerosols collected at the line outlet). These features indicate that the formation silver molybdate seems less favoured compared to that of cadmium molybdate in our test condition. Even if In_2O_3 was injected in lower amount (in default relative to Mo but in excess compared to Cs), the formation of indium molybdate seems favoured at high temperature, compared to that of pure caesium molybdates, as $CsIn(MoO_4)_3$ and $In_2(MoO_4)_3$ are the dominant species in the 500-750°C temperature range. Caesium was found mainly as a mixed InCs molybdate compounds over all the temperature range, pure caesium molybdates appearing less abundant. In the oxidative atmosphere of this test (steam injection and no reducing species), the excess Mo was found mainly as α-MoO_3 from 500°C down. It is nevertheless difficult to know exactly if the species are formed in the gas phase and/or in the solid phase after condensation of In, Mo and Cs species in oxide or hydroxide forms.

Formation enthalpies referenced in the literature show that caesium molybdates are probably the most stable compared to cadmium, silver and indium molybdates even if the thermodynamic date are uncomplete with no mixed elements (see Table 3.14). The $\Delta H_f°(298K)$ remains nevertheless close enough so that in our conditions the large excess of Cd, Ag and In reagents compared to Cs may have displaced equilibrium in favour of Cd, Ag or In-molybdates in the high temperature zone. Consumption of these elements resulted then in the formation of the more stable Cs molybdates at lower temperature as experimentally observed. In this discussion, possible kinetic limitations in the thermal-hydraulic transient are not taken into account and thermodynamic data are nevertheless not all available in the literature.

Table 3.14: Standard Enthalpy of formation of molybdates of interest taken from literature.

Chemical species	**standard formation enthalpy for condensed species (kJ/mol) at 298K**	**standard formation enthalpy for gaseous species (kJ/mol)at 298K**
α-MoO_3(s) and MoO_3(g)	-745.5 (Crouch-Baker *et al.*, 1984)	-364.4 ± 20.0, (Cordfunke and Konings, 1990)
Cs_2MoO_4	-1514.4 (Gamsjäger and Morishida, 2015)	-1179.2 (Tangri *et al.*, 1989)
In_2MoO_4	Not available	
Ag_2MoO_4	-838.2 (Gamsjäger and Wiessner, 2018; Gamsjäger and Morishida, 2015)	-459.6 (CCSD(T)/CBS(TZ-QZ) value, method described in Saab and Souvi, 2018)
$CdMoO_4$	-1034 ± 5.7 ; –1015.4 ± 14.5 Ali *et al.*, 2005 ; Mishra *et al.*, 2006	-606.0 (CCSD(T)/CBS(TZ-QZ) value, method described in Saab and Souvi, 2018)
$SnMoO_4$	Not available	-699 ± 29 (Shugurov *et al.*, 2015)

Even if trends could be inferred from a direct comparison of stability of the identified compounds, a full understanding of the main reactions which occurred in the CHIP line with these chemical systems will be gained by simulation of the experiments with severe accident calculation codes as ASTEC/SOPHAEROS (Cousin *et al.*, 2008; Cantrel *et al.*, 2013). Nevertheless, up to date, thermodynamic data of some metallic molybdates evidenced in these experiments are not available in the literature and cannot be accounted in the thermodynamic database of the simulation tools. DFT calculations, which are ongoing in SAM/LETR laboratory, may help to provide some of the missing thermodynamic data for gaseous species.

3.8 Conclusion: In, Ag and Cd reactivity on MoCsI chemical system

This series of tests performed in the CHIP line with the MoCsI chemical system and one SIC CR element (In or Cd or Ag) revealed that the behaviour of each component of the SIC control rod considered separately is much more complex than initially expected. Indeed, combined on-line sampling, elemental post-test analyses and an

extended characterization of deposits allowed to identify most of compounds formed during the transport in the thermal gradient (1600-150°C) of the CHIP line. These species were not evidenced in the larger scale Phébus tests or VERCORS HT tests due to the too integral objective of the test.

In the case of indium injection, a release of gaseous iodine similar to the PL_MoCsI_3 reference test was still observed. Indium iodide formation was not observed as expected from the low stability of $InI_x(g)$ species. The fully oxidative conditions contributed to maintain Mo mainly in the +VI oxidation state and thus its capabilities to form metallic molybdates. Beside, strong deposition of In_2O_3 at high temperature (> 750°C) owing to the refractive property of this species, the main contribution of In injection was the formation of indium molybdates and mixed In-Cs molybdates. Owing to the large excess of Mo relative to both In and Cs, Mo still played its Cs-Sink role, promoting a large fraction of gaseous iodine transported at low temperature.

In the case of both cadmium or silver injection, the formation of metallic iodide other than CsI seems not to be the main reaction pathway leading to a strong reduction of gaseous iodine release despite the injection of very strong excess relative to all the other elements (I, Cs and Mo). The formation of various metallic silver or cadmium molybdates entering in competition with caesium molybdates contribute to significantly reduce the Cs-scavenging role of Mo.

It can be stated that due to the high stability of caesium iodide, only absence of Cs can prevent its formation but as various polymolybdates are formed, as detailed beforehand, caesium cannot be totally consumed by molybdemun in presence of control rod materials resulting from the molar contents respectively present in the RCS in SA conditions.

Role or SIC elements were further investigated in the CHIP+ programme by considering the combined effect of several control rod elements (Cd and Ag) on the FPs transport (I, Cs, Mo) (Grégoire, 2021). The role of boron on the FPs transport was finally considered – firstly alone and then in combination with Cd and Ag (Grégoire, 2021).

3.9 Chemical reactivity in the RCS during a severe accident phase: outcomes of the CHIP and CHIP+ programmes

With the CHIP and CHIP+ programmes, large efforts were sustained over 10 years with the aim to improve the knowledge of physico-chemical behaviour of the material released from a degraded core during its transport in the RCS in a SA situation.

The main achievement of the CHIP and GAEC lines was the capability of reproducing quite representative conditions to that prevailing in the RCS in SA: large temperature gradient changes and short residence time, steam or steam/hydrogen atmospheres and above all relevant element concentrations and ratios. In addition, larges efforts were devoted to develop suitable samplings and chemical analyses to cover the complexity of the analysis. Both the CHIP and GAEC lines operated at Cadarache and extended cooperation with academic partners (University of Lille and later University of Bordeaux) helped to achieve significant progresses in the understanding of chemical reactivity in the thermal conditions prevailing in the RCS in SA conditions (1600°C-150°C). Main results were shared with CHIP and CHIP+ partners (experimental reports and synthesis report, Grégoire 2021) and later with the scientific community though oral communications or posters (Roki *et al.*, 2008; Délicat el al., 2011; Grégoire and Mutelle 2012; Gouello *et al.*, 2012; Colombani *et al.*, 2015, Grégoire and Morin, 2018, Grégoire *et al.*, 2016), publications (Roki et al, 2008, Roki *et al.*, 2013, Roki *et al.*, 2014, Roki *et al.*, 2015, Gouello *et al.*, 2013; Grégoire *et al.*, 2015; Grégoire *et al.*, 2017; Grégoire *et al.*, 2021). Thesis manuscript were also shared as open data (Roki, 2009; Lacoué-Nègre, 2010; Gouello, 2012; Délicat, 2012).

The main outcomes of FPs chemistry in conditions of a RCS in SA can be summarized as follows:

Gaseous iodine reactivity in the gas phase is kinetically limited, mainly under oxidising conditions, as it has been evidenced by the experiments performed on the I-O-H system. Experimental observations can be satisfactorily described by the thermo-kinetic mechanism developed by IRSN in collaboration with the University of Lille. This kinetic network was implemented in the ASTEC/SOPHAEROS simulation software.

With caesium in excess relative to iodine in the CsIOH system (as expected in severe accident scenarios), large caesium iodide formation prevents any gaseous iodine transport. Experiments failed to highlight any kinetic limitations so that the caesium chemistry is quite well simulated by considering thermodynamic chemical equilibrium in the gas phase, thermodynamic data being well known (Roki *et al.* 2013, Roki *et al.,* 2014, Badawi *et al.*, 2012).

Mo and B act both as a Cs sink resulting in the formation/release of gaseous molecular iodine (main species) and hydrogen iodide in a lesser extent. The formation in the gas phase of stable caesium molybdates (Cs_2MoO_4, Cs_2MoO_7…) by reaction of Cs-species with molybdenum trioxide MoO_3 prevents the formation of CsI and thus enhance gaseous iodine formation. Molybdenum is strongly sensitive to reducing conditions, leading to the formation of the weakly reactive Mo(IV) and Mo(V) species. The reactivity of the MoCsIOH system is quite well reproduced by ASTEC/SOPHAEROS simulations assuming Mo/Cs species at thermodynamic equilibrium and addressing I-O-H kinetics. With respect to caesium, and compared to molybdenum trioxide, boron oxides are less reactive in oxidative conditions, and more reactive in (slightly) reducing conditions. The expected formation of caesium borates (computer simulation) by reaction of Cs-species with either boric acid or metaborate or even boron oxide forms present in the gas phase could be unambiguously confirmed by TOF SIMS examination of deposits collected in the CHIP line (B-MoCsIOH test; Grégoire, 2021). As a consequence, the CHIP experiment with the B-MoCsIOH system featured significant gaseous iodine transport, even in slightly reducing conditions, consistently with the Phébus FPT3 test observations for which high gaseous fractions were observed.

Among the three component of the SIC control rod, indium is the less reactive on the MoCSIOH system - so that Mo still acts as a Cs-sink inducing important iodine gaseous transport. In the presence of Cd or Ag, iodine gaseous transport is strongly reduced, even though the formation of CdI_2 or AgI does not appear as a major reaction pathway to explain this observation. Based on the experimental data collected, it is assumed that both the competitive formation of metallic polymolybdates (Cd, Ag) versus caesium polymolybdates and the reducing role of the injected metallic species (Cd, Ag) contribute to reduce significantly the Cs-scavenging role of Mo and thus allow CsI formation preferentially to CdI_2 and AgI.

The addition of silver **and** cadmium to the MoCsI system results in the release of iodine almost only as particulate species. In the high temperature range, formation/deposition of the cadmium and silver molybdates species are formed preferentially to caesium molybdates, thus Cs may remain available for reaction with iodine in the gas phase. Iodine is probably transported as metallic iodide, identified as mainly a mix of CsI and/or CdI_2, with a low amount of AgI. In our test conditions, the addition of boron has no/weak influence on the direct transport of gaseous iodine in presence of Cd and Ag, even if the formation of metallic borates (caesium and silver) could be clearly evidenced by TOF SIMS technique.

One major issue of this programme was to better assess which conditions favour the transport of gaseous iodine species through the RCS and the reasons of this formation. For ST applications, it appears that the gaseous iodine fraction is strongly linked to gas atmosphere (oxidising versus reducing) as well as element ratio, noticeably the Mo/Cs ratio released from the fuel and also the amount and nature of control rod elements present inside the RCS. Some points remain to be investigated. The role of Boron when injected with SIC material should to be further considered in both pure steam conditions or slightly reducing conditions (H_2/H_2O ~0.1) to get firm conclusions. Identification of transported metallic iodide (CsI or CdI_2) remains also an issue to be addressed in order to better assess the Cd role (Mo-scavenging effect or direct reactivity with Iodine). Further, it is difficult to assess from an experimental point of view if species formation occurs only in the gas phase or if gas/condensed or condensed/condensed phase reactions play also a role, notably for metallic molybdates or metallic borates: analytical tests in condensed phase coupled to theoretical chemistry simulations may help unravelling this issue.

Efforts are now ongoing to improve the ASTEC/SOPHAEROS modelling: improvement/completion of thermodynamic database linked to species experimentally evidenced (metallic molybdates, metallic borates), implementation of non-congruent condensation which is not presently modelled. The final aim is to reproduce as much as possible all the trends experimentally observed in terms of iodine chemical reactivity and also FPs deposits to next extrapolate to reactor case simulations wit ha high degree of confidence .

4 REVAPORIZATION FROM RCS SURFACES: LATE PHASE RELEASES

During the late phase of a severe accident, revaporisation of volatile FPs (Cs, I, Te) and less volatile FPs (Ru) deposited on the surface of the RCS can contribute to significant delayed releases into the environment as observed in the aftermath of the Fukushima Daichii accident for iodine, caesium (Terada *et al.*, 2012; Katata *et al.*, 2015) and even tellurium (Doi *et al.*, 2013; Dickson *et al.*, 2019 and references herein).
During the Phébus FP tests (Haste *et al.*, 2013), it has been shown that deposition on the surface of the RCS is significant : up to ~29% of the caesium initial inventory is found deposited in the hottest zone of the Phébus experimental circuit (> 700°C) and up to 10% in the steam generator (SG) pin hot leg (700-100°C). Iodine deposited less in the hot section of the circuit (~ 5% at most) and slightly more on the SG pin (up to 17%). As Cs, tellurium was also found strongly deposited in the hot leg of the experimental circuit (up to 50% of its initial bundle inventory) and up to 12% in the SG pin inlet. Except for the case of very oxidative conditions during a SA scenario (such as air ingress), ruthenium release will be limited and represents 1-5% of its initial inventory (Grégoire and Haste, 2013); nevertheless, Ru deposition in the hot zone of the RCS is expected to be significant as deposition/transport ratio is in between 40-90%during the Phébus FP tests (Haste *et al.*, 2013).

The main deposition processes being either direct vapours condensation or deposition of airborne particles led by thermophoresis in the strong thermal gradient zone (SG pin inlet) as predicted by Hidaka *et al.* (1995) and Maruyama *et al.* (1999) or even gravitational deposition. Though no direct identification of deposited species could be performed during the Phébus tests, deposits involving iodine are expected to be metallic iodide: CsI mainly, but other forms were detected (Girault *et al.*, 2013). CHIP experiments showed that the formation of CdI_2 and AgI (to a lesser extent) may be formed (Grégoire *et al.*, 2021). Whereas caesium may also deposit as CsOH or mixed with metallic molyddates as was observed in the CHIP experiments. For tellurium, caesium telluride (Kissane and Drosik, 2006) are expected whereas ruthenium is supposed to be deposited as RuO_2. Based on the deposited fractions observed in the Phébus tests, deposits representing up to several $mg.cm^{-2}$ can be expected in the strong deposition zones of a PWR RCS.
These deposits may act as a source for medium term releases if thermal and/or chemical changes occur in the RCS. Indeed, significant remobilisation of Cs deposits from the hot leg of the Phébus experimental circuit was evidenced at the end of the degradation phase representing about 15-75% of the deposited Cs mass (Haste *et al.*, 2013).

Those phenomena are not accounted for yet by the SA simulation tools and it is difficult to predict their extent/impact, mostly because of the lack of experimental/theoretical data. Indeed, at the beginning of the FD accident the ASTEC severe accident simulation software predicts similar Cs and I release as the inverse source term evaluations from Katata et al (2015) and Terrada et al (2012). Nevertheless, after 6 days both Cs and I ASTEC calculated releases, in the standard version, are strongly underestimated (~2 decades) compared to the inverse ST evaluations.

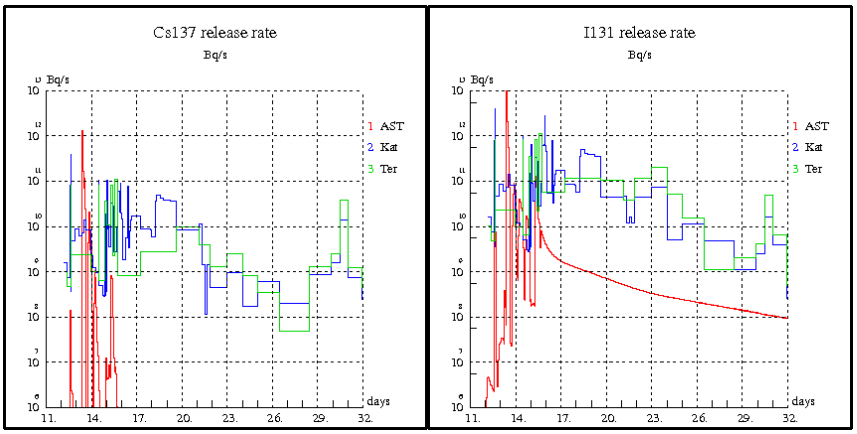

Figure 4.1: ^{137}Cs and ^{131}I release rate-comparison between ASTEC source term and environment source term (Cousin *et al.*, 2019) – AST : Astec simulation, Kat: inverse source term from Katata *et al.*, 2015, Ter: inverse source term from Terada at al., 2012.

Qualifying the potential medium term releases of volatile FPs due to remobilisation or revaporisation is an important issue, as it may result in delayed releases and have direct consequences on onsite emergency plan. Late phase releases of volatile iodine species is indeed of main concern as is can occur in strongly degraded configuration of the power plant – in which the mitigation means may be out of operation so that direct release to the environment cannot be excluded.
One part of the MIRE (MItigation of outside RElease) project conducted by IRSN (2013-2019) was aimed at this end combining experimental analytical studies and theoretical studies on metallic iodide and ruthenium oxide. Experimental work on revaporization metallic iodine was conducted in the framework of a Ph-D (Obada, 2017) under the supervision of J. F. Paul, A.-S. Mamede (UCCS of University of Lille) and myself.
In the following sections, I present the main features concerned with metallic iodine revaporization behaviour and the main outcomes of the experimental study carried out at IRSN up to now.

4.1 Caesium and Iodine revaporization - State of the Art

In the past, several attempts have been made to understand the phenomenon of FPs remobilization. As a follow-up of the Phebus-FP tests, a series of research programs had been launched by different institutions (AEA-T, VTT, JAEA) (Grégoire *et al.*, 2021b). Both interaction of fission products deposits with stainless steel surfaces representative of a RCS and revaporisation were considered. Most of these studies focused on CsOH and less frequently on CsI. The influence of other FPs (Mo) and CR material (Cd, Ag, B) on CsI thermal stability was also considered as well as the vaporisation of other metallic iodine (AgI).

4.1.1 Stainless steel oxidation in SA conditions

RCS piping are most frequently composed Fe- base stainless steel alloys (304L and 316L for instance in the French PWR characterised by high Cr and Ni contents and low Mn and Si contents) and steam generators of Ni- base SS (Inconel 600 or 900 grade) (Allen *et al.*, 2010). In severe accident conditions, the surface of the RCS evolves when exposed for several hours up to several days to a high temperature (500-1000°C) environment and mild oxidative to severe oxidative atmospheres (mix of steam/hydrogen or air as in air-ingress scenario). As a results, a thick oxide layer is formed (up to several tens of µm, Elrick *et al.*, 1984) compared to the oxide film formed in normal operation conditions (at most a few hundred nanometres, Stellwag *et al.*, 1998). For 304(L) and 316(L) SS grades, the oxide layer mostly presents a duplex structure which composition depends mainly on the SA oxidation conditions. In steam conditions, the outer thinner layer is mostly Fe –rich in which Fe_2O_3, or Fe_3O_4 structures could be identified (Elrick *et al.*, 1984; Allen *et al.*, 1987). In the case of air, Cr-Mn rich outer layer is observed but with still a low amount of Fe oxide (Botella *et al.*, 1998). The inner thicker layer is chromium rich with complex structures of Cr_2O_3 or mixed Fe-Cr spinels or even in a mix with Mn for all oxidation conditions. At the metal-oxide interface, a silicon-rich layer is sometimes observed beneath the chromium-manganese oxide (steam/hydrogen oxidation conditions) as reported by Elrick *et al.* (1984) and Allen *et al.* (1987). Si is not observed in the outer oxide layer. The oxide formed at the surface of Ni base SS steel is in general thinner and sometimes feature only one Cr_2O_3 rich- layer (Elrick *et al.*, 1984).

4.1.2 CsOH and CsI deposition and interaction with oxidised stainless steel surfaces

Studying revaporization of FPs from the RCS surfaces implies to take account of the deposition processes and FP-surface interactions. Given the strong temperature gradient occurring in the RCS during a SA phase, deposition processes evolve from vapour deposition (adsorption) to vapour condensation and then deposition or airborne particles led by thermophoresis, gravitational settling and impaction (Hidaka *et al.*, 1995; Maruyama *et al.*, 1999). Caesium hydroxide and caesium iodide deposition and interaction with stainless steel surfaces were thus considered both above and below vapour saturation temperatures, mostly in steam atmosphere.

In the hottest zone of the RCS (> 600°C) CsOH reacts significantly with SS surface and diffuse into the oxide layer inducing the formation of Cs-Fe mixed oxide; Cs-Fe-Si and Cs-Si oxides (depending on the presence or not of Si in the oxide layers) are observed at higher temperatures together with Cs diffusion in the oxide layer (Elrick, *et al.*, 1984; Sallach *et al.*, 1986; Allen et al, 1987; Di Lemma *et al.*, 2016). The formation of Cs-Cr oxide is only observed in presence of air (Sasaki et al, 2013). The formation of caesium molybdates on 316 or 316L SS grades is observed but remains limited compared to the formation of Cs-Fe and Cs-Si oxides (Di lemma *et al.*, 2017). Owed to its

reactivity, significant Cs deposition is expected in the high temperature zone of the RCS as was observed in the hot leg of the Phébus experimental circuit during the Phébus FP test series (Haste *et al.*, 2013). Below vapour saturation temperature (342°C for CsOH at atmospheric pressure) deposit of CsOH are still important (Le Marois and Megnin, 1994) but deposited species do not interact with surfaces.

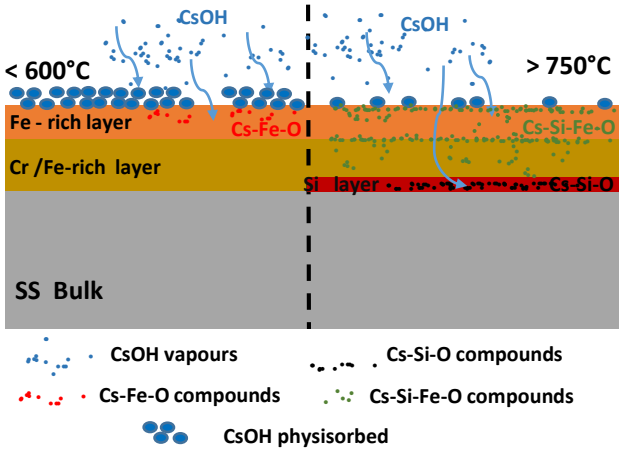

Figure 4.2: Schematic summary of CsOH interaction with SS surface at high temperature in mild oxidative conditions.

On the contrary, owed to a stronger stability, CsI vapour interacts less with SS at high temperature (Hidaka et al, 1995; Hashimoto et al, 1996). As a consequence, CsI deposition is expected to be low in the hot zone of the RCS. CsI vapours are transported in colder zone (below 650°C) where they condense on the RCS surfaces or nucleate in the carrier gas, in presence of already existing particles, to produce aerosols. A part of the CsI aerosols are deposited in the RCS led by thermophoresis or by impaction. The expected CsI deposition pattern in the RCS (low at high temperature, significant in the condensation zone, e.g. in the SG zone) is consistent with iodine deposition observed in the Phébus experimental circuit (Haste *et al.*, 2013). Following deposition as condensate or aerosols in the colder zone of the RCS, no interaction with the SS surface was evidenced.

4.1.3 Cesium and iodine revaporization behaviour

Experimental works concerned exclusively separate effect tests at a laboratory scale, mainly performed with fission products simulants (stable isotopes). Precursor were either synthetic deposits obtained after high temperature deposition of CsOH or CsI (Anderson *et al.*, 2000) either commercial powders (Auvinen *et al.*, 2000; Kalilainen *et al.*,2014; Gouello *et al.*, 2016 Gouello *et al.*, 2018; Shibazaki *et al.*,2001; Berdonosov and Sitova,. 1997; Berdonosov and Baronov 1999;. Kulyukhin *et al.*, 2004). Bottomley (2014) and Knebel (2014) considered deposits issued from the Phébus-FP tests, which are as realistic as possible however for such studies only Cs behaviour could be monitored. Kinetic studies were performed in Knudsen cell coupled to a mass spectrometer (Anderson *et al.*, 2000) or in open flow reactor with radioactive tracers (^{134}Cs or ^{137}Cs), coupled to on-line γ-spectrometry (Auvinen, 2000; Bottomley, 2014; Knebel; 2014). The revaporised species (transported aerosols and gaseous species, iodine compounds) were also characterised (Kalilainen, 2014; Gouello 2018; Shibazaki *et al.*, 2001; Berdonosov and Sitova,. 1997; Berdosonov and Baronov 1999; Kulyukhin *et al.*, 2004). A large revaporisation temperature range was explored (400 up to 1300°C depending on the studies) either in isothermal conditions or with slow heating rates or even with flash vaporization up to very temperatures (Kulyukhin *et al.*, 2004). Reducing (steam/hydrogen), to mild oxidative (steam) and more oxidative atmosphere (air; oxygen) were investigated. The main outcomes can be summarized as follows.

As for CsOH, two processes were experimentally observed when reheating surfaces that have been previously exposed their vapours (Andersen *et al.*, 2000; Auvinen *et al.*, 2001). A first revaporization process starting at 500°C in steam condition and similar to vaporization of pure CsOH, is attributed to the vaporization of physisorbed CsOH. Revaporization of such species seems to be mass transfer limited between 600°C and 800°C. For higher temperatures, a second process occurs, the revaporization is much slower and mostly monitored by the chemisorbed species which are less volatile (Cs-Si-O of Cs-Fe-Si-O phases). Steam in the carrier gas seems to accelerate revaporization compared to hydrogen. Air (oxygen) tends to lower the temperature onset of Cs revaporization down to 300°C (Bottomley, 2014). Influence of O_2 remains to be further investigated. Remarkably,

Cs deposited on the Phébus samples behaved as the synthetic deposits – independently of the presence of the other elements in the deposited layer (Anderson *et al.*, 2000). Revaporized species were not fully characterized and are expected to be either CsOH or Cs-surface compounds. Transport is quite efficient as up to 80% of revaporized species are released as aerosols.

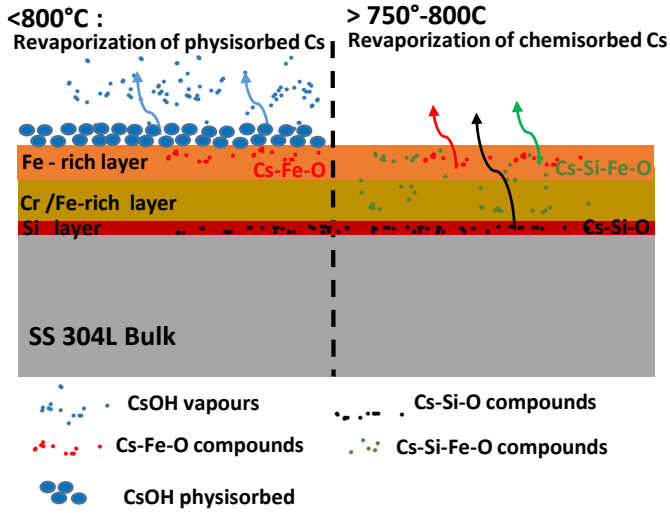

Figure 4.3: Summary of CsOH revaporization behaviour from SS surface in conditions of a RCS in long term phase (steam or air).

As for CsI, less reactive with SS surface, revaporization in steam is reported to start close to 500°C and stop around 750°C (Andersen *et al.*, 2000; Auvinen *et al.*, 2000; Shibazaki *et al.*, 2001). CsI is the main expected released species in steam conditions, e.g. in atmosphere featuring low O_2 potential (Shibazaki, 2001). On the contrary, Kalilainen (2014) and Gouello (2018) found that following the vaporisation of CsI at 650°C (dwell experiments), 10% - 27% of transported iodine is in gaseous form in an argon/steam atmosphere. Iodine gaseous fraction is much more higher following vaporization at 400°C but the overall transported mass is about 100 times lower than at 650°C. Gaseous iodine fraction decreases with the introduction of hydrogen in the carrier gas (~5%). By heating CsI at higher temperature (flash heating up to 1250-1300°C) in more oxidative atmosphere (oxygen), the formation of gaseous molecular iodine has been observed (Berdonosov and Sitova, 1997, Berdonosov and Baronov 1999; Kulyukhin *et al.*, 2004). When mixed with an excess CsOH powder relative to CsI powder (Gouello *et al.*, 2018), iodine is only transported in aerosol form whatever the nature of the atmosphere.

4.1.4 FPs and CR elements influence on CsI revaporisation

The influence of other FPs and CR materials on the vaporisation of CsI and the nature of released iodine was also investigated: Mo (Grégoire *et al.*, 2015; Gouello al., 2020), Cd and Ag (Gouello *et al.*, 2018) and finally boron (Kalilainen, 2014; Gouello, 2018; Sato *et al.*, 2015, Okane *et al.*, 2016; Shibazaki *et al.*, 2001).

Heated mixture of CsI and Mo powders (as Mo metal or molybdenum oxide) featured a strong transport of gaseous iodine (up to 80-100% of overall transported iodine and identified as mainly as I_2), in both steam and steam/air conditions (Kalilainen, 2014; Grégoire *et al.*, 2015; Gouello *et al.*, 2020). CsI and α-MoO_3 dominate the composition of the residue with traces of Cs molybdates in some cases (Gouello *et al.*, 2020). In more reducing conditions (mixture of steam and hydrogen), the release of gaseous iodine is strongly reduced (consistently with observation performed in the CHIP experiments (Grégoire *et al.*, 2015). Simulations at thermodynamic equilibrium with FactSage 5.5 software and FACT5.3 database (Gouello *et al.*, 2020) reproduce well the experimental observations.

The addition of cadmium in excess to CsI powder resulted in contrasted gaseous iodine releases when heated at 650°C (Gouello *et al.*, 2018). In steam condition, the presence of Cd seems to have no strong effect on gaseous iodine transport though the experimental data are difficult to interpret. On the contrary, in more reducing conditions (steam/hydrogen atmosphere), a significant increase of transported gaseous iodine fraction is observed compared to vaporisation of pure CsI in the same conditions: 13% of transported iodine is in gaseous form in presence of Cd compared to less than 1% with pure CsI. The formation of metallic cadmium iodide could

not be evidenced. Compared to the behaviour of heated CsI powder, the addition of metallic silver on caesium iodine precursor did not have a significant influence on the fraction of transported gaseous iodine (Gouello, 2020).

Under severe accident conditions, boron can be extensively released to the reactor coolant system (RCS) by vaporization of the primary circuit water or following the degradation of B_4C control rods at high temperature (Elrick *et al.,* 1987; Haste *et al.*, 2012; Miwa *et al.*, 2020a). Boron potentially present in large excess with respect to Cs may affect the transport and/or deposition of radiological important fission products such as iodine and caesium. Modelling of the high temperature thermokinetic behaviour of the B-O-H-C system (Yetter *et al.*, 1991; Miwa *et al.*, 2016, Miwa *et al.*, 2020b) allow to identify boron oxide (B_2O_3) and metaboric acid (HBO_2) as the main gas phase species present at high temperature (1000-1600°C) in presence of steam (oxygen-hydrogen rich environment). Below 1000°C, main species in the gas phase are expected to be HBO_2 and H_3BO_3 (Miwa, 2020a). Very low boron deposits are expected in the high temperature zone of the RCS, boron oxide starting to condense below 800°C. At lower temperatures (< 300°C), boric acid species condenses rapidly inducing the formation of strong deposits (and even plugs – Elrick *et al.*, 1987).

From the early 80's up to now, numerous experimental studies were focused on the possible interactions between boric acid, boron oxide or boron carbide degradation products and the most probable released caesium compounds (CsI and CsOH) in a wide range of temperatures (300-1000°C). Depending on the experimental conditions, vapour phase reactivity (Bowsher *et al.*, 1985; Bowsher *et al.*, 1986, Elrick *et al.*, 1987, Gouello 2012, Grégoire 2021) or vapour (boron)/condensed phase (CsI) reactivity (Sato *et al.*, 2015; Okane, 2016; Shibazaki, 2001; Gouello *et al.*, 2021; Rizaal et al., 2021) or even only condensed phase reactivity (Kalinainen, 2014; Gouello *et al.*, 2016; Gouello *et al.*, 2018a) were investigated. The general trend which can be inferred from this series of experiments is the dissociation of CsI compounds both in gaseous and condensed phase in presence of boron oxide species inducing a release of volatile gaseous iodine species even in presence of an excess of caesium (Gouello *et al.*, 2018). Released gaseous iodine species are expected to be I_2. The dissociation of CsI is assumed to be owed to the formation of caesium boron mixed compounds such as $CsBO_2$. Nevertheless, as pointed out by Gouello (2012), the nature of the caesium borate compounds could not be fully determined. CsI dissociation was not quantified.

Besides experimental studies, thermodynamic and thermokinetic modelling of boron reactivity in the B-Cs-I-O-H chemical system in SA conditions was undertaken. Thermochemical properties of caesium borates at high temperature were re-assessed by theoretical investigations (Vandeputte's phD, 2015 ; Vandeputte *et al.*, 2019). In the gas phase at high temperature, it was shown that in presence of steam, gaseous $CsBO_2$ is stable over a large temperature range (725 1725°C) and even below 725°C where it condenses (Vandeputte *et al.*, 2019; Miwa *et al.*, 2016). No significant kinetic limitations were evidenced (Miyahara *et al.*, 2019). CsI decomposition in gas phase by boron compounds is thermodynamically favoured only at high temperature: with HBO_2 above 1450°C, with H_3BO_3 above 1000°C, with BO_2 above 750°C (Vandeputte *et al.*, 2019). At lower temperatures, boron species reactivity with condensed CsI was less investigated. Calculations at thermodynamic equilibrium (Sato *et al.* 2015; Gouello *et al.* ,2018a) indicated that CsI reaction with gaseous boron oxide is favorable from a thermodynamic point of view only in presence of oxygen and for temperatures above 425°C resulting in the formation of $CsBO_2$ and molecular iodine:

$$2\ CsI_{(C)} + B_2O_{3(G)} + 1/2\ O_2 \leftrightarrows 2\ CsBO_{2(G)} + I_{2(G)} \quad \text{Equation 4-1}$$

In presence of steam, CsI decomposition is not predicted (Gouello *et al.*, 2018a) contrarily to experimental observations featuring the release of gaseous iodine. This point remains to be explained. The role of oxygen potential[9] was underlined by both studies. No thermokinetic calculations were performed at low temperature.

4.1.5 Other metallic iodide

Only one reference focused on metallic iodide thermal stability in the nuclear context (Gouello *et al.*, 2018b). The decomposition of AgI powder was investigated at 400°C and 650°C in steam and steam/ hydrogen flow. The main result is that gaseous iodine is transported during the thermal treatment, and that reducing (steam/

[9] the oygen potential corresponds to ΔG_{O2} value with $\Delta G_{O2} = \mu_{O2} - \mu^\circ_{O2} = RT \ln(f_{O2}/p^\circ)$, where p° is the standard state pressure (1 bar) and f_{O2} is the oxygen fugacity

hydrogen atmosphere) conditions seems to be more favorable than steam conditions. Nevertheless, the very low solubility of silver iodide may have led to an underestimation of the quantity of iodine transported as AgI aerosols . As a consequence, the fractional release of gaseous iodine species may have been overestimated.

4.1.6 Conclusion and objectives of metallic iodide revaporization study in the MiRE programme

Past experiments have evidenced the possible revaporization of caesium and iodine deposits and the release of gaseous iodinated species in some conditions but are still too much uncomplete to develop models. However, some key parameters were not fully taken into account. For instance, the nature of the deposited species (aerosol deposition or vapour condensation) and their possible interaction with the substrate surface was not clearly stated in most studies. Besides, the vaporization experiments seldom considered oxidative atmosphere. Indeed air is likely to penetrate in the RCS in case of an air-ingress accidental scenario (Powers, 2000) and be a major contributor to the release of gaseous iodine.

In the framework of the MiRE program ("Mitigation des Rejets à l'Environnement en cas d'accident nucléaire") founded by the French National Research Agency (ANR), the study of metallic iodide deposits (CsI, CsI+Cs_2MoO_4 and AgI) vaporization from pre-oxidized stainless steel surface was undertaken (Obada, 2017; Obada *et al.*, 2017; Obada *et al.*, 2018; Obada *et al.*, 2020). The work was aimed at fill in the gap in knowledge on metallic iodide re-vaporization in conditions as representative as possible of a late phase of a SA scenario, in terms of: i/ substrate nature (pre-oxidised 304L and 316 L stainless steels surfaces) ii/ deposit generation reproducing the different temperature deposition processes from high temperature deposition, down to aerosol impaction iii/ re-vaporization thermal condition, iv/ atmosphere composition.

In this view, an experimental multi step approach was developed including substrate preparation, CsI deposition and finally thermal treatment. We aimed at a better assessing gaseous iodine release with the identification of re-vaporized species and their kinetics – depending on the test conditions. Interaction between deposits and substrate surface during thermal treatment was investigated too.

In order to interpret the experimental results, a first approach consisted in simulation at thermodynamic equilibrium with Gemini software and Coach 5.2 data base (Obada, 2017). This approach was completed by Density Functional Theory (DFT) calculations in the framework of the IRSN-UCCS collaboration (Obada et al, 2020) in order to improve the understanding of the reaction mechanism especially at the deposits/gas phase interface.

4.2 Experimental facilities and instrumental development

Protocols for oxidation of the substrate coupons as well as the different devices operated for the deposits generation were extensively described in Obada et al. (2017). The release rate of revaporisation was in a first step monitored by thermogravimetric analysis (TGA). The nature of released iodine vapours (I_2 or other) and the subsequent release kinetic during thermal treatment was then determined in an open flow reactor (RIGolo device). This section is focussed on the RIGolo facility and gaseous iodine monitoring developed specifically for this study.

4.2.1 Revaporisation facility: the RIGolo device

The re-vaporisation of CsI deposits from pre-oxidized stainless steel surfaces was firstly carried out in a thermogravimetric analysis device (TGA, Setsys EVO instrument) as described by Obada *et al.* (2017). The thermal treatment consisted in a heating of the samples up to 750°C (except for a few tests, where samples were heated up to 970°C) at a rate of 5°C/min and hold for 1 hour, before cooling down by natural convection. The heating ramp rate is a compromise between chemical equilibrium conditions and test duration. During the thermal cycle, the sample is swept by a low carrier gas flow (30-70 mLn/min) either composed of synthetic air or air/argon/steam mixtures. Air/steam mixtures were injected at temperature above 150°C and switched off during the cooling phase (below 400°C). The main outcome of the TGA tests is the onset temperature of the mass loss linked to the start of the re-vaporization process. The overall mass change (loss) cannot be considered as a measure of CsI re-vaporization as the oxidation of the substrate during the thermal treatment may counterbalance the mass loss linked to re-vaporization.

To complement the results obtained by TGA, the RIGolo (**R**e-vaporisation of **I**odine in **G**aseous form and "picc**olo**"="small" in Italian) experimental device has been developed with a double purpose:

- Establish the nature and quantity of released iodine-containing species;
- Determine the release kinetics for gaseous molecular iodine.

It is an open flow reactor (Figure 4.4) composed of a tubular furnace composed of a central high temperature heating element (950°C maximum heating temperature) and upstream and downstream insulated sections in which an alumina tube (20 mm inner diameter) is inserted. The sample is placed at the center of the heated section and the carrier gas is fed up at the inlet of the test line. The upstream insulated section can be replaced by additional heating elements (not represented here) so as to overheat the carrier gas in order to reproduce representative situations in a late phase of a SA scenario when the mix of steam/air passes though hot zone of the reactor vessel or the RCS before passing though the colder zone where deposited material may revaporise. The vaporized vapour and/or generated aerosols from the heated sample are transported by the carrier gas to the line outlet. Based on the type of information searched in the experiment, the downstream part of the RIGolo device has two configurations: "integral measurement" for determining the nature and quantity of released iodine-containing species and "online measurement" for establishing the gaseous I_2 release kinetics.

The "integral measurement" configuration is described by Obada *et al.* (2017) and consists in connecting the alumina tube outlet to a series of selective liquid scrubbers, containing a mix of toluene/acidic water. It has been shown that in these conditions molecular iodine will be selectively trapped in the organic phase, while inorganic iodine compounds (CsI, HI…) will be trapped in the aqueous phase (see section 3.2.2). Nevertheless, the detection limit of I_2 in toluene by UV-Visible spectroscopy is between 2 10^{-8} and 6 10^{-7} mol/L, it is thus necessary to accumulate I_2 over a long period of time (2 h) preventing any kinetic study.

The "online measurement" configuration consists in analyzing the outlet flow by on-line spectrophotometry able to monitor molecular gaseous iodine release kinetics. A specific instrument was developed in the laboratory (Johansson *et al.*, 2014; Bahrini *et al.*, 2018) in order to fulfill the experimental constraint imposed by the revaporisation experiments: low iodine concentration and possibly transport of a low aerosol flow; carrier gas composed of important water vapour fractions. The required time resolution of spectral acquisition was set at 1-2 min at most to be sure to match every revaporisation events. The retained technique is based on Incoherent Broadband Cavity Enhanced Absorption Spectroscopy (IBB-CEAS) and presented in section 4.2.2.

The thermal treatment in the RIGolo device is similar to the one applied in the TGA device: heating up to 750°C (rate 5°C/min) and hold for 1 hour, before cooling by natural convection. The carrier gas during the tests was either air (53 mL_n/min) or a mixture of air/steam (200 mL_n/min) of variable composition. The gas flow rates have been adjusted to the new alumina tube inner diameter, in order to have the same gas velocity above the sample as in the TGA tests.

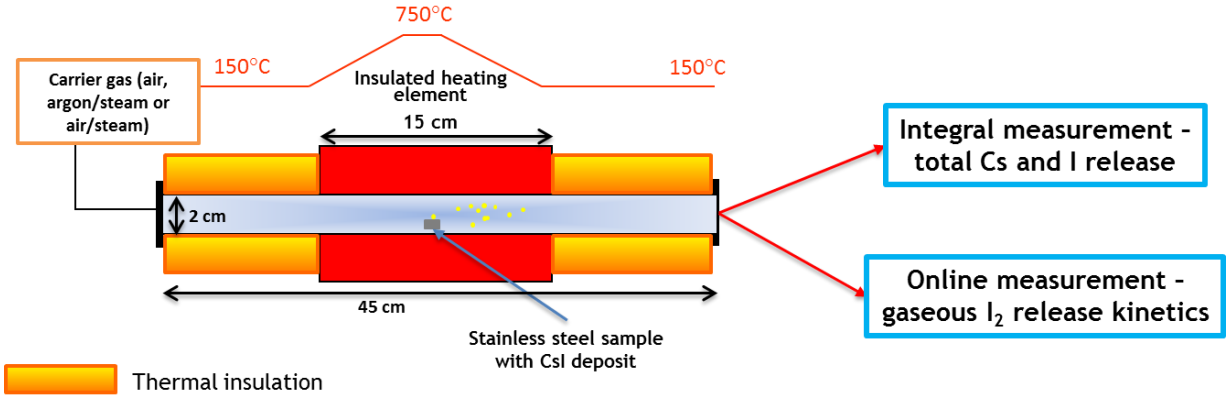

Figure 4.4. General design of the RIGolo experimental device.

4.2.2 Iodine on line monitoring

Within the framework of studies dedicated to follow the fate of iodine compounds in the troposphere, several techniques were developed to monitor iodine at trace level: Long path Differential Optical absorption spectroscopy- LP DOAS (Saiz-Lopez *et al.*, 2006), Laser Induced Fluorescence (Lin *et al.*, 1996; Kireev *et al.*, 2017), denuder sampling coupled to ICP MS (Leigh *et al.*,2010; Chance *et al.*, 2010), chemical ionization mass spectrometry (Lawler *et al.*, 2014), broad band cavity ring down spectroscopy (Bitter *et al.*, 2005; Sakamoto *et al.*, 2009) and Incoherent broad band cavity enhanced absorption spectroscopy - IBB CEAS (Vaughan *et al.*, 2008). All these techniques feature high sensitivity for iodine gaseous compounds ranging from 5 pptv for LP DOAS up to 20-30 pptv for IBB CEAS with accumulation times ranging from 30 min for LP DOAS down to 1 minute for the IBB CEAS instrument (depending on sampling conditions and presence of other species). Taking into account sensitivity, acquisition frequency, compatibility with laboratory scale experiments (e.g. compactness of the instrument) and simplicity of instrumental design, IBB CEAS technique appears as a suitable technique for our applications.

IBB CEAS instrument is in his principle close to standard absorption spectroscopy with the advantage of a high finesse cavity allowing strongly increased sensitivity compared to single path or even long path length gas cells. Molecular iodine in the gas phase presents a highly structured absorption spectra in the 500-570 nm range owed to B3 ← X electronic transition which was fully described by Saiz-Lopez *et al.* (2004). Taking advantage of this structured spectra, it is possible by recording broad band absorption to separate contributions from other species (absorbing species as water vapor or scattering species as aerosols featuring in the latter case an unstructured background evolution) and thus perform quantitative absorption measurements of I_2 even in a perturbed environment as the transported flow at the outlet of the RIGolo device.

4.2.2.1 IBB CEAS principle

IBB CEAS technique is based on the measurements of lights transmitted through a high finesse cavity, e.g. featuring high reflectivity mirrors. With reflectivity coefficient close to one, the optical extinction coefficient $\boldsymbol{\alpha}(\boldsymbol{\lambda})$ can be approximated by (Bahrini *et al.*, 2018; Johansson *et al.*, 2014):

$$\boldsymbol{\alpha} \approx \frac{\mathbf{1}-\boldsymbol{R}}{\boldsymbol{d}}\left(\frac{\boldsymbol{I_{in}}}{\boldsymbol{I}}-\mathbf{1}\right) \textbf{ with } \boldsymbol{\alpha}(\boldsymbol{\lambda}) = \boldsymbol{n}\boldsymbol{\sigma}(\boldsymbol{\lambda}) \qquad \text{Equation 4-2}$$

Where ***I*** : light intensity after transmission, $\boldsymbol{I_{in}}$: incident light intensity, $\boldsymbol{\lambda}$: wavelength (nm), $\boldsymbol{\alpha}$: optical extinction coefficient of the media (cm^{-1}), $\boldsymbol{\sigma}$: absorption cross section (cm^2.$molecule^{-1}$), ***d*** : effective path length (cm), R (λ) : mirror reflectivity; ***n*** : number of molecules per unit of volume (cm^3)

With R very close to 1, effective path length of several km can be obtained for optical cell of less than 1 meter. In theory, iodine absorbance can be thus directly determined knowing the mirror reflectivity R (λ, T), the effective path length (both parameters can be experimentally determined) and the iodine absorption cross section (from literature data).

The unstructured background effects including aerosol absorption was taken into account by differential optical absorption spectroscopy (DOAS) approach. The principle of DOAS is to separate the low frequency components of the absorption spectrum (here background variation, I_2 continuum absorption and aerosol particle scattering; Platt and Stutz, 2008) from the high frequency contribution of iodine absorption. For the instrument developed here, it was found that a polynomial interpolation of order 25 fits satisfactorily the slow varying part of the measured spectrum (Johansson *et al.*, 2014) and allows to isolate the high frequency contribution of the I_2 absorption (see) which intensity is directly proportional to iodine concentration in the optical cell.

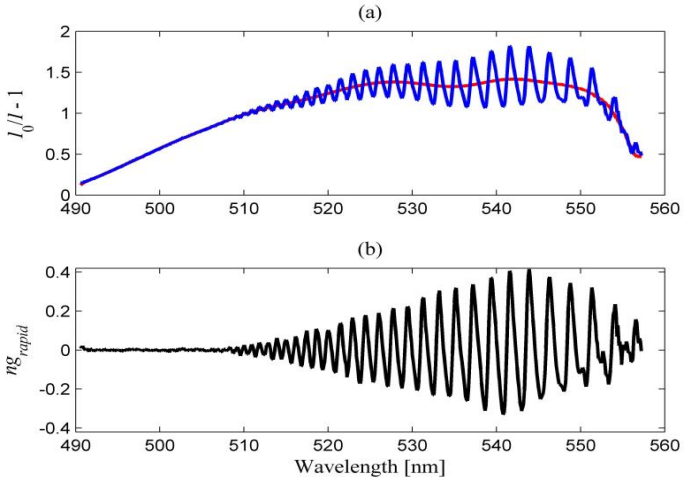

Figure 4.5 : IBB CEAS experimental spectra and data processing to separate low frequency part from the iodine high frequency contribution.
a) I0/I-1 spectra recorded without aerosols and with an I_2 concentration of 4.1 nmol/l (solid blue lines) , polynomial function of degree 25 fitted to the experimental spectra (solid red line); b) high frequency part of the spectrum after subtraction of the fitted polynomial (Johansson *et al.*, 2014).

4.2.2.2 IBB CEAS instrument developed at L2EC

The instrument operates in the 450-550 nm spectral range thank to a light emitting diode (LED). The LED is coupled to a 50 cm cavity ended on both sides with high reflectivity mirrors (silver coated, R > 99.99% at 532 nm) allowing an effective path length of 1-10 km. The mirrors are protected from iodine or aerosol deposition by a low argon flow injected directly at the upper part of each mirror. The cavity output is focused on a CCD spectrometer (Andor iDus). Careful power and temperature stabilization are applied to the LED and the CCD spectrometer is cooled at -72°C to ensure low noise background.

The overall scheme of the instrument is reported in Figure 4.6. The gas supply system is formed of several lines allowing either calibration of the instrument with a source of gaseous I_2 of known concentration or sampling on the RIGolo facility with the possibility of dilution in argon flow (by a factor up to 20 times). All lines converge to a 2 metres long mixing lines to ensure homogeneity of the gas flow. The gas to be analyzed is fed into the centre of the cavity and its flow is controlled by a critical orifice implemented at the cell outlet. The excess gas from the mixing line is evacuated trough a by-pass connected at the inlet of the cavity. The whole system is temperature and pressure controlled and heated up to 100°C to avoid iodine and water vapour condensation.

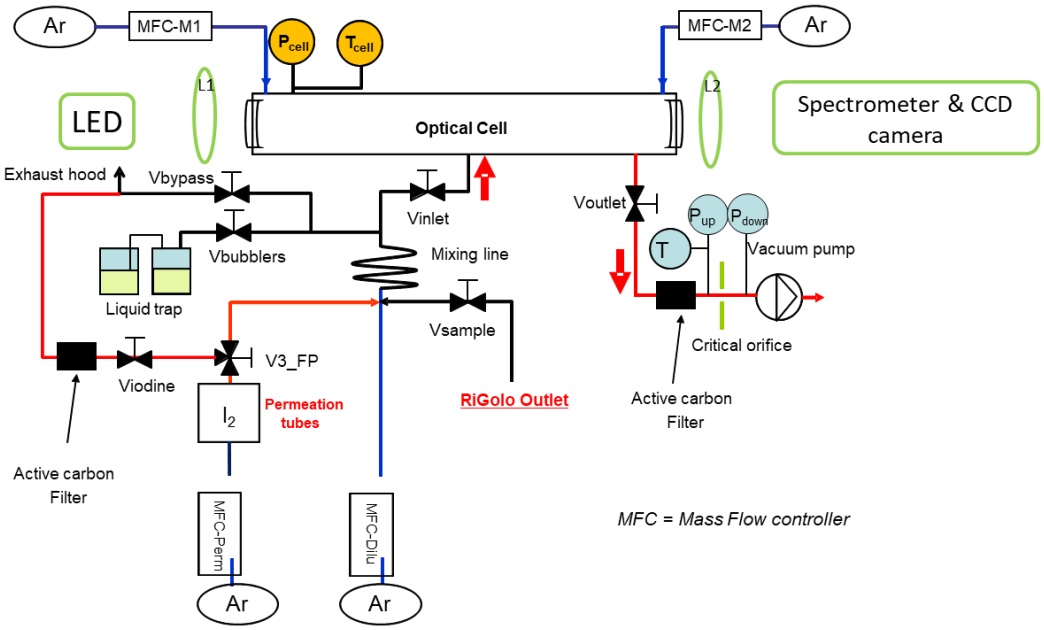

Figure 4.6 : IBB CEAS scheme and gas line supply.

After retrieving the low frequency contribution to the spectrum, it is theoretically possible to determine the iodine concentration in the gas flow entering the cell based on equation (3-1). Nevertheless, with argon protective flow on the mirror and gas inlet in the middle of the cavity, the absorption path length in the cell (d) will depend on the gas flow in the cell and will be lower than the effective length of the cell (~35-37 cm instead of 50 cm). Moreover, iodine cross section were not determined for the retained working temperature of the cell but only at 15°C (Saiz-Lopez *et al.* 2004). An alternative approach for iodine concentration determination is external calibration with a source of iodine of known concentration (I_2 generation by the mean of permeation tubes and flow rate characterization by trapping in alkaline gas scrubbers and subsequent ICP MS analyses). Therefore, iodine concentration in the sample is then displayed as the dimensionless N_{rel} value which is the ratio of I_2 sample concentration to the calibration source concentration. Absolute concentration determination in the samples requires then to be adjusted for the sampling, calibration and dilution flow rates. In our case, as the main objective is to determine the release kinetic, it was decided to stay with relative concentration.

The characteristic of the instrument was extensively investigated (Johansson *et al.*, 2014; Bahrini *et al.*, 2018) and showed up to be appropriate for the revaporisation experimental conditions. The instrument provides a detection limit of 5 10^{-2} nmol/l (1 ppbv) for an acquisition time of 10 s and allow measurements in a large dynamic concentration range thanks to strong dilution capacities. A remarkable stability was observed over several hours acquisition thank to a good power and temperature control of the LED emitting source. The presence of water vapor which presents very weak absorption lines in the recorded spectral region can be easily overcome by performing iodine calibration in presence known amount of water vapor. The presence of aerosols – in limited to concentrations (< 3-4 10^6 particles .cm^{-3}) does not influence significantly gaseous iodine monitoring (less than 10% deviation from measurements without aerosols). At higher aerosol concentration levels, the light extinction due to aerosol light scattering increases rapidly, inducing large underestimation of the iodine concentration determination. As already observed in the CHIP experiments, the implementation of filter in order to separate gaseous species from aerosols causes heterogeneous losses of gaseous iodine on the particles trapped on the filter media so that the gas/aerosol mixture must be entirely directed in the IBB CEAS instrument.

4.2.3 Post-test analysis

Similar to the the experimental studies performed in the CHIP and GAEC lines (see section 3), each section of the RIGolo facility were post-test leached in appropriate aqueous media, for deposits recovery. After suface characterization, the residue on the coupons was leached too. The solutions were analyzed by ICP-MS for elemental quantification. The organic phase of the liquid scrubbers has been also recovered and analyzed by UV-Visible spectroscopy for quantification of I_2 in toluene.

The coupon surface was characterized by combination of X-ray Photoelectron Spectroscopy (XPS) and Time-of-Flight Secondary Ion Mass Spectrometry (ToF-SIMS). XPS provides chemical composition of less than 10 nm depth scale of the surface while the ToF-SIMS was used in depth profiling mode to reach composition up to several micrometers in depth. The morphology of the surface before and after re-vaporisation was investigated by Scanning Electron Microscopy (SEM). The objective was to determine the nature of the residue and interaction with SS surface if any after thermal treatment.

4.3 Revaporisation of CsI

This study was aimed at assessing gaseous iodine release during re-vaporization of CsI deposits, through small-scale analytical tests in thermal ramp (Obada *et al.*, 2017; Obada *et al.*, 2018; Obada *et al.*, 2020). A summary of the main features will be presented here.

Stainless steels of different grades (304L or 316L) were used to represent the inner surface of the RCS. The coupons were pre-treated as recommended by Mamede *et al.*, 2016 (pre-oxidation of as received coupons at 750°C in steam conditions for several hours) so as to feature a surface state representative of the RCS in case of a SA. As reported by Obada *et al.* (2018, 2020), the surface oxide presents a duplex structure (1-15 µm thick) featuring an outer layer either Fe–rich accordingly to literature data or Mn-rich as already observed by Mamede *et al.* (2016). Inner oxide layer is Cr-rich in every cases. No Si-rich layer at oxide –bulk interface was observed.

In a first approach, CsI revaporization was studied with ramp heating, similarly to studies reported in the literature (Shibazaki, 2001; Auvinen *et al.*, 2000; Anderson *et al.*, 2000). The thermal cycle maximum temperature was set at 750°C. This final temperature is high enough to be able to catch each release event concerning CsI re-vaporization and remains within the expected temperature range which could prevail in the RCS during a late SA. A Ramp rate of 5 °C/min was applied as a compromise between chemical equilibrium conditions and test duration (2-3 hours). The study was focused on the main following parameters:

- The CsI deposition process, to be able to reproduce the different deposition zones in the RCS: room temperature aerosol impaction (simulating CsI deposition in the cold leg of the RCS), high temperature vapour deposition (above 620°C, simulating deposition in the hot leg of the RCS and SG inlet), vapour condensation (620-400°C, simulating SG deposition) and temperature aerosol deposition (around 400°C, SG deposition).
- The atmosphere composition featuring either air, air/steam mixtures and argon/steam. Pure air is not representative of SA scenario but may help in understanding the CsI re-vaporization behaviour and gaseous iodine production. Realistic atmospheres are mixture of air/steam with a low air content. Re-vaporization of CsI aerosols (RT aerosol impaction) on 304L coupons featured the largest atmosphere compositions (5 different compositions from pure air contents to argon/steam). Tests were performed in both TGA and RIGolo devices. Based on the results of this test series, the number of tested atmospheres has been reduced for the tests performed with the other CsI deposition processes (vapour deposition, vapour condensation and temperature aerosol deposition). The tests have been performed in the RIGolo device only.
- The Substrate nature with one test with an inert substrate to assess the contribution of deposit/surface interaction in terms of nature of re-vaporized species (especially for iodine). Tests conditions featured air atmosphere and a thermal cycle (5°C/min up to 750°C) similar to conditions 1.

Experimental results will be discussed in terms of nature and quantity of released iodine species and whenever the case, the release kinetics of gaseous molecular iodine. Interaction of deposit with the substrate surface and its consequence on the revaporization behaviour will be taken into account. Table summarize the main test conditions

Table 4.1: CsI re-vaporization - Experimental matrix for test performed with thermal cycle up to 750°C at 5°C/min (Obada *et al.*, 2017; Obada *et al.*, 2018; Obada *et al.*, 2020).

Substrate	Deposition process	Re-vaporization carrier gas (% vol)	Experiment type (repeat)		
			Integral[1]	Kinetic[2]	TGA[3]
Pre-oxidized 304L	Aerosols impaction at room temperature	Air (100%)	x	x	x
		Air/steam (50/50)	x	x	
		Air/steam (20/80)	X (2)	x	x
		Air/steam (3/97)	x	x	x
		Argon/steam (70/30)	x		x
Pre-oxidized 316L	High-temperature vapour deposition (720-620°C)	Air (100%)	x	x	
		Air/steam (20/80)	x		
		Argon/steam (70/30)	x		
	Vapour condensation (620-440°C)	Air (100%)	x (2)	x	
		Air/steam (20/80)	X	x	
		Argon/steam (70/30)	X		
	Aerosols deposits (< 400°C)	Air (100%)	X		
		Argon/steam (70/30)	x		
Gold (Au)	RT aerosol impaction	Air (100%)	x	x	x

[1] RIGolo with biphasic liquid scrubbers ; [2] RIGolo coupled to the IBB-CEAS; [3] Thermogravimetric analysis

4.3.1 CsI initial deposit characterization

Aerosols deposits at room temperature were obtained after impaction of CsI aerosols generated by nebulization of a concentrated CsI solution (wet route) and drying in a strong argon flow (Obada *et al.* 2018). Deposited CsI amount ranges from 0.8 to 4.2 mg/cm^2 from one experiment to another. SEM analyses revealed the presence of particles with irregular shapes and agglomerates with sizes from 5 to 20 µm (see Figure 4.7). After several weeks, the particles also appear to hydrate, given the hygroscopic nature of CsI (Riggs *et al.*, 2007).

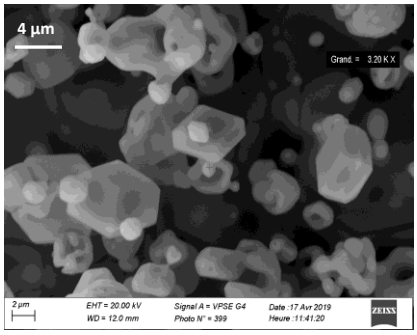

Figure 4.7: SEM image of CsI aerosols deposited by wet route at room temperature (magnification x 3200).

High temperature vapour deposits, vapour condensate and temperature aerosol deposits were obtained in using CsI powder vaporization (at 750°C). Generated vapours were then transported in a thermal gradient tube lined with an oxidised 316L foil. Depending on the temperature, several deposition zone were obtained corresponding to the three depositions processes mentioned above, showing different sizes and morphologies. For instance, in the 720-620°C temperature range, SEM analysis has revealed an amorphous deposit, homogeneously spread across the entire surface of the 316L foil (Figure 4.8 a) – corresponding to deposition of liquid droplets. The average amount of caesium and iodine per surface unit in this temperature range is about 2.9 mg/cm^2, as determined by ICP-MS analysis. Also, the Cs/I mass ratio of 0.94 is consistent with to the theoretical value (1.05) taking into account uncertainties measurement, which strongly suggests that caesium and iodine were deposited as CsI. In the 620-440°C temperature range, the deposit is composed of polyhedrons that range between 10 and 30 µm in size, as well as weaving-shuttle like particles with lateral dendrites that reach several hundred microns in size (Figure 4.8 b). The deposit in this temperature range is the most important in terms of quantity, up to 8.3 mg/cm^2, and the Cs/I mass ratio (0.96) suggests that the chemical species is CsI. Below 440°C, the deposit consists of spherical particles that reach up to 4 µm in diameter (Figure 4.8 c). The amount of deposit decreases

progressively from 4.3 mg/cm^2 at 440°C to 0.7 mg/cm^2 at 150°C. Given the Cs/I mass ratio (0.89-0.99), it is highly likely that the deposit is composed of CsI.

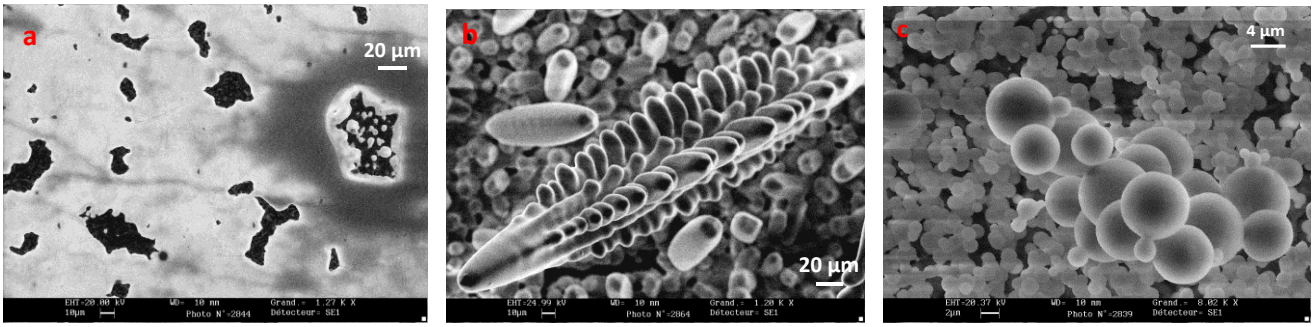

Figure 4.8: SEM image of CsI deposit on pre-oxidized 316L foil.
(a) high-temperature vapour deposition (720-620°C), (b) vapour condensation (620-440 °C) and (c) aerosol deposition at ~200 °C. (a) and (b) obtained at X1200 Magnification (Obada *et al.*, 2020), (c) at x 8000 (Obada, 2017).

Interaction with substrate was not investigated as CsI is the main expected deposited species whatever the temperature range (based on ICP MS data). Those results are consistent with previous studies showing no significant CsI decomposition nor interaction with the hot steel surfaces (Hashimoto *et al.*, 1996, Shibazaki *et al.*, 2001; Hidaka *et al.*, 1995, Le marois and Megnin, 1993) and were confirmed with the first TeRRa experiment with CsI injection in steam atmosphere (Miyahara *et al.*, 2020).

4.3.2 CsI revaporization and gaseous iodine transport

Thermal ramp treatments on CsI deposits were performed both in the RIGolo open flow reactor and by thermogravimetric analyses in the 150°C-750°C temperature range (heating rate of 5°C/min). Results are summarized in Table 4.2.

In steam/argon atmosphere, CsI revaporization starts at 470-490°C, and revaporization rate increases rapidly with temperature up to 650 °C-750°C were it stabilizes owing to mass transfer limitations. Whatever the initial precursor (impacted aerosol, condensed vapour or deposited vapour), CsI is stable featuring no significant decomposition during its transport.

Air[10] was considered either alone or mixed with steam in different concentrations (from 3% air/steam up to 50% air/50% steam). In presence of dry air, the re-vaporization of CsI deposits (aerosol or high temperature vapour deposition) from pre-oxidized stainless steel surfaces leads to the release of 45-75% of I_2 (relative to I initial amount[11]). Only, CsI deposit obtained by vapour condensation showed a lower gaseous I_2 release (12%). A part of Cs is retained on the surface (2.5-10% of initial amount). The re-vaporization of CsI aerosols from an inert surface (gold) in air leads to the formation of 28% of molecular iodine, which is lower compared to the re-vaporization from a stainless steel surface.

In a mixed air/steam atmosphere, between 12-33% of iodine is released as I_2, regardless of the air content in the carrier gas. These results contrast with tests performed in isotherm conditions at 650°C and featuring only very low gaseous iodine releases even in air: 5% of released iodine were identified as I_2 by Gouello *et al.* (2018a) compared to up to 75-78% for thermal ramp tests. It should be noted that the experimental protocol is different with CsI powder in a crucible (Gouello et al., 2018a) from on one side and CsI deposits on SS coupons on another side (our work) that may affect the results.

With air, the kinetic pattern of the gaseous molecular iodine release is generally the same, regardless of carrier gas composition, deposit or substrate nature and consists of two steps: an initial reduced release between ≈440-550°C and a second rapid release above 550°C. In the case of CsI high-temperature deposits (720-620°C) there is an additional I_2 release peak between 200°C-350°C. Typical I_2 release kinetics is reported in Figure 4.9.

[10] In this series of test, synthetic air (80%Ar/20%O_2) was also used.

[11] When considering released iodine (e.g. iodine amount transported to the sampling line), I_2 fraction amounts up to 75-78%.

Table 4.2: Summary of main experimental results (Obada et al., 2017; Obada et al., 2018; Obada et al., 2020).

Substrate	CsI deposit	Re-vaporization carrier gas (% vol)	Main results				
			Temp. of release initiation (°C)[4]	I_2 released[1,2]	Cs residual [1,3]	I residual [1,3]	Cs/I line1
Pre-oxidized 304L	Aerosols impaction at room temperature	Air (100%)	420	50-75 %	<10%	<1%	5-11
		Air/steam (50/50)	460	26%	6.5%	< l.d.	1.5
		Air/steam (20/80)	470	23-33%	7-9%	< l.d.	1.6
		Air/steam (3/97)	450	26%	2%	< l.d.	1.4
		Ar/steam (70/30)	480	0%	3.4%	< l.d.	1.1
Pre-oxidized 316L	High-temperature vapour deposition (720-620°C)	Air (100%)		53%	3.4%	< l.d.	10
		Air/steam (20/80)		13%	9.7%	8.6%	1.6
		Ar/steam (70/30)		0%	1.9%	< l.d.	3.8
	Vapour condensation (620-440°C)	Air (100%)		7-15%	2.4-4.5%	<1%	1.3
		Air/steam (20/80)		12%	2.0%	<1%	1.1
		Ar/steam (70/30)		0%	0.5%	0.6%	3.1
	Aerosols deposits (< 400°C)	Air (100%)		45%	2.4%	< l.d.	12
		Ar/steam (70/30)		0%	2.9%	1.0%	1.2
Gold (Au)	Aerosols Impaction	Air (100%)		28%	0.4%	< l.d.	1.6

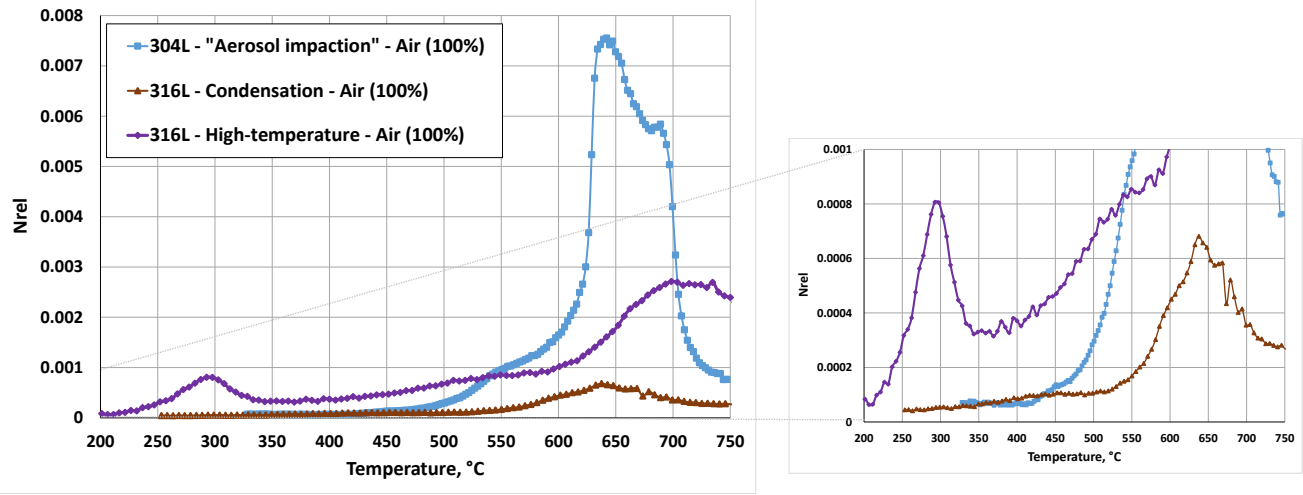

Figure 4.9: Release and transport kinetics of I_2 during revaporization of CsI deposits in pure air with a heating rate of 5°C/min up to 750°C.
blue curve: CsI RT aerosol impaction" (air flow rate 53 mL_n/min), brown curve: CsI vapour condensation (air flow rate 200 mL_n/min); purple curve: CsI high-temperature vapour deposition (air flow 200 mL_n/min) (Obada *et al.*, 2020).

4.3.3 Surface characterization of the residue

A detailed surface characterization by XPS and ToF-SIMS of the sample after CsI re-vaporization was performed. For CsI deposit obtained by room temperature aerosol impaction on 304L coupons (Obada *et al.*, 2017; Obada *et al.*, 2018), the results show evidence of the formation of mixed Cs-Cr oxides, specifically Cs_2CrO_4 and $Cs_2Cr_2O_7$ for all tests performed with air injection. This observation is supported by XPS analysis which revealed the presence of two chemical forms of chromium: Cr(III) and Cr(VI) oxides (see Figure 4.10). ToF-SIMS analysis has also revealed the presence of secondary ion clusters $Cs_2CrO_3^+$ and $Cs_2Cr_2O_9H^+$, which is a strong indication that the said oxides have been formed during the re-vaporization process. These results demonstrate that the chromium of the support can react with the air (Souvi *et al.*, 2017) and then affect the behaviour of residual Cs+ but not that the same support participates to the iodine oxidation.

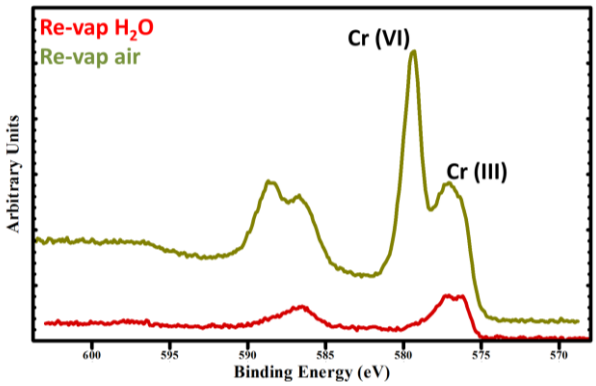

Figure 4.10 : XPS Cr 2p spectra for 304L coupon after vaporisation of CsI aerosols deposit in air atmosphere (green) and steam atmosphere (red). (Obada *et al.*, 2017)[12].

Similar surface characterizations were performed on the 316L foils after CsI re-vaporization of high temperature deposits and condensed vapour (as displayed in). The presence of the mixed Cs-Cr-O compounds described above is confirmed after TOF SIMS depth profiling (Figure 4.11), as soon as air is present in the carrier gas. Also, in both cases, the Cs depth profile indicates that Cs had migrated in the oxide layer during the thermal treatment – or that the oxide layer may have growth up to the CsI deposit. Indeed the Cs_2^+ and Cs_2I^+ signals are very low at the surface and in the first oxide layer (composed of Fe and Mn) and increase strongly in the second Cr-Mn oxide layer (figure 6, depth profile in positive polarity). Migration of CsI inside the oxide layer may explain the significantly more important residual mass of Cs (9.7%) and I (8.6%) observed on the 316L foil after re-vaporization of high-temperature vapour deposit in steam/air (Table 4.2).

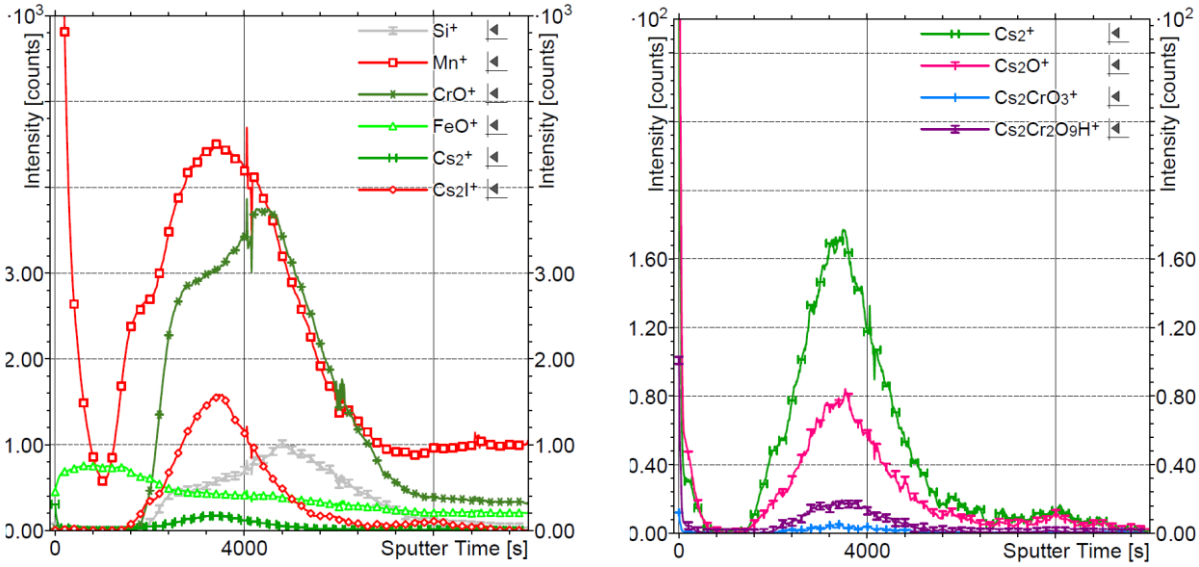

Figure 4.11. TOF-SIMS profile[13] of CsI vapour condensation deposition 316L pre-oxidised foil and re- vaporized in air/steam atmosphere (condition 10, table 3). a) major fragments b) minor fragments.

[12] XPS measurements were carried out on a Kratos AXIS Ultra^{DLD} spectrometer equipped with a monochromatic Al Kα source (1486.6 eV). Calibration was done by using the C 1s component of adventitious at BE (binding energy) = 285.0 eV. Binding energy value uncertainty is +/-0.1 eV and uncertainty on quantitative elemental analysis is +/- 10%.

[13] ToF-SIMS analyses were carried out using a ToF-SIMS 5 instrument (ION-TOF GmbH). Pulsed Bi^+ primary ions have been used for analysis (25 keV, ≈1 pA) and O_2^+ for sputtering (2 keV, ≈500 nA). Given the sputter parameters, estimated sputter speed is 1.6 nm/s. Mass spectra were recorded in positive (for each sample) and negative for one sample polarity from an analysis area of 100µm x 100µm centered into a 300µm x 300µm sputtered area. Charging effects, due to analysis and erosion ion beam, were compensated using low energy electrons (20 eV).

4.3.4 Discussion on a possible mechanism of CsI revaporization

There seem to be several mechanisms responsible for I_2 formation in presence of O_2, depending on the temperature. Below 550°C the results suggest a solid-gas (heterogeneous) phase interaction between the deposit and the carrier gas. Above 550°C, the CsI starts to vaporize and the interaction will be also in the gas (homogeneous) phase.

Density Functional Theory (DFT) calculations of the possible oxygen interaction in small CsI aerosols was carried out (Hijazi, 2017; Obada *et al.*, 2020). In the first step, the support (SS surface) was not included in the calculations. This hypothesis is supported by the fact that with deposits thickness of several µm (average surface deposits mass density of 1-2 $mg.cm^{-2}$), a large part of the CsI particles will not be directly in contact with the substrate surface. Furthermore, the kinetic of I_2 release at relatively low temperatures (500-650°C) is mostly independent of the nature of the support. Various models of the CsI crystal surface were taken into consideration to account for the different deposit preparation conditions (aerosol impaction, aerosol deposition, vapour condensation or vapour deposition): perfect surface (the most stable configuration), and a surface resulting from the combination of step and a terrace (default). The main outcome of the DFT calculations is that interaction of O_2 is not probable on perfect CsI surfaces even at high temperature (endothermic process). On the contrary, dissociative O_2 adsorption is favoured on surface defects (especially edges) leading to the release of $IO^{\bullet}$ radicals in the gas phase. This strongly reactive species can then convert into I_2 due to iodine oxide decomposition processes (Fortin *et al.*, 2019). The oxygen reactivity depends then on the numbers of surface defects and thus the CsI deposition process. Once the O_2 reacted with the surface and induces the release of $IO^{\bullet}$ radicals, new defects appears on the surface enabling further interaction with O_2 gas. This mechanism may be then responsible for the very fast increase of the reaction rate with temperature that is experimentally observed (Figure 4.9). On well crystallized particles, as observed on CsI obtained by vapour condensation, fewer surface defects are expected, so that higher temperature are needed for CsI decomposition that can explain the lower I_2 release observed in this case.

CsI interaction with the surface oxide layer may be of secondary order but a still significant pathway to the release of gaseous iodine. Indeed, revaporization of CsI aerosols in air from an inert substrate yields less gaseous iodine release than from oxidised SS. Heterogeneous reactivity between oxygen and CsI deposit only cannot alone account for this difference. Furthermore with air, significant Cs retention was observed with the formation of a Cs-Cr phase. The formation of Cs-Cr oxides is thermodynamically favoured as mentioned by Sasaki et al (2013) in presence of oxygen and can contribute to the release of molecular iodine following the reactions:

$$4\ CsI_{(C)} + 5/2\ O_2 + Cr_2O_{3(C)} \leftrightarrows 2Cs_2CrO_{4(C)} + 2I_{2(G)} \qquad \text{Equation 4-3}$$

$$2\ CsI_{(C)} + 2\ O_2 + Cr_2O_{3(C)} \leftrightarrows Cs_2Cr_2O_{7(C)} + I_{2(G)} \qquad \text{Equation 4-4}$$

With ΔG_R ranging from -140 to -115 $kJ.mol^{-1}$ and -110 to -98 $kJ.mol^{-1}$ respectively in the 450-650°C temperature interval as calculated with COACH software, based on the thermodynamic data bank TH05 (thermodata online).

4.4 Revaporization of AgI

Even if AgI is not the main expected metallic iodide formed and deposited in the RCS based on the results of the CHIP programme (Grégoire *et al.*, 2021), possible decomposition of such species in late accidental phase may contribute to the release of gaseous iodine compounds as was mentioned by Gouello *et al.* (2018). In this view, AgI deposit thermal stability was studied in the same condition as for the CsI deposit revaporization.

Owing to the insolubility of AgI in aqueous media, deposits were generated by a dry process. AgI grinded powder (particles of ~3 µm average diameter) was impacted on 304L coupons at room temperature (Obada 2017,): AgI particle deposits of 0.5-2 $mg.cm^{-2}$ on stainless steel coupons (preoxidised 304L) were obtained. The main drawback of this process is the inhomogenities of the deposited layer as can be observed from SEM examination (Figure 4.12).

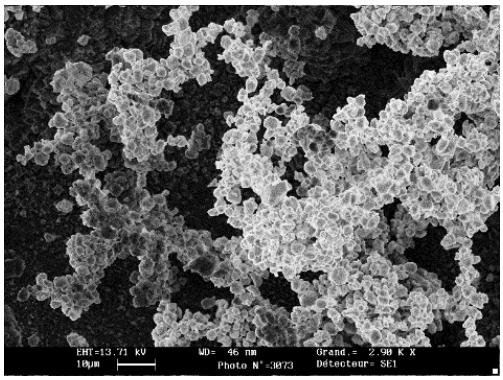

Figure 4.12: SEM image of CAgI particles deposited by dry process at room temperature on 304L coupons (magnification x 3200). (Obada, 2017).

The silver iodide deposits were reheated up to 750°C by a thermal ramp treatment (@5°C/min) in air, steam and steam/air atmospheres in the RIGolo line. The overall iodine and silver releases could not be determined with accuracy as silver iodide is insoluble even in strongly acidic media preventing the determination of a reliable mass balance at the end of the test. Nevertheless, interesting trends could inferred form the post test elemental analysis. Very low amounts of silver were detected downstream the SS coupon (less than 3-5% of the Ag initial mass) whatever the test conditions – consistently with low volatility of silver species. Concerning iodine, a significant transport is systematically observed: representing 20% of the initially deposited mass in steam conditions up to 50% in presence of oxygen (air and air/steam conditions).

Molecular iodine is the main released and transported species in presence of air and its kinetic of release could be established (see Figure 4.13). A similar kinetics pattern as for CsI revaporization is observed. In pure steam, no molecular iodine was evidenced but iodine is found downstream the coupon in large excess relative to silver, indicating a probable transport in a gaseous form distinct from I_2. Nevertheless, except for iodine and silver, no other elements were searched for in the experimental line, so that the formation and transport of volatile metallic iodide with the main components of the oxidation layer of the 304L coupons cannot excluded.

XPS examination of coupons after thermal treatment showed that the residue is mainly composed of silver (Ag/I ~2 to 2.5). Chemical displacement of Ag 3d lines do not allow to discriminate expressly between silver iodide and silver oxide forms (charge effect and low chemical displacement between those species prevented in-depth analysis). Both silver iodide and silver oxide species were detected by TOF SIMS (qualitative analysis), but no other compounds involving silver could be evidenced. As a consequence, silver interaction with oxide layer compounds seems most unlikely (contrarily to Cs which can react with chromium(VI) of the oxide layer). Analysis of the residue, even if only qualitative, indicate that iodine release is most probably due to silver iodide decomposition in the condensed phase.

Calculations at thermodynamic equilibrium (Gemini software with Coach 5.2 data base) do not allow to explain the large molecular iodine releases, as they predict a limited decomposition of silver iodide even in presence of air and a reduced formation of molecular iodine. DFT calculations may help to explain the interaction of O_2 with AgI crystal and determined if a similar process to that proposed for CsI is favourable or not (Hijazi, 2017).

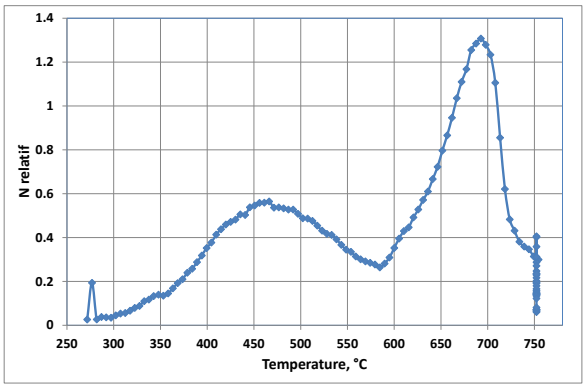

Figure 4.13: Kinetics of I_2 release during revaporization of AgI deposits in Steam/air (70/30) with a heating rate of 5°C.min^{-1} up to 750°C (Obada, 2017).

4.5 Revaporization phenomena – conclusion and perspectives

The thermal ramp experiments performed in the RIGolo set-up with CsI and AgI deposits (Obada, 2017; Obada al., 2017; Obada *et al.*, 2018 ; Obada *et al.*, 2020) allowed to build a reliable data base on metallic iodide revaporization behaviour and to identify the main parameters contributing to the transport of gaseous iodine species

For CsI, less reactive with SS surface, revaporization in steam is reported to start close below 400/500°C and to be terminated around 750°C. CsI is the main identified released species in steam and steam/hydrogen conditions, e.g. in atmosphere featuring low O_2 potential. In presence of air, release of gaseous iodine compounds is observed, consistent with previous experimental results (Berdosonov *et al.*, 1999; Kulyukhin *et al.*, 2004) but at much lower temperatures than previously mentioned. Molecular iodine can dominate the iodine transported form. In such conditions, the gaseous molecular iodine release consists of two steps: an initial reduced release between ≈440-550°C and a second rapid release above 550°C. In the case of CsI high-temperature deposits (720-620°C) there is an additional I_2 release peak between 200-350°C. Several mechanisms are hypothesised to account for this kinetics: solid-gas phase mechanisms below 550°C and gas phase reactivity above 550°C when CsI starts to vaporize.

If the condensed phase reactions between CsI and Cr oxide of the SS surface is thermodynamically favoured in the 450-650°C range and in presence of O_2, this mechanism is only of secondary importance owing to the fact that a low fraction of CsI is in contact with the SS surface. In addition to this reaction pathway, another heterogeneous mechanism is proposed in which oxygen can directly react on CsI crystal defects resulting in the release of $IO^{\bullet}$ radicals in the gas phase which then forms I_2. $IO^{\bullet}$ release and then direct CsI vaporization above 550°C may enhance the formation of crystal defects thus accelerating this process. This mechanism is supported by DFT calculations and may explain both initial reduced I_2 release and the large amounts of I_2 released above 550°C. As for gas phase O_2 reactivity with CsI, this point is questionable as this reaction is not thermodynamically favoured in the explored temperature range. Figure 4.14 presents a summary scheme of CsI revaporization behaviour as of the present state-of-art.

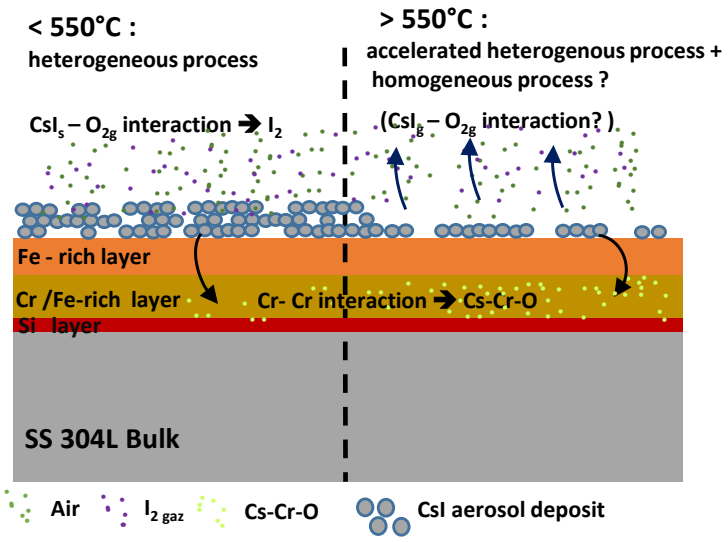

Figure 4.14: Summary of CsI revaporization behaviour from SS surface in presence of air.

For silver iodide, its decomposition in the condensed phase when heated above 500°C seems to be the main reaction pathway leading to the release of gaseous iodine species. If molecular iodine could be unambiguously identified in presence of oxygen, the exact nature of iodine release in poorly oxidative conditions remains to be identified.

These results – in addition to literature data – have confirmed that revaporization is a phenomena that must be taken into account in late phase of an accidental scenario – especially as it may results in delayed gaseous iodine releases. Nevertheless, this experimental database does not cover all conditions expected in case a SA scenario and thus does not allow either to have a complete view of the governing chemical mechanism nor to be capable of deriving models to be implemented in SA simulation codes.

In continuation of the MIRE programme, the ESTER project will complement the experimental database at different scales, from analytical to semi-integral tests with the objective to address the lack of data needed to develop a comprehensive modelling approach of revaporization. In this view, the following parameters will be considered:

- Influence of dwell thermal treatment versus ramp temperature as very slow temperature evolution – comparable to "dwell" - is the expected thermal evolution in the RCS on long term resulting in sections maintained in between 300-700°C for several hours up to several days. It was observed that significant revaporization occurs in this temperature range – resulting in the transport of both gaseous and aerosols species.
- Role of the oxidative potential of the atmosphere, and especially the reactivity of $OH^\bullet$ and $O^\bullet$ radicals on CsI and CsOH deposits in RCS conditions. These radicals results from high temperatures cracking or radiolysis of O_2 or H_2O in the degraded core and may persists at lower temperatures in the RCS due to kinetic limitations for their recombination at lower temperatures.
- Role of boron species vapours (H_3BO_3) on revaporization of CsI and CsOH. Owing to the reduced set of experiments of CsI revaporization when exposed to boron compounds, there is still an important lack of data on the influence of key parameters such as atmosphere composition (e.g. oxygen potential), thermal treatment, nature of boron vapours or interactions with stainless steel oxidized surface. CsOH revaporization when submitted to boron vapours was not investigated. Modelling of heterogeneous reactivity between condensed CsI phase and gaseous boron species was also not fully investigated.
- Revaporization of the other metallic iodide (AgI, CdI_2) expected to be deposited in the RCS. Indeed, the first scoping studies (Gouello *et al.*, 2018; Obada , 2017) evidenced the possible release of gaseous iodine species, even at low temperatures. Stability of such compounds when exposed to boric acid/boron oxide

vapours was not investigated. Even if those compounds are expected to be minor forms of metallic iodides (compared to CsI), their lower stability may result in a significant delayed gaseous iodine source.

- Tellurium revaporization, as it is one of the main deposited FP in the RCS and will be possibly a delayed source of released radioactive iodine (though radioactive decay of ^{132}Te and ^{131}Te). Its revaporization behaviour is poorly documented in the literature (Grégoire *et al.*, 2021b) so that its contribution to delayed releases cannot be evaluated in the present simulation tools. Analytical scale experiment will firstly consider revaporization behaviour of Te oxide (H_2TeO_3) and possible caesium tellurides (Cs_2Te, Cs_2TeO_3 and Cs_2TeO_4) in different conditions. Special attention will be brought on the identification and quantification of released species. Experiments will be supported by thermodynamic calculations.

Experimental work is already in progress in the framework of a second Ph-D (2019-2022) still in partnership with the UCCS laboratory of the Lille University, this work being part of the OECD ESTER project (2020-2023). This first stage will be devoted to analytical tests considering single species deposits. Tests at a larger scale are also planned from 2022 on, on the CHIP line. The aim will be to consider multicomponent deposits – as this line allows to consider complex chemical systems with several FPs (I, Cs, Mo) and CR material.

5 EXERIMENTAL STUDY OF HETEROGENEOUS INTERACTIONS OF GASEOUS IODINE (CH_3I) WITH ATMOSPHERIC AEROSOLS

Following a severe accident in a NPP, large radionuclide atmospheric releases can occur as was observed after the Chernobyl (Ukraine, 1986), and more recently Fukushima (Japan, 2011) accidents. More specifically, iodine releases are of most concern as gaseous releases (essentially I_2 and RI – R = alkyl group/chain type CH_3I). Indeed, such gaseous forms may be not fully retained by the current filtered containment venting systems (Bosland *et al.*, 2010; Bosland *et al.*, 2014; Chebbi *et al.*, 2018; Leroy and Monsanglant-Louvet, 2019). Iodine dispersion is dependant of local meteorological conditions that can cause a great variability in activity concentrations/deposits (Lebel *et al.*, 2016), but also of its reactivity with other species present in the atmosphere (gas or particles) that may contribute to a rapid evolution of its nature. Indeed, field measurements performed after the Chermobyl and Fukushima accident showed that the gaseous iodine forms (I_2 and CH_3I) become predominant at long distance (several hundred of km, from the emission point) whatever the nature of the initial iodine release (Masson *et al.*, 2011; Steinhauser *et al.*, 2014; Imanaka *et al.*, 2015,).

In order to predict such dispersion and be able to apply adapted counter measures to protect public health, IRSN develops specific simulation softwares - C3X plateform (Tombette *et al.*, 2014, Saunier *et al.*, 2020) - capable of reproducing the dispersion of the radionuclides in the atmosphere. One major gap of the current version of this tool is that the transport of iodine is modelled without considering the physical/chemical evolution of iodine in the atmosphere, i.e. the gas phase evolution or interaction with atmospheric aerosols. The radiological consequence (thyroid equivalent dose which is dependant of the iodine form: I_2, CH_3I or particulate) are thus predicted without considering the actual forms of the dispersed iodine. The development of an iodine atmospheric mechanism has been recently undertaken at IRSN (Trincal, 2013; Fortin *et al.*, 2019); this mechanism is based on atmospheric iodine cycle initially developed by Saiz-Lopez *et al.* (2012) and updated with some key reactional pathway involving interaction volatile organic compounds. This mechanism is based on gas phase reactivity only, gas – aerosol interactions being not yet considered by lack of data.

5.1 Atmospheric heterogeneous reactivity – case of iodine

Aerosol particles play a key role in atmospheric processes: on atmospheric radiative transport and thermal structure by light scattering and absorption, on formation of clouds and precipitation by inducing water vapour condensation and finally by heterogeneous interactions with semi volatile vapours (condensation/ evaporation) or trace reactive gas (reactive uptake). A full understanding of their impact implies an extended identification of their sources, composition or concentration but also to determine the mechanism of their physico-chemical transformation during their atmospheric lifetime. As a part of this ageing process, heterogeneous reactions with atmospheric trace gases are of rising interest since the past two decades given the role in modifying atmospheric gas phase cycle of trace gas, as for instance key gaseous pollutants (SO_2, NO_2 and N_2O_5).

5.1.1 Atmospheric aerosols

Overall annual aerosol emission to the atmosphere represents in average 3.4 10^9 tons (Laj and Sellegri, 2003). Aerosol particles directly emitted to the atmosphere (primary particules) originate from a wide variety of natural (sea salt, mineral desert dust, volcanic ashes and biological debris) or anthropic sources (i.e., industrial emissions, agricultural activities…). Aerosol resulting from gas-to-particles conversion or chemical transformation of primary particles (secondary particles) are mainly sulphate, nitrate or organic aerosols from both natural and anthropogenic sources (Pöschl *et al.*, 2005; Després *et al.*, 2012; Lei *et al.*, 2011). Sea salt and mineral dust represent ~80% of the total aerosol emission whereas anthropic sources account for roughly 10%. Nevertheless, this proportion varies considerably when estimates are made on a regional or urban scale (Pöschl *et al.*, 2005, Laj *et al.*, 2009; Monks *et al.*, 2009, Mohiuddin *et al.*, 2014; Viana *et al.*, 2008).

Aerosol atmospheric lifetime is strongly dependant of aerosol size: lifetimes up to 10 days in the troposphere and up to 1 year in the stratosphere are observed for micrometric and submicrometic size range, whereas large particles (> 10 µm) feature much shorter lifetimes (1 days) due to gravitational settling and wet deposition (Feichter *et al.*, 2009; Pellerin *et al.*, 2017). Given aerosol sources, lifetime and geographical distribution, strong

variation in concentration and composition over the earth can be observed in the range of about 10^2–10^5 particles.cm^{-3} and 1–100 µg.m^{-3}, respectively (Seinfeld *et al.*, 1998; Hidy *et al.*, 2013, Pöschl *et al.*, 2005; Raes *et al.*, 2000; Krejci *et al.*, 2005; Putaud *et al.*, 2010).

The main constituents of the atmospheric aerosols are inorganic species (such as sulphate, nitrate, ammonium and sea salt), organic species, carbonaceous, mineral species (mostly desert dust) and primary biological aerosol particles. At the particle scale, complex heterogeneous structures featuring both organic and inorganic part can be observed due to the complexity of atmospheric reaction (Tervahattu *et al.*, 2005; Barger *et al.*, 1976). The chemical composition of aerosols differs considerably, depending on its source (primary or secondary) and its atmospheric lifetime (ageing) (Putaud *et al.*,2010;, Jimenez *et al.*, 2009; Karagukian *et al.* 2015). For instance, measurements in the marine boundary layer (MBL) reveal that the primary inorganic sea salt component dominates the marine aerosols (Schiffer *et al.*, 2018; Finlayson –Pitts at el., 2000, Chi *et al.*, 2015). It is well known that sea salt aerosols are constituted of inorganic species mainly sodium chloride (NaCl) as well as various organic species. In many investigations, fatty acids (FA) are reported to be major constituents of the organic fraction on marine aerosols (Ault et al., 2013; Russell *et al.*, 2010; O'Dowd *et al.*, 2004; Lovrić *et al.*, 2016). In contrast, urban aerosols have a more complex composition and are dominated by sulphate, nitrate and carbonaceous aerosols (Liang *et al.*, 2016) with a significant contribution of carboxylic acids such as malonic, succinic and glutamic acids Kitanovski *et al.*, 2011; Chan *et al.*, 2011).

5.1.2 Heterogeneous reactivity in the atmosphere – Processes for gas uptake

As they affect both trace gas concentration (photochemical oxidants, acid gases, free radical, etc.) and aerosols key physical properties (size, optical properties and ability to nucleate cloud droplets, the heterogeneous interactions of gases with liquid and solid particles can strongly influences atmospheric processes (formation of photochemical smog, ozone layer depletion etc.). Thus, determination of kinetics and mechanism of heterogeneous reactions has become increasingly important in understanding the chemistry of the troposphere.

One comprehensive kinetic model network for heterogeneous interactions was proposed by Kolb *et al.* (2010) which is a combination of kinetic theories of gases, condensed phases, and interfaces based on NASA–JPL and IUPAC evaluations (Pöschl *et al.*, 2007; Crowley *et al.*, 2010). The observable interactions of a gaseous species on a particle or a droplet surface are indeed the results of a complex process, which can be decomposed on several elementary processes. When a gas is in contact with a condensed phase (solid or liquid), gaseous molecules driven by thermal agitation can diffuse towards this phase and hit the surface. A fraction of the molecules that hit the condensed surface can be taken up due to heterogeneous elementary processes including gas phase diffusion, accommodation, desorption and possible reaction at the gas/surface interface and for liquids and some amorphous solid surfaces, absorption, dissolution and bulk reaction.

It is often difficult to experimentally determine which ones, if any, of the processes defined above, is actually controlling the heterogeneous uptake of trace gas species on a given surface. Thus, the overall process can be described with a global parameter: the uptake coefficient which is the ratio of the number of collisions of a given trace gas species leading to uptake on the surface to the total number of possible collisions per unity of surface and time (ɣ) (Crowley *et al.*, 2010):

$$\gamma = \frac{\boldsymbol{Number\ of\ taken\ up\ molecules\ per\ unity\ of\ surface\ and\ time}}{\boldsymbol{Number\ of\ colliding\ molecules\ per\ unity\ of\ surface\ and\ time}} \qquad \text{Equation 5-1}$$

ɣ is then a dimensionless parameter and represents the probability ($0 < \gamma < 1$) that a gas species is removed irreversibly from the gas phase to an active surface at a given temperature.

The actual quantity measured with most of heterogeneous experimental studies is the observed overall trace gas uptake, γ_{obs}. Observed uptake is usually determined from the decrease of the concentration of the trace gaseous (x) species of interest (equation 5-2) when exposed to a reactive surface (Scolaro, 2016) . To a lesser extent and for a purely reactive uptake, γ_{obs} in some measurements can also be obtained by quantification of the surface product (Y) concentration (Vogt and Finlayson-Pitts, 1994) (equation 5-3).

$$\gamma_{obs\ (g)} = \frac{d[X]_g}{dt} \times \frac{1}{A \times [X]_g \times \omega/4} \qquad \text{Equation 5-2}$$

$$\gamma_{obs\ (s)} = \frac{d\{Y\}_s}{dt} \times \frac{1}{A \times [X]_g \times \omega/4} \qquad \text{Equation 5-3}$$

$[X]_g$ is the gas phase concentration of X and $\{Y\}_s$ is the surface species concentration. ω is the mean thermal velocity ($m.s^{-1}$) given by $\omega = [8RT/(\pi M)]^{1/2}$, M is the molar mass ($kg.mol^{-1}$) of X, R is the gas constant ($J.mol^{-1}$), and T is the temperature in Kelvin. A corresponds to the effective surface area.

Several experimental methods dedicated to laboratory experiments can be used to study heterogeneous interactions and to determine uptake coefficients (Kolb *et al.*, 1995, Davidovits, 2006, Kolb *et al.*, 2010). The general principle of these methods is to put a gaseous phase in contact with a solid or liquid phase of known surface. The number of gaseous molecules taken up by the solid or the liquid is measured during a known time interval through either surface or gas monitoring. Table 5.1 summarizes the commonly used methods for the determination of reactive uptake in gas-solid / liquid reactions. The surface characteristics, the range of accessible ɣ, the gas-solid contact time and the working pressure range for each method are listed in Table 5.1

Table 5.1: Summary of the principle commonly used methods for the measurement of reactive uptake in gas-solid / liquid reactions. (Kolb *et al.*, 1995; Davidovits *et al.*, 2006; Kolb *et al.*, 2010).

Method	Surface	Monitored phase	Accessible ɣ range	Contact time	Working pressure (Bar)
Coated/wetted flow tube	Solid or liquid film	Gaseous	10^{-5}- 10^{-1}	0-10^3 s	0.0007-1.013
Aerosol flow tube	Solid or liquid aerosol particles	Gaseous and solid or liquid	10^{-4} -1	0- 30 s	0.001-1.013
Knudsen Cell	Powder sample or aerosol particles	Gaseous	10^{-5} - 1	10-10^4 s	< 1.33×10^{-5}
DRIFTS Cell	Solid surface or aerosol particles	Solid	10^{-10} -10^{-2}	40 -800 min	0.003-1.013
Droplet train flow reactor	Liquid droplets	Gaseous and droplet	10^{-3}-1	2-20 ms	0.080-0.03
Atmospheric simulation Chamber	Aerosol particles	Gaseous and solid	10^{-8} -10^{-4}	100 -900 min	1.013

5.1.3 Iodine interaction with aerosols– state of the art

Surprisingly, the interaction of gaseous iodine compounds with atmospheric aerosols and its resulting speciation are not well documented, yet. Indeed, only few laboratory studies have investigated the interaction of iodinated species with atmospheric aerosols surrogates. For instance, it was found that HOI can react with solid NaCl and NaBr to form ICl or IBr in gaseous phase in the 5-25 °C temperature range (Allanic *et al.*, 1999; Mossinger *et al.*, 2001; Holmes *et al.*, 2001). The steady state uptake coefficient was determined either in Knudsen cell or coated flow tube and it is in the order of 10^{-2}. Similarly, uptake of CH_3I (Wang *et al.*, 2016) and C_2H_5I (Shi *et al.*, 2008) by commercial soot film and carbon thin film, respectively, was determined to be in the order of 10^{-2} at 25°C. Most of the studies imply that iodine species are highly reactive and may interact with the other species (gas or particles) present in the atmosphere to evolve in gaseous or particulate form. However, neither uptake processes nor influence of condensed phase on gaseous iodine reactivity, were unravelled. To the best of our knowledge, there is no literature report about the uptake coefficient of methyl halides (CH_3Br, CH_3Cl, CH_3I) by atmospheric aerosols.

Some studies have investigated the interaction of gaseous iodine species such as HOI, INO_2, HI, IBr, ICl, I_2 with ice films or halogen doped ice (Allanic *et al.*, 1999, Fluckiger *et al.*, 1998; Barone *et al.*, 1999; Percival *et al.*, 1999, Allanic *et al.*, 2000). Again Knudsen cell or coated flow tube methods were applied. Strong uptake coefficients were observed in every case (10^{-2} to 10^{-1}) but the experiment temperature (-100°C up to -40°C) are not relevant of atmospheric conditions prevailing in the vicinity of a NPP. To date, the heterogeneous reactivity of iodine species in the atmosphere is not fully accounted by the atmospheric community (Saiz-Lopez *et al.*, 2012), nor in the field of nuclear safety.

5.1.4 Objectives of the investigations on iodine /aerosol interaction in atmospheric context

The goal of this work is to improve the understanding of the heterogeneous reactivity between gaseous iodinated species and aerosols present in the troposphere based on laboratory experimental studies.

Methyl iodide is the first considered gaseous species as it is one the of main expected iodine species which can be released in case of a severe accident. It is considered as stable in tropospheric conditions with a lifetime

ranging from 5 up to 11 days, compared to I_2 which is rapidly photolysed (lifetime of ~ 10 s (Saiz-Lopez *et al.*, 2008; Law *et al.*, 2006)). Surrogates of the main aerosols found in the boundary marine layer were retained in this first approach – as numerous power plant are located on seashore. The main objectives were to determine – at laboratory scale – the occurrence of interaction between methyl iodide and the selected aerosols surrogate, to define its nature (adsorption or chemisorption) and finally to determine the uptake coefficient.

In this view, I participated to the development of specific devices dedicated (breakthrough reactors and aerosol flow tube) which are suitable for both CH_3I and I_2. Experiments with methyl iodide were performed in the framework of a Ph-D in partnership with the University of Bordeaux under the supervision of S. Sobanska and myself. In the following paragraphs I will shortly presents the main outcomes of this work.

5.2 Experimental devices developed for iodine/aerosol reactivity study

Experiments were firstly conducted on solid static phase reactors. Breakthrough type reactors in which the reactive gas is constantly injected though a solid bed composed of the aerosol surrogates were used. Depending on the phase which is monitored (solid or gas phase), two static reactors were considered: a cell dedicated to Diffuse Reflectance Infrared Fourier Transform Infrared Spectroscopy (DRIFTS) allowing to monitor the changes at the solid phase surface when exposed to a reactive gas (Vogt and Finlayson-Pitts, 1994) and the flow reactor in which the concentration of the reactive gas is monitored by gas chromatography.

5.2.1 DRIFTS cell

DRIFTS technique requires the solid to be a diffusing medium. The fine powdered sample is put in the reaction chamber (provided with ZnSe windows), which is located inside an FTIR instrument as shown on the Figure 5.1. A parabolic mirror focuses the probe beam on the solid sample and the diffused reflected radiation is focused by another parabolic mirror on to the detector surface. This method allows the monitoring of solid-phase products formation. Spectral evolution of the solid (50-150 mg) with exposition duration to the reactive gas can give quantitative insights on the gaseous molecules taken up by solid sample (i.e. spectro kinetic measurements).

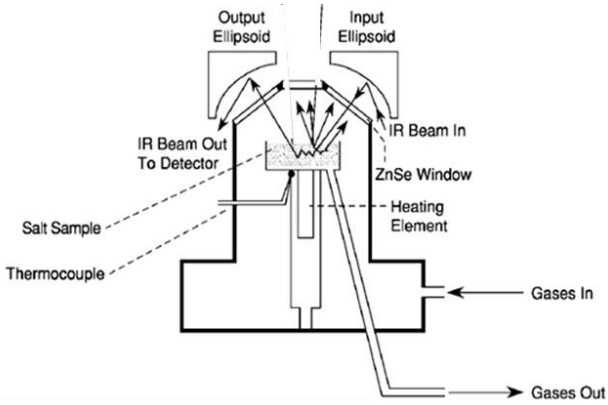

Figure 5.1: Scheme of a DRIFT cell (Vogt and Finlayson -Pitts, 1994).

This technique is well suited for the IR transparent alkali halides solids (as NaCl) so that formation of infrared absorbing intermediates and products, can be easily detected. The formation rate of absorbed/adsorbed products on the solid is determined by quantitative interpretation of the DRIFTS spectra. Coupled to a post-test complementary technique allowing the determination of the total amount of adsorbed/absorbed products during an experiment (ICP MS is our case), the uptake coefficients can be determined knowing the characteristics of the solid (sample mass and solid effective surface determined by the Brunauer – Emmett- Teller method for instance) following equation 5.2. The high sensitivity of the technique allows to determine uptake value in the 10^{-10} to 10^{-2} range.

Measurement difficulties may arise with highly IR absorbing solids (organic solids or secondary inorganic salts such as nitrate or sulphate). Moreover, DRIFTS can provide signal of gas phase near the surface which has to be identified before interpretation of the spectral evolution. Solid sample cannot be renewed during the experiment thus surface ageing of the solid sample can be a limitation.

5.2.2 Breakthrough type reactor

In case of IR absorbing solids, methyl iodide interaction was monitored by the methyl iodide gas phase concentration. Gas chromatography coupled to an electron capture detector was adapted to our intentions with determination of methyl gas phase concentration in the 1 ppb- 100 ppb range. The breakthrough reactors were designed with a gas inlet placed on the top and a gas outlet on the bottom of the reactor (see Figure 5.2). The solid samples were placed on a porous support (metallic or glass) allowing the gases to pass through. Gas sampling was performed at the reactor inlet and outlet and collected in gas bags.

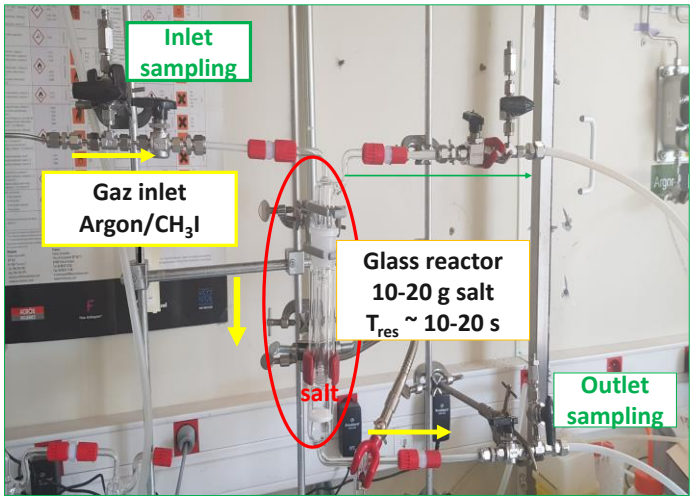

Figure 5.2 : Scheme of breakthrough reactor developed at L2EC (Houjeij et aL., 2021).

In continuous gas flow conditions, the equation 5-2 does not apply as the methyl iodide gas phase concentration at the reactor inlet is constant. The main parameters that must be taken into account here is the contact time (T_c) between gas phase and solid phase as for wall coated reactors (Percival *et al.*, 1999; Kolb *et al.*, 2010). With our reactor configuration, the contact time (T_c) depends on the solid bed volume, particles size, packing of particles, surface area and gas flow rate. In a first approach, the contact time was estimated by considering only the geometrical volume of the solid bed (eq 5-3):

$$T_c = \frac{\text{Solid bed volume}}{\text{Total gas flow}} \qquad \text{Equation 5-3}$$

In case of interaction with a given solid, depletion of outlet gas phase concentration is expected as of experiment onset. If no saturation of the solid occurs, a steady state is reached in which the outlet methyl iodide gas phase concentration remains constant. By varying the volume of the solid bed, the contact time of the reactant gas to the condensed phase can be varied, allowing a pseudo-first order rate constant for removal of the gas, k_s , to be measured, provided there is not significant surface saturation (Percival *et al.*, 1999). The net uptake is then proportional to k_s:

$$\gamma = \alpha . k_s / \omega \qquad \text{Equation 5-4}$$

where α is linked to the geometry of the solid bed and ω to mean gas velocity.

In case of low uptake, surface saturation will occur inducing the outlet gas concentration to increase with experiment time until observing a breakthrough which correspond to saturation of the solid bed. In this case only the initial uptake (corresponding to zero experiment time) can be determined. This type of reactor is suited for uptake determination in the 10^{-5} up to 10^{-1} range.

5.3 Study of the heterogeneous reactivity of CH_3I with NaCl by DRIFTS

In a first approach, the interaction processes of CH_3I with NaCl as surrogate of sea salt was investigated using DRIFTS (Houjeij, 2021; Houjeij *et al.*, 2021). The experimental conditions were aimed at

reproducing as close as possible an atmospheric environment in night conditions (ambient air conditions with 20% R.H, dry salt and dark reactor), except for CH_3I gaseous concentration which is much more important (ranging from 200 up to 1000 ppm) than the mean concentration in the atmosphere. Though not realistic, such CH_3I concentration levels allow to study interaction processes in a quite large range of uptakes – even for low reacting gaseous species.

5.3.1 NaCl surface monitoring by FTIR

For the whole experiments, the infrared spectra were recorded in the 600-4000 cm^{-1} spectral range. The C-I stretching mode at 572 cm^{-1} could not be observed given the cut-off frequency of the ZnSe cell window (600 cm^{-1}). The DRIFTS spectra were reported as log (1/R∞) "pseudo-absorbance", where R is the reflected diffuse signal of the sample. For poorly absorbing solid, pseudo-absorbance gives a better linear representation of DRIFTS band intensity against the adsorbate surface concentrations than Kubelka–Munk function (Sirita *et al.*, 2007).

For every conditions, the presence of CH_3I at the NaCl surface could be evidenced in the three main spectral region assigned to CH_3 stretching, deformation (see Figure 5.3a and 5.3b respectively) and rocking (not shown here) (Houjeij et al., 2021). CH_3I adsorption is clearly evidenced by the red shift of symmetrical deformation band of CH_3v from 1262 cm^{-1} (gas phase) to a large band centred at 1244 cm^{-1} and which intensity increased with time (see Figure 5.3b). Spectral decomposition (assuming Gaussian shape) of this band allows to identify 5 bands of which four can be assigned to adsorbed CH_3I (1275, 1244, 1220 and 1183 cm^{-1}) and the last (1262 cm^{-1}) to gaseous CH_3I close to the NaCl surface, based on literature data (Su *et al.*, 2000; Chebbi *et al.*, 2016; Colaianni *et al.*, 1992, Jenks *et al.*, 2000). Although less intense, bands in the stretching region (2900-3000 cm^{-1}) could be also observed (Figure 5.3a) and properly assigned to either gaseous or adsorbed CH_3I. The presence of several bands for a given vibrational mode is owed to different geometrical orientations that can take absorbed CH_3I molecules on NaCl whose surface present numerous orientations and defects compared to single metallic surface (Colaianni *et al.*, 1992, Jenks *et al.*, 2000, Henderson *et al.*, 1987, Solymosi *et al.*, 1993, Lin *et al.*, 1992). In the CH_3 rocking spectral region (900-700 cm^{-1}) the observed bands were not enough resolved to be correctly assigned.

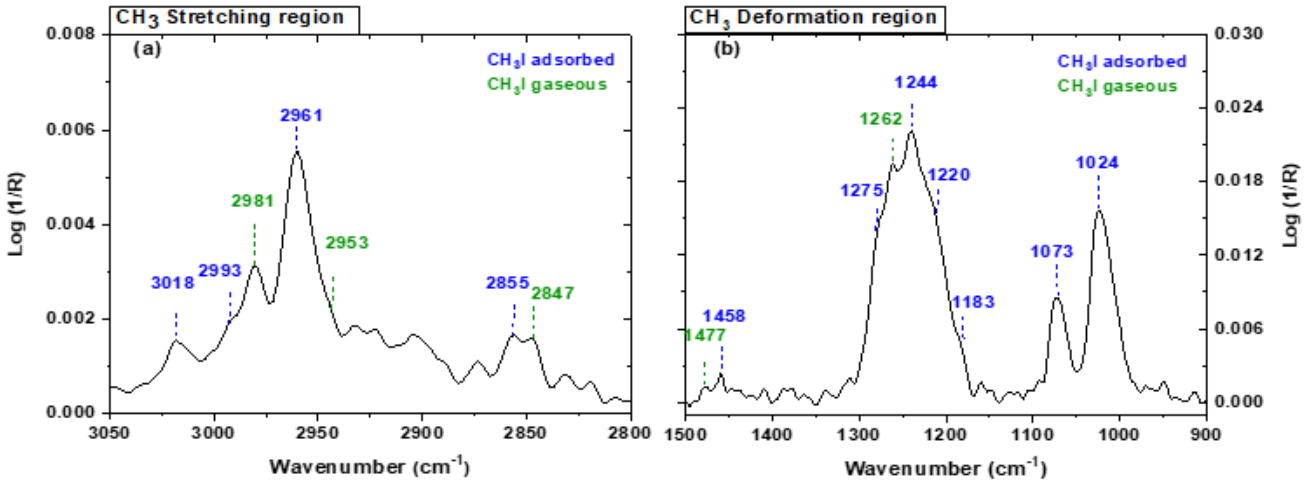

Figure 5.3 : DRIFTS spectra of NaCl exposed to 5 hours of CH_3I continuous flow (108mL.min^{-1}, 1000 ppm) at 23°C and 1 atm in the 3050-2800 cm^{-1} (a) and in the 1500-900 cm^{-1} (b) IR spectral range.
Blue bands are CH_3I adsorbed on NaCl and green bands are CH_3I in gas phase near the NaCl surface.

In addition, two intense bands at 1073 and 1024 cm^{-1} were observed - strongly red shifted compared to the CH_3 deformation band of free CH_3 at 1262 cm^{-1} (Figure 5.3). These bands were not reported in the literature for CH_3I molecules adsorbed on surfaces. Based on their wavenumbers, they can be assigned to CH_2I_2 (Klivényi *et al.*, 1995, Weldon *et al.*, 1994, Scheer *et al.*, 2002), CH_3OH (Chebbi *et al.*, 2016) or CH_3Cl (Makino *et al.*, 2018; Cserenyi *et al.*, 2000; Gu *et al.*, 2019)). Nevertheless, the hypothesis of formation of such species on NaCl was discarded because experimental conditions required to form such

species were drastically different in term of temperature or surfaces, compared to the conditions used in our experiments. The time evolution of these bands is strongly correlated to that of the deformation bands assigned to adsorbed CH_3I suggesting a vibrational mode correlated to adsorbed/absorbed CH_3I. It is assumed that these new bands are attributable to additional geometrical form of CH_3I on NaCl surface as C3v (Houjeij *et al.*, 2021).

5.3.2 Time evolution of CH_3I adsorption and desorption on NaCl

The time evolution of CH_3I adsorbed or desorbed on NaCl surface was evaluated by following the sum of the band areas related to $CH_3I_{(ads)}$ in the deformation region (i.e. bands at 1275, 1244, 1220, 1183, 1073 and 1024 cm^{-1} labelled as $\sum CH_3I_{adsorbed}$) as reported in Figure 5.4. The area of $\sum CH_3I_{adsorbed}$ bands increases during the CH_3I exposure phase with no significant saturation even after 5 hours exposition to CH_3I. Methyl iodide interaction with NaCl surface is probably chemisorption as no measurable desorption is observed, either spontaneous, or induced by an argon flow (Figure 5.4b) or thermally activated (up to 350°C).

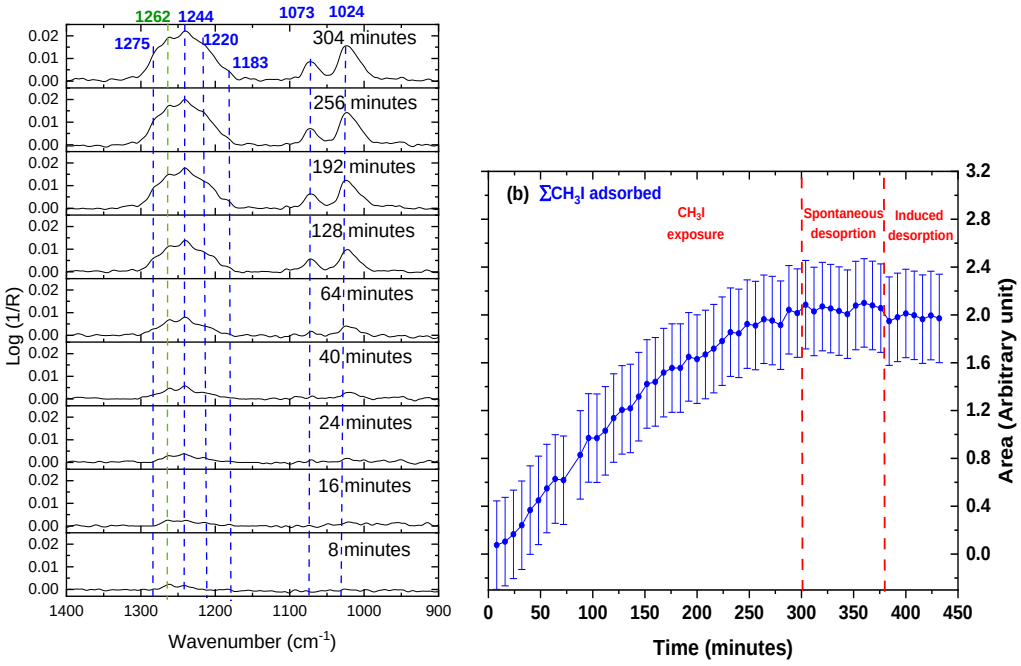

Figure 5.4 : Time evolution of DRIFTS spectra of NaCl surface in the deformation region of CH_3 (1400-900 cm^{-1}) as a function of exposure time to the CH_3I continuous flow (108mL.min^{-1}, 1000 ppm) at 23°C and 1 atm .
Bands in blue are adsorbed CH_3I on NaCl and green are gaseous CH_3I near the surface.
(b) Area of the $\Sigma CH_3I_{adsorbed}$ bands as a function of time during CH_3I exposure, spontaneous and induced desorption phases. Exposure phase denotes the continuous flow of 108 mL.min^{-1} of CH_3I (1000 ppm) on NaCl. The spontaneous desorption phase denotes the static conditions after 5 hours of CH_3I flow and induced desorption phase denotes the continuous pure Ar flow after the static condition.

The time evolution of methyl iodine adsorption can be interpolated by a linear function allowing to determine an average rate of adsorption (k); it amounts up to (6.91±0.23) ×10^{-3} arbitrary unit.min^{-1} when NaCl is exposed to CH_3I gaseous concentration of 1000 ppm. The average rate of adsorption shows a first order kinetic rate law with CH_3I gas phase concentration (200-1000 ppm concentration range).

5.3.3 Determination of CH_3I uptake coefficient on NaCl surface

The CH_3I concentration on the solid was determined by ICP-MS assuming that the overall amount of adsorbed iodine is in CH_3I form. The average concentration of iodine found in NaCl exposed to CH_3I (1000 ppm) during 5h amounts up to (1.68± 0.86) × 10^{14} molecule.mg^{-1}_{NaCl}. Taking into account the total mass of NaCl involved in the experiment, the total amount of adsorbed CH_3I (noted **{CH_3I_{ads}}**) can thus be determined. Comparing the total amount of injected gaseous CH_3I_g during the exposure phase to the

total amount of adsorbed CH_3I_{ads} on NaCl, it is found that only $3x10^{-3}$ % of initially injected methyl iodide was adsorbed on NaCl, indicating a very low residual amount of CH_3I on NaCl.

Based on the pseudo absorbance equation (Sirita *et al.*, 2007), the amount of CH_3I adsorbed on NaCl was determined assuming a linear relation between area of IR bands in the 1400-900 cm^{-1} frequency range ($\sum CH_3I_{adsorbed}$) and the amount of total iodine taken up by NaCl and determined by ICP MS:

$$\{CH3I\} = F.\ area\ (\sum CH_3I_{adsorbed}) \qquad \text{Equation 5.5}$$

An average conversion factor (F) of $(1.14 \pm 0.37) \times 10^{16}$ at 95% confidence level could be determined from three repetitive tests (NaCl exposed 5 hours to 1000 ppm CH_3I).

By applying equation 5.2, uptake values in the range of 10^{-11} were obtained in our conditions (23°C, low humidity conditions and CH_3I gaseous concentration range 200-1000 ppm). These values were much lower than the uptake coefficient reported previously for HOI, $HOI/IONO_2$ and ICl on halide salts (Allanic *et al.*, 1999; Mossinger *et al.*, 2001; Holmes *et al.*, 2001) and of CH_3I on soot film (Wang *et al.*, 2016). This reflects the low colliding probability of CH_3I with NaCl compared to the high affinity of CH_3I for soot particles and to the reactivity of gaseous inorganic iodinated species (HOI, $HOI/IONO_2$, ICl) with halide particles. Kinetics of CH_3I uptake being of first order relative to gas phase concentration, final uptake is thus independent of it - which is confirmed by experiments at 1000-500 and 200 ppm, featuring similar uptake coefficient.
The initial adsorption rate of CH_3I was enhanced with NaI and its uptake coefficient is increasing by ~30 in comparison to NaCl and KBr. This trends (i.e. NaCl ≈ KBr < NaI) reflects the influence of electronegativity on the CH_3I-halide salt interaction process. Interaction of methyl iodide with moist NaCl (was also investigated but did not show strong influence of water compared to low humidity conditions (Houjeij, 2021). Such observations are consistent with the low affinity/solubility of methyl iodide towards water.

5.4 Conclusion and environmental implications

Though atmospheric and severe nuclear accident CH_3I concentrations, are 10^{-5}-10^{-9} lower (Saiz-Lopez *et al.*, 2008; Lebel *et al.*, 2016; Steinhauser *et al.*, 2014; Winiarek *et al.*, 2012) than the concentrations used in this study, a very low uptake on NaCl can be expected - at least of the same order (10^{-11}). The influence of sea salt like aerosols on the behaviour of gaseous CH_3I can be considered as low impacting though showing an irreversible character for CH_3I adsorption.
Reactivity of methyl iodide was further investigated with solid surrogates of secondary inorganic aerosols (sodium bicarbonate, sodium nitrates, sodium sulphate) or organic aerosols such as carboxylic acids (citric acid, oxalic acid, tartric acid) and fatty acid (palmitic acid). The strongly absorbing capacities of those compounds in the IR range prevented the use of the DRIFTS technique so that the experiments were performed in breakthrough type reactor. Expecting a low interaction of gaseous methyl iodide, the experimental conditions were adjusted as to feature long contact time with the solid bed (1-16 s) and a low methyl iodide concentration in the carrier gas (1 -100 ppb). Whatever the experimental conditions, no uptake of methyl iodide by the studied compounds could be evidenced – indicating a low affinity for numerous class of aerosols both of inorganic and organic nature. The strong reactivity with soot particles mentioned in the literature seems to be an exception but this latter point should be confirmed. Owing to these observations, methyl iodide is expected to remain in the gaseous phase during its lifecycle in the troposphere and be mainly involved in photochemical gas phases processes as mentioned in the literature.
In order to complete the understanding of the iodine atmospheric cycle, the interaction of gaseous I_2 with atmospheric aerosols remains to be investigated. Compared to CH_3I, I_2 higher reactivity may contribute to an enhanced uptake – depending of the class of aerosols, and potentially modify its atmospheric transport. Indeed, as was shown by Figueiredo *et al.* (2020) with model SiO_2 particles, molecular iodine adsorption on aerosols particles can indirectly extend its atmospheric life-time by preventing gas phase photolysis and have direct

consequences on its atmospheric dispersion. Similarly to CH_3I, breakthrough reactor experiments and even aerosol flow tube studies have to be used to investigate I_2-aerosol interactions.

6 CONCLUSION - PERSPECTIVES

These 20 years devoted to experimental research works on FP chemistry in severe accident conditions allowed me to cover a large panel of research thematic concerning high temperature gas phase chemistry, gas/solid interaction both in nuclear context and atmospheric chemistry and to handle chemical systems rarely considered in the literature. In this view, I got the opportunity to develop and operate several experimental devices from semi integral scale (CHIP PL line) and laboratory scale (GAEC line, aerosol flow tube reactors). Addressing the numerous technical issues linked to experimental studies of complex systems was one of the main challenge of these experiments. Chemistry of FPs in SA condition is indeed supported by a narrow scientific community represented by the main TSO's of the main nuclear countries and the related research teams, so that experimental studies in such conditions needed each time a specific development and had very rarely benefited from past experiences.

Success in these studies could not be achieved without a close link with academic partners to benefit from their experience to find, adapt and apply the most relevant techniques (sometimes unexpected) capable to bring reliable responses to our issues… The community of atmospheric chemistry was also of a great help for its support to develop analytical techniques dedicated to the detection of iodine in our conditions (IBB CEAS) and for its knowledge in the thematic of gas/aerosol interactions… Finally, iterative process with the simulation laboratories of IRSN allowed experimental data interpretation, chemical mechanism understanding and validation of simulation tools (SOPHAEROS) - such work is still ongoing. These projects gave me the opportunity to supervise numerous internship from bachelor up to master degree, to co – direct several Ph-D's (one in progress) and one post-doctoral position.

The achievements of these research programmes have given rise to new questions and are extended into many experimental perspectives, which I shall detail below.

Concerning the iodine transport issues in the reactor coolant system which were raised by the Phébus integral tests, the CHIP and CHIP+ programs allowed to bring several answers. CHIP experiments confirmed that beside CsI, other iodine form (gaseous /condensed) can be transported in the RCS in severe accident conditions. The persistence of a significant gaseous iodine fraction in cold leg break conditions seems to be strongly linked to nature of gas atmosphere and the ratio of the other released elements, especially Mo/Cs ratio. Control rod elements were highlighted as playing also a role, but the main reactional path could not be completely understood (formation of other metallic iodide or competition in the formation of metallic molybdates). Efforts are now ongoing to improve modelling to be capable of reproducing the trends experimentally observed. Meanwhile, new issues have raised with the development of accident tolerant fuel (e.g. featuring extended resistance in loss of coolant accident scenario) with a significant Cr-enrichment compared to conventional fuel (Cr_2O_3 doped fuel pellets plus/or Cr coated Zircaloy or FeZrAl cladding). In SA conditions, significant Cr release may be expected with such advanced fuel concept and the formation of hexavalent forms of Cr known to be strongly oxidative cannot be excluded (for instance in high steam partial pressure and/or early air ingress scenario). Such forms may then impact Cs transport by formation of Cs-Cr_2O_3 compound and consequently iodine speciation. At the present time, effect of hexavalent Cr species on Cs transport has not been considered and its knowledge is incomplete (PIRT, 2021). In order to fill in this gap of data, it is proposed to start, in 2023, an experimental study at small scale (GAEC line) on Cr(VI) transport issues in order to define which conditions may favour a possible Cs-scavenging role for chromium.

Revaporization issues of deposits in the RCS and their contribution to late phase releases were firstly considered at a small scale with single compound deposit. The first tests with caesium iodide and silver iodide highlighted the role of the oxidative potential of the atmosphere in the release of gaseous iodine species but also the role of heterogeneous reactivity. Indeed, both reaction with oxidised stainless steel surface and heterogeneous reaction with air atmosphere resulted in CsI decomposition producing gaseous iodine species in a temperature range (from 300-500°C) far much lower than CsI vaporisation. In support to the experiments, DFT calculations confirmed the oxidative role of oxygen on CsI surface defects allowing the release of gaseous iodine species. On the contrary homogeneous gas phase oxidation of CsI is not thermodynamically favoured. Nevertheless, this first study did not allow to cover all expected late phase SA scenarios and the present experimental data set is too small to allow for a reliable modelling. In the objective of completing the knowledge on revaporisation issue,

experimental studies were resumed within the framework of the OECD ESTER program (2020-2024) with laboratory scale tests followed by semi integral tests in the CHIP PL facility. Based on the main results gained from the first studies, low temperature experiments (300-500°C) will be performed in association with various atmosphere composition (variable oxygen potential and presence of boric acid). Different deposits composition will be considered from single compounds featuring either CsI, CdI_2 and also tellurium compounds up to bi-component mix and finally complex deposits compositions (featuring both FPs and CR elements such as Mo, Cs, I, Cd, Ag and possible Te) as obtained in the CHIP PL line. In this view, the CHIP line will be implemented with additional sampling lines dedicated to monitor within the revaporisation phase either particle release in real time (particle counter) or gaseous iodine release (denudeur device coupled to gas scrubbers).

The study devoted to iodine/aerosol interactions concerned firstly methyl iodide as one the of main expected iodine species which is released in case of a severe accident. The main outcome is that interaction of methyl iodide with the surrogate of the main aerosols atmospheric classes (sea salt, secondary inorganic aerosols and secondary organic aerosols) seems to be low impacting compared to gas phase chemistry. Methyl iodide is thus expected to remain in the gaseous phase during its lifecycle in the troposphere – and be mainly involved in photochemical gas phases processes as mentioned in the literature. Further work will be devoted to molecular iodine as interactions with atmospheric particles may indirectly enhance its atmospheric lifetime and thus contribute to extend its atmospheric dispersion. The same classes of surrogates will be considered, tests will be conducted in conditions representative of atmospheric one's in terms of humidity, day/night conditions and temperature. Similarly to methyl iodide, the experiments will consider breakthrough reactor and/or aerosol flow tube – in the objective of monitoring iodine gas phase concentration. These bulk experiments will allow to get information on the global interaction and to determine the uptake coefficient. The main challenge will be to develop a technique allowing to monitor solid surface changes when exposed to molecular iodine in order to get insight of the heterogeneous interaction. The potentiality of UV Vis spectroscopy or Raman spectroscopy will be investigated for such purpose.

Finally I will be involved in a new thematic linked to post accidental management and waste water treatment. Radiocontamination of aqueous effluent is a major issue for post accidental management, as highlighted by the Fukushima Daichii Nuclear Power plant accident, but can also find a strong interest in long-term storage and decommissioning problematics. Indeed, some fission products are highly soluble in aqueous media and can thus significantly contribute to water radiocontamination in accidental situations – as the case of caesium. The aim of this project is to develop innovative MOFs (Metal Organic Framework) materials dedicated to the treatment of caesium from contaminated waters. MOF materials present numerous interesting properties which makes them suitable candidates for the development of sustainable processes: easy synthesis by green processes, very high porosity, chemical tunability, stability under severe conditions. These relative recent materials could be used to restrict radionuclides dissemination, both in the environmental field as well as for on-site treatment of highly contaminated effluents. This project involves two academic partners known for their expertise in MOFs synthesis (MATHYB team of the UCCS laboratory- Lille University) and in Cs treatment from contaminated waste waters (LNER team of the ICSM institute), it will start in 2022.

GLOSSARY

AEA-T: Atomic Energy Authority Technology (UK)
ASTEC: Accident Source Term Evaluation Code
CEA: Commissariat à l'Energie Atomique
CHIP: Chemistry Iodine Primary circuit
DRIFTS: Diffuse Reflectance Infrared Fourier Transform Infrared Spectroscopy
EPMA: Electron Probe Micro Analyses
FD NPP: Fukushima Daiichi Nuclear Power Plants
FP: Fission Product
FTIR: Fourier Transform Infrared Spectroscopy
GSM-ISM : Groupe de Spectrométrie Moléculaire – Institut des Sciences Moléculaire (Université Bordeaux)
HAXPES: Hard X ray photoelectron spectroscopy
ICP MS: Inductively Coupled Plasma – Mass Spectrometry
ICP OES: Inductively Coupled Plasma – Optical Emission Spectroscopy
IRSN: Institut de Radioprotection et de Sûreté Nucléaire
ISTP : International Source Term Program
ITU: Institut for TransUran (Karslruhe – Germany)
JAEA: Japan Atomic Energy Agency
JAERI: Japan Atomic Energy Research Institute (merged in 2005 with Japan Nuclear Cycle Development Institute to form JAEA)
LASIR : Laboratoire de Spectrochimie Infrarouge et Raman (Université de Lille)
LEIS: Low Energy Ion Scaterring
MIRE :Mitigation of outside Releases in case of nuclear accident
PC2A : laboratoire des Processus de Combustion et de Chimie Atmosphérique (Université de Lille)
PWR: pressurised Water reactor
RCS: reactor Coolant System
RMS : Raman MicroSpectromety
SA: Severe Accident
SEM-EDS: Scanning Electron Microscopy – Energy Dispersive Spectroscopy
SIMS: Secondary Ions Mass Spectrometry
STEM-STEM2 : Source Term Evaluation and Mitigation Program
TMI: Three Miles Island
TOF SIMS: Time of Flight - Secondary Ions Mass Spectrometry
UCCS : Unité de Catalyse et de Chimie du Solide (Université de Lille)
VTT: Technical Research Centre of Finland / Valtion Teknillinen Tutkimuskeskus
XRD: X-Ray Diffraction

REFERENCES

Académie des Sciences –Avis (2021). L'apport de l'énergie Nucléaire dans la transition énergétique, aujourd'hui et demain. https://www.academie-sciences.fr/pdf/rapport/20210614_avis_nucleaire.pdf

Agrawa B. S., Kirby R. D., Hardy J. R. (1975). Theoretical and experimental studies of the second-order Raman spectra of CsCl, CsBr, and CsI, Physical Review B, 11, n° 12. https://doi.org/10.1103/PhysRevB.11.5153

Ali (Basu) M, Bharadwaj S R, Das D. (2005). The standard molar enthalpy of formation of CdMoO4. Journal of Nuclear Material, 336, pp 110-112. https://doi.org/10.1016/j.jnucmat.2004.09.006

Allanic A., Oppliger R., Van den Bergh H., Rossi M.J. (2000). The Heterogeneous Kinetics of the Reactions ClONO2 + HX/ice (X = Br, I), BrONO2 + HI/ice and the Reactivity of the Interhalogens BrCl, ICl and IBr with HX/ice (X = Cl, Br, I) in the Temperature Range 180 to 205 K, Zeitschrift Fur Physikalische Chemie, 214, pp 1479–1500. https://doi.org/10.1524/zpch.2000.214.11.1479

Allanic A., Rossi M.J. (1999). Heterogeneous reactions of HOI on substrates of atmospheric importance, Journal of Geophysical Research, 104, pp 18689–18696. https://doi.org/10.1029/1999JD900285

Allen G.C. *et al.* (1987). Surface Studies of the Interaction of Cesium Hydroxide Vapor with 304 Stainless Steel, Oxidation of Metals, vol.28, issue 1-2, pp 33-59. https://link.springer.com/article/10.1007/BF00666470
Allen T. *et al.* (2010). Materials challenges for nuclear systems, Materials Today, vol 13 (12), ISSN: 13697021. https://www.osti.gov/pages/servlets/purl/1027874

Alpy N., Giordano P., Cantrel L., Kissane M. (2004). General specification for the CHIP programme. IRSN report SEMIC-2004/12, ISTP report 26.

Anderson A.B. (2000). Revaporisation Tests on Samples from Phébus Fission Products: Final report AEA-Technology, AEAT/R/NS/0124 – issue 2, restricted diffusion.

Ault A.P., Moffet R.C., Baltrusaitis J., Collins D.B., Ruppel M.J., Cuadra-Rodriguez L.A., Zhao D., Guasco T.L., Ebben C.J., Geiger F.M., Bertram T.H., Prather K.A., Grassian V.H. (2013). Size-dependent changes in sea spray aerosol composition and properties with different seawater conditions, Environmental Science and Technology, 47, pp 5603–5612. https://doi.org/10.1021/es400416g

Auvinen A., Lehtinen K.E.J., Enriquez J., Jokineimi J.K., Zilliacus R. (2000). Vaporisation rates of CsOH and CsI in conditions simulating a severe nuclear accident, Journal of Aerosol Science, 31, pp 1029–1043. https://doi.org/10.1016/S0021-8502(00)00027-6

Badawi M., Xerri B., Canneaux S., Cantrel L., Louis F.(2012). Molecular structures and thermodynamic properties of 12 gaseous cesium-containing species of nuclear safety interest: Cs_2, CsH, CsO, Cs_2O, CsX, and Cs_2X_2 (X = OH, Cl, Br, and I), Journal of Nuclear Materials 420, 1-3, 452-462. https://doi.org/10.1016/j.jnucmat.2011.10.034

Bahrini C., Grégoire A.-C., Obada D., Mun C., Fittschen C. (2018). Incoherent broad-band cavity enhanced absorption spectroscopy for sensitive and rapid molecular iodine detection in the presence of aerosols and water vapour. Optics & Laser Technology, 108, p. 466–479. https://doi.org/10.1016/j.optlastec.2018.06.050

Barger W.R. and Garrett W.D. (1976). Surface-active organic material in air over the Mediterranean and over the eastern equatorial Pacific, Journal of Geophysical Research, 81, pp 3151–3157. https://doi.org/10.1029/jc081i018p03151

Barin I. (1995). Thermochemical Data of Pure Substances (3rd Ed), VCH, Weinheim., Print ISBN:9783527287451 , Online ISBN:978352761982. https://doi.org/10.1002/9783527619825

Barone S.B., Zondlo M.A., Tolbert M.A. (1999). Investigation of the Heterogeneous Reactivity of HCl, HBr and HI on Ice Surfaces, Journal of Physical Chemistry A., 103, pp 9717–9730. https://doi.org/10.1021/jp990400c

Beahm E. C., Weber C.F., Kress T. S., Parker, G. W. (1992). Iodine Chemical Forms in LWR Severe Accidents – Final Report, NUREG/CR-5732 – ORNL/TM-11861.

Beltran A., Lourdes G. *et al.* (2014). First-principles study of pressure-induced phase transitions and electronic properties of Ag_2MoO_4. Journal of Physical Chemistry C, 118, pp 3724-3732. https://doi.org/10.1021/jp4118024

Berdonosov S. S. and Baronov S. B. (1999). Interaction of cesium Iodide with an Air Flow at High Temperatures. Radiochemistry, 41, pp 63–66.

Berdonosov S. S. and Sitova M. A. (1997). Chemical Forms of Iodine Occurring at Evaporation and Condensation of Cesium Iodide in Air. Radiochemistry, 39, pp 341–342.

Bitter M., Ball S. M., Povey I. M., Jones R. L. (2005). A broadband cavity ringdown spectrometer for in-situ measurements of atmospheric trace gases, Atmospheric Chemistry and Physics, 5, pp 2547-2560. https://doi.org/10.5194/acp-5-2547-2005

Bosland L., Cantrel L., Girault N., Clement B. (2010). Modeling of Iodine Radiochemistry in the ASTEC Severe Accident Code : Description and Application to FPT-2 PHEBUS Test, Nuclear Technology, 171, pp 99–107. https://doi.org/10.13182/NT10-A10774

Bosland L., Dickinson S., Glowa H. C., Herranz G. A., Kim L. E., Powers D. A., Salay M. and Tietze S. (2014). Iodine-paint interactions during nuclear reactor severe accidents, Annals of Nuclear Energy, 74, pp 184–199. https://doi.org/10.1016/j.anucene.2014.07.016

Botella J., Merino C., Otero O. (1998). A Comparison of the High-Temperature Oxidation of 17Cr-2Ni and 18Cr-8Ni Austenitic Stainless Steels at 973 K. Oxidation of metals, 49, pp 297-324. https://doi.org/10.1023/A:1018830424480

Bottomley PDW, Knebel K, Van Winckel S, *et al.* (2014). Revaporisation of fission product deposits in the primary circuit and its impact on accident source term, Annals of Nuclear Energy, 74, pp 208–223. https://doi.org/10.1016/j.anucene.2014.05.011

Bowsher B.R. and Dickinson, S. (1986). The interaction of caesium iodide with boric acid: vapour phase and vapour condensed phase reactions, 1986, AEE-Winfrith R-2102.

Bowsher, B.R. and Nichols, A.L. (1985). High temperature studies of simulant fission products: Part IV, Interaction of caesium iodide with boric acid over the temperature range 400 to 1000 °C, AEE-Winfrith R-1973.

Canneaux S., Xerri B., Louis F., Cantrel L. (2010). Theoretical study of the gas-phase reactions of iodine atoms ($_2P_{3/2}$) with H_2, H_2O, HI, and OH, Journal of Physical Chemistry A, 114 (34), pp 9270.-9288. https://doi.org/10.1021/jp104163t

Cantrel L., Louis F., Cousin F. (2013). Advances in mechanistic understanding of iodine behaviour in Phebus-FP tests with the help of *ab-initio* calculations, Annals of Nuclear Energy, 61, pp 170-178. https://doi.org/10.1016/j.anucene.2013.02.034

Cantrel, L. and Cousin F. (2007). First test matrix of the CHIP programme, IRSN report SEMIC-2007-076 and ISTP report 38.

Cénérino G. (2008), Accidents graves des réacteurs à eau de production d'électricité. Rapport IRSN2008-98/FR. https://www.irsn.fr/FR/Larecherche/publications-documentation/collection-ouvrages-IRSN/Documents/IRSN_reference_Accidents_Graves_REP.pdf

Chan M.N., Choi M.Y., Ng N.L., Chan C.K. (2005). Hygroscopicity of water-soluble organic compounds in atmospheric aerosols: Amino acids and biomass burning derived organic species, Environmental Science and Technology, 39, pp 1555–1562. https://doi.org/10.1021/es049584l

Chance R.J., Shaw M., Telgmann L., Baxter M., Carpenter L. J. (2009). A comparison of spectrophotometric and denuder based approaches for the determination of gaseous molecular iodine. Atmospheric Measurement Techniques Discussions, 2, pp 2191–2215. https://doi.org/10.5194/amt-3-177-2010

Chance R.J., Shaw M., Telgmann L., *et al.* (2010). A comparison of spectrophotometric and denuder based approaches for the determination of gaseous molecular iodine, Atmospheric Measurement Techniques, 3, pp 177-185. https://doi.org/10.5194/amt-3-177-2010

Chapelot P., Grégoire A-C., Grégoire G. (2004). Phébus FP, FPT4 Final report, (IRSN) - PH-PF report IP/04/553.

Chatelard P., Belon S., Bosland L., Carénini L., Coindreau O., Cousin F., Marchetto C., Nowack H., Piar B. (2016). Main modelling features of the ASTEC V2.1 major version, Annals of Nuclear Energy, 93, pp 83–93. https://doi.org/10.1016/j.anucene.2015.12.026

Chebbi M., Azambre B., Cantrel L., Koch A. (2016). A Combined DRIFTS and DR-UV-Vis Spectroscopic in Situ Study on the Trapping of CH3I by Silver-Exchanged Faujasite Zeolite, Journal of Physical Chemistry C, 120, pp 18694–18706. https://doi.org/10.1021/acs.jpcc.6b07112

Chebbi M., Azambre B., Volkringer C., Loiseau T. (2018). Dynamic sorption properties of Metal-Organic Frameworks for the capture of methyl iodide, Microporous and Mesoporous Materials, 259, pp 244–254. https://doi.org/10.1016/j.micromeso.2017.10.018

Cheynet B., Rivet A., Fisher E. (1992). COACH Version 1.0, computer aided chemistry, in THERMODATA/INPG/CNRS. Grenoble France

Chi J.W., Li W.J., Zhang D.Z., Zhang J.C., Lin Y.T., Shen X.J., Sun J.Y. (2015). Sea salt aerosols as a reactive surface for inorganic and organic acidic gases in the arctic troposphere, Atmospheric Chemistry and Physics, 15, pp 16715–16745. https://doi.org/10.5194/acpd-15-16715-2015

Cingolani A., Ferrara M., Lugar M. (1984), The Raman spectra of CdI2, Solid State Communications, 50, No. 10, 911-913.

Clément B. and Zeyen R. (2005). The Phébus Fission Product and Source Term International Programs. Proc. Int. Conf. on Nuclear Energy for New Europe, Bled, Slovenia, 5-8 September, Nuclear Society of Slovenia.

Clément B. *et al.* (2007). State of the art report on iodine chemistry, NEA/CSNI/R(2007)1.

Clément B., Zeyen R. (2013). The objectives of the Phébus experimental program and the main lessons learned. Annals of Nuclear Energy, 61, 4-10. https://doi.org/10.1016/j.anucene.2013.03.037

Colaianni M. L., Chen P. J., Gutleben H., Yates J. T. (1992). Vibrational studies of CH3I on Si(100)-(2×1): adsorption and decomposition of the methyl species, Chemical Physics. Letters, 191, pp 561–568. https://doi.org/10.1016/0009-2614(92)85589-3

Colombani J., Grégoire A.C., Morin S. (2015). Main findings of the IRSN experimental *programmes* performed on iodine chemistry in severe accident conditions", Proceedings of the International OECD-NEA/NUGENIA-SARNET Workshop on the Progress in Iodine Behaviour for NPP Accident Analysis and Management, March 30, April 1, 2015 - Marseille (France). Communication

Cordfunke E. H. P. and Konings R. J. M. (1990). Thermochemical Data for Reactor Materials and Fission Products; Elsevier: Amsterdam, 1990. ISBN 10: 0444884858 / ISBN 13: 9780444884855

Cordfunke E.H.P. and Prins G. (1985).The thermochemical properties of caesium iodide. I thermodynamic functions of solid CsI, Thermochimica Acta, 90, pp 169-176. https://doi.org/10.1016/0040-6031(85)87094-5

Cousin *et al.* (2019). Analyses of fission products behaviour and environmental releases during the Fukushima-Daiichi accident by direct and inverse approach at IRSN, In Proc. of NURETH-18 conference, Portland, OR, August 18-22, 2019.

Cousin F., Dieschbourg K., Jacq F. (2008). New capabilities of simulating fission product transport in circuits with ACTEC/SOPHAEROS V.1.3, Nuclear Engineering and Design, 238 (9), pp 2430–2438. https://doi.org/10.1016/j.nucengdes.2008.03.018

Cousin F., Kissane M.P., Girault N. (2013). Modelling of fission-product transport in the reactor coolant system. Annals of Nuclear Energy, 61, pp 135-142. https://doi.org/10.1016/j.anucene.2013.02.035

Crouch-Baker S. and Dickens P.G. (1984). Standard molar enthalpy of formation of a-MoO3- H2O by solution calorimetry, Journal of Chemical Thermodynamics, 16, pp 301-302. https://doi.org/10.1016/0021-9614(84)90093-4

Crowley J.N., Ammann M., Cox R.A., Hynes R.G., Jenkin M.E., Mellouki A., Rossi M.J., Troe J., Wallington T.J. (2010). Evaluated kinetic and photochemical data for atmospheric chemistry: Volume v - heterogeneous reactions on solid substrates, Atmospheric Chemistry and Physics, 10, pp 9059–9223. https://doi.org/10.5194/acp-10-9059-2010

Cserenyi J., Ovari L., Bansagi T., Solymosi F. (2000). Adsorption and reactions of CH3Cl on Mo2C based catalyst, Journal of Molecular Catalysis A: Chemical, 162, pp 335–352. https://doi.org/10.1016/S1381-1169(00)00301-0

De Boer R. and Cordfunke E.H.P. (1995). On the Caesium rich part of the Cs-Te phase diagram, Journal of Alloys and Compounds, 228, pp 75-78. https://inis.iaea.org/collection/NCLCollectionStore/_Public/27/010/27010183.pdf?r=1&r=1

Delaney M.J. and S. Ushioda (1976). Comparison of the Raman spectra of superionic conductors AgI and $RbAg_4I_5$, Solid State Communications, 19, pp 297—301. https://doi.org/10.1016/0038-1098(76)91336-3

Delicat Y. (2012). Experimental and kinetic study of the iodine reactivity in low pressure H2/O2/H2O/HI/Ar premixed flames, Ph-D, University of Lille (in French). https://www.irsn.fr/FR/Larecherche/Formation_recherche/Theses/Theses-soutenues/DPAM/Documents/2012-These-Delicat.pdf

Delicat Y., Gasnot L. Pauwels J.F., Grégoire A.C., Cantrel, L. (2011). Experimental and kinetic study of the iodine reactivity inlow pressure $H_2/H_2O/HI/O_2$/Ar premixed flames, Proceedings of International Conference on Advances in Nuclear Power Plants, Nice, France, May 2-5, 2011, Communication.

Després V.R., Huffman J. A., Burrows S.M., Hoose C., Safatov A.S., Buryak G., Fröhlich-Nowoisky J., Elbert W., Andreae M.O., Pöschl U., Jaenicke R. (2012). Primary biological aerosol particles in the atmosphere: A review, Tellus B: Chemical and Physical Meteorology, 64, 15598(pp 1-59). https://doi.org/10.3402/tellusb.v64i0.15598

Di Lemma F.G. *et al.* (2016). Surface analyses of caesium hydroxide chemisorbed onto type 304 stainless steel, Nuclear Engineering and Design, 305, pp 411-420. https://doi.org/10.1016/j.nucengdes.2016.06.023

Di Lemma F.G. *et al.* (2017a). Experimental investigation of the influence of Mo contained in stainless steel on Cs chemisorption behavior, Journal of Nuclear Materials, 484, pp 174-182. https://doi.org/10.1016/j.jnucmat.2016.11.031

Dickson R. and Glowa G. (2019). Tellurium behaviour in the Fukushima Dai-ichi Nuclear Power Plant accident, Journal of Environmental Radioactivity, 204, pp 49–65. https://doi.org/10.1016/j.jenvrad.2019.03.024

Dillard G., Moers. H., Klewe-Nebenius H., Kirch G., Pfennig G. And Ache H.J. (1984). The absorption of methyl iodide on uranium and uranium dioxide: surface characterisation using X-ray photoelectron spectroscopy, Surface Science, 145, pp 62-86. https://doi.org/10.1016/0039-6028(84)90766-0

Doi T., Masumoto K., Toyoda A., Tanaka A., Shibata Y., Hirose K. (2013). Anthropogenic radionuclides in the atmosphere observed at Tsukuba: characteristics of the radionuclides derived from Fukushima, Journal of Environmental Radioactivity, 122, pp 55–62. https://doi.org/10.1016/j.jenvrad.2013.02.001

Ducros, G., Malgouyres, P.P., Kissane, M., Boulaud, D., Durin, M., 2001. Fission product release under severe accidental conditions: general presentation of the program and synthesis of VERCORS 1–6 results. Nuclear Engineering and Design 208 (2), 191–203. https://doi.org/10.1016/S0029-5493(01)00376-4

https://www.rte-france.com/eco2mix :éCO_2mix. Toutes les données de l'électricité en temps réel .. (real time data, website visited the 17/09/2021)

electricityMap's. Mapping Global emission together. https://www.electricitymap.org/map (day-to-day update, website visited the 17/09/2021)

Elrick R.M. *et al.* (1984). Reaction Between Some Cesium-Iodine Compounds and the Reactor Materials 304 Stainless Steel, Inconel 600 and Silver; Volume I Cesium Hydroxide Reactions, Sandia National Laboratories, NUREG/CR-3197/1 of 3.

Elrick R.M., *et al.* (1987). Boron Carbide – Steam Reactions with Cesium hydroxide and with Cesium Iodide at 1270 K in an Inconel 600 system, NUREG CR-4963, SAN87-1491.

Elrick R.M., Sallach R.A., Ouellette A.L., and Douglas S.C. (1987). Boron carbide – steam reactions with cesium hydroxide and with cesium iodide at 1270K in an inconel 600 system. NUREG/CR-4963, SAND87-1491.

ESTER-OECD (2020). ESTER Project – OECD site https://www.oecd-nea.org/jcms/pl_46387/new-joint-project-experiments-on-source-term-for-delayed-releases-ester

Feichter J., Leisner T. (2009). Climate engineering : A critical review of approaches to modify the global energy balance, The European Physical Journal Special Topics, 176, pp 81–92. https://doi.org/10.1140/epjst/e2009-01149-8

Figueiredo AQ., Strekowski R.S., Bosland L., Durand A., Wortham H. (2020), Photolytic degradation of molecular iodine adsorbed on model SiO2 particles, Science of Total Environment, 723, 137951. https://doi.org/10.1016/j.scitotenv.2020.137951

Filipek E., Rychlowska-Himmel I. Paczesna A. (2012). Thermal stability of $In_2(MoO_4)_3$ and phase equilibria in the MoO_3-In_2O_3 system, Journal of Thermal Analysis and Calorimetry, 109, pp 711-716. https://doi.org/doi: 10.1007/s10973-012-2224-7

Finlayson-Pitts B.J. and Pitts J N. (2000). Chemistry of the Upper and Lower Atmosphere: Theory, Experiments, and Applications, Academic Press, California, ISBN: 978-0-12-257060-5. https://doi.org/10.1016/B978-0-12-257060-5.X5000-X

Fluckiger B., Thielmann A., Gutzwiller L., Rossi M.J. (1998). Real Time Kinetics and Thermochemistry of the Uptake of HCl , HBr and HI on Water Ice in the Temperature Range 190 to 210 K, Berichte der Bunsen Gesellschaft fur physikalische Chemie, 122(7), 915–928. https://doi.org/10.1002/BBPC.19981020704

Fortin C, Fèvre-Nollet V, Cousin F, *et al.* (2019). Box modelling of gas-phase atmospheric iodine chemical reactivity in case of a nuclear accident, Atmospheric Environment, 214, 116838. https://doi.org/10.1016/j.atmosenv.2019.116838

Gallais-During A., Bonnin, J., Malgouryres, P.-P., Bernard, S., Pontillon, Y., Hanus, E., Ducros, G., 2012. VERDON Laboratory: Performances of the Experimental LWR Severe Accident Device and First Results of Fission Product Release on High Burn-up UO2 fuel. In: Proceedings of the International Conference ''Nuclear Energy for New Europe 2012'', Ljubljana, Slovenia, September 5–7.

Gamsjäger E. and Wiessner M. (2018). Low temperature heat capacities and thermodynamic functions described by Debye–Einstein integrals, Monatshefte für Chemie, 149, 357–368. https://doi.org/10.1007/s00706-017-2117-3.

Gamsjäger H. and Morishita, M. (2015). Thermodynamic properties of molybdate ion: reaction cycles and experiments, Pure Applied Chemistry, 87(5), 461-476. https://doi.org/10.1515/pac-2014-1105.

Girault N. and Payot F. (2013). Insights into iodine behaviour and speciation in the Phébus primary circuit. Annals of Nuclear Energy, 61, pp 143–156. https://doi.org/10.1016/j.anucene.2013.03.038

Girault N., Bosland L., Dickinson S., Funke F., Güntay S., Herranz L.E., Powers D., (2012). LWR severe accident simulation: Iodine behaviour in FPT2 experiment and advances on containment iodine chemistry. Nuclear Engineering and Design, 243, pp 371-392. https://doi.org/10.1016/j.nucengdes.2011.11.011

Girault N., Bosland L., Dienstbier J., Dubourg R., Fiche C. (2010). LWR severe accident simulation fission product behavior in FPT2 experiment. Nuclear Technology, 169, pp 218-238. https://doi.org/10.13182/NT10-A9375

Girault N., Fiche C., Bujan A., Dienstbier J. (2009). Towards a better understanding of iodine chemistry in RCS of nuclear reactor. Nuclear Engineering and Design, 239 (6), pp 1162-1170. https://doi.org/10.1016/j.nucengdes.2009.02.008

Gonze M.A., Garcia Sanchez L., Boyer P., Mourlon C., Tamponnet C. (2002). SYMBIOSE : A Modeling Platform for Environmental Chemical Risk Assessment in Proceedings of the 3rd International Symposium on the Protection of the Environment from Ionising Radiation -22/26 July 2002 -Darwin (Australia), pp.266-277

Gouello M. (2012). Chimie de l'iode et composition des aérosols dans le circuit primaire d'un réacteur nucléaire en situation d'accident grave. Ph-D of Lille university (in french). https://tel.archives-ouvertes.fr/tel-00832204v2/document.

Gouello M., Hokkinen J., Karkela T, Auvinen A. (2018a). A scoping study of the chemical behavior of cesium iodide in the presence of boron in the condensed phase (650 -400°C) under primary circuit conditions, Nuclear Technology, 203, pp 66-84. https://doi.org/10.1080/00295450.2018.1429111

Gouello M., Kalilainen, J., Karkela T., Auvinen A. (2018b). Contribution to the understanding of iodine transport under primary circuit conditions: CsI/Cd and CsI/Ag interactions in condensed phase, *Nucl. Matt and Ener*. 17, p. 259-268. https://doi.org/10.1016/j.nme.2018.11.011

Gouello M., Hokkinen J., Karkela T. (2020). Advances in understanding of molybdenum effects on iodine and caesium reactivity in condensed phase in the primary circuit in nuclear severe accident conditions, Nuclear Engineering and Technology, 52(8), pp 1638-1649. https://doi.org/10.1016/j.net.2020.01.029

Gouello M., Hokkinen J., Suzuki E., Horiguchi N., Barrachin M., Cousin F. (2021). Interaction between caesium iodide particles and gaseous boric acid in a flowing system through a thermal gradient tube (1030 K–450 K) and analysis with ASTEC/SOPHAEROS, Progress in Nuclear Energy, 138, 103818. https://doi.org/10.1016/j.pnucene.2021.103818

Gouello M., Kalilainen, J., Karkela T., Auvinen A., (2016). Experimental study of the boron and air effects on iodine transport in the primary circuit during a severe nuclear accident, Proceeding of the International Conference on Advances in Nuclear Power Plants, San Francisco, CA April 17-20 2016.

Gouello M., Mutelle H., Cousin F., Sobanska S., Blanquet E. (2013). Analysis of the iodine gas phase produced by interaction of CsI and MoO3vapours in flowing steam, Nuclear Engineering and Design 263, 462– 472. https://doi.org/10.1016/j.anucene.2013.06.016

Grandjean A., Blanchet E., Finidori E. (2014). Etude des 4 trajectoires du DNTE. https://www.carbone4.com/wp-content/uploads/2016/08/Etude_Trajectoires_DNTE_C4.pdf

Grégoire A.C. (2021). CHIP and CHIP+ programmes, Synthesis report of the experimental work – rev1 IRSN report 2021-00211.

Grégoire A.C. and Haste T. (2013). Material release from the bundle in Phébus FP, Annals of Nuclear Energy, 61, 2013, pp 63–74. https://doi.org/10.1016/j.anucene.2013.02.037

Grégoire A.C., Assaf, E., Sobanska S. (2016). Study of the formation of aerosols of FPs (I, Cs, Mo) and control rod material (Cd) in conditions representative of the RCS during a severe accident and consequences on gaseous iodine release, European Aerosol Conference, 2016, Tours September 4-9- Oral Communication.

Grégoire A.C., Délicat Y., Tornabene C., Cousin F., Gasnot L. Lamoureux N., Cantrel L. (2017). Study of the iodine kinetics in thermal conditions of a RCS in nuclear severe accident, Annals of Nuclear Energy 101, pp 69-82. https://doi.org/10.1016/j.anucene.2016.10.013

Grégoire A.-C., Kalinainen J., Cousin F., Mutelle H., Cantrel L., Auvinen A., Haste T., Sobanska S. (2015). Studies on the role of molybdenum on iodine transport in the RCS in nuclear severe accident conditions, Annals of Nuclear Energy, 78, 117–129. https://doi.org/10.1016/j.anucene.2014.11.026

Grégoire A.C., le Fessant E., Cantrel L. (2021b). ESTER program- State of the art on revaporization from RCS surfaces – Assessment of late phase releases after nuclear power plant severe accident , IRSN report 2021-00282, ESTER report 2021-01.

Grégoire A.C., March P., Payot F., Zabiego M., De Bremaecker A., Biard B., Schlutig S., Grégoire G. (2008). Phébus FP, FPT2 Final report, (IRSN) - PH-PF report IP/08/579.

Grégoire A.C., Morin S., Cantrel L. (2018). Main outcomes of the IRSN experimental CHIP and CHIP+

programmes, in Proc. of the Conference Nuclear Energy for New Europe, 2018, Portoros 10-13 September (Slovenia).

Grégoire A.C., Mutelle H. (2012). Experimental Study of the [B, Cs, I, O, H] and [MO, Cs, I, O, H] Systems in the Primary Circuit of a PWR in Conditions Representative of a Severe Accident. in Proc. Of Conference Nuclear Energy for New Europe, Ljubljana 5-7 September (Slovenia).

Grégoire A.C., Sobanska, S., Tornabene C., Talage D., Mamede A.S., Morin S., Cantrel L. (2021). Influence of SIC control rod material on iodine release in nuclear severe accident – Chemical reactivity in thermal conditions of RCS (Revised paper submitted Nov 2021 to Annals of Nuclear Energy).

Gu M., Liu X., Yang L., Sun S., Zhang J. (2019). Dynamics of Cl-(H_2O) + CH_3I Substitution Reaction: The Influences of Solvent and Nucleophile, Journal of Physical Chemistry A., 123 (11), pp 2203-2210. https://doi.org/10.1021/acs.jpca.9b00348

Guillaumont R., Demailly J.P., Duplessy, J.-C., Candel S., Fontecave M. (2021). Considérations sur les systems électrogènes et le systèmpe électronucléaire, Rapport de l'Académie des Sciences, Comité prospective en énergie. https://www.academie-sciences.fr/pdf/rapport/210614_rapport_nucleaire.pdf

Gurvich L.V., Veyts I.V., Alcock C.B. (1991). Thermodynamic Properties of Individual Substances - 4th edition. ISBN : 0-89116-533-9

Hammaecher C., Canneaux S., Louis F., Cantrel L. (2011). A Theoretical Study of the H-Abstraction Reactions from HOI by Moist Air Radiolytic Products (H, OH, and O (^3P)) and Iodine Atoms ($^2P_{3/2}$), Journal of Physical Chemistry A, 115(24), pp 6664-6674. https://doi.org/10.1021/jp202760u

Hanniet-Girault N., Repetto G. (1999). Phébus FP, FPT0 Final report, (IRSN) - PH-PF report IP/99/423.

Hashimoto, K. *et al.* (1996). Enhancement of CsI Aerosol Size in Superheated steam in reactor Piping under Severe Accidents, Journal of Nuclear Science and Technology, 33, pp 1047-1053. https://doi.org/10.1080/18811248.1996.9732006

Haste T., Barrachin M., Clément B., Grégoire A.-C., Girault N., Laurie M., de Luze O., March P., Payot F., Repetto G., Simondi-Teisseire B. (2012). Synthesis of the Phébus FP programme experimental results IRSN report PSN-RES/SAG/2012-00018

Haste T., Payot F., Bottomley P.D.W. (2013). Transport and deposition in the Phébus FP circuit, Annals of Nuclear Energy, 61, 102-121. https://doi.org/10.1016/j.anucene.2012.10.032

Haste T., Payot F., Dominguez C., March P., Simondi Teisseire B., Steinbrück M. (2012). Study of boron behaviour in the primary circuit of water reactor under severe accident conditions: a comparison of Phébus FPT3 results with other recent and separate effects data, Nuclear Engineering and Design, 246, pp 147-156. https://doi.org/10.1016/j.nucengdes.2011.08.031

Henderson M. A., Mitchell, J. M. White (1987). The chemisorption of methyl halides (Cl, Br and I) on Pt(111), Surface Science Letters, 184, pp 325–331. https://doi.org/10.1016/0167-2584(87)90754-7

Hidaka A. *et al.* (1995). Experimental and Analytical Study of the Behavior of Caesium Iodide Aerosol/Vapor Deposition onto Inner Surface of Pipe Wall under Severe Accident Conditions, Journal of Nuclear Science and Technology, 32, pp 1047-1053. https://doi.org/10.1080/18811248.1995.9731813

Hidy G.M., Mohnen V., Blanchard C.L. (2013). Tropospheric aerosols: Size-differentiated chemistry and large-scale spatial distributions, Journal of the Air & Waste Managment Association, 63, pp 377–404. https://doi.org/10.1080/10962247.2012.760499

Hijazi, Réactivité chimique des aérosols d'iode en conditions accidentelles dans un réacteur nucléaire, Ph-D of Lille university (in french). https://pepite-depot.univ-lille.fr/LIBRE/EDSMRE/2017/50376-2017-Hijazi.pdf

Hirschfelder J.O., Curtiss C.F., Campbell D.E (1953). The theory of flames and combustion. Symposium (International) on combustion, volume 4, Issue 190-211.

Hoekstra H.R. (1973). The Cs_2MoO_4-MoO_3 system, Inorganic and Nuclear Chemistry Letters, 9, 1291-1301. https://doi.org/10.1016/0020-1650(73)80013-3

Houjeij H. (2020). Etude expérimentale des reactions de capture/désorption des iodes gazeux (I2, CH3I) sur des aérosols environnementaux, Ph-D, University of Bordeaux (in French). https://hal-lirmm.ccsd.cnrs.fr/UNIV-BORDEAUX/tel-03331636v1

Houjeij H., Grégoire A.-C., Le Bourdon G., Sobanska S., Cantrel L. (2021). Interaction process between gaseous CH_3I and NaCl particles : implication for iodine dispersion in the atmosphere , Environnmental science : Processese and Impacts, 2021, 23, 1771-1781. https://doi.org/10.1039/d1em00266j

Huang R.J. and Hoffmann T. (2009). Development of a coupled diffusion denuder system combined with GC – MS for the separation and quantification of molecular iodine and the activated iodine compounds iodine monochloride and hypoiodous acid in the marine atmosphere, Anal. Chem , 81 , pp 1777-1783. https://doi.org/10.1021/ac801839v

Huang R.–J., Seitz K., Buxmann J. *et al.*(2010). In situ measurements of molecular iodine in the marine boundary layer: the link to macroalgae and the implications for O_3, IO, OIO and NO_x, Atmospheric Chemistry and Physics, 10, pp 4823-4833. https://doi.org/10.5194/acp-10-4823-2010

Imanaka T., Hayashi G. and Endo S. (2015). Comparison of the accident process , radioactivity release and ground contamination between Chernobyl and Fukushima-1, Journal of Radiation Research, 56, pp 56–61. https://doi.org/10.1093/jrr/rrv074

IPCC, 2021: Summary for Policymakers. In: Climate Change 2021: The Physical Science Basis. Contribution of Working Group I to the Sixth Assessment Report of the Intergovernmental Panel on Climate Change [Masson-Delmotte, V., P. Zhai, A. Pirani, S.L. Connors, C. Péan, S. Berger, N. Caud, Y. Chen, L. Goldfarb, M.I. Gomis, M. Huang, K. Leitzell, E. Lonnoy, J.B.R. Matthews, T.K. Maycock, T. Waterfield, O. Yelekçi, R. Yu, and B. Zhou (eds.)]. Cambridge University Press. https://www.ipcc.ch/report/ar6/wg1/downloads/report/IPCC_AR6_WGI_SPM.pdf

IRSN website (2013). Coût économique des accidents nucléaires entraînant des rejets radioactifs dans l'environnement https://www.irsn.fr/FR/connaissances/Installations_nucleaires/Les-accidents-nucleaires/cout-economique-accident/Pages/sommaire.aspx#.YTd6EBlxeUk (Last update 2013)

IRSN website (2019). Accident de Three Mile Island (USA) – 1979. https://www.irsn.fr/FR/connaissances/Installations_nucleaires/Les-accidents-nucleaires/three-mile-island-1979/Pages/sommaire.aspx#.YTd6oRlxeUk (Last update : March 2019)

IRSN website (2021a). Accident à la centrale de Fukushima Daiichi (Japon). https://www.irsn.fr/FR/connaissances/Installations_nucleaires/Les-accidents-nucleaires/accident-fukushima-2011/Pages/sommaire.aspx.(Last update : 2021)

IRSN website (2021b). Les leçons de Tchernobyl. https://www.irsn.fr/FR/connaissances/Installations_nucleaires/Les-accidents-nucleaires/accident-tchernobyl-1986/Pages/Tchernobyl.aspx .(Last update : 2021)

Jacquemain D (Coord), 2015. Nuclear Power Reactor Core Melt accident, current state of knowledge, edp science isbn : 978-2-7598-1835-8. https://www.edp-open.org/images/stories/books/fulldl/Nuclear_Power_Reactor_Core_Melt_Accidents.pdf

Jacquemain D., Bourdon S., De Bremaecker A., Barrachin M., (2000). Phébus FP- FPT1 Final report, (IPSN) - PH-PF report IP/00/479.

Jenks C. J., Bent B. E., Bernstein N., Zaera F. (2000). The Chemistry of Alkyl Iodides on Copper Surfaces, Journal of Physical Chemistry B, 104, pp 3008–3016. https://doi.org/10.1021/jp993021s

Jimenez J.L., Canagaratna M.R., Donahue N.M., Prevot A.S.H., Zhang Q. *et al.* (2009). Evolution of Organic Aerosols in the Atmosphere, Science, 326, pp 1525–1530. https://doi.org/10.1126/science.1180353

Johansson O., Mutelle H., Parker A.E. *et al.* (2014) Quantitative IBBCEAS measurements of I_2 in the presence of Aerosols, Applied Physics B 114, pp 421–432. https://doi.org/10.1007/s00340-013-5536-9

Kalilainen J. *et al.* (2014). Chemical reactions of fission product deposits and iodine transport in primary circuit conditions, Nuclear Engineering and Design, 267, pp 140–147. https://doi.org/10.1016/j.nucengdes.2013.11.078

Karagulian F., Belis C.A., Francisco C., Dora C., Prüss-Ustün A.M., Bonjour S., Adair-Rohani H., Amann M. (2015). Contributions to cities' ambient particulate matter (PM): A systematic review of local source contributions at global level, Atmospheric Environment, 120, pp 475–483. https://doi.org/10.1016/j.atmosenv.2015.08.087

Katata G. *et al.* (2015). Detailed source term estimation of the atmospheric release for the Fukushima Daiichi Nuclear Power Station accident by coupling simulations of an atmospheric dispersion model with an improved deposition scheme and oceanic dispersion model, Atmospheric Chemistry and Physics, 15, pp 1029–1070. https://doi.org/10.5194/acp-15-1029-2015

Kaye, M.H., Kissane, M.P., Mason, P.K. (2010). Progress in chemistry modelling for vapour and aerosol transport analyses. International Journal of Materials, Research 101, p 12. https://doi.org/10.3139/146.110440

Kireev S. V, Shnyrev S. L. (2017). Laser-induced fluorescence method of molecular iodine detection in the atmosphere in real time using copper-vapor laser at the wavelength of 510.6 nm, Laser Physics Letter, 14(6), 065701. https://doi.org/10.1088/1612-202X/aa6c7f

Kissane M.P., Drosik I. (2006). Interpretation of fission-product transport behaviour in the Phébus FPT0 and FPT1 tests, Nuclear Engineering and Design, 236, pp 1210–1223. https://doi.org/10.1016/j.nucengdes.2005.10.012

Kitanovski Z., Grgić I., Veber M. (2011). Characterization of carboxylic acids in atmospheric aerosols using hydrophilic interaction liquid chromatography tandem mass spectrometry, Journal of Chromatography A, 1218, pp 4417–4425. https://doi.org/10.1016/j.chroma.2011.05.020

Klivényi G. and Solymosi F. (1995). Generation of CH_2 species: thermal and photo-induced dissociation of CH_2I_2 on Rh(111) surface, Surface Science, 342, pp 168–184. https://doi.org/10.1016/0039-6028(95)00767-9

Knebel K. *et al.* (2014). An experimental device to study the revaporisation behaviour of fission product deposits under severe accident conditions, Progress in Nuclear Energy, 72, pp 77–82. https://doi.org/10.1016/j.pnucene.2013.07.022

Kolb C.E., Cox R.A., Abbatt J.P.D., Ammann M., Davis E.J., Donaldson D.J., Garrett B.C., George C., P.T. Griffiths, Hanson D.R., Kulmala M., McFiggans G., Pöschl U., Riipinen I., Rossi M.J., Rudich Y., Wagner P.E., Winkler P.M., Worsnop D.R., O'Dowd C.D. (2010). An overview of current issues in the uptake of atmospheric trace gases by aerosols and clouds, Atmospheric Chemistry and Physics, 10, pp 10561–10605. https://doi.org/10.5194/acp-10-10561-2010

Kolb C.E., Worsnop D.R., Zahniser M.S., Davidovits P., Keyser L.F., Leu M.T., Molina M.J., Hanson D.R., Ravishankara A.R., Williams L.R., Tolbert M.A. (1995). Laboratory studies of atmospheric heterogeneous chemistry, Advanced Series in Physical Chemistry, 3, pp 771–875. https://doi.org/10.1142/9789812831712_0018

Konings R.J.M, Cordfunke E.H.P., Ouweltjes W. (1991). The standard molar enthalpies of formation of CdI2(s) and Cs2Cd2I4(s), .Journal of Chemical Thermodynamics, 25, pp 271-276. https://doi.org/10.1006/jcht.1993.1026

Krejci R., Ström J., de Reus M., Williams J., Fischer H., Andreae M.O., Hansson H.-C. (2005). Spatial and temporal distribution of atmospheric aerosols in the lowermost troposphere over the Amazonian tropical rainforest, Atmospheric Chemistry and Physics Discussions, 5, pp 1527–1543. https://doi.org/10.5194/acpd-4-3565-2004

Kulyukhin S.A.*et al.* (2004). Oxidative Hydrolysis in Water Vapor-Air Phase of CsI Radioaerosols Produced by CsI Sublimation from Metallic Surface. Radiochemistry, 46, pp 63–66. https://doi.org/10.1023/B:RACH.0000024639.33411.68

Lacoué-Nègre M. (2010). Iodine chemistry in the reactor coolant system of a nuclear power plant in case of a severe accident – study of CsI/MoO3 mixture under steam, Ph-D, university USTL, Lille (in French). https://www.irsn.fr/FR/Larecherche/Formation_recherche/Theses/Theses-soutenues/DPAM/Documents/2010-these-lacoue-negre.pdf

Laj P., Klausen J., Bilde M., Plaß-Duelmer C. *et al.* (2009). Measuring atmospheric composition change, Atmospheric Environment, 43, pp 5351–5414. https://doi.org/10.1016/j.atmosenv.2009.08.020

Laj P., Sellegri K. (2003). Les aérosols atmosphériques: Impacts locaux, effets globaux, Revue Française des Laboratoires, 349, pp 23–34.

Law K., Struges W. (2007). Halogenated short-lived substances in: scientific assessment of ozone depletion, chapter 2, Report No. 50. https://csl.noaa.gov/assessments/ozone/2006/chapters/contentsprefaceexecutivesummary.pdf

Lawler M. J., Mahajan A. S., Saiz-Lopez A., Saltzman E. S. (2014). Observations of I_2 at a remote marine site, Atmospheric Chemistry and Physics, 14, pp 2669-2678. https://doi.org/10.5194/acp-14-2669-2014

Le Gros G. (2016). La naissance du parc nucléaire français : le plan Messmer. https://www.sfen.org/rgn/naissance-parc-nucleaire-francais-plan-messmer

Le Marois G. and Megnin M. (1994). Assessment of fission product deposits in the reactor coolant system: the DEVAP program, Nuclear safety, 35(2), pp 213-222.

Lebel L.S., Dickson R. S., Glowa G. A. (2016). Radioiodine in the atmosphere after the Fukushima Dai-ichi nuclear accident, Journal of Environmental Radioactivity, 2016, 151, pp 82–93. https://doi.org/10.1016/j.jenvrad.2015.06.001

Lei Y., Zhang Q., He K.B., Streets D.G. (2011). Primary anthropogenic aerosol emission trends for China, 1990-2005, Atmospheric Chemistry and Physics, 11, pp 931–954. https://doi.org/10.5194/acp-11-931-2011

Leigh R. J., Ball S. M., Whitehead J. *et al.* (2010). Measurements and modelling of molecular iodine emissions, transport and photo destruction in the coastal region around Roscoff, Atmospheric Chemistry and Physics, 10, pp 11823-11838. https://doi.org/10.5194/acp-10-11823-2010

Leroy O., Monstanglant-Louvet C. (2019). Trapping measurements of volatile iodine by sand bed and metallic filters, Journal of Radioanalytical and Nuclear Chemistry, Open Access, 322(2), pp 913 – 9221. https://doi.org/10.1007/s10967-019-06786-1

Liang C., Duan F., He K., Ma Y. (2016). Review on recent progress in observations, source identifications and countermeasures of PM2.5, Environment International, 86, pp 150–170. https://doi.org/10.1016/j.envint.2015.10.016

Lin J. and Bent B. E. (1992). Iodomethane dissociation on Cu(111): Bonding and chemistry of adsorbed methyl groups, Jounral of Vacuum Science and Technology A, 10, pp 2202–2209. https://doi.org/10.1116/1.578005

Lin Q., Liu X., Jin Z. *et al.* (1996). Buffer gas effect on the detection of iodine by laser induced fluorescence, Journal of Radioanalytical and Nuclear Chemistry, Letters, 212, pp 313-320. https://link.springer.com/content/pdf/10.1007%2FBF02162524.pdf

Lopatin S.I., Panin A.I. ., Shugurov S.M (2013). Stability and structures of gaseous In2MoO4, In2WO4 and In2W2O7, Dalton Transactions, 42, pp 8339–8346. https://doi.org/10.1039/c3dt32719a

Lovrić J., Duflot D., Monnerville M., Toubin C., Briquez S. (2016). Water-Induced Organization of Palmitic Acid at the Surface of a Model Sea Salt Particle: A Molecular Dynamics Study, J. Phys. Chem. A., 120, pp 10141–10149. https://doi.org/10.1021/acs.jpca.6b07792

Maczka M. (1997). Vibrational Characteristics of the alkali metal-indium double molybdate M-In(MoO4)2 and tungstate M-In(WO4)2 (M=Li, Na, K, Cs), Journal of Solid State Chemistry, 129, pp 287-297. https://doi.org/10.1006/jssc.1996.7248

Makino T., Zulaehah S., Gueriba J. S., Diño W. A., M. Okada (2018). CH3Cl/Cu(410): Interaction and Adsorption Geometry, Journal of Physical Chemistry C, 122, pp 11825–11831. https://doi.org/10.1021/acs.jpcc.8b01296

Mamede A.S., Nuns N., Cristol A.L. *et al.* (2016). Multitechnique characterisation of 304L surface states oxidized at high temperature in steam and air atmospheres, Applied Surface Science, 369, pp 510-519. https://doi.org/10.1016/j.apsusc.2016.01.185

March P. and Simondi-Teisseire B. (2013). Overview of the facility and experiments performed in the Phébus FP. Annals of Nuclear Energy, 61, pp 11-22. https://doi.org/10.1016/j.anucene.2013.03.040

Maruyama Y. *et al.* (1999). Vapor Condensation and Thermophoretic Aerosol Deposition of Cesium Iodide in Horizontal Thermal Gradient Pipes, Journal of Nuclear Science and Technology, 36, pp 433-442. https://doi.org/10.1080/18811248.1999.9726226

Masson O. *et al.* (2011). Tracking of airborne radionuclides from the damaged Fukushima Daiichi nuclear reactors by European networks, Environmental Science and Technology, 45, pp 7670–7677. https://doi.org/10.1021/es2017158

McFarlane J., Leblanc, J.L. (1996). Fission product Tellurium and Cesium telluride. Chemistry revisited. AECL report 11333 COG 95-L76-I (nov 96).

McFarlane J., Wren J.-C., Lemire R.J. (2002). Chemical speciation of iodine source term to containment. Nuclear Technology, 138, pp 162-178. https://doi.org/10.13182/NT138-162

Mishra R., Bharadwaj S. R., Das D. (2006). Determination of thermodynamic stability of CdMoO4 by Knudsen effusion vapor pressure measurement method. Journal of Thermal Analysis and Calorimetry, 86, pp 547–552. https://doi.org/10.1007/s10973-005-7285-4

Miwa S, Yamashita S., Osaka M. (2016) Prediction of the effects of boron release kinetics on the vapor species of cesium and iodine fission products, Progress in Nuclear Energy, 92, pp 254-259. https://doi.org/10.1016/j.pnucene.2016.02.023

Miwa S., Nakajima K., Nishioka S., Suzuki E., Horiguchi N., Lui J., Miradji F., Imoto J., Mohamad A., Takase G., Karasawa H., Osaka M. (2020b). Development of fission product chemistry database ECUME for LWR severe accident, Mechanical Engineering Journal, 7(3), pp 1-10. https://doi.org/10.1299/mej.19-00537

Miwa S., Takase G., Imoto J., Nishioka S., Miyahara N., Osaka M. (2020a). Boron chemistry during transportation in the high temperature region of a boiling water reactor under severe accident conditions, Journal of Nuclear Science and Technology, 57(3), pp 291-300. https://doi.org/10.1080/00223232.2019.1671913

Miyahara N., Miwa S., Horiguchi N., Sato I., Osaka M. (2019). Chemical reaction kinetics dataset of Cs-I-B-Mo-O-H system for evaluation of fission product chemistry under LWR severe accident conditions, Journal of Nuclear Science and Technology, 56(2), pp 228-240. https://doi.org/10.1080/00223232.2018.1544939

Mohiuddin K., Strezov V., Nelson P.F., Stelcer E., Evans T. (2014). Mass and elemental distributions of atmospheric particles nearby blast furnace and electric arc furnace operated industrial areas in Australia, Science of the Total Environment, 487, pp 323–334. https://doi.org/10.1016/j.scitotenv.2014.04.025

Monks P.S., Granier C., Fuzzi S. *et al.* (2009). Atmospheric composition change - global and regional air quality, Atmospheric Environment, 43, pp 5268–5350. https://doi.org/10.1016/j.atmosenv.2009.08.021

Mossinger J.C., Cox R.A. (2001). Heterogeneous Reaction of HOI with Sodium Halide Salts, Physical Chemistry Chemical Physics, 105, pp 5165–5177. https://doi.org/10.1021/jp0044678

O'Dowd C.D., Facchini M.C., Cavalli F., Ceburnis D., Mircea M., Decesari S., Fuzzi S., Young J.Y., Putaud J.P. (2004). Biogenically driven organic contribution to marine aerosol, Nature, 431, pp 676–680. https://doi.org/10.1038/nature02959

Obada D. (2017). phD Evaluation de rejets à moyen terme en situation accidentelle grave d'un réacteur à eau pressurise: étude expérimentale de la re-vaporisation de dépôts de produits de fission (Cs, I) – Université de Lille, https://ori-nuxeo.univ-lille1.fr/nuxeo/site/esupversions/862a7a89-8097-4d76-8c01-3ce976c853c8.

Obada D., Gasnot L., Mamede A.-S., Grégoire A.C. (2017). Assessment of medium-term radioactive releases in case of a severe nuclear accident on a Pressurized Water Reactor: experimental study of fission products re-vaporisation from deposits (Cs, I) in Proc. of International Congress on Advances in Nuclear Power Plants, April 24-28, 2017 - Fukui and Kyoto (Japan) – paper 17328

Obada D., Hijazi H, Paul J.F., Gasnot L. Grégoire A.C., Mamede A.-S., Cantrel L. (2020). Chemical stability of caesium iodide deposits in air/steam atmosphere, Journal of Hazardous Material, 409, 124519. https://doi.org/10.1016/j.jhazmat.2020.124519

Obada D., Mamede S., Nuns N., Grégoire A.-C., Gasnot L. (2018). Combined TOF-SIMS and XPS characterization of 304L surface after interaction with caesium iodide under PWR severe accident conditions, Applied Surface Science 459, pp 23–31; https://doi.org/10.1016/j.apsusc.2018.07.212

Okane T. Kobata M., Sato I, Kobayashi K., Osaka M.,Yamagami H. (2016). Hard X-ray photoelectron spectroscopy study for transport behavior of CsI in heating test simulating a BWR severe accident condition: Chemical effects of boron vapors, Nuclear Engineering and Design, 297, pp 251-256. https://doi.org/10.1016/j.nucengdes.2015.10.029

Ozkan U.S., Gill R.C., Smith M.R. (1990).Synergy in CdMoO4/MoO3 catalysts in partial oxidation reactions of C4 hydrocarbons, Applied Catalysis, 62, pp 105-117. https://doi.org/10.1016/S0166-9834(00)82240-X

Payot F., Haste T., Biard B., Bot Robin F., Devoy J., Garnier Y., Guillot J., Manenc C., March P. (2010). Phébus FP – FPT3 Final Report(IRSN) PH-PF report IP/10/587.

Pellerin G., Maro D., Damay P., Gehin E., Connan O., Laguionie P., Hébert D. (2017). Aerosol particle dry deposition velocity above natural surfaces : Quantification according to the particles diameter, Journal of Aerosol Science, 114, pp 107–117. https://doi.org/10.1016/j.jaerosci.2017.09.004

Percival C.J., Mo J.C., Cox R.A. (1999). The uptake of HI and HBr on ice, Physical Chemistry Chemical Physics, 1, pp 4565–4570. https://doi.org/10.1039/A904651H

Phuruangrat A., Ekthammathat, E., ThongtemT., Thongtem S.(2011). Microwave-assisted synthesis and optical property of CdMoO4 nanoparticles, Journal of Physics and Chemistry of Solids,72 (3), pp 176–180. https://doi.org/10.1016/j.pcs.2010.12.003

Platt U. and Stutz J. (2008). Differential Optical Absorption Spectroscopy, Principles and applications, book, Editor Springer, ISBN 978-3-540-21193-8, eISBN : 978-3-540-75776-4.

Pontillon Y. and Ducros G (2010). Behaviour of fission products under severe PWR accident conditions The VERCORS experimental programme—Part 2: Release and transport of fission gases and volatile fission products, Nuclear Engineering and Design, 240 (2010), pp 1853–1866, https://doi.org/10.1016/j.nucengdes.2009.06.024

Pöschl U. (2005). Atmospheric aerosols: Composition, transformation, climate and health effects, Angewandte Chemie - International Edition, 44, pp 7520–7540. https://doi.org/10.1002/anie.200501122

Pöschl U., Rudich Y., Ammann M. (2007). Kinetic model framework for aerosol and cloud surface chemistry and gas-particle interactions: Part 1: general equations, parameters, and terminology, Atmospheric Chemistry and Physics Discussion, 7, pp 5989–6023. https://doi.org/10.5194/acpd-5-2111-2005

Powers D.A. (2000). Technical Issues Associated with Air Ingression During Core Degradation, http://www.iaea.org/inis/collection/NCLCollectionStore/_Public/32/016/32016788.pdf?r=1

Putaud P., Van Dingenen R., Alastuey A., *et al.* (2010). A European aerosol phenomenology - 3: Physical and chemical characteristics of particulate matter from 60 rural, urban, and kerbside sites across Europe, Atmospheric Environment, 44, pp 1308–1320. https://doi.org/10.1016/j.atmosenv.2009.12.011

Raes F., Dingenen R. Van, Elisabetta V., Wilson J., Putaud J.P., Seinfeld J.H., Adams P. (2002). Formation and cycling of aerosols in the global troposphere, Developments in Environmental Science, 1, pp 519-563 (First published in Atmospheric Environment 34 (2000) 4215-4240). https://doi.org/10.1016/S1474-8177(02)80021-3

Riggs C.A., Tompson R.V., Ghosh T.K. *et al.* (2007). Water Adsorption Isotherms for Charged and Uncharged Cesium Iodide Aerosol Particles, Nuclear Technology, 157, pp 74–86. https://doi.org/10.13182/NT07-A3803

Rizaal M., Miwa S., Suzuki E., Imoto J., Osaka M., Gouello M. (2021). Revaporization behavior of cesium and iodine compounds from their deposits in the steam- boron atmosphere, Omega. https://doi.org/10.1021/acsomega.1c04441

Roki F.Z. (2009). Kinetic and thermodynamic studies of reactive systems (X_I_O_H) by high temperature mass spectrometry, Ph-D, University J. Fourier, Grenoble (in French). https://tel.archives-ouvertes.fr/tel-00367690/document

Roki F.Z., Chatillon C, Ohnet M.N., Jacquemain D. (2008). Thermodynamic study of the CsOH(s,l) vaporization by high temperature mass spectrometry, The Journal of Chemical Thermodynamics, 40, pp 401-416. https://doi.org/10.1016/j.jct.2007.09.013

Roki F.Z., Ohnet M.N, Simondi-Teisseire B. (2008). Thermodynamic and Kinetic Studies of Iodine and Caesium Transport in Nuclear Severe Accident by High Temperature Mass Spectrometer, in Proc. Of Conference Nuclear Energy for New Europe, 2008, Portoroz 8-11 September (Slovenia). Oral Communication.

Roki F.Z., Ohnet M.N., Fillet S., Chatillon C., Nuta I. (2013). Knudsen cell mass spectrometric study of the $Cs_2IOH(g)$ molecule thermodynamics, The Journal of Chemical Thermodynamics, 65, pp 247–264. https://doi.org/10.1016/j.jct.2013.05.032

Roki F.Z., Ohnet M.N., Fillet S., Chatillon C., Nuta I. (2015). Improvements in the assessment of the thermodynamic properties of condensed and gaseous phases of the CsOH compound, The Journal of Chemical Thermodynamics , 80, pp 147–160. https://doi.org/10.1016/j.jct.2014.08.021

Roki F.-Z., Ohnet M-N.. Fillet S., Chatillon C., Nuta I. (2014). Critical assessment of thermodynamic properties of CsI solid, liquid and gas phases, The Journal of Chemical Thermodynamics, 70, pp 46-72. https://doi.org/10.1016/j.jct.2013.09.038

RTE (2021). Futurs énergétiques 2050, Principaux résultats. https://assets.rte-france.com/prod/public/2021-10/Futurs-Energetiques-2050-principaux-resultats_0.pdf

Russell L.M., Hawkins L.N., Frossard A. A., Quinn P.K., Bates T.S. (2010). Carbohydrate-like composition of submicron atmospheric particles and their production from ocean bubble bursting, Proceeding of the National Academy of Science of the United State of America, 107, pp 6652–6657. https://doi.org/10.1073/pnas.0908905107

Saab M., Souvi S (2018). Quantum Modelling of AgHMoO4, $CsHMoO_4$ and $AgCsMoO_4$ Chemistry in the Field of Nuclear Power Plant Safety, International Journal of Chemical and Molecular Engineering 12(5), 244-248. https://doi.org/10.5281/zenodo.1317244

Saiz-Lopez A., Plane J. M. C., Baker A. R., Carpenter L. J., R. Von Glasow, C. G. Juan, G. Mcfiggans and R. W. Saunders (2012). Atmospheric Chemistry of Iodine, Chemical Reviews, 112, pp 1773–1804. https://doi.org/10.1021/cr200029u

Saiz-Lopez A., Plane J.M.C., Mahajan A.S., Anderson P.S., Jones A.E., Roscoe H.K., Salmon R.A., Bloss W.J., Lee J.D. (2008). On the vertical distribution of boundary layer halogens over coastal Antarctica : implications for O3, HOx, NOx and the Hg lifetime, Atmospheric Chemistry and Physics, 8, pp 887–900. https://doi.org/10.5194/acp-8-887-2008

Saiz-Lopez A., Saunders R.W., Joseph D.M., Ashworth S.H., Plane J.M.C. (2004). Absolute absorption cross-section and photolysis rate of I_2, Atmospheric Chemistry and Physics, 4, pp 1443-1450. https://doi.org/10.5194/acp-4-1443-2004

Saiz-Lopez A., Shillito J. A., Coe H., Plane J. M. C. (2006). Measurements and modelling of I_2, IO, OIO, BrO and NO_3 in the mid-latitude marine boundary layer, Atmospheric Chemistry and Physics, 6, pp 1513-1528. https://doi.org/10.5194/acp-6-1513-2006

Sakamoto Y., Yabushita A., Kawasaki M., Enami S. (2009). Direct Emission of I_2 Molecule and IO Radical from the Heterogeneous Reactions of Gaseous Ozone with Aqueous Potassium Iodide Solution, Journal of Physical Chemistry A, 113, pp 7707-7713. https://doi.org/10.1021/jp903486u

Sallach R.A. *et al.* (1986). Reaction between Some Cesium-Iodine Compounds and the Reactor Materials 304 Stainless Steel, Inconel 600 and Silver; Volume II: Cesium Iodide Reactions, Sandia National Laboratories, NUREG/CR-3197/2 of 3.

Sasaki K. *et al.* (2013). Microstructure Analysis for Chemical Interaction between Cesium and SUS316 Steel in Fast Breeder Reactor Application, Journal of Energy and Power Engineering, 7, pp 716-725.

Sato I., Onishi T., Tanaka K., Iwasaki M., Koyama S. (2015). Influence of boron vapor on transport behavior of deposited CsI during heating test simulating a BWR accident condition, Journal of Nuclear Material, 461, pp 22-28. https://doi.org/10.1016.jnucmat.2015.02.032

Saunier O., Korsakissok I., Didier D., Doursout T., Mathieu A. (2020). Real-time use of inverse modeling techniques to assess the atmospheric accidental release from a nuclear power plant, Radioprotection, 55, pp 107–115. https://doi.org/10.1051/radiopro/2020044

Scheer K. C., Kis A., Kiss J., White J. M.(2002). Adsorption and reactions of CH_2I_2 on clean and oxygen-modified Ag (111): a RAIRS and TPD study, Topics in Catalysis, 2(20), pp 43–51. https://doi.org/10.1023/A:1016395214602

Schiffer J.M., Mael L.E., Prather K.A., Amaro R.E., Grassian V.H. (2018). Sea Spray Aerosol: Where Marine Biology Meets Atmospheric Chemistry, ACS Central Science, 4, pp 1617–1623. https://doi.org/10.1021/acscentsci.8b00674

Schlömer S., Bruckner T., Fulton L., Hertwich E., McKinnon A., Perczyk D., Roy J., Schaeffer R., Sims R., Smith P. andWiser R. (2014). Annex III: Technology-specific cost and performance parameters. In: Climate Change 2014: Mitigation of Climate Change. Contribution of Working Group III to the Fifth Assessment Report of the Intergovernmental Panel on Climate Change [Edenhofer, O., R. Pichs-Madruga, Y. Sokona, E. Farahani, S. Kadner, K. Seyboth, A. Adler, I. Baum, S. Brunner, P. Eickemeier, B. Kriemann, J. Savolainen, S. Schlömer, C. von Stechow, T. Zwickel and J.C. Minx (eds.)]. Cambridge University Press, Cambridge, United Kingdom and New York, NY, USA. https://www.ipcc.ch/site/assets/uploads/2018/02/ipcc_wg3_ar5_annex-iii.pdf

Schwarz, M., Hache, G., Van der Hardt, P. (1999). Phébus FP: A severe accident research program for current and advanced light water reactors. Nuclear Engineering and Design, 187, p 47. https://doi.org/10.1016/S0029-5493(98)00257-X

Scolaro S. (2009). Ph.D. thesis on effects of humidity and fatty acid surfactants on the uptake of NO_2 to NaCl : Combined study of kinetics and surface analysis, Lille university. https://tel.archives-ouvertes.fr/tel-00674517

Seinfeld J.H., Pandis S.N. (1998). Atmospheric Chemistry and Physics: From Air Pollution to Climate Change, 3rd Edition, Stockholm, Sweden, ISBN: 978-1-118-94740-1.

Shahri Z., Sobhani A., Salavati-Niasari, M. (2013). Controlable synthesis and characterization of cadmium molybdate octahedral nanocrystals by coprecipitation method, Materials Research Bulletin, 48, pp 3901–3909. https://doi.org/10.1016/j.materresbull.2013.05.100

Shi Y., Weigang W., Maofa G. (2008). The uptake of ethyl iodide on black cabon surface, Chinese Science Bulletin, 53, pp 733-738. https://doi.org/10.1007/s11434-007-0488-2

Shibazaki H. *et al.* (2001). Revaporization of a CsI Aerosol in a Horizontal Straight Pipe in a Severe Accident Condition, Nuclear Technology, 134, pp 62–70. https://doi.org/10.13182/NT01-A3186

Shugurov S.M., Panin A.I., Lopatin S.I., Emelyanova K.A. (2015). Thermodynamic study of gaseous tin molybdates by high-temperature mass spectrometry. Rapid Communications in Mass Spectrometry, 29(5), 1427-1436. https://doi.org/10.1002/rcm.7237

Shugurov S.M., Panin A.I., Lopatin S.I., Panaeva M.A. (2021). Vapor pressures and thermodynamic properties of simple and complexe iodides.Thermochimica Acta 703, 178996. https://doi.org/10.1016/j.tca.2021.178996

Simondi Teisseire, B., Girault, N., Payot, F., Clément B. (2013). Iodine Behaviour in the containment in Phébus FP tests, Annals of nuclear Energy, 61, pp 157-169. https://doi.org/10.1016/j.anucene.2013.02.039

Sirita J., Phanichphant S., Meunier F.C. (2007). Quantitative analysis of adsorbate concentrations by diffuse reflectance FT-IR, Analytical Chemistry, 79, pp 3912–3918. https://doi.org/10.1021/ac0702802

Smith A.L., Vlieland J., Pignié M.C., Abbink M., Mikaelian G., Benigni P. (2021). New insights into the Cs-Mo-O system: Experimental studies of the Cs2MoO4-MoO3 pseudo-binary system, Thermochimica Acta 696, 178825. https://doi.org/10.1016/j.tca.2020.178825

Solymosi F. and Klivényi G.(1993). HREELS study of CH3I and CH3 adsorbed on Rh(111) surface, Journal of Electron Spectroscopy and Related Phenomena, 64/65, pp 499–506. https://doi.org/10.1016/0368-2048(93)80115-3

Souvi S.M.O., Badawi M., Virot F. *et al.* (2017). Influence of water, dihydrogen and dioxygen on the stability of the Cr_2O_3 surface: A first-principles investigation, Surface Science, 666, pp 44–52. https://doi.org/10.1016/j.susc.2017.08.005

Souvi, S. (2017)."Modélisation par SOPHAEROS des essais CHIP (I, Cs, Mo avec ou sans Cd ou Ag), IRSN report PSN-RES/SAG/2017-00207.

Spies J.R., (1936), Process for obtaining free silver and iodine from silver iodide, Patent n°2,060,539 (Nov.10,1936)

Steinhauser G., Brandl A., Johnson T.E. (2013). Comparison of the Chernobyl and Fukushima nuclear accidents: A review of the environmental impacts, Science of the Total Environment, 470–471, pp 800–817. https://doi.org/10.1016/j.scitotenv.2013.10.029

Stellwag, B. (1998). The mechanism of oxide film formation on austenitic stainless steels in high temperature water, Corrosion Science, 40, pp 337-370. https://doi.org/10.1016/S0010-938X(97)00140-6

STEM&STEM2 Programs https://www.oecd-nea.org/jcms/pl_25255/source-term-evaluation-and-mitigation-stem-project (visited 2021) START Ruthenium tests are part of the OECD/NEA Source Term Evaluation and Mitigation (STEM) project.

Su C., Yeh J. C., Chen C. C., Lin J. C. Lin J. L. (2000). Study of adsorption and reactions of methyl iodide on TiO2, Journal of Catalysis, 194, pp 45–54. https://doi.org/10.1006/jcat.2000.2909

Tangri R.P., Venugopal V., Bose D.K., Sundaresan M. (1989). Thermodynamics of vaporisation of caesium molybdate, Journal of Nuclear Materials 167, pp 127-130. https://doi.org/10.1016/0022-3115(89)90433-9

Taylor H.S., Anderson W.T. (1921). The heat of formation of silver iodide, Journal of the American Chemical Society , 43 (9), pp 2014–2017. https://doi.org/10.1021/ja01442a004

Terada H., Katata G., Chino M., Nagai H. (2012). Atmospheric discharge and dispersion of radionuclides during the Fukushima Dai-ichi Nuclear Power Plant accident. Part II: verification of the source term and analysis of

regional-scale atmospheric dispersion, Journal of Environmental Radioactivity, 112, pp 141–154. https://doi.org/10.1016/j.jenvrad.2012.05.023.

Tervahattu H., Juhanoja J., Vaida V., Tuck A.F., Niemi J. V., Kupiainen K., Kulmala M., Vehkamäki H. (2005). Fatty acids on continental sulfate aerosol particles, Journal of Geophysical Research Atmospheres, 110 (D6), pp 2071-2079. https://doi.org/10.1029/2004JD005400

Thomas, T.R., Pence, D. T. and Hasty R.A. (1980). The disproportionation of hypoiodous acid, Journal of inorganic and Nuclear Chemistry, 42, pp 183-186 . https://doi.org/10.1016/0022-1902(80)80237-5

Tombette M., Quentric E., Quélo D., Benoit J., Mathieu A., Korsakissok I., Didier D. (2014). C^3X : A software platform for assessing the consequences of an accidental release of radioactivity into the atmosphere, 4th European IRPA Congress, Geneva, Switzerland, June 2014.

Tombette M., Quentric E., Quélo D., Benoît J.P., Mathieu A., Korsakissok I., Didier D. (2014). C3X : A software platform for assessing the consequences of an accidental release of radioactivity into the atmosphere. 4th European IRPA (International Radiation Protection Association) Congress, Geneva, Switzerland, June 2014.

Trincal. J. (2015). Modélisation du Comportement de l'Iode dans l'atmosphère, Thèse de Doctorat de l'université de Lille-1. http://www.theses.fr/2015LIL10121

Tsinalizara A., Diop C.M., Nimal, B., Detoc M., Lunéville L., Chiron M., Huynh T.D., Brésard I., Eid M., Klein J.C., Roque B., Marimbeau P., Garzenne C., Parize J.M. and Vergne C. (2000). DARWIN: An Evolution Code System for a Large Range of Applications, Journal of Nuclear Science and Technology, Supplement1, p 845-849. https://doi.org/10.1080/00223131.2000.10875009

Tsyrenova G. D. and Pavlova N. N. (2011). Synthesis, Structure, and Electrical and Acoustic Properties of Cs2Cd2(MoO4)3, Inorganic Materials, 47(7), pp 786–790. https://doi.org/10.1134/S0020168511070235

Vandeputte R., Khiri D., Lafont C., Cantrel L., Louis F. (2019). Theoretical investigation of thermochemical properties of cesium borate species. Journal of Nuclear Materials 517, pp 63-70. https://doi.org/10.1016/j.nucmat.2019.01.036

Vasil'ev, Ya.V.; Matskevich, N.I.; Stenin, Yu.G. (1987). New determination of enthalpies of indium tri- and monoiodide formation. Massive adiabatic calorimeter, Izvestiya Sibirskogo Otdeleniya Akademii Nauk SSSR, Seriya Khimicheskikh Nauk; ISSN 0002-3426; CODEN IZSKA; (no.2); p. 3-8

Vaughan S., Gherman T., Ruth A. A., Orphal J. (2008). Incoherent broad-band cavity-enhanced absorption spectroscopy of the marine boundary layer species I_2, IO and OIO, Physical Chemistry – Chemical Physics, 10, pp 4471-4477. https://doi.org/10.1039/B802618A

Viana M., Kuhlbusch T.A.J., Querol X., Alastuey A., Harrison R.M., Hopke P.K., Winiwarter W., Vallius M., Szidat S., Prévôt A.S.H., Hueglin C., Bloemen H., Wåhlin P., Vecchi R., Miranda A.I., Kasper-Giebl A., Maenhaut W., Hitzenberger R. (2008). Source apportionment of particulate matter in Europe: A review of methods and results, Journal of Aerosol Science, 39, pp 827–849. https://doi.org/10.1016/j.jaerosci.2008.05.007

Vogt R. Finlayson Pitts B.J. (1994). A Diffuse Reflectance Infrared Fourier Transform Spectroscopic (DRIFTS) study of the surface reaction of NaCl with gaseous NO_2 and HNO_3, Journal of Physical Chemistry, 98, pp 3747-3755. https://doi.org/10.1021/j100065a033

Wang W., Ge M., Tian Y., Yao L. (2007). A flow tube study of methyl iodine uptake on soot surface, Chemical Physics Letter, 440, pp 348–351. https://doi.org/10.1016/j.cplett.2007.04.053

Wang Y. L.. Nagy J.C., Margerum D.W. (1989). Kinetics of hydrolysis of iodine monochloride measured by the pulsed-accelerated-flow method, Journal of the American Chemical Society, 111, pp 7838-7844. https://doi.org/10.1021/ja00202a026

Weldon M. K. and Friend C. M. (1994). Spectroscopic characterization of surface methylene on Mo(110), Surface Science, 321, pp 202-208. https://doi.org/10.1016/0039-6028(94)90175-9

William D.A. (1994). OECD International Standard Problem Number34 Falcon Code Comparison Report, NEA/CNSI/R(94)27.

Winiarek V., Bocquet M., Saunier O., Mathieu A. (2012). Estimation of errors in the inverse modeling of accidental release of atmospheric pollutant: Application to the reconstruction of the cesium-137 and iodine-131 source terms from the Fukushima Daiichi power plant, Journal of Geophysical Research Atmospheres, 117 (D5), D05122 (16 p). https://doi.org/10.1029/2011JD016932

World Nuclear Association (2021) World Nuclear Power Reactors and Uranium Requirements in Information Library, facts and figures. https://www.world-nuclear.org/information-library/facts-and-figures/world-nuclear-power-reactors-and-uranium-requireme.aspx (last update : September 2021).

Xerri B., Canneaux S., Louis F., Trincal J., Cousin F., Badawi M., Cantrel L. (2012).Ab initio calculations and iodine kinetic modeling in the reactor coolant system of a pressurized water reactor in case of severe nuclear accident. Computational and Theoretical Chemistry, 990, pp 194–208. https://doi.org/10.1016/j.comptc.2012.02.024

Xing G. Xu y., Zhao C., Wang Y. Li Y., Wu Z., Liu T. Wu G. (2011). Photoluminescence properties of $CdMoO_4$ disk and hollow microsphere-like crystals synthetized by hydrothermal conventional method, Powder Technology, 213, pp 109–115. https://doi.org/10.1016/j.powtec.2011.07.012

APPENDICES

Appendix 1. Curriculum Vitae

GREGOIRE Anne Cécile
48 ans – maried - two children

Ingénieur de recherche à l'Institut de Radioprotection et de Sûreté Nucléaire
Pôle de Sûreté Nucléaire – Recherche en Sûreté Nucléaire
Service d'Etude et de Recherche Expérimentale
Laboratoire
CEN Cadarache – Bât 328, F-13115 Saint Paul les Durances Cedex
04 42 19 97 40
Anne-cecile.gregoire@irsn.fr

Education

2001 - Ph-D, University of Pierre et Marie Curie, Paris
Caractérisation Physico-Chimique des solutions aqueuses de nitrate de neptunium aux degrés d'oxydation (IV) et (V) (advisors : Prof. G. Cote, Ph. Moisy)
1998 - M.Sc. Chimie Analytique- University of Pierre et Marie Curie, Paris
1994-1998 – Engineer of the "Ecole Supérieure de Physique et Chimie", Speciality : Chemistry

Professional positions

2006- present : Research Engineer, Laboratoire d'Expérimentation Environnement et Chimie
2002 – 2006 : Research Engineer, Service d'Etude et de Recherche Expérimentale sur les Accidents

Present research activities

Research on Fission Product chemistry in the RCS in severe accident conditions (2007 to present)

2016 - present : IRSN expert in fission product chemistry and analyses

Responsible of the CHIP phenomenological and analytical lines

Contribution to the definition of the experiments in support to modelling (RCS chemistry, source term assessment at short and medium term), test conduct, analyses and interpretation. Presently involved in the international ESTER OECD programme., formely in the ISTP CHIP and CHIP+ programmes.

Development of test facilities devoted to high temperature FP chemistry at small and medium scale and of associated sampling devices and analytical procedures. Special attention devoted to compounds identification (gaseous iodine species, particulate and condensed material)

Involved in several partnership with academic laboratories of Lille university (PC2A and UCCS) and of Bordeaux University (GSM group of the Institut des Sciences Moléculaires).

Research on iodine behaviour in atmospheric compartment (2017 to present)

Contribution to experiment definition devoted to the study of iodine/ aerosol interaction : design and development of dedicated reactors at laboratory scale allowing to monitor solid and/or gas phase and development of specific devices dedicated to iodine monitoring (I_2, CH_3I).

Partnership with GSM group of ISM institute (University of Bordeaux) within the SPECAERO programme (Région Aquitaine). Co supervisor of a Ph-D.

Work package leader of a ANR projet (ANR IODAT – WP2) submitted for the CALL 2017 but not retained.

2016 - 2022 Lead of IRSN internal multidisciplinary group on radio-iodine fate in incidental or accidental situation.

Future research activities

Mitigation of severe accident consequences : FP epuration from waste waters – case of Cs and Sr

2022-2023 : development of grafted MOF materials dedicated for Cs epuration – collaborative work with UCCS MATHYB team and LNER laboratory of the ICSM (Marcoule) – Co-supervision of a post doctoral position

Submission of two projects :

EPURAD for French ANR 2022Call : "Développement de matériaux innovants pour l'épuration des eaux radiocontaminées en Cs et Sr ». *Co Leader of WP3 :*

EXCESIM for HORIZON EURATOM 2021 Call : "Extended base of knowledge for Cesium behaviour during Severe Accident and Innovative Mitigation tools". Leader of WP4 : selection and development of innovative means to trap cesium in solution.

Past research activities

Fission Product, Control Rod and structure material behaviour during the Large scale Phébus FP tests

2002-2006 : Lead of the international working group on Phébus post test analyses involving laboratories of CEA (France), PSI (Switzeland), AEA-T (UK), Chalmers University (Sweden) and ITU (EEC- Germany). Follow up of chemical analysis performed on radioactive samples. Synthesis of Phébus tests experimental data on material release and transport in the experimental circuit (chemical analysis, γ-spectrometry and thermohydraulic data).

2003-2004 : main contributor to the Phébus FPT4 test experimental report

2005-2008 : main contributor to the Phébus FPT2 test experimental report

Courses Taught

University of Lille (2013-2018)

Fission Product reactivity in NPPs severe accident conditions (3 hours conference, M.Sc. level)

Aerosol Produced in NPPs severe accident conditions (4 hours conference, M.Sc. level)

Ecole de Chimie de Montpellier (2020-…)

Presentation of IRSN (2 hours conference, M.Sc. level)

Fission Product reactivity in NPPs severe accident conditions (3 hours conference, M.Sc. level)

PhD supervision :

2019- 2023 : LE FESSANT Elouan, Etude expérimentale du rôle du Bore sur la remobilisation de dépôts de produits de fission en situation accidentelle grave University of Lille. Supervisors : A.S. Mamede, J.F. Paul.

2017-2020 : HOUJEIJ Hanaa, Etude expérimentale des réactions de capture/désorption des iodes gazeux (I2, CH3I) sur des aérosols environnementaux, University of Bordeaux. Supervisor : S. Sobanska. https://hal-lirmm.ccsd.cnrs.fr/UNIV-BORDEAUX/tel-03331636v1

2014-2017 : OBADA Dorel, Evaluation de rejets à moyen terme en situation accidentelle grave d'un réacteur à eau pressurise: étude expérimentale de la re-vaporisation de dépôts de produits de fission (Cs, I) – University of Lille. Supervisors L. Gasnot, A.S. Mamede. https://ori-nuxeo.univ-lille1.fr/nuxeo/site/esupversions/862a7a89-8097-4d76-8c01-3ce976c853c8.

2008-2012 : DELICAT Yathis, Experimental and kinetic study of the iodine reactivity in low pressure H2/O2/H2O/HI/Ar premixed flames, University of Lille. L. Supervisors : Gasnot, JF Pauwels supervisors.

Post Ph-D supervisor

2022-2023 (18 months) : ABDALLAH Ahmad, Développement de matériaux MOF innovants pour l épuration de l'ion Cs+ d'eaux contaminées.

2015-2017(18 months) : BAHRINI Chiheb, Développement de la technique IBB CEAS pour l'analyse d'iode moléculaire gazeux en ligne.

Training period supervisor from bachelor (6) up to Master of Science (9) levels

Others :

Member of thesis defence committee : 2018. Le Gall Claire, Contribution à l'étude du relâchement des produits de fission hors de combustibles nucléaires en situation d'accident grave : effet de la pO_2 sur la spéciation du Cs, Mo, Ba.

Review of publications submitted to Progress in Nuclear Energy, Journal of Aerosol Science, Nuclear Engineering and Design, Nuclear Engineering and Technology.

Review of written communications for NENE (New Energy fr New Europe) and RAD (Radiation) conferences.

Research contributions to date

Refereed journal publications: 14

Grégoire A.C., Sobanska, S., Tornabene C., Talage D., Mamede A.S., Morin S., Cantrel L. (2022). Influence of SIC control rod material on iodine release in nuclear severe accident – Chemical reactivity in thermal conditions of RCS, Annals of Nuclear Energy, 162, 108900. https://doi.org/10.1016/j.anucene.2021.108900

Houjeij H., Grégoire A.-C., Le Bourdon G., Sobanska S., Cantrel L. (2021). Interaction process between gaseous CH3I and NaCl particles : implication for iodine dispersion in the atmosphere , Environnmental science : Processes and Impacts, 2021, 23, 1771-1781. https://doi.org/10.1039/d1em00266j

Sobanska S., Houjeij H., Coussan S., Aupetit C., Taamalli S., Louis F., Cantrel L., Gregoire A.C., Mascetti J. (2021) Infrared matrix-isolation and theoretical studies of interactions between CH3I and water. Journal of Molecular Structure, 130342. https://doi.org/10.1016/j.molstruc.2021.130342

Obada D., Hijazi H, Paul J.F., Gasnot L. Grégoire A.C., Mamede A.-S., Cantrel L. (2020). Chemical stability of caesium iodide deposits in air/steam atmosphere, Journal of Hazardous Material, 409, 124519. https://doi.org/10.1016/j.jhazmat.2020.124519

Obada D., Mamede S., Nuns N., Grégoire A.-C., Gasnot L. (2018). Combined TOF-SIMS and XPS characterization of 304L surface after interaction with caesium iodide under PWR severe accident conditions, Applied Surface Science 459, pp 23–31; https://doi.org/10.1016/j.apsusc.2018.07.212

Bahrini C., Grégoire A.-C., Obada D., Mun C., Fittschen C. (2018). Incoherent broad-band cavity enhanced absorption spectroscopy for sensitive and rapid molecular iodine detection in the presence of aerosols and water vapour. Optics & Laser Technology, 108, p. 466–479. https://doi.org/10.1016/j.optlastec.2018.06.050

Grégoire A.C., Délicat Y., Tornabene C., Cousin F., Gasnot L. Lamoureux N., Cantrel L. (2017). Study of the iodine kinetics in thermal conditions of a RCS in nuclear severe accident, Annals of Nuclear Energy 101, pp 69-82. https://doi.org/10.1016/j.anucene.2016.10.013

Grégoire A.-C., Kalinainen J., Cousin F., Mutelle H., Cantrel L., Auvinen A., Haste T., Sobanska S. (2015). Studies on the role of molybdenum on iodine transport in the RCS in nuclear severe accident conditions, Annals of Nuclear Energy, 78, 117–129. https://doi.org/10.1016/j.anucene.2014.11.026

Grégoire A.C. and Haste T. (2013). Material release from the bundle in Phébus FP, Annals of Nuclear Energy, 61, 2013, pp 63–74. https://doi.org/10.1016/j.anucene.2013.02.037

Bottomley P.D.W., Grégoire A.-C., Carbol P., Glatz J.P., Knoche D., Papaioannou D., Solatie D., Van Winckel S., Grégoire G., Jacquemain D. (2006). Fission product and actinide release from the debris bed test Phébus FPT4: synthesis of the post-test analyses and of the revaporisation testing of the plenum samples, Nuclear Engineering and Technology, 38(2), special Issue on ICAPP'2005 conference. https://www.koreascience.or.kr/article/JAKO200603018221374.pdf

Grégoire-Kappenstein A.C., Moisy P., Cote G., Blanc P. (2003). Dimerization of Np(V) and media effects in concentrated solutions, A, Radiochimica Acta, 91, 665-672. https://doi.org/10.1524/ract.91.11.665.23472

Den Auwer C., Kappenstein-Grégoire A.-C., Moisy P. (2003). Np(V) cation-cation interactions. A new contribution from EXAFS spectroscopy?, Radiochimica Acta, Rapid communication 91, 773-776. https://doi.org/10.1524/ract.91.12.773.23419

Kappenstein-Grégoire A.-C., Moisy P., Cote G., Blanc P. (2003). Determination of binary data for Neptunium(V) nitrate, Radiochimica Acta, 91, 371-378. https://doi.org/10.1524/ract.91.7.371.20015

Kappenstein A.-C., Moisy P., Cote G., Blanc P. (2000). Contribution of the concept of simple solution to the calculation of the stoechiometry activity coefficient and density of ternary mixture of hydroxylammonium or hydrazinium nitrate with nitric acid and water, PC-CP, 2, 2725. https://doi.org/10.1039/B001351J

International and national conferences

Grégoire P.D.W., Blanchardon E., L. Bosland, F. Coppin, F. Cousin, B. Fievet, O. Masson, C. Mourlon, G. Phan, D. Quelo, M. Souidi, S. Vecchiola, (2019), Radioactive Iodine in the atmosphere : from source term to dose - Status of IRSN research , 2nd international conference in radioanalytical and nuclear chemistry, May 5-10 Budapest , Hungary. Oral communication.

Grégoire A.C., Morin S., Cantrel L. (2018). Main outcomes of the IRSN experimental CHIP and CHIP+ *programmes*, Conference Nuclear Energy for New Europe, Portoros 10-13 September (Slovenia). Oral communication and paper in conference proceedings.

Grégoire A.C., Assaf, E., Sobanska S. (2016), Study of the formation of aerosols of FPs (I, Cs, Mo) and control rod material (Cd) in conditions representative of the RCS during a severe accident and consequences on gaseous iodine release, EAC conference, Tours September 4-9. Oral Communication.

Colombani J, Grégoire A.C, Morin S.(2015). Main findings of the IRSN experimental programs performed on iodine chemistry in severe accident conditions, Proceedings of the International OECD-NEA/NUGENIA-SARNET Workshop on the Progress in Iodine Behaviour for NPP Accident Analysis and Management Marseille (France), March 30, April 1. Oral communication and paper in conference proceedings.

Grégoire, A.-C., Mutelle, H.(2012).Experimental study of the [B, Cs, I, O, H] and [Mo, Cs, I, O, H] systems in the primary circuit of a PWR in conditions representative of a severe accident, International Conference on Nuclear Energy for New Europe 2012, Ljubljana, Slovenia, 5-7 September (2012). Oral communication and paper in conference proceedings.

Grégoire A.-C., Haste T. (2012). Synthesis of the Phébus FP-tests – Material release from the degraded bundle. Final seminar of the Phebus program, Aix en Provence, 13-15 juin 2012. Oral communication

Grégoire A.-C., Payot F. (2009) PHEBUS FPT2: Overview of Fission Product and Material Release and Transport in the Experimental Circuit, ICAPP 09 conference, 10-14 may 2009, Tokyo. Oral communication and paper in conference proceedings.

Bottomley P.D.W., Grégoire A-C. *et al*. (2005) Fission product and actinide release from the debris bed test Phébus FPT4: synthesis of the post-test analyses and of the revaporisation testing of the plenum samples, ICAPP 05 conference , may 2005, Séoul. Oral communication and paper in conference proceedings.

Kappenstein A.-C., Charrin N., Moisy P., Cote G., Blanc P. (2000) Contribution of the simple solution concept to the determination of the binary data of HN ad $U(NO_3)_4$, 5th international Conference on Nuclear and Radiochemistry, 3-8 september 2000, Pontresina. Poster communication.

Main Internal IRSN and OECD report

Grégoire A.C. (2021). CHIP and CHIP+ programmes, Synthesis report of the experimental work – rev1 IRSN report 2021-00211.

Grégoire A.C., le Fessant E., Cantrel L. (2021b). ESTER program- State of the art on revaporization from RCS surfaces – Assessment of late phase releases after nuclear power plant severe accident , IRSN report 2021-00282, ESTER report 2021-01.

A.-C. Grégoire , E. Blanchardon, L. Bosland, F. Coppin, F. Cousin, B. Fievet, O. Masson, C. Mourlon, G. Phan, D. Quelo, M. Souidi, S. Vecchiola (2019), L'iode dans l'atmosphère: du terme source à la dose, état de l'art, R&D en cours – Perspectives , Rapport IRSN 2019-00035.

T. Haste, M. Barrachin, B. Clément, A.-C. Grégoire, N. Girault, M. Laurie*, O. de Luze, P. March, F. Payot, G. Repetto, B. Simondi-Teisseire (2012), Synthesis of the Phébus FP programme experimental results , IRSN Report PSN-RES/SAG/2012-00018

Grégoire A.C., March P., Payot F., Zabiego M., De Bremaecker A., Biard B., Schlutig S., Grégoire G. (2008). Phébus FP, FPT2 Final report, (IRSN) - PH-PF report IP/08/579.

Chapelot P., Grégoire A-C., Grégoire G. (2004). Phébus FP, FPT4 Final report, (IRSN) - PH-PF report IP/04/553.

Participation to more than 30 technical IRSN reports

Appendix 2. Relevant publications

Houjeij H., Grégoire A.-C., Le Bourdon G., Sobanska S., Cantrel L. (2021). Interaction process between gaseous CH3I and NaCl particles : implication for iodine dispersion in the atmosphere , Environnmental science : Processes and Impacts2021, 23, 1771-1781. https://doi.org/10.1039/d1em00266j

Obada D., Hijazi H, Paul J.F., Gasnot L. Grégoire A.C., Mamede A.-S., Cantrel L. (2020). Chemical stability of caesium iodide deposits in air/steam atmosphere, Journal of Hazardous Material, 409, 124519. https://doi.org/10.1016/j.jhazmat.2020.124519

Grégoire A.C., Sobanska, S., Tornabene C., Talage D., Mamede A.S., Morin S., Cantrel L. (2022). Influence of SIC control rod material on iodine release in nuclear severe accident – Chemical reactivity in thermal conditions of RCS, Annals of Nuclear Energy, 162, 108900. https://doi.org/10.1016/j.anucene.2021.108900

Grégoire A.C. and Haste T. (2013). Material release from the bundle in Phébus FP, Annals of Nuclear Energy, 61, 2013, pp 63–74. https://doi.org/10.1016/j.anucene.2013.02.037

Annals of Nuclear Energy 61 (2013) 63–74

Contents lists available at SciVerse ScienceDirect

Annals of Nuclear Energy

journal homepage: www.elsevier.com/locate/anucene

Material release from the bundle in Phébus FP

A.-C. Grégoire *, T. Haste

Institut de Radioprotection et de Sûreté Nucléaire (IRSN), PSN-RES/SEREX, PSN-RES/SAG, Cadarache, St. Paul-lez-Durance 13115, France

ARTICLE INFO

Article history:
Received 24 October 2012
Accepted 20 February 2013
Available online 23 April 2013

Keywords:
Reactor severe accident
Phébus FP
Fission product
Control rod
Release kinetics

ABSTRACT

The experiments Phébus FP FPT-0 to FPT-3 tests conducted by IRSN have produced a large quantity of data on fission product, structural material and actinide release under prototypic nuclear reactor accident conditions that form a consistent set of data suitable for assessment of release models implemented in severe accident codes. Additionally, FPT4 provides valuable complementary data in a late phase debris bed geometry.

Based on on-line and post-test measurements, the release of the main fission products could be assessed as well as their release kinetics in relation with bundle degradation progresses. Noble gases (Xe, Kr) are considered as very highly volatile; the other fission products can be classified as high-volatile (Cs, I, Te, Mo), semi-volatile (Rb) and low-volatile (Ru, Ba, La). Release of fission products is observed mainly in the oxidation phases, with the proportions depending on the elements concerned. Molten pool formation corresponds to a decrease of the release process. Post-test gamma-measurements show that deposition of fission products over the upper parts of the fuel rods is important with lower steam flow rates as given in FPT2 and FPT3.

The fuel material fractional release (mainly U) is very low but could represent a significant fraction of the transported aerosol mass (FPT0 and FPT1).

Release from the silver–indium–cadmium control rod is characterised by the initial Cd burst release on failure of the control rod, followed by a steady release of Ag, In and Cd from the molten absorber pool remaining in the stub. These elements are important as they can affect the physical and chemical forms of fission products such as iodine, hence their transmission to the containment. A large boron release, linked to an extended degradation of the boron carbide control rod, was observed during FPT3.

The established link between bundle degradation and release mechanisms is clearly confirmed for both fuel and control rod materials, with the release being dependent on temperature, burnup, interactions between fuel and structural materials (mainly Zircaloy cladding, i.e. for Ba) and atmosphere (oxidising/reducing conditions, as can be noticed for Mo, Sn and Te), and mass flow rate.

Comparison with the results of separate-effects test series (VERCORS, QUENCH) performed under similar temperature and atmosphere conditions will also be presented.

1. Introduction

The assessment of the source term (ST) – e.g. the amount of fission products, fuel, control rod and structural material released from the damaged reactor core – in the case of a severe accident of a PWR, is a main issue for the evaluation of the radiological consequences of such accidents.

The determination of fission product release and its kinetics in relation to fuel bundle degradation progress was thus a key purpose of the Phébus FP test series (Clément and Zeyen, this issue). Bundle degradation and material release in the model primary circuit and containment building were thus studied, under steam-rich (FPT0/1) or steam-poor atmospheres (FPT2/3), and under low pressures (~0.2 MPa). The potential influence of the fuel burn-up (fresh fuel FPT0 and irradiated fuel FPT1), the nature of the control rod (SIC CR or B_4C CR) and the initial geometry of the fuel (intact bundle for FPT0/3 tests and debris bed geometry for FPT4) were considered too.

The test sequences involved heating of the fuel bundle through a succession of power ramps and plateaus, leading to an oxidation

Abbreviations: B_4C, boron carbide; CR, control rod; CV, containment vessel; FP, fission product(s); ISTP, international source term program; LV, low volatile; PWR, pressurised water reactor; SS, stainless steel; SIC, silver indium cadmium (Ag–In–Cd); SG, steam generator; V, volatile.

* Corresponding author. Address: Institut de Radioprotection et de Sûreté Nucléaire (IRSN), PSN-RES/SEREX, Bât 328, Cadarache, St. Paul lez Durance 13115, France. Tel.: +33 4 42 19 97 40; fax: +33 4 42 19 91 62.

E-mail addresses: anne-cecile.gregoire@irsn.fr (A.-C. Grégoire), tim.haste@irsn.fr (T. Haste).

0306-4549/$ - see front matter © 2013 Elsevier Ltd. All rights reserved.
http://dx.doi.org/10.1016/j.anucene.2013.02.037

runaway, further ramps and plateaus leading to fuel melting and relocation, with the degradation phase being terminated by reactor shutdown about 5 h after the beginning of the heating phase. Special attention was brought to fission products behaviour the release of which was followed on-line during the degradation phase by means of γ-spectrometry targeted at key positions of the experimental circuit. Post test measurements on the degraded fuel bundle, in the experimental circuits and containment vessel, and on samplings performed during the tests completed the experimental data set for the FPs, the control rod, fuel and structural material which could not be followed on-line (March and Simondi-Teisseire, this issue).

The following sections present a short summary of the experimental measurements and the methodology used to assess the integral material release from the degraded fuel bundle. The main results are then reported, in terms of integral release for the main FPs, (I, Cs, Mo, Te, Ba, etc.) the control rod (SIC or B_4C), fuel (U) and structural material (high alloy steels and cladding). Some data concerning instrumentation material specific to the Phébus test (thermocouple material Re, W) are displayed too, as a possible interaction between released FPs and such material were identified. The main features of the release kinetics – in relation with bundle degradation – are reported too. Complete results can be found in the final report of each test (Hanniet-Girault and Repetto, 1999; Jacquemain et al., 2000; Chapelot et al., 2004; Grégoire et al., 2008; Payot et al., 2011).

The results are then discussed as a function of the different test conditions and some separate effect tests (VERCORS, QUENCH tests).

2. Experimental

A complete description of the in-pile test section, the experimental circuits and related instrumentation as well as the experimental conditions are given in (March and Simondi-Teisseire, this issue) and in the corresponding experimental reports (see references above).

2.1. On line detection of release phases

The detection of fission products and structural material release and their kinetics in relation with bundle degradation events, was obtained by various measurements located both in the experimental circuit and the containment vessel (see Figs. 1 and 2):

- Two optical devices dedicated to aerosol characterisation were implemented respectively in the hot leg of the circuit (FPT0/2) and in the containment vessel (FPT1/2). They provided qualitative data on the kinetics of aerosols release.
- Several on-line γ-stations were targeted at key positions in the experimental circuit (hot leg, steam generator and cold leg) and containment vessel (containment atmosphere) and monitored the release and the transport and/or deposition of various γ-emitters during the degradation phase.

In addition to this instrumentation, the circuit and containment vessel were intensively instrumented with thermal hydraulic sensors (temperature, pressure, humidity, etc.). Instrument devoted to the gas phase composition determination were implemented both on the cold leg of the circuit – (hydrogen sensors) and in the containment vessel (H_2, O_2). For FPT3, carbonaceous gas sensors dedicated to the on-line measurement of CO, CO_2 and CH_4 were implemented in the containment vessel – these gases being produced by the oxidation of the B_4C control rod material.

The FPT4 in-pile test train was equipped with aerosol filters (March and Simondi-Teisseire, this issue) so that only gaseous species were released in the experimental circuit. As a consequence, the experimental circuit and the related on-line instrumentation were greatly simplified and only two γ-stations were implemented in the horizontal line and in the containment vessel to monitor the release of gaseous fission products.

2.2. Post-test determination of material distribution

The on-line measurements were complemented by post-test γ-spectrometric measurements of the degraded bundle and experimental circuit. These analyses provided a mass distribution for the main γ-emitters (^{131}I, ^{129m}Te, ^{129}Te, ^{137}Cs, ^{134}Cs, ^{114m}In, ^{110m}Ag, ^{140}Ba, ^{140}La, ^{103}Ru, ^{154}Eu, ^{99}Mo).

- The in-pile test device was post-test examined (γ-scans, X-ray radiography, and emission tomography) in order to identify the axial and radial profile of the various γ-emitters still present in the degraded fuel bundle or deposited along the upper plenum or the vertical line (and on the 5 sequential filters of FPT4). As no re-irradiation was performed prior to FPT4, only the long lived FPs could be detected.
- For the bundle tests, various sections of the circuit (inner tube of the hot leg horizontal line, sections of the steam generator) were post test γ-scanned, providing a reliable deposition profile of the main γ-emitters in these parts of the circuit.

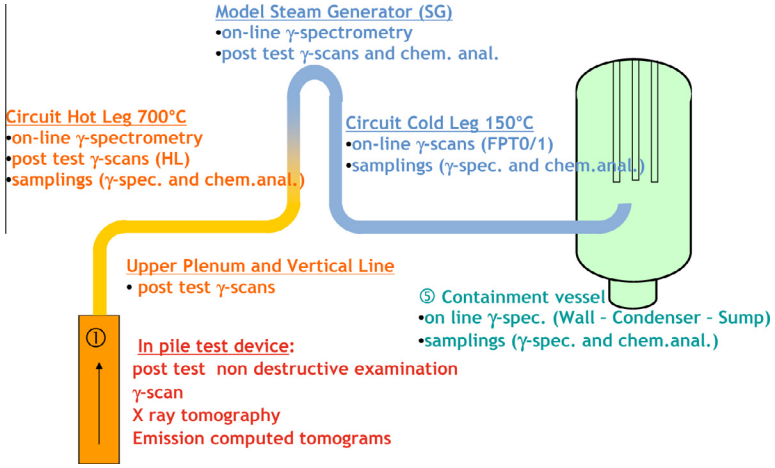

Fig. 1. Simplified schematics of the experimental circuits in the bundle tests FPT0/3 and localisation of on-line/post test measurements and samplings dedicated to material release/deposition/ transport in the circuit and up to the containment vessel (γ-spec: γ-spectrometry; chem. anal.: chemical analyses).

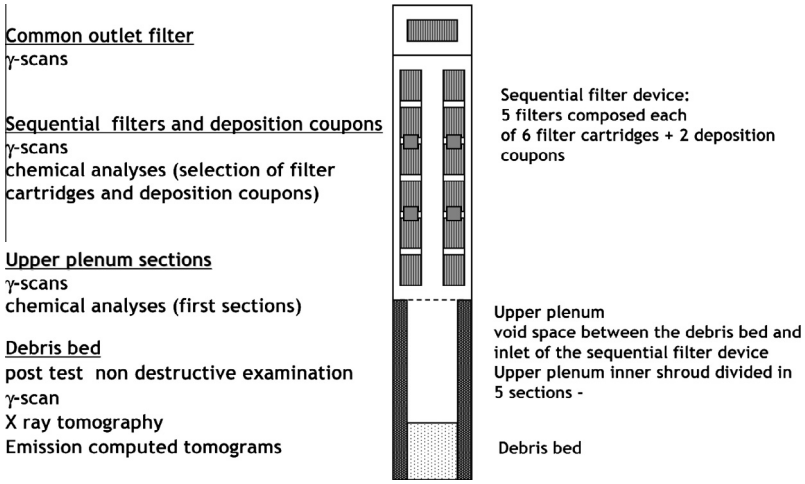

Fig. 2. Simplified schematics of FPT4 in-pile test section and localisation of the post test measurements dedicated to the determination of final mass distribution.

- All the sampling devices (aerosols filters, impactor devices and iodine species characterisation devices) located in the furnaces along the experimental circuit were post test γ-scanned too. They provided information on material transport through the circuit during the transient.

A selection of these samplings (aerosol filters and steam generator sections for FPT0/3 tests and upper plenum sections and sequential filters for the FPT4 test) were further examined by destructive chemical analyses[1]. The objectives of these analyses were to obtain a mass determination for the elements not measurable by γ-spectrometric methods. These elements include material from the fuel bundle (U and Pu), fission products (Sr, Y, Rb, Tc, Nb, Eu, Ce, Pr), neutron absorber (Ag, In, Cd, and B for the FPT2 and FPT3 tests), material from the structures (Zr, Sn) and from the instrumentation (Re, W). The latter represent a significant (if not the main) part of the released aerosol mass. Mass determination required acidic dissolution followed by elemental analysis by using the Inductively Coupled Plasma – Mass Spectrometry technique or the Inductively Coupled Plasma – Optical Emission Spectroscopy techniques. No direct chemical speciation could be gained from these analyses.

2.3. Methodology for the determination of material release

Based on the quantitative data gained from the post-test analyses, it was possible to build up a circuit mass distribution and to determine an integral release for most of nuclides of interest.

- The initial bundle material inventory for the fuel, the fission products, the control rod and the structural materials.
- The amount of material remaining in the test bundle zone or redeposited in the upper plenum and the vertical line at the exit of the test bundle at the end of the degradation phase.
- The amount of material deposited in the circuit experimental lines (horizontal hot leg, steam generator and horizontal cold leg) at the end of the transient.
- The amount of material (mainly aerosol and a small fraction of gaseous species) which transited through the circuit cold leg and was finally released into the containment vessel during the degradation phase.

2.3.1. Initial bundle inventory

The fission product and the heavy nuclide inventories of the initial bundle were calculated with the PEPIN2 code of the DARWIN package (Tsilanizara et al., 1999, 2003). It relies on the specification of the power/burn up history experienced by the irradiated fuel, including the prior in-reactor irradiation (the BR3 reactor for FPT1, FPT2 and FPT3 irradiated rods and the Gravelines 5 plant for the FPT4 fuel), the Phébus re-irradiation phase (except for FPT4) and the Phébus transient phase.

The validation of the APOLLO2/PEPIN2 calculated inventories by comparison with experimental data is discussed in (Jacquemain et al., 2000) for FPT1, (Chapelot et al., 2004) for FPT4, (Grégoire et al., 2008) for FPT2 and (Payot et al., 2011) for FPT3. For a large number of fission products and for some heavy nuclides (the inventory of which could be experimentally measured only for FPT4) a good consistency between the experimental and calculated inventories was obtained. Thus for those nuclides, the data gained from the APOLLO2/PEPIN2 calculation were retained as the reference initial bundle inventory (with a relative uncertainty comprised between ±5 and 15%). The determination of the activation product inventory (mainly ^{134}Cs and the activation products of the control rod material: ^{110m}Ag and ^{114m}In) by APOLLO2/PEPIN2 is known to be less accurate (Grégoire et al., 2008); so those inventories were either considered with a large uncertainty (up to ±50%) or indirectly determined by comparison with post-test chemical analyses performed on a selection of samples (FPT2 test, nevertheless with still a large uncertainty ~±30%).

The inventory of natural element present in the fuelled part of the test section (cladding, structure and control rod material) was deduced from its description.

For each Phébus FP test, the initial material inventory is displayed in the corresponding experimental reports.

2.3.2. Methodology for the determination of the integral release

For the elements detected by γ-scanning in the in-pile test section (including the degraded bundle, upper plenum and vertical line), the integral release was directly determined assuming that it corresponds to the difference between the initial inventory and the remaining part in the degraded bundle. For the other elements, as no data were available for the in-pile test section, the integral

[1] The chemical analyses were performed in partner laboratories of the Phébus programme: Institute for Transuranium Elements (EC/JRC/ITU-Karlsruhe), Commissariat à L'Energie Atomique (CEA Saclay and Cadarache), AEA Technology (Winfrith), Chalmers University (Göteborg), Paul Scherrer Institute (PSI-Villingen), Studiecentrum voor Kernenergie–Centre d'Etude de l'Energie Nucléaire (SCK-CEN/Mol) and Studsvik (Nyköping).

release was estimated assuming that it corresponds exactly to the sum of the inventory fractions deposited in the hot leg, the steam generator, the cold leg and released in the containment vessel. In this case, the calculated release is a minimum value, since the possible deposits in the upper plenum and vertical line were not accounted for and were thus considered as not released.

2.3.3. Establishment of a mass balance closure

For the well-detected γ-emitters, independent measurements were available for transit and deposit in the experimental circuit and for material remaining in the bundle. For FPT1/3 tests, an overall check of the consistency of the data could thus be performed for the following elements: barium (γ-spectrometry data for ^{140}Ba/La), caesium (data for ^{137}Cs), iodine (data for ^{131}I), ruthenium (γ-spectrometry data for ^{103}Ru completed by chemical data for $^{101-102}$Ru), tellurium (^{129m}Te and ^{132}Te/I), molybdenum (^{99}Mo data completed by chemical analyses on the non-radioactive isotopes of Mo), silver (^{110m}Ag data); additional data for cerium (^{144}Ce/Pr data), europium (^{154}Eu) and zirconium (^{95}Zr, fission product and fuel tracer).

The mass balance closure for most of the detected elements is consistent within the experimental errors; for the low volatile elements (such as Ba, Ru, Ce, Zr) the uncertainty is dominated by the amount remaining in the degraded bundle. Though substantial deficits may be noted for some elements (I, Ag, Te for FPT3, Te for FPT2), a satisfactory mass balance closure between the degraded fuel bundle and the circuit could be obtained for most of the detected elements.

3. Release from the degraded bundle

3.1. Integral release from the degraded bundle or debris bed during the transient

Based on the methods presented in the previous section, the integral release from the degraded bundle or debris bed could be determined for most of elements of interest (fission products, fuel, control rod, structure and instrumentation material). The results for all the Phébus FP tests are reported in Table 1. The main elements listed in the second column of the table were measured either by γ-spectrometry or by chemical analyses (stable isotopes). Some nuclides were measured by both methods (Mo, Ag, Cs, and In); but, except for Mo, γ-spectrometry data were systematically preferred to chemical analyses since the latter were performed on only a reduced set of samples. In general release data are given as a fraction of initial inventory (i.i.).

The consistency analysis of the circuit and fuel data (as reported in Table 1 which is an simplified version of extended Table SD-1 in the Supplementary data files) indicate that the local measurements performed both on the fuel (whenever possible) and in the circuit are not biased by any systematic errors (see also Section 2.2); thus, no correction or adjustment has to be applied to the data reported in Table 1. The uncertainties remain between ±20–25% for all elements listed in Table 1 except for Ag and In as control rod material for FPT0, FPT1 and FPT2. Due to the bad initial inventory evaluation of ^{114m}In (tracer of In) and ^{110m}Ag (tracer of Ag), the uncertainty of Ag and In releases is close to ±35–50%.

Table 1
Integral release from the degraded bundle (or debris bed) or the test section for the FPT0–FPT1–FPT2–FPT3 and FPT4 Phébus tests -% of initial inventory – circuit and containment vessel data (Hanniet-Girault and Repetto, 1999; Jacquemain et al., 2000; Chapelot et al. 2004; Grégoire et al., 2008; Payot et al., 2011).

		Integral release from the degraded bundle (or debris bed) - % of initial inventory				
		FPT0	FPT1	FPT2	FPT3	FPT4
Noble gases	Xe	~ 70–80	84	60	74	100
	Kr	no data	77	79	82	90-100
Fission products	Cs	> 66	84	58	72	84
	I	> 91	90	73	78	97
	Te	> 92	91	58	62	44
	Sb	> 63	> 31	n.d.	40	31
	Rb	n.d.	> 65	> 43	35	53
	Mo	n.d.	52	40	32	77
	Cd (FP)	n.d.	n.d.	n.d.	> 40	44
	Ag (FP)	n.d.	n.d.	n.d.	59	9.2
	Ba	> 0.84	> 1.0	1.1	3.4	35
	Tc	n.d.	> 25	> 2.0	> 1.4	7.1
	Ru	> 2.1	1.2	0.15	0.50	1.8
	Nb	>0.070			0.05	1.5
	Sr	>0.23			1.0	
	Y	n.d.	n.d.	> 0.11	0.003	n.d.
	La	n.d.	n.d.	> 0.1	> 0.059	0.36
	Ce	> 0.0060	n.d	> 0.36	> 0.28	0.34
	93Zr (FP)	n.d.	n.d	n.d.	n.d.	0.41
Control Rod	Ag	> 13	15	2.7	n.c.	n.c.
	In	> 19	> 9	> 8.5	n.c.	n.c.
	Cd	> 47	> 67	> 26	n.c.	n.c.
	B	n.c.	n.c.	n.d.	> 16	n.c.
Fuel	U	> 0.14	> 0.14	> 0.0064	> 0.075	0.41
	Pu	n.d.	>0.027	n.d.	> 0.00090	0.31
Cladding	Zr	> 0.036	0.017	> 0.014	> 0.0108	0.08
	Sn	> 33	> 38	9	> 29	68
Intrumentation	Re	> 9.8	> 7.2	> 0.85	> 2.8	3.7
	W	> 13	n.d.	> 6.7	> 12.1	0.39

The integral release was determined as the sum of material transiting in the hot leg plus the deposits located in between the top of the degraded fuel (or debris bed for FPT4) and the hot leg (upper plenum, vertical line and horizontal line). For the elements for which we have no data in this upstream hot zone, the integral release should be considered as a minimal value and is reported like this (>). The integral releases are rounded to two significant figures (uncertainty +/- 20%). For the noble gases, the containment vessel data are considered too.
Xe data for FPT0 is an estimation only.
n.d.: no data available (below detection limits in most samples or too few samples analysed for this element, or no reliable measurements).
n.c.: not concerned (for instance boron for the FPT0, FPT1 and FPT4 tests; Ag, In, Cd from the control rod for FPT3 and FPT4).

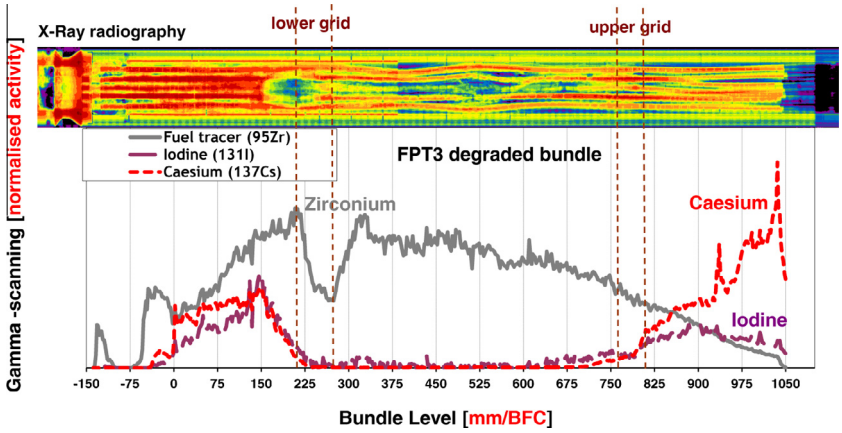

Fig. 3. FPT3 – final state of the fuel bundle and isotope distribution (^{95}Zr, ^{140}Ba/La, ^{103}Ru, ^{131}I, ^{137}Cs) – (Payot et al., 2011).

Concerning the release from the degraded fuel bundle (for the FPT0–FPT3 experiments) or the degraded debris bed (for the FPT4 test), the elements may be classified as follows.

- The noble gases (Xe and Kr), which are strongly released from the fuel for all the tests: about 80% of the initial inventory.
- Volatile elements, which are mainly fission products (I, Cs, Te, Sb, Rb, Mo), are characterized by a released fraction in excess of 25–75% of initial inventory. For the FPT3 and FPT4 tests, where no SIC control rod was implemented in the fuel, cadmium is also identified as a volatile fission product. For silver, the trend is less clear, with a high release observed for FPT3 (>44% of i.i.) and a more moderate one for FPT4 (~9.2% of i.i.). Sn from the cladding is also identified as a volatile element (except for the FPT2 test with a minimum release corresponding to 9% of i.i.) as well as cadmium from the SIC control rod. For molybdenum, high releases were observed in FPT1/2 (~50% i.i.), and even higher in FPT4, (77% i.i). Ba behaves as a volatile element only for the FPT4 test (with a release reaching 35% of its initial inventory), for the other experiments it is considered as a low volatile element. This particular behaviour of Ba during FPT4 will be discussed in Section 4.1.
- Semi-volatile elements are identified by ~6–25% of initial inventory being released during the transient. These include the instrumentation materials mainly released from the fuel high temperature thermocouples (W for all tests and Re for FPT0/1), the SIC control rod material (In for all tests and Ag for FPT0/1) and some FPs such as Tc (technetium) during FPT1 and FPT4.
- Low-volatile elements are identified by low release fraction from the bundle (~1–6% of i.i.), such as Ba (except for FPT4 test), Tc (for FPT2/3), Ru (all tests).
- Non-volatile elements which remain almost entirely in the fuel zone (releases <1% of i.i.), where they contribute to the residual power. These include fission products (Sr, Ru, Nb, elements from the Ln series, ^{95}Zr), cladding (natural Zr) and fuel material. Release of fuel material was very low for all the experiments: even during FPT4, for which a complete data set is available concerning fuel release: an integral release of only 0.41% i.i. of U and 0.31% i.i. of Pu was observed.
- The SIC control rod material behaved differently from one test to another: if Cd can be always considered as a volatile element, Ag is semi-volatile for FPT0 and FPT1 and low volatile for FPT2. Despite the fact that In can always be considered as a semi-volatile, its release during FPT1 and FPT2 was a factor of two lower than that observed during FPT0.

Table 2
FPT2 test – material release determined from bundle data – as a fraction of initial inventory (Grégoire et al., 2008).

Element (isotope)	Bundle data% i.i	Bundle release% i.i	Upper rod deposits %i.i. (estimation)	Fuel release % i.i. (estimation)
Cs (^{137}Cs)	33 ± 8	67	7	74
I (^{131}I)	28 ± 5	72	6	78
Te (^{132}Te/^{132}I)	19 ± 4	81	8	89
Mo (^{99}Mo)	48 ± 10	52	15	67
Ba (^{140}Ba/La)	86 ± 17	14	3	17
Ru (^{103}Ru)	89 ± 20	11	6	17
Ag (^{110m}Ag)	86 ± 31	14	5	19

♦Silver is a control rod material for FPT2; "bundle data" stands for the amount detected in the degraded bundle, "bundle release" is the difference between initial inventory and amount remaining in the bundle after the test, "upper rods deposits" stands for the fraction of volatilized material which has redeposited on the more intact upper part of the fuel rods; "fuel release" correspond to the sum of bundle release + deposit on the upper rods

Table 3
FPT3 test – material release determined from bundle data – as a fraction of initial inventory (Payot et al., 2011).

Element (isotope)	Bundle data% i.i.	Bundle release% i.i.	Upper rod deposits% i.i. (estimation)	Fuel release% i.i. (estimation
Cs (^{137}Cs)	36 ± 6	64	9	73
I (^{131}I)	21 ± 4	79	1	80
Te (^{132}Te/^{132}I)	20 ± 4	80	1	81
Mo (^{99}Mo)	77 ± 16	23	30	53
Ba (^{140}Ba/La)	94 ± 16	6	5	11
Ru (^{103}Ru)	99 ± 16	1	7	8
Ag (^{110m}Ag)	30 ± 16	70	27	97

"bundle data" Stands for the amount detected in the degraded bundle, "bundle release" is the difference between initial inventory and amount remaining in the bundle after the test, "upper rods deposits" stands for the fraction of volatilized material which has redeposited on the more intact upper part of the fuel rods; "fuel release" correspond to the sum of bundle release + deposit on the upper rods.

- Concerning FPT3, the control rod element B (boron) is a special case. Based on carbonaceous gas production (mainly CO and CO_2 resulting from the degradation of the B_4C control rod material) and observation of the bundle by non-destructive examinations (de Luze et al., this issue; Barrachin et al., this issue), 70–80% of boron carbide was consumed, but only 16% of boron initial inventory was found released, from circuit data, and only 2.3% reached the containment. This feature points to the formation of an extensive boron-related blockage in the experimental

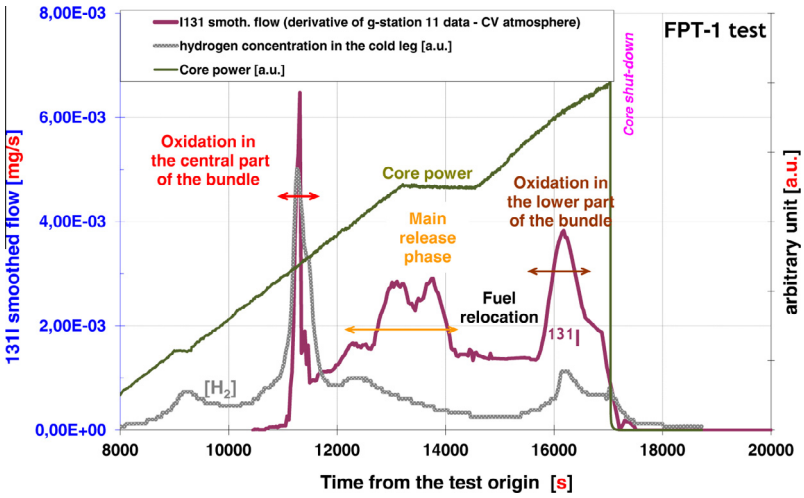

Fig. 4. FPT1 – ^{131}I release kinetics during the transient from containment data – correlation with bundle degradation events (Jacquemain et al., 2000).

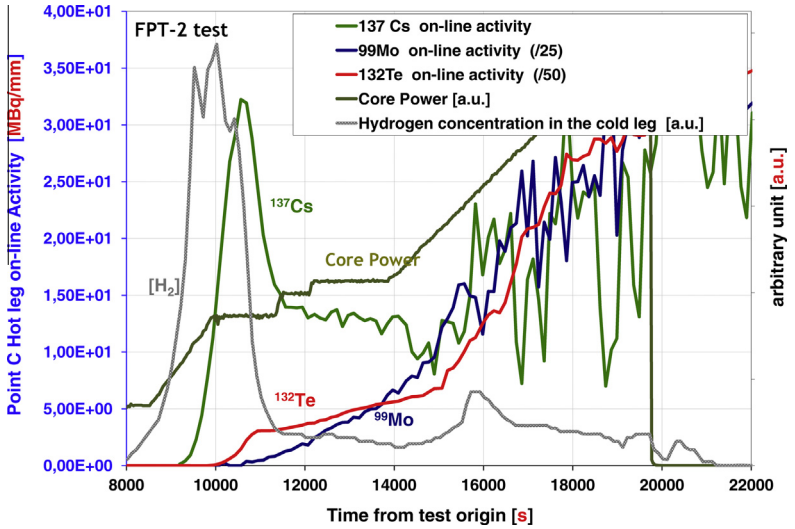

Fig. 5. FPT2 – ^{137}Cs, ^{99}Mo and ^{132}Te on-line detection in the hot leg (Grégoire et al., 2008).

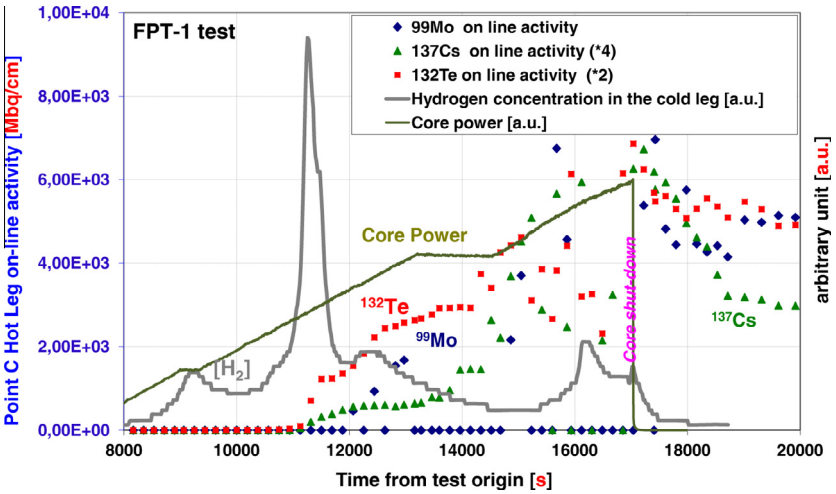

Fig. 6. FPT1 – ^{137}Cs, ^{99}Mo and ^{132}Te on-line detection in the hot leg (Jacquemain et al., 2000).

circuit (localised just before the inlet of the steam generator), see (Haste et al. 2012, this issue); though we have no direct data regarding a large boron release, the data gained from the carbonaceous gas sensors seem to be sufficiently reliable.

The material release (including FP, fuel, cladding, control rod and instrumentation material) is much lower for FPT2/3 (~70 g of material released from the degraded fuel bundle) compared to FPT0/1 (up to 200 g of material released) – for an initial bundle mass of 13,500–14,000 g. This may be linked to the fact that the FPT2/3 experiments were conducted in steam-poor conditions with an injection flow rate four times lower than for FPT0/1. For FPT2 and FPT3, the overall material released mass may be nevertheless underestimated due to:

i/higher deposition on the upper plenum and vertical line surfaces (enhanced by the low steam injection flow rate) compared to the FPT1/0 tests. No extensive chemical analysis was performed on these sections of the circuit, thus for the stable elements (Sn, Re, W, In, Cd and B for FPT3) and fuel elements (U, Pu), the amount deposited in this zone could not be determined. Based on the FPT4 upper plenum analyses (Haste et al., this issue), the fraction of material deposited in the very hot zone can represent a significant fraction of released material.

ii/The formation of a boron related blockage in the circuit, at the inlet of the steam generator, leading to significant material retention: there was evidence for material deposition upstream the steam generator inlet for FPT2 (though smaller than for FPT3) – but no chemical leaching of this zone was performed. For FPT3, attempts were made to dissolve the boron blockage – but material recovery was not complete.

In FPT0/1 the control rod, cladding and instrumentation material dominates with up to 75–90% of the released mass, whereas the FPs (FPT1 only) represent less than 15% and fuel (U) 5%. In FPT2/3, the contribution of the control rod, cladding and instrumentation material is of lesser extent and represents roughly 55% of the released mass, whereas the FPs represent now 30–40%, the fuel material contribution being comprised between 1 (FPT2)-10% (FPT1). In FPT4, the contribution of the cladding and instrumentation material in the overall released mass is only 25% (no control rod material for this test), the FP release representing 50% and the fuel 25% (but almost all released fuel particles deposited on the upper plenum surface).

The aerosol mass reaching the containment vessel is 2–3 times lower, owing to deposition processes in the circuit (Haste et al., this issue).

3.2. Release from the degraded fuel (FPT2 and FPT3 cases)

For FPT4, FPT2 and FPT3 the low steam injection rate (~0.5 g/s) favoured significant deposition of volatile and semi-volatile fission products in the upper section of the degraded fuel bundle: above the upper grid at the level of the remaining fuel rods for FPT2 and FPT3 (see Fig. 3) and on the vault formed by sintered material for FPT4 (Chapelot et al., 2004). This contrasts with results from FPT0 and FPT1 both performed with a higher steam injection rate (~2 g/s) where deposition occurred rather in downstream sections of the circuit.

For FPT2 and FPT3, a detailed final distribution of the fission products detected in the degraded fuel bundle could be established from post test examinations (Grégoire et al., 2008; Payot et al., 2011). Depending on the behaviour of the detected elements (fuel tracer such as ^{95}Zr, low volatile such as Eu and Ba, and volatile such as I and Cs), it was possible to determine their location along the degraded fuel bundle: either still within the fuel rods, or in the relocated material between the fuel rods (mainly in the lower part of the degraded bundle, below the cavity) or deposited on the more intact fuel rods (and even instrumentation) in the zone above the upper grid.

For the volatile elements found partly deposited over the upper rods, summing this deposited fraction and the released fraction from the bundle gives the fraction released from the fuel itself (Tables 2 and 3). It is worth noting that for the volatile fission products (Cs, I and Te) deposition on the upper rods represents at most ~10% of the fraction released from fuel; whereas for elements considered as less volatile, those deposits account for a large part of the material released from the fuel (~30 up to 50%) as is the case for Mo and Ag.

3.3. Main release events

3.3.1. Tests with initial fuel bundle configuration

For the FPT0–FPT3 tests, the release of material from the degraded fuel and its transport through the circuit during the transient were strongly correlated with bundle degradation events. The duration of material release and its injection into the containment lasted for 6000/7000 s for FPT0 and FPT1, ~10,000 s for FPT2, ~8000 s for FPT3. Several successive periods could be identified during the degradation phase (de Luze et al., this issue; Barrachin et al., this issue), each associated with specific fission product and material release (Fig. SF-1, Supplementary data file).

- The fuel clad rupture occurred at temperatures between 700 and 800 °C. Material release at the time of this first degradation event was low. Traces of aerosols were detected in the circuit (on-line optical device) and traces of noble gases in the containment (^{135}Xe) on line γ-spectrometric measurements.
- The Zircaloy cladding oxidation phase is correlated with the change of the heat–up rate of the fuel rods and with the detection of H_2 release in the circuit and containment vessel. On average, this phase started at ~9000–10,000 s after the beginning of the degradation phase and for temperature of ~1000 °C. It continued until the reactor shutdown, albeit occurring in two main distinct phases referred to as the first and second oxidation, respectively. For the FPT0 and FPT1 tests, the first oxidation was rather strong (tests performed in steam rich conditions) whereas for the FPT2 and FPT3 tests, smoother oxidation conditions were observed (tests performed in steam-poor conditions). The second oxidation phase occurred roughly from ~15,000–16,000 s on and lasted ~1000–2000 s; it led to a smaller hydrogen production. This second oxidation phase appears to be related to fuel re-location events.
- The control rod clad rupture at 1100–1400 °C during the main oxidation phase was associated with the detection of the first significant control rod material release (^{114m}In detection for FPT0 and FPT1, ^{115m}Cd burst for FPT2 and detection of carbonaceous species for FPT3).
- The first significant fission product release was observed during the main oxidation phase (generally correlated to the control rod clad rupture) and concerns volatile fission products such as I, Cs, Te, Rb. This release is characterized by a major activity peak for most volatile fission products detected by the on-line instrumentation (see Fig. 4, FPT1 test). For FPT2 and FPT3, Mo release became measurable after the first oxidation only (Fig. 5, FPT2 test, similar data are available for FPT3) suggesting that its release became only significant in steam-rich oxidising conditions as well as Sn (as a clad component). The oxide forms of those two elements seem to be more volatile than their metallic forms. A delay is also observed for Te in FPT2 and FPT3 though one notes that for both tests there was a particularly strong deposit in the earlier parts of the circuit that may vary with time and thus affect the transit of material to the

containment (Haste et al., this issue). For FPT1, performed in steam-rich conditions, Te and Mo releases are observed during the first oxidation phase (see Fig. 6).
- Thereafter, a fairly steady release was observed for all these elements until the second oxidation phase, suggesting that the degradation of the fuel bundle was progressive.
- Then a second large material release occurred at the time of the second oxidation and lasted up to the reactor shutdown (for FPT1, FPT3) or just before (for FPT0 and FPT2) as temperature in the bundle increased further. At this time, even low volatile materials were significantly released (low volatile fission products such as Ru, Sr, Ba, fuel material and Zr as a main component of the cladding).

Two notable pieces of information can be added to the main release events described above.

- As regards the volatile fission products, some strong release events were identified as intense activity peaks captured by on-line measurements in the circuit hot leg for Cs, I (Fig. 4) and Te for FPT1 and FPT2 (Grégoire et al., 2008; Payot et al., 2011). Those activity peaks were not systematically caught by the samplings located in the circuit (unfortunately triggered between the peaks).
- A decrease of the aerosol mass transported in the circuit was observed even before reactor shut down for FPT0 (Hanniet-Girault and Repetto, 1999) and FPT2 (Grégoire et al., 2008), while the fuel temperature was still increasing. This fact cannot be explained just by a decrease of the nuclide content in the test assembly. It can rather be explained by a large change of the assembly geometry with the formation of an extended molten pool reducing the exchange surface between the steam flow and the degraded fuel.

Looking further at the noble gas release, the first detection of ^{135}Xe indicates the first ruptures of the fuel rod claddings in the degradation history; these ruptures take place near the mid-height of the bundle and the gases released from part of the gap inventories of the rods. The amounts released are small, given that the rods are at this stage scarcely degraded. More significant releases take place later, during the first part of the first phase of cladding oxidation; the release of fission gas is always greatest during the first phase of this oxidation. Also, the longer the half-life, the earlier tends to be the release during the transient. This agrees with the release mechanisms for these gases (Lösönen, 2000; White, 2004), principally by interconnection of intergranular bubbles at low temperatures (less than 1200 °C) and by intragranular diffusion at higher temperatures. Differences in release behaviour amongst different isotopes is explained by the differences in their

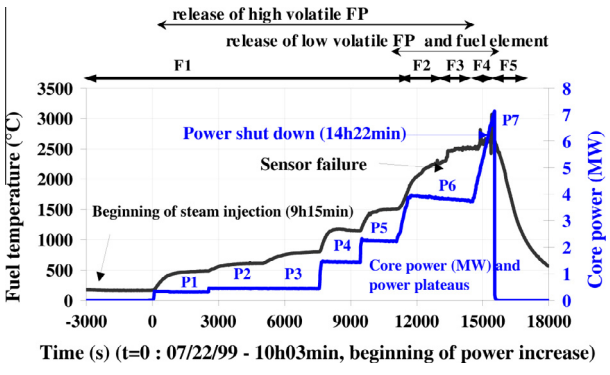

Fig. 7. FPT4 – Test conduct and temperature in the debris bed; F1–F6 correspond to the filter operations (Chapelot et al., 2004).

localisation within the fuel (intra or intergranular); this itself depends on the irradiation history and on the burn-up. After the first phase of cladding oxidation, the kinetics of noble gas release depends mainly on the temperature increase of the fuel.

3.3.2. Test with an initial debris bed configuration (FPT4 test)

As the FPT4 test train was provided with aerosol filters, only the release kinetics of gaseous species could be monitored on-line in the experimental circuits. The short-lived isotopes of Kr (^{90}Kr, ^{91}Kr) and Xe (^{138}Xe, ^{140}Xe) were detected with a release kinetics strongly correlated to the irradiation history during the transient indicating a strong release during each phase of the test (Chapelot et al., 2004). No gaseous iodine was detected downstream the test train (detection limit <1% of the inventory). The released iodine should have been already under condensed or aerosol form when reaching the filter stage. It should be noted that the temperature of the filtration stage was rather low with a maximum inlet temperature of 460 °C and an average outlet temperature of 180 °C.

Concerning the vapour and aerosol release, the kinetics of release could only be inferred from the sequential filter operation time schedule (Fig. 7):

- High releases were observed during the calibration phase and release from a solid debris bed up to a temperature of 2300 °C (filter F1 and filter F2 operations), for all classes of elements. These releases represent about 60–70% of the integral release for most volatile fission products (Cs, Mo, Te). Even for the majority of the low-volatile fission products and fuel elements that could be detected on the filters (Tc, Ag, U), the highest releases were observed during this phase of the test.
- Lower releases were observed from the degraded debris bed, and during the molten pool phase initiation and propagation (filter F3 and filter F4 operations): less than 20% of the integral release of the volatile fission products occurred during this second phase of the test. A similar behaviour was observed for most low volatile fission products and fuel elements. However, this trend seems less clear for Sr and for low volatile structural material (Zr and thermocouple element W), for which similar releases or even higher releases were observed during this second phase of the test. It should be noted that the integral release of these low volatile elements remains nevertheless very low (at most 1.4% for Sr, see Table 1).

The decrease of aerosol release (fission products and fuel elements) observed during power plateau P6 up to the end of the test transient can be connected to the blockage of the test section (due to fuel swelling) which started at ~12,800 s – (Barrachin et al., this issue; Chapelot et al., 2004) and then to the progressive formation of a molten pool during the last power ramp (Chapelot et al., 2004). The blockage of the test section induced the formation of a steam flow by-pass through the thoria–zirconia shroud, and thus some significant decrease of the steam flow rate through the debris bed, as well as some cooling at the top of the debris bed. Moreover, in the configuration of a molten pool, the partial pressure of most fission products, and, hence, their volatility decreases. The combined effect of the decrease of the steam flow rate in the upper part of the fuel debris bed and then of the lowering of fission product volatility in the molten pool can explain the global decrease in aerosol release observed during this late phase of the test.

4. Discussion

The purpose of this section is to discuss specific points and effects regarding the previous release of fuel, control rod and structural material, which have already been described in the

previous section, see Table 1 as a summary of the results. In our discussion, it is important to note that the reference values for release are those from the fuel rod (i.e. fuel pellets and cladding) rather than the release from the bundle itself that enters the circuit, see Table 2 for FPT2 and Table 3 for FPT3. Thus, those fission products that deposit on the cooler upper parts of the rods in FPT2 and FPT3 are taken into account in this total mass. These are the values that are appropriate to compare with the results of separate-effects tests.

4.1. Fission product release

4.1.1. Classification of fission products and consistency with separate-effects tests

It is instructive to compare the fission product release in Phébus FP as summarised in Section 3.1 with the results of the VERCORS programme (Ducros et al., 2001; Pontillon et al., 2010; Pontillon and Ducros 2010a, 2010b), because of similar conditions of temperature and in the gas phase. In VERCORS, the classification is as follows:

- Volatiles (Ag(FP), Cd(FP), Cs, I, Rb, Sb, Sn, Te) and the noble gases (Xe, Kr) characterised by strong releases from the fuel (can be up to 100%), the release starts at quite low temperatures and is weakly dependent on the oxygen potential, or not at all.
- Semi-volatiles (Ba, In(FP), Mo, Tc) with a wide range of releases from a few% upwards, that starts at higher temperatures, and in certain cases there is a strong dependence on the oxygen potential.
- Low volatiles (Ce, Eu, La, Nb, Ru, Sr, Y), with releases of a few% and starting at high fuel temperatures. The release of some of them, such as Ru, is strongly dependent on the oxygen potential.
- Non-volatiles (Nd, Pr, Zr) with very weak releases even at high fuel temperatures.
- Actinides (Am, Cm, Np, Pu, U) characterised by low or very low releases (less than 1%). The releases of U and Np are the largest, and favoured by oxidising conditions.

Only the maximum value of the integral release was considered in formulating these classifications. The Phébus results for volatiles are in complete agreement with this classification; similar remarks apply to the low volatile and non-volatile groups.

In the semi-volatile category, only the Mo results are in agreement with the VERCORS classification, the others falling into the low-volatile class. A notable case is Ba, weakly released in Phébus (except for the FPT4 test), strongly in VERCORS (Ducros et al., 2001). This matter is discussed by (Dubourg and Taylor, 2001) for FPT0 and by (Dubourg et al., 2005) for FPT0 and FPT1: the strong interactions between fuel and structural materials, mainly Zr and Fe are mentioned as possibly being a reason for the particular behaviour of Ba compared with that in VERCORS. Another explanation for the strong Ba release observed in VERCORS (especially for the VERCORS 4 and 5 tests) may be the combination of high temperature and low oxygen potential which favours the volatility of metallic barium and barium oxides. Such conditions were not encountered during the Phébus FPT0/3 test transients.

In the final report of FPT2 (Grégoire et al., 2008) it is stated that the finding that Ba is only weakly released contrasts not only with VERCORS but also with ORNL HI/VI (Lorentz and Osborne, 1995), HEVA (Leveque et al., 1994) and FPT4 (Chapelot et al., 2004). Up to now, there is no clear explanation for the strong Ba release observed during the FPT4 transient (35% i.i).

Further discussion of the matter awaits detailed interpretation of FPT2 and FPT3 in the same way as has been done for FPT0 and FPT1.

4.1.2. Effect of irradiation

The effect of irradiation on fission product release has been analysed by Dubourg et al. (2005) on the basis of FPT0 and FPT1 results, noting the differences in disposition of fission products between trace-irradiated (FPT0) and fully-irradiated (FPT1) fuel. In FPT1, the main part of the release can be explained by considering mechanisms in intact fuel geometry, where it can be interpreted as an initial release of inter-granular content, then by the behaviour of the gas contained in grain bubbles. In FPT0, there is an early transfer of the main part of the gases to intergranular locations, but there is no interlinkage because of the low burnup. It is not possible to explain the early release mechanism observed in intact fuel; instead fuel dissolution at grain boundaries is offered as a probable explanation. This study also concluded that the release from the molten pool would be very low, less than 3% of the bundle inventory for the semi- and non-volatile fission products; this is consistent with the experimental observations where molten pool formation is followed by lower releases.

4.1.3. Effect of oxidising/reducing atmospheres

The results of oxidising/reducing atmospheres have been discussed above in Section 3.3, in relation to the steam-poor periods in FPT2 and FPT3. In brief, Mo release becomes measurable in FPT2 and FPT3 only after the first oxidation, when steam is again available, and not in the steam-poor period, also for Sn as a clad component. It is noted that the oxide forms of those two elements seem to be more volatile than their metallic forms. A similar delay, though less marked, is observed for Te. The possibility of

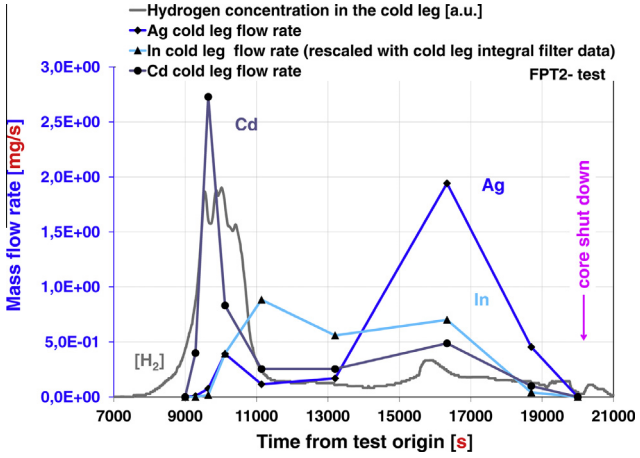

Fig. 8. Control rod material release in Phébus FPT2 (Grégoire et al., 2008), FPT2 bundle temperature is displayed in (De Luze et al., this issue).

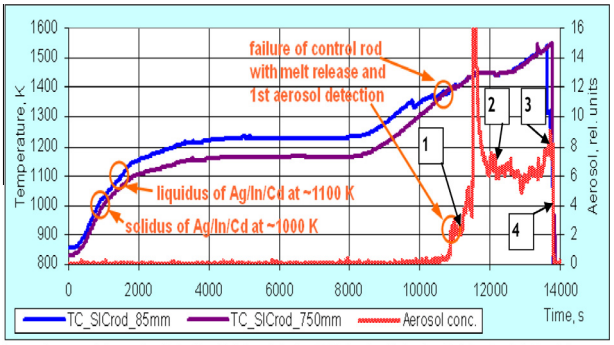

Aerosol composition : 1 = (Cd), 2 = (Cd, In, Ag), 3 = (Cd, In, Ag, Fe), 4 = (Cd, In, Ag, Fe,Zr, Sn)

Fig. 9. Control rod material release in QUENCH-13 test (Sepold et al., 2009 and Lind et al., 2010).

interactions between fuel and structural materials affecting Mo release is discussed in (Dubourg et al., 2005) in relation to FPT0 and FPT1; similar studies for FPT2 and FPT3 would seem beneficial. This is an area where further detailed interpretations seem necessary.

4.1.4. Effect of control rod materials

There is no evidence from the Phébus FP experiments that the presence of control rod materials affects the release of fission products from fuel rods per se. However, they may affect the deposition and transmission in the circuit, and hence the amounts reaching the containment, through affecting the chemical and physical forms, this is discussed in (Haste et al., this issue).

4.1.5. Further experimental work

The Phébus experiments have indicated that complementary separate-effect tests in several technical areas would be necessary to help in their interpretation and to provide data that would form the basis of improved models in integral severe accident codes such as ASTEC (Van Dorsselaere et al., 2009; Chatelard et al., 2010). Such tests were proposed in the International Source Term programme (ISTP) initiated by IRSN and the European Commission (Clément and Zeyen, 2005). In the fission product release area the need for complementary studies focused on the possible effect of very high burnup (up to 70 GWd/tU), as well as the presence of MOX fuel and/or a strongly oxidising atmosphere (air injection) on the fission product release was specifically pointed out. Such studies are currently in progress in the ISTP/VERDON experimental program performed by CEA (Ferroud-Plattet et al., 2009), up to now the results from the first experiment, on high burnup fuel, have been reported (Gallais-During et al., 2012). Analysis of these results is now in progress.

4.2. Control rod material release

4.2.1. Silver–indium–cadmium

The degradation of (Ag, In, Cd) control rods has been discussed in (de Luze et al., this issue; Barrachin et al., this issue), where it is noted that there is considerable variation amongst experiments (Phébus FP and others) in the temperature of control rod failure, which has been observed to occur anywhere in the range from Zr to Fe eutectic formation around 1415 K, right up to the melting temperature of stainless steel, about 1700 K. The mechanisms of control rod failure are discussed for example in (Dubourg et al., 2010) and (Haste and Plumecocq, 2003), initial local failure of the control rod cladding (caused by stainless steel/Zircaloy interaction) being followed by gross failure of the cladding. The stub of the control rod would contain a molten pool of Ag/In/Cd, as the transient progresses this stub would melt further and shorten, with further relocation of the material within. The initial local failure would result in limited release of the volatile Cd vapour, the general failure by a large "burst" release of Cd vapour and the start of In and Ag release by evaporation from the surface of the Ag/In/Cd pool. This is consistent with FPT1 as discussed in (Haste and Plumecocq, 2003) and also with the low Cd fraction seen in refrozen absorber melt (Dubourg et al., 2010). For FPT2, a similar time dependence of Ag/In/Cd release is observed as shown in Fig. 8 (Grégoire et al., 2008): the large Cd burst release could be observed at the beginning of the first oxidation phase, with Ag and In being released more steadily, with a first peak in the first oxidation phase followed by a larger peak in the second heat-up, with a lower release in between.

In QUENCH-13, the absorber material release was observed on-line for the first time (Sepold et al., 2009), (Lind et al., 2010), as shown in Fig. 9: a small Cd release is seen initially followed by a large burst release of Cd later, then a steady release of Ag and In, as well as of Cd, up to the end of the experiment. The QUENCH-13 results and those of Phébus FPT2, show an overall consistency in the time dependence, considering the coarser time resolution of the FPT2 results, the results of which as shown here being recovered by discrete filter measurements (note that for In, on-line gamma-measurement data were also available).

It was not possible in Phébus FP to differentiate amongst metal, oxide and hydroxide forms of these released control rod elements; the most probable chemical form was deduced from interpretation, see for example (Haste et al., this issue) on circuit matters, where assumed equilibrium speciation were used in estimating what total mass of aerosols could have been transported to the containment, including the mass of oxygen. Given the results of the interpretation works, it is assumed that the Ag release is in metallic form, the Cd is transported in oxide form given sufficient steam availability, while the In release may depend more strongly on the oxidation potential of the atmosphere, see (Haste and Plumecocq, 2003, who quote earlier IRSN studies by Dubourg et al. and Taylor, who show that In release is enhanced by the formation of In_2O and InOH, favoured in a steam atmosphere). Thus, oxidation effects need to be considered while modelling In release.

For Ag, In and Cd control rod materials quoted in Table 1, the results concerning release are quite consistent though some variation are observed for FPT0, FPT1 and FPT2 (the mechanisms for release of Ag(FP) seen in FPT3 are different so those results cannot be compared). Circuit data are lower for FPT2 for Ag on account of deposition in the bundle region. In and Cd data are lower bounds as the possible deposits of those elements in the upper plenum and vertical line zones could not be determined (natural elements).

4.2.2. Boron carbide

The release of materials resulting from the degradation of B_4C is discussed in (de Luze et al., this issue; Barrachin et al., this issue), where it is shown that the degradation seen is broadly consistent with that observed in other experiments, noting that the different ratios of B_4C to Zircaloy and stainless steel in control rods of PWR/VVER design and control blades as used in BWRs will affect relocation and melt progression. The oxidation of B_4C leading to carbonaceous gas formation (CO, CO_2 depending on the thermal hydraulic and temperature conditions, with CH_4 being under the detection limit) is also discussed there, as a combustion product rather than release per se. Carbon oxide production in the bundle rather than that of methane would be expected thermodynamically, discussion of potential methane formation in the circuit (lower than the limit of detection in FPT3 because of kinetic effects) and of its importance is displayed in (Haste et al., this issue) on circuit matters. One notes here only that about 77% of the carbon from the B_4C was injected into the containment in the form of CO and CO_2 ($\sim$28% and $\sim$49% respectively), see (Payot et al., 2011), with a maximum of 1% further in the form of methane if any.

The release of boron is more difficult to determine accurately because it is hard to detect by the methods available; the best that can be done is to give a lower limit of 16% from circuit measurements, as given in Table 1. Its overall mass balance remains very uncertain, not least because of a likely substantial blockage in the bundle upstream of the steam generator of unknown size and composition, but likely to be rich in B oxides, see (Payot et al., 2011) and (Haste et al., 2012).

5. Conclusions for material release

The integral release of the main fission products, fuel, control rod and structural material from the degraded fuel bundle could be quantitatively established for all 5 tests of the Phebus FP program, with the following classification:

- The noble gases (Xe and Kr) are strongly released from the fuel for all the tests, at about 80% of the initial inventory.
- Volatile elements, which are mainly fission products (I, Cs, Te, Sb, Rb, Mo), are characterized by a released fraction in excess of 25–75% of initial inventory. For the FPT3 and FPT4 tests, where no SIC control rod was implemented in the fuel, cadmium was also identified as a volatile fission product. For silver as a fission product, the trend is less clear, with a high release observed for FPT3 (>59% of i.i.) and a more moderate one for FPT4 (~9.2% of i.i.). Tin (cladding material) and cadmium (as control rod material) are also identified as volatile elements.
- Semi-volatile elements are identified by ~6–25% of initial inventory being released during the transient. These include the instrumentation materials mainly released from the fuel high temperature thermocouples (W for all tests and Re for FPT0/1), the SIC control rod material (In for all tests and Ag for FPT0/1) and some FPs such as Tc (technetium) during FPT1 and FPT4.
- Low-volatile elements are identified by low release fraction from the bundle (~1–6% of i.i.), such as Ba (except for FPT4 test), Tc (for FPT2/3), Ru (all tests).
- Non-volatile elements remain almost entirely in the fuel zone (releases <1% of i.i.), where they contribute to the residual power. These include fission products (Sr, Ru, Nb, elements from the Ln series, ^{95}Zr), cladding (natural Zr) and fuel material.

The release of boron from the FPT3 test boron carbide control rod, is a special case. Based on the carbonaceous gas production (CO and CO_2 resulting from the degradation of the B_4C) 70–80% of the boron carbide was consumed, but the measured release of boron amounts only to 16% of its initial inventory. This feature may be linked to the formation of an extensive boron-related blockage in the experimental circuit (upstream of the steam generator) which could not be fully characterised.

The release of fission products was observed mainly in the first and second oxidation transients, with the proportions depending on the elements concerned. For the FPT4 test (initial debris bed geometry), the main releases were observed from the solid debris bed up to 2300 °C for all class of elements. For all tests, the molten pool formation corresponded to a slowing of release for every element, partly due to a strong reduction of the exchange surface between the steam flow and the degraded fuel. For Mo, Sn and to a lesser extent for Te, the release was observed to be delayed in steam-poor periods in FPT2 and FPT3 until steam was once more available; the increased volatility of the oxide forms compared to the metal form of these elements has been advanced as an explanation.

The release of volatile fission products from irradiated fuel (FPT1/FPT3 tests) can be explained by considering mechanisms in intact fuel geometry, but this explanation is not appropriate for trace-irradiated fuel (FPT0 test) – early release here may be due to fuel dissolution at grain boundaries. The nature of the control rod (SIC for FPT0/2 and B4C for FPT3) does not seem to have a dramatic influence on the final release of fission products from the fuel. However, it introduces different interaction mechanisms that considerably affect the fission product chemistry and potential source term.

A significant deposition of fission products over the upper parts of the fuel rods was observed in FPT2 and FPT3 with their lower flow rates (such deposits can revaporise later), and this needs to be taken into account in evaluating the total release from the fuel and in comparison with calculation results.

Comparison with the results of the extensive series of separate-effects tests VERCORS performed under similar temperature and atmosphere conditions shows good consistencies overall with the classification of fission products (volatile, low-volatile, non-volatile) seen in FPT0–FPT3, but weaker correspondence for semi-volatile elements – the release of which is more dependent on external conditions. The difference is more marked in the case of barium, which is much less released in Phébus experiments than in VERCORS; explanations have been advanced in terms of chemical interactions between the Zircaloy cladding and fuel materials.

The time dependence of the release from SIC (Ag–In–Cd) control rods corresponds well with those seen in other experiments (QUENCH-13 test): a Cd release burst on gross failure of the rod, followed by a steady release of Ag and In. These materials are important as they can affect the physical and chemical forms of fission products such as iodine, hence their transmission to the containment (similar remarks pertain to boron).

The Phébus FP experiments have produced a large quantity of data on fission product, structural material, control rod and actinide release under prototypic conditions that form a consistent set suitable for assessment of release models in severe accident analysis codes. The link between degradation and release mechanisms has been clearly established in detail for both fuel and control rod materials, with the release being dependent on temperature, burnup, interactions between fuel and structural materials (principally Zircaloy cladding) and atmosphere (oxidising/reducing conditions, flowrates). These tests have nevertheless pointed out the need for complementary studies focused on the possible effect of very high burnup (up to 70 GWd/tU), as well as the presence of MOX fuel and/or a strongly oxidising atmosphere, (air injection) on the fission products release and these are currently in progress in the ISTP/VERDON experimental programme.

Appendix A. Supplementary material

Supplementary data associated with this article can be found, in the online version, at http://dx.doi.org/10.1016/j.anucene.2013.02.037.

References

Barrachin, M., Haste, T., Repetto, G., de Luze, O., this issue. Late Phase Fuel Degradation in the Phébus FP Tests, Annals of Nuclear Energy.

Chapelot P., Grégoire, A.-C., Grégoire, G., 2004. PHEBUS FPT4 Final Report. Note DPAM/DIR – 2004-0135 – Document PHEBUS PF IP/04/553.

Chatelard, P., Reinke, N., Arndt, S., Bosland, L., Cantrel, L., Cousin, F., Cranga, M., Guillard, G., Marchetto, C., Piar, L., Seropian, C., 2010. Status of ASTEC V2 Development: Focus on the Models of the V2.0 version. In: 4th European Review Meeting on Severe Accident Research (ERMSAR-2010), Bologna, Italy, May 11–12.

Clément, B. Zeyen, R., 2005. The Phébus Fission Product and Source Term International Programmes. In: Proceedings of the International Conference "Nuclear Energy for New Europe 2005", Bled, Slovenia, September 5–8.

Clément, B., Zeyen, R., this issue. The Objectives of the Phébus FP Experimental Programme and Main Findings, Annals of Nuclear Energy.

De Luze, O., Haste, T., Barrachin, M., Repetto, G., this issue. Early Phase Fuel Degradation in Phébus FP: Initiating Phenomena of Degradation in Fuel Bundle Tests, Annals of Nuclear Energy.

Dubourg, R. et al., 2010. Understanding the behaviour of absorber elements in silver–indium–cadmium control rods during PWR severe accident sequences. Progress in Nuclear Energy 52, 97–108.

Dubourg, R., Faure-Geors, H., Nicaise, G., Barrachin, M., 2005. Fission product release in the first two PHEBUS tests FPT0 and FPT1. Nuclear Engineering and Design 235, 2183–2208.

Dubourg, R., Taylor, R., 2001. A qualitative comparison of barium behaviour in the PHEBUS FPT0 test and analytical tests. Journal of Nuclear Materials 294, 32–38.

Ducros, G., Malgouyres, P.P., Kissane, M., Boulaud, D., Durin, M., 2001. Fission product release under severe accidental conditions: general presentation of the program and synthesis of VERCORS 1–6 results. Nuclear Engineering and Design 208 (2), 191–203.

Ferroud-Plattet, M.P., Bonnin, J., Gallais-During, A., Bernard, S., Grandjean, J.P., Ducros, G., 2009. The VERDON Laboratory at the CEA Cadarache: New Hot Cell Facilities Devoted to the Study of Irradiated Fuel Behaviour and Fission Products Release Under Simulated Accidental Conditions. In: 46th Annual Meeting of Hot Laboratories and Remote Handling Working Group, Prague, Czech Republic, 20–23 September.

Gallais-During A., Bonnin, J., Malgouryres, P.-P., Bernard, S., Pontillon, Y., Hanus, E., Ducros, G., 2012. VERDON Laboratory: Performances of the Experimental LWR Severe Accident Device and First Results of Fission Product Release on High Burn-up UO2 fuel. In: Proceedings of the International Conference "Nuclear Energy for New Europe 2012", Ljubljana, Slovenia, September 5–7.

Grégoire, A.C., March, P., Payot, F., Ritter, G., Zabiego, M., de Bremaecker, A., Biard, B., Grégoire, G., Schlutig, S., 2008. FPT2 Final Report, IRSN report DPAM/DIR-2008-272, PHEBUS PF IP/08/579, October.

Hanniet-Girault, N., Repetto, G., 1999. FPT0 Final Report, IPSN report PH-PF IP/99/423.

Haste T., Payot, F., Bottomley, P.D.W., this issue. Transport and Deposition in the Phébus FP Circuit, Annals of Nuclear Energy.

Haste, T., Payot, F., Dominguez, C., March, P., Simondi-Teisseire, B., Steinbrück, M., 2012. Study of boron behaviour in the primary circuit of water reactors under severe accident conditions: a comparison of Phebus FPT3 results with other recent integral and separate-effects data. Nuclear Engineering and Design 246, 147–156.

Haste, T., Plumecocq, W., 2003. Control Rod Release and Structural Release Modelling in ELSA2. In: 9th International QUENCH Workshop, FZ Karlsruhe, 13–15 October.

Jacquemain, D., Bourdon, S., de Bremaecker, A., Barrachin, M., 2000. FPT1 Final Report, IRSN report PH-PF IP/00/479.

Leveque, J.-P., Andre, B., Ducros, G., Le Marois, G., Lhiaubet, G., 1994. The HEVA experimental programme. Nuclear Technology 108, 33–44.

Lind, T., Pintér Csordás, A., Nagy, I., Stuckert, J., 2010. Aerosol behaviour during SIC control rod failure in QUENCH-13 test. Journal of Nuclear Materials 397, 92–100.

Lorentz, R.A., Osborne, M.F. 1995. Summary of ORNL Fission Product Release Tests With Recommended Release Rate and Diffusion Coefficients, Technical Report ORNL/TM-12801, NUREG/CR-6261, ORNL (USA), July.

Lösönen, P., 2000. On the behaviour of intra-granular fission gas in UO_2 fuel. Journal of Nuclear Materials 280, 56–72.

March, P., Simondi-Teisseire, B., this issue. Overview of the Phébus Facility and Experiments Performed, Annals of Nuclear Energy.

Payot, F., Haste, T., Biard, B., Bot-Robin, F., Devoy, J., Garnier, Y., Guillot, J., Manenc, C., March, P., 2011. FPT3 Final Report. IRSN Document PHEBUS PF IP/10/587, July.

Pontillon, Y., Ducros, G., 2010a. Behaviour of fission products under severe PWR accident conditions: the VERCORS experimental programme—Part 2: release and transport of fission gases and volatile fission products. Nuclear Engineering and Design 240 (7), 1853–1866.

Pontillon, Y., Ducros, G., 2010b. Behaviour of fission products under severe PWR accident conditions: The VERCORS experimental programme—Part 3: Release of low-volatile fission products and actinides. Nuclear Engineering and Design 240 (7), 1867–1881.

Pontillon, Y., Ducros, G., Malgouyres, P.P., 2010. Behaviour of fission products under severe PWR accident conditions: VERCORS experimental programme—Part 1: general description of the programme. Nuclear Engineering and Design 240 (7), 1843–1852.

Sepold, L., Lind, T., Pintér Csordás, A., Stegmaier, U., Steinbrück, M., Stuckert, J., 2009. AgInCd control rod failure in the QUENCH-13 bundle test. Annals of Nuclear Energy 36, 1349–1359.

Tsilanizara, A., et al., 1999. DARWIN: an evolution code system for a large range of applications. In: Proceedings of the ICRS-9 Conference (Tsukuba, Japan), October.

Tsilanizara, A. et al., 2003. DARWIN: an evolution code system for a large range of applications. Journal of Nuclear Science and Technology Supplement 1, 845–849.

Van Dorsselaere, J.-P., Seropian, C., Chatelard, P., Jacq, F., Fleurot, J., Giordano, P., Reinke, N., Schwinges, B., Allelein, H.J., Luther, W., 2009. The ASTEC integral code for severe accident simulation. Nuclear Technology 165, 293–307.

White, R.J., 2004. The development of grain-face porosity in irradiated oxide fuel. Journal of Nuclear Materials 325, 51–77.

Annals of Nuclear Energy 168 (2022) 108900

Contents lists available at ScienceDirect

Annals of Nuclear Energy

journal homepage: www.elsevier.com/locate/anucene

Influence of SIC control rod material on the iodine release in case of nuclear severe accident – Chemical reactivity with fission products in thermal conditions of RCS

A.C. Grégoire [a,*], S. Sobanska [b], C. Tornabene [a], D. Talaga [b], A.S. Mamede [c], S. Morin [a], L. Cantrel [a]

[a] Institut de Radioprotection et de Sûreté Nucléaire, Pôle Sûreté Nucléaire, CEN Cadarache, Saint Paul lez Durance F-13115, France
[b] Institut des Sciences Moléculaires, Université de Bordeaux, UMR5255 CNRS, 33405 Talence cedex, France
[c] Unité de Catalyse et Chimie du Solide, Université de Lille, CNRS, Centrale Lille, Université d'Artois, UMR 8181, F-59000 Lille, France

ARTICLE INFO

Article history:
Received 2 September 2021
Received in revised form 24 November 2021
Accepted 6 December 2021

Keywords:
Severe accident
Reactor Coolant System
Metallic molybdates
Chemical reactivity
Iodine transport

ABSTRACT

The effect of Silver-Indium-Cadmiun (SIC) control rod on the transport of volatile fission products (I, Cs, Mo) in conditions of a Reactor Coolant System under NPP severe accident was investigated within three semi-integral tests in a thermal gradient tube. The experiments addressed separately the effect of each SIC element. Nature of transported and deposited species was investigated by ICP MS, ESEM-EDX, Raman Microspectrometry, XRD and XPS techniques.

For the first time, numerous metallic molybdates involving SIC components were evidenced. The formation of such metallic molybdates competes with the formation of Cs-molybdate and may in certain conditions strongly reduce the scavenging effect of Mo towards Cs. As a result the nature of transported iodine can be strongly modified, compared to chemical systems involving only Mo, Cs and I. The data obtained are useful to guide what species have to be added in the thermodynamic database used in the SA simulation software.

1. Introduction

During a severe accident (SA) occurring on a nuclear power plant (NPP), strong releases of volatile fission products (FPs) such as iodine, caesium or even molybdenum are expected. These FPs can contribute to high radiological consequences in case of releases into the environment following early containment venting procedure or containment failure - as was the case during the Fukushima Daichi NPP accident (Masson et al., 2011; Chino et al., 2011; Huh et al., 2012; Stohl et al., 2012; Lebel et al., 2016). In such situation, the accident management is strongly linked to the physico-chemical forms of the released radioisotopes, especially for iodine as gaseous or particulates species do not contribute to the same extent to radiological consequences (Hoeve and Jacobson, 2012; Geng et al., 2017; Masson et al., 2019).

In early accidental phase, the nature of the radioisotope released from the Reactor Coolant System (RCS) and accumulated in the nuclear containment building is directly linked to the physico-chemical phenomena prevailing in the RCS. Little information is available in the literature concerning the chemical speciation inside the RCS (Clément et al., 2007). The phenomena occurring in the RCS during a SA are indeed very complex involving strong thermal gradients, rapid atmosphere changes from reducing to oxidizing conditions, complex chemical systems involving some more or less volatile FPs (Cs, I, Mo, Te), control rod (CR material such as Ag, In, Cd and B) and structure materials with release kinetics and thus element ratio depending on the extent of fuel degradation.

The chemical form of iodine and its behaviour after entering containment from the RCS break were previously documented in NUREG/CR-5732 (Beahm et al., 1992). On the basis of thermodynamic computation it was considered that iodine entering the containment was at least 95 % under CsI form with the remaining 5% as I and HI under gaseous form. For caesium, the main prevailing assumption is that the CsOH is in large excess (Williams, 1994).

Glossary: ASTEC, Accident Source Term Evaluation Code; BSE, Back Scattering Electron imaging; CHIP, Chemistry Iodine Primary circuit; EdF, Electricité de France; ESEM-EDX, Environmental Scanning Electron Microscopy – Energy Dispersive X-ray Spectroscopy; FD NPP, Fukushima Daiichi Nuclear Power Plants; FP, Fission Product; GAEC, Generation of AErosols in the reactor Coolant system; ICP AES, Inductively Coupled Plasma – Atomic Emission Spectroscopy; ICP MS, Inductively Coupled Plasma – Mass Spectrometry; LWR, Light Water Reactor; PWR, pressurised Water reactor; RCS, reactor Coolant System; RMS, Raman Micro Spectrometry; SA, Severe Accident; SE, Secondary Electron imaging; SIC CR, Silver-Indium-Cadmium Control Rod; XRD, X-Ray Diffraction.

* Corresponding author.

https://doi.org/10.1016/j.anucene.2021.108900
0306-4549/

After extensive experimental research and modelling on fission product release and transport in severe accident conditions over the past thirty years, the situation appears much more complex.

Indeed the large scale Phébus FP test series showed that in addition to CsI, other condensable iodide forms may exist in the RCS (Girault and Payot, 2013). Indeed, the deposits collected on the thermal gradient tubes (700–150 °C temperature range) of the Phébus experimental circuit and determined by γ-spectrometric measurements presented several iodine condensation peaks not systematically correlated to caesium deposit. Moreover, the fractions of aerosol/gaseous iodine transported into the Phébus containment vessel (150 °C) were variable and strongly dependent on the test scenario (Girault et al., 2010, Girault et al., 2012, Haste et al., 2013), suggesting a complex chemistry during the transit though the experimental circuits. In addition, the small-scale Falcon ISP1/2 tests performed with simulant fuel pellets (Williams, 1994) and VERCORS HT2/3 tests performed with actual spent fuel pellets (Pontillon and Ducros, 2010) supported also the assumption of iodine being transported in others forms than CsI; CdI_2 is suggested as a possible alternative. Deposition profile of the other main released FPs (Mo, Cs, Te ...) and CR elements (Ag, In, Cd) in the thermal gradient was also determined for these tests either by γ-spectrometry (VERCORS HT test) or after chemical leaching and elemental analysis (ICP OES – Falcon tests). Based on the elements condensation peaks, the formation of various metallic molybdates were put forward (McFarlane et al., 2002) as well as the formation of CsTe species (McFarlane and Leblanc, 1996), (de Boer and Cordfunke, 1995) supporting the fact that caesium chemistry is also more complex than initially expected. The formation of caesium borates was also assumed based on separate effect tests (Bowsher and Dickinson, 1986)(Bowsher and Nichols, 1985)(Elrick et al., 1987) but boron deposition profile could not be determined (no γ-emitter). The use of actual spent fuel for such experiments allows to be as close as possible of a reactor case but induces experimental issues due to the handling of highly reactive samples. As a consequence, the characterization of the deposited/-transported material was limited mainly to γ-spectrometry which cannot provide any chemical speciation. Interpretation of such experiments relies thus mostly on computer simulations which in turn needs reliable thermodynamic and thermokinetic data for chemistry of FPs and CR material at high temperature, even if recent works were performed to improve these data (Grégoire et al., 2017; Miyahara et al., 2019) works are still ongoing on this.

In order to improve the understanding of the main chemical formation, decomposition, deposition processes in which released FPs and control rod elements are involved in the RCS during a SA and also to build an experimental database allowing the validation process for models, the ISTP-CHIP (2005–2012) and the follow-up CHIP+ (2012–2018) experimental programs were launched at IRSN (Clément and Zeyen, 2005). The CHIP (Chemistry Iodine Primary circuit) experimental set-up and its small scale GAEC (Generation of AErosols in the reactor Coolant system) analog were designed as open flow reactors in which reagents are continuously mixed at high temperature (1600 °C) and transported into a controlled thermal profile using carrier gas (steam/H_2) reproducing as much as possible conditions of the RCS of a Light Water Reactor (LWR) during a SA. Chemical systems involving iodine, main released FPs which can interfere with iodine (Cs and Mo) and control rod material (B, Cd, Ag and In) were considered. Tellurium was not retained as this FP is about 5 times less abundant than Cs in the spent fuel (Jacquemain et al., 2000; Grégoire et al., 2008) and is not expected to have a significant influence on Cs reactivity. Only the natural stable isotopes of these elements were handled for safety consideration. One of the main issues was to achieve element concentrations and relative ratio as relevant as possible of conditions of interest. Deposited species, transported aerosols and gases were collected for off-line characterization with a focus on gaseous iodine quantification. Working with stable elements allowed involving various surface analytical techniques capable to unravel the nature of deposited and transported species that could not be applied for experiments with highly radioactive material. The studied chemical systems involved firstly only iodine with carrier gas (the I-O–H system) and were then extended to other main FPs (Cs, Mo) and Cr materials involving up to 7 elements (Grégoire et al., 2018).

The experiments performed on the I-O–H system evidenced kinetic limitations for gas phase iodine reactivity (Grégoire et al., 2017). The addition of caesium, in quite large excess relative to iodine to be relevant of severe accident scenarios, resulted in quantitative formation of caesium iodide, preventing thus any gaseous iodine transport whatever the gas atmosphere (steam or steam/hydrogen). No relevant kinetic limitations were evidenced (Grégoire et al., 2015), so the main caesium species (CsI, CsOH) can be simulated with the thermodynamic equilibrium assumption. Mo is expected to act as a Cs sink by the formation in the gas phase of stables caesium molybdates as expected by thermochemical data (Tangri et al. 1989; Cordfunke and Konings, 1990) which then condenses on the colder parts of the RCS. The formation of caesium molybdates of various composition could be clearly identified in the deposits collected in the test lines (Lacoue-Nègre, 2010; Gouello et al., 2013; Grégoire et al., 2015) when both Mo and Cs were considered. The reactivity of the Mo-Cs-I-O–H system is quite well reproduced by simulation tools and its consequence on iodine transport well predicted both in reductive or oxidative atmosphere. First results obtained from the B-Cs-I-O–H systems tends to show that the formation of caesium borates is less favourable (Gouello, 2012; Grégoire and Mutelle, 2012).

As a follow up to the test performed only with the main FPs, the study of the extended systems addressed separately the influence of each element of the Silver-Indium-Cadmium control rod compared to tests performed with the Mo-Cs-I-O–H system in steam condition. In steam condition, we have demonstrated that the formation of stable caesium molybdates prevents CsI recombination and thus enhance the release of gaseous iodine (Grégoire et al., 2015). On the contrary, silver, indium and cadmium (SIC) are expected to react with iodine to form metallic iodide (AgI, CdI_2 and possibly InI_x species). Nevertheless, the formation of metal-molybdates is not excluded that would compete either with metal iodide or caesium molybdate generation.

Within that context this work aims at evaluating the chemical reactivity between FPs (I, Cs and Mo) and SIC control rod material (either Ag, or In or Cd) in thermal conditions of a RCS in order to highlight the role of SIC in the release of gaseous iodine during a SA. The main objective was to assess the influence of each additional element (Ag, In, Cd) on the nature of deposited and transported species compared to the Mo-Cs-I-O–H chemical system alone. A special attention was brought on the formation of metallic iodide and metallic molybdates which may play a key role on gaseous iodine persistence at 150 °C. Three tests were performed; each based on the Mo-Cs-I-O–H system in steam conditions plus one element of the SIC control rod: the [In + MoCsI] test, the [Cd + MoCsI] test and finally the [Ag + MoCsI] test. We are thus presenting the main results obtained from the extended system test series with a special attention on the determination of the deposited and transported species.

Hereafter, the CHIP experimental set-up, the test conditions and post-test operations including the analytical techniques dedicated to species identification will be detailed. Experimental results will be focused on element transport in the CHIP line with a special attention on iodine behaviour and the identification of the condensed species. Discussion will be held in comparison with literature data.

2. Material and methods

2.1. CHIP line description

The CHIP line has been described previously (Grégoire *et al.*, 2012; 2015; 2018) so that only features concerning injection of I, Cs, Mo plus Cd, In and Ag will be detailed here.

The test line (3.5 m long and 60 mm in internal diameter) is composed of two tubes assembled by a specific junction (Fig. 1): an alumina tube (2 m) located in the high temperature zone and a stainless steel tube (1.5 m) in the transport zone - simulating RCS piping. The thermal profile is obtained by mean of several furnaces (High temperature tri zone CARBOLITE furnace completed by a series of WATTLOW ceramic heaters) and is composed of three zones (injection zone, reaction zone and aerosol/deposit and gas collection zone). Thermal profile is obtained after ~ 20–24 h of slow heating. Residence time (10–11 s) from the high temperature zone to the outlet is representative of an accident scenario featuring a break in the cold leg of the RCS.

In order to allow working with various chemical systems featuring a wide range of concentrations and elemental ratio, elements are injected either in their metal, oxide or hydroxide form, depending on their stability and volatility. One major issue to be addressed was the achievement of a controlled injection of cadmium (as Cd metal), indium (as In_2O_3 powder) and silver (as Ag metal) so as to achieve concentrations and ratios relative to iodine relevant of an accidental scenario as observed during the Phébus FP tests (Grégoire and Haste, 2013; Haste et al., 2013; Girault and Payot, 2013). Several years of development were necessary to succeed injecting those refractive and poorly soluble elements in a controlled way.

Except for silver, vapours or aerosols are produced by the mean of external generators connected to the inlet flange. The carrier gas (steam/Ar or He) is directly injected at the main line inlet (800 °C) whereas other reagents are transported directly into the high temperature zone via separate alumina nozzles. At 1600 °C, all the injected species are under vapour form at thermodynamic equilibrium. Gaseous iodine is obtained by sublimation of molecular iodine pellets. Caesium, molybdenum and cadmium vapours are produced by vaporization of respectively caesium hydroxide, molybdenum trioxide and metallic cadmium. Indium oxide vapours are obtained by the injection of dry indium oxide aerosols produced at room temperature (RBG 1000 aerosol generator, PALAS) and then gradually vaporised in the pre-heating zone. Being more refractive than the other elements, silver is directly vaporised in the main line (at temperatures above 1200 °C) from silver powder deposited in crucibles. At steady state, these generators produce a stable mass flow rate of each reagent for several hours – allowing thus the different sampling operations.

Apart from the carrier gas, at the outlet of the transport zone and in the sampling lines (150 °C), only iodine can be possibly found in gaseous form, the other elements (FPs simulant and CR material) being transported as particulate material at this temperature level. In order to quantify the fraction of gaseous iodine released at the outlet, the CHIP line is terminated by an integral aerosol filter followed by gas scrubbers filled with an alkaline solution dedicated to trap gaseous iodine species and condensed steam. The integral aerosol filter is composed of quartz fibre cartridge with 0.9 μm porosity resulting in aerosol retention superior to 99.9%, for aerosol diameter ranging between 0.3 and 0.7 μm (see Table S1 in SD). The line outlet collects transported species over the entire test. Several sampling lines which can be sequentially operated, are also implemented on the CHIP experimental set-up. These lines are connected to the main CHIP line just before the outlet filter (Fig. 1) and dedicated to sample a fraction (2 up to 8%) of the main flow at 150 °C (temperature corresponding to a cold leg break of a RCS). These lines can be operated for short period and are able to catch changes in the transported flow depending on the test conditions. Different design have been developed to address different sampling objectives:

- collection of the transported aerosols and quantification of the total released gaseous iodine fraction. Such line is implemented with an inlet quartz fibre membrane filter (0.7 μm porosity resulting in aerosol retention > 99%, see Table S1) allowing to trap the transported aerosols and downstream gas scrubbers filled with alkaline media (NaOH 0.1 M) in which all expected gaseous iodine species are readily soluble allowing the quantification of the total iodine gaseous fraction. Such line is labelled "$I_{aerosol\&gas}$ line";
- determination of the gaseous iodine speciation (Gouello et al., 2013, Grégoire et al., 2015). The line is still composed of an inlet filter but in this case, the gas scrubbers located downstream are filled with a biphasic mix of toluene dedicated for I_2 trapping and diluted nitric acid (0.015 M) dedicated for the other inorganic gaseous iodine species (e.g. HI, HOI) allowing to determine the composition of the gaseous iodine fraction (molecular iodine vs other inorganic forms). Such line configuration is labelled "I_{gas} speciation line";
- quantification of molecular iodine in presence of reactive species. As mentioned by Gouello et al.(2013), the drawback of the "$I_{aerosol\&gas}$ line" and "I_{gas} speciation line" is the possible loss of gaseous iodine due to interactions between gaseous iodine and reactive aerosols trapped on the filter (e.g. CsOH for

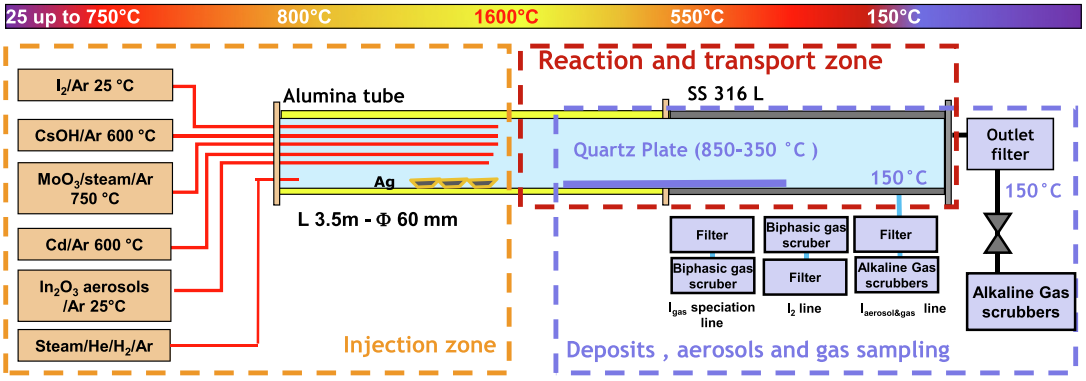

Fig. 1. CHIP line configuration for injection of Ag, In and Cd.

instance). In order to address this difficulty, a third line configuration was developed in which the flow composed of gaseous species and aerosols is directed in gas scrubbers filled with a mix of toluene/diluted nitric acid. Molecular iodine is collected in the organic phase whereas inorganic iodine species and other aerosols are trapped in the aqueous phase. The line is terminated by a filter to trap the aerosols reminder. In such configuration, only the fraction of molecular iodine can be determined. Such line design is labelled "I_2 line".

The redundancy of information which can be gained from the different sampling lines allows to characterize the iodine release at 150 °C (gas/aerosol distribution, nature of gaseous iodine forms) with a good reliability.

In addition to the sampling of material transported at 150 °C, a quartz plate is inserted in the main line for collecting condensed material in 850–350 °C temperature range. Thus, two types of samples were collected: (i) condensed phases deposited on quartz substrate (1 × 5 cm) between 850 and 350 °C and (ii) particles sampled at 150 °C using a glass fibre filter.

Specification on line structure and chemical reagents are displayed in the Supplementary Information data files (Table S1 and Table S2) as well as the thermal profile in the transport zone (Figure S1).

2.2. Test conditions

Three tests were performed consisting in injecting the Mo-Cs-I-O–H chemical system in steam as previously described in Grégoire et al. (2015) (the [PL_MoCsI_3] test) plus one element representative of the SIC control rod: the [In + MoCsI] test, the [Cd + MoCsI] test and finally the [Ag + MoCsI] test.

The [PL_MoCsI_3] test will serve as reference test; it featured steam atmosphere with a chemical system involving an excess of Cs relative to I (Cs/I molar ratio of ~ 4) and Mo itself in excess relative to Cs (Mo/Cs ~ 3) in the range of ratios observed during Phébus FP test sequences (Haste et al., 2013). The steam atmosphere is relevant of the Phébus test main release phase during which the transport of Cs, I, Mo in the experimental circuit was observed (Grégoire and Haste, 2013). The thermal hydraulic conditions simulate as close as possible a large RCS cold leg with high thermal gradient and short residence time in the transport zone (Jacquemain, 2015). Inert gas (Ar or He) was added to adjust the residence time of elements in the CHIP line. In such conditions, formation of caesium molybdates partially prevents CsI to be formed in the gas phase and contributes to the transport of high gaseous iodine fraction (up to 90% of injected iodine mass, Grégoire et al., 2015).

[In + MoCsI], [Cd + MoCsI] and [Ag + MoCsI] tests with extended chemical systems were performed with similar element injection for Mo, Cs and I. The SIC CR elements were injected in large excess relative to iodine. Similar thermal gradient and residence time were applied. As for the carrier gas composition, a mix of steam/inert gas was injected for the [In + MoCsI] and [Cd + MoCsI] tests as it was observed that those CR elements were also released during the Phébus tests main release phase (in steam atmosphere). A low amount of hydrogen (1.8% of the total atmosphere) was added for the test featuring silver, as this element was released later during the so-called "second oxidation phase" where low amounts of H_2 were measured in the Phébus circuit (Grégoire and Haste, 2013).

The thermal hydraulic conditions and element generation are reported in Table 1. Conditions of the reference [PL_MoCsI_3] test are recalled too. The element mean mass flow rates were determined from the total injected element masses (based on the final element mass distribution in the line) and the injection duration assuming a steady injection rate. Given uncertainty on ICP-MS analyses of each leaching solution, an average uncertainty of +/-7 % could be estimated for the element mean mass flow rate. As silver crucibles were placed directly in the main line, significant vaporization occurred as soon as the temperature in the crucible reached ~ 1100 °C. As a consequence, injection of low silver level in the line could not be avoided during the pre-heating phase, before injection of the other elements. Given the relative short duration of this pre-heating phase and low carrier gas flow applied during this phase, it is assumed that the main part of silver was injected during the main phase of the test as the other elements. The silver mass flow rate (displayed in Table 1) was determined from the overall silver mass collected in the CHIP line, including the deposits formed during the pre-heating phase and should be thus considered as a maximal value.

2.3. Element mass concentration and distribution along the thermal profile of CHIP line

In order to determine the element distribution in the CHIP line, several successive washing operations were performed post-test to solubilize the deposited material. For the test series with injection of SIC control rod material, the following solutions were used:

- alkaline media (NaOH 0.1 M) for easily soluble species such as I_2, HI, HOI, CsI or CdI_2 and partly caesium molybdates;
- nitric acid (2 M) for an overall recovery of molybdates (MoO_3, molybdic acid, metallic molybdates) and cadmium species (Cd metal, oxide and possibly hydroxide);
- nitric acid (5 M) for metallic silver;
- boiling concentrated nitric acid (8 M) for indium oxides.

A last treatment was necessary for AgI recovery as this species is still insoluble in concentrated acidic media. This treatment (Spies, 1936; Wang et al., 1989) is based on the decomposition of AgI by hot aqua regia (1/3 nitric acid; 2/3 hydrochloric acid). In presence of a large excess of chlorides, the insoluble form of AgCl is favoured and I solubilized as iodine monochloride (ICl^-). The solution is then filtered and the filtrate treated with sodium hydroxide (final pH above 13) allowing to hydrolyse the iodine monochloride and form iodates and iodides. Analyses of solubilised iodine allows then to quantify the amount of silver iodide. No similar approach could be developed for CdI_2/CsI separation and quantification due to their strong solubility in aqueous media. Formation of such species will be then deduced by default of other species.

The solutions were then analysed by multi-elemental analysis techniques: Inductively Coupled Plasma Mass-Spectrometry (ICP-MS) for I, Cs, Mo, Cd and In (Varian 810 MS) or Inductively Coupled Plasma Atomic Emission Spectroscopy (ICP-AES) for Ag (Perkin Elmer, 8100) with a relative uncertainty of +/-8% at 95% confidence level. UV–visible quantification of I_2 in toluene was performed with an Agilent 8453 spectrometer at 309 nm and 498 nm with an uncertainty of +/- 6% (at 95 % confidence level).

2.4. Characterization of collected material

Material deposited in the thermal gradient onto quartz plate samples and aerosols collected on quartz filters, were post-test analysed. Size and morphology have been determined by Environmental Scanning Electron Microscopy (ESEM Quanta 200 FEI®) used in low vacuum mode (50–130 Pa), allowing to examine sample without metallisation. Measurements were carried out at an accelerating voltage of 10–25 kV to perform either Secondary electron or Back Scattering Electron (BSE) imaging with a lateral resolution of several hundred of nm. Semi-quantitative elemental

Table 1
Conditions of [In + MoCsI], [Cd + MoCsI] and [Ag + MoCsI] tests and [PL_MoCsI_3] reference test.

Test Name	[In + MoCsI]	[Cd + MoCsI]	[Ag + MoCsI]	[PL_MoCsI_3] (Grégoire et al., 2015).
Test Loop	CHIP PL			
Main test tube material	Alumina (HT zone – 600 °C) / stainless steel (600 °C-150 °C)			
Thermal hydraulic conditions:				
Pressure (Mpa)	0.2 MPa			
Carrier gas flow (l/min – NPT)	38.2 l/min	35.3 l/min	35.1 l/min	34.3 l/min
Max. temperature in the HT zone (°C)	1600 °C			
Temperature profile in the transport zone	Strong temperature decrease to outlet (150 °C)			
Residence time in the transport zone (s)	~12 s			
Test duration (min)	357	337	338	421
Carrier gas composition (v/v %)	H_2O/Ar 45.7/54.3	H_2O/He/Ar 49.4/ 42.8/7.8	H_2O/Ar/H_2 49.6/48.6/1.8	H_2O/He/Ar 50.8/44.1/5.1
Element injection mean mass flow rate (mol/s) in the HT zone‡				
Iodine (as I_2)	1.8 10^{-7} mol/s	1.7 10^{-7} mol/s	1.5 10^{-7} mol/s	1.5 10^{-7} mol/s
Caesium (as CsOH)	4.4 10^{-7} mol/s	5.5 10^{-7} mol/s	5.6 10^{-7} mol/s	6.0 10^{-7} mol/s
Molybdenum (as MoO_3)	2.2 10^{-6} mol/s	2.0 10^{-6} mol/s	2.1 10^{-6} mol/s	1.9 10^{-6} mol/s
Indium (as In_2O_3)	8.1 10^{-7} mol/s	–	–	–
Cadmium (as Cd metal)		2.1 10^{-5} mol/s	–	–
Silver (as Ag metal)		–	7.4 10^{-6} mol/s[a]	–

NPT conditions: 0 °C, 0.101325 MPa ; ‡ Element flow rate based on the final mass distribution in the line and assuming a steady injection rate (relative uncertainties below ± 5% except for iodine in the [Ag + MoCsI] test : ± 50%); [a:] maximum flow rate as silver vaporization may also occur during the pre-heating phase.

composition was obtained by an energy-dispersive X-ray detector (EDX, Quantax-Roentec®) coupled to the ESEM microscope. ZAF (Atomic Number Z, Absorption and Fluorescence) corrections were applied. Elemental composition of single particles and cartography of larger zones (~20*20 up to 100*100 μm^2) could be determined with a resolution of ~ 1 μm^3. Raman microspectrometry (RMS) was performed on the same sample zones to identify both elemental and molecular composition of condensed species. The Raman spectra and optical images were recorded by Labspec6 using a confocal Raman microspectrometer (Labram HR evolution, Horiba Jobin Yvon) equipped with a 100 × 0.85 numerical aperture objective (Olympus). An excitation Nd:YAG laser with a wavelength of 532 nm and 6 mW power was used, and the scattered Raman signals were detected using an air-cooled multichannel charge-coupled device (CCD) detector. The data acquisition time for each measurement was 30 s with 2 accumulations. The spectral resolution was 1.8 cm^{-1} using 1800 gr/mm grazing. A spatial resolution of 1 μm^3 is estimated. Measurements were carried out in both single point or automated imaging modes. Surfaces of 10*10 μm^2 up to 50*50 $\mu m^2$with ~ 2 μm as a minimum step (representing 2000–5000 spectra per zone) were scanned. After spectral treatment (LABSPEC6 software), the components were identified by comparison with reference spectra from Raman libraries and literature data or by acquiring spectra from reference materials. Complementary identification of samples was obtained from X-ray diffraction (XRD) analyses. Diffractograms were obtained using a AXS D8 or D2 PHASER diffractometers (Bruker) operating with Cu Kα radiation (λ = 1.54 Å). Samples were analysed at room temperature in the 2θ range of 10–70°, with a step size of 0.02°.

Complementary, speciation of Cd, Mo, Cs and I in samples was provided by X-ray Photoelectron Spectroscopy (XPS). Measurements were carried out on a Kratos Analytical AXIS Ultra^{DLD} spectrometer using monochromatic Al Kα source (1486.6 eV). Calibration was performed by taking the adventitious C1s peak (binding energy, BE = 285.0 eV). The uncertainties on the binding energy and on quantitative elemental analysis are +/-0.1 eV and +/- 10–20%, respectively. Assignment of photoelectron peaks was performed by comparison with photoelectron peaks acquired on reference compounds.

3. Results

3.1. Element distribution along the CHIP line and transported iodine forms

Element distributions are reported in Table 2 in terms of high/low temperature deposition, aerosol/gas transport at 150 °C (conditions of a cold leg break). Distributions are expressed in % relative to the total mass injected in the high temperature (HT) zone for each element.

3.1.1. Nature of iodine released at 150 °C

The sampling lines allowed to evaluate the level and nature of iodine release at 150 °C for each test. Results are presented in the Table 2 as gaseous form "I(gas)" and aerosol form "I(aerosol)". The nature of each form is detailed in "Iodine gas identification", and "Iodine aerosol identification" respectively, whenever it could be determined.

For the [In + MoCsI] test, indium was injected in excess relative to iodine (In/I ~ 4.4), this weak excess is within the range of In/I ratios observed during the Phébus FP Tests (Grégoire et al., 2008; Jacquemain et al., 2000). Almost only gaseous iodine was released at 150 °C ("$I_{aerosol\&gas}$ line" data), with average fraction close to 90% at 150 °C (relative to the initial iodine mass injected in the HT zone). The molecular iodine fraction can be determined from the "I2 line"data. For this test, the sampling in the "Igas speciation line" failed, so that the fraction of other inorganic gaseous iodine species is determined by difference between the "$I_{aerosol\&gas}$ line" and "I2 line" data. Roughly one half of the gaseous iodine is identified as molecular iodine, the rest being attributed to an inorganic form, assumed to be mostly HI because the formation of HOI is less probable in such conditions (Grégoire et al., 2017). Results are comparable to the reference [PL_MoCsI_3] test, indicating that the presence of indium does not significantly alter the chemical Mo-Cs-I-O–H system in steam atmosphere. As a consequence, it is confirmed that aerosols composed of InIx species are not formed in these experimental conditions.

For the [Cd + MoCsI] test, cadmium vapours were generated in a very large excess relative to iodine (Cd/I ~ 125, much higher than

Table 2
[In + MoCsI], [Cd + MoCsI], [Ag + MoCsI] tests and [PL_MoCsI_3] reference test – Element distribution and iodine Gas/aerosol partition.

Test Name	[In +MoCsI]	[Cd + MoCsI]	[Ag + MoCsI]	[PL_MoCsI_3] (Grégoire et al., 2015).
Carrier Gas composition (v/v %)	Ar/H_2O 54.3/45.7	$H_2O/He/Ar$ 49.4/42.8/7.8	$H_2O/Ar/H_2$ 49.6/48.6/1.8	$H_2O/He/Ar$ 50.8/44.1/5.1
Element molar Ratio in the HT zone				
Cs/I	**2.5 ± 0.2**	**3.1 ± 0.2**	**3.6 ± 1.8**	**4.0 ± 0.4**
Mo/Cs	**5.0 ± 0.4**	**3.7 ± 0.2**	**3.7 ± 0.3**	**3.2 ± 0.3**
X/I (X = Cd or In or Ag)	**4.5 ± 0.3**	**126 ± 9**	**48 ± 24**[a]	
Mo/X	**2.7 ± 0.2**	**0.1 ± 0.01**	**0.3 ± 0.02**	
Element molar ratio in the sampling lines				
At 150 °C				
Cs/I	2.2 ± 0.5	3.1 ± 0.6	~3–12	
Mo/Cs	5.3 ± 0.3	2.3 ± 0.5	1.9 ± 0.1	2.7 ± 0.6
X/I (X = Cd or In or Ag)	2.7 ± 1	48 ± 23	~20–65	3.4 ± 0.5
Deposition in the main line	1600–600 °C (alumina tube) and *600–150 °C (stainless steel tube)*			
I	0% *(0.1 ± 0.01)%*	0% *(13 ± 1.3)%*	0% *(15 ± 7)%*	0 % *(0.2 ± 0.02)%*
Cs	(13 ± 1.2)% *(13 ± 1.2)%*	(10 ± 0.9)% *(16 ± 1.5)%*	(6 ± 0.6)% *(14 ± 0.1)%*	(11 ± 0.9)% *(16 ± 1.3)%*
Mo	(7.0 ± 0.6)% *(21 ± 2)%*	(31 ± 2.8)% *(10 ± 0.9)%*	(47 ± 4.4)% *(10 ± 0.9)%*	(4.0 ± 0.3)% *(21 ± 1.7)%*
X (X = Cd or In or Ag)	(42 ± 3.8)% *(10 ± 0.9)%*	(3.0 ± 0.3)% *(41 ± 3.8)%*	(57 ± 5.4)% *(6.0 ± 0.6)%*	
Sampling line data: iodine transport at 150 °C				
I (gas)	**(89.9 ± 6.5)%** [b]	**(28 ± 6.3)%** [d] **Other lines < 1%**	**< (2 ± 1)%** [b]	**(88.3 ± 6.4)%**[b, c]
Iodine gas identification				
I as I_2	~ 1/2 [d]	1	nd	~ 2/3[c, d]
I as HI	~ 1/2[b, d]	–	nd	~ 1/3[c, d]
I(aerosol)	**(10 ± 6.5)%** [b]	**(59 ± 6.3)%** [d] **Other lines> 86%**	**> (83 ± 8)%** [b]	**(11.5 ± 6.4)%** [b, c]
Iodine aerosol identification	nd	Traces of CdI_2^s	AgI ~ 1/10 to 1/4[b]	nd
Sampling line data: transport of other element 150 °C				
Cs (aerosol)	(74 ± 2.0)%	(74 ± 2.0)%	(80 ± 1.5)%	(73 ± 1.6)%
Mo (aerosol)	(72 ± 2.0)%	(59 ± 3.0)%	(43 ± 4.4)%	(75 ± 1.7)%
X (aerosol) (X = Cd or In or Ag)	(48 ± 4.0)%	(56 ± 4.0)%	(37 ± 5.4)%	

Data rounded to two significant figures; **a**: maximum ratio as silver vaporization may also occur during the heating phase; **b** : '$I_{aerosol\&gas}$ line' data; **c**: 'I_g speciation line' data ; **d**: 'I_2 line' data ; max. value for I_g (resp. min value for I_{aer}); **e**: Cd and I detected on few particles (main line deposit -EDX examination).

observed in Phébus tests). For both "$I_{aerosol\&gas}$ line" and "I_{gas} speciation line", the gaseous iodine fraction detected downstream of the aerosol filter is very low (< ~1%). On the contrary, a significant amount of gaseous molecular iodine is observed in the "I_2 line" (without inlet filter), representing 28% of initially injected gaseous iodine. The fact that a measurable gaseous iodine fraction could be detected only in the "I_2 line" can be accounted for by a significant retention of gaseous iodine species on aerosols collected on the inlet filter of the other sampling lines. Such retention was not observed during the reference [In + MoCsI] and [PL_MoCsI_3] tests, and may be due to presence of cadmium species in the case of the [Cd + MoCsI] test. We thus retain the value gained from the "I_2 line" (28% of initially injected iodine) for the gaseous iodine fraction. This value is considered as a minimum as only I_2 fraction could be quantified in this line. The gaseous iodine fraction is nevertheless almost three times lower than that observed during the [PL_MoCsI_3] reference test (88.3%), indicating that cadmium species contribute to reduce the transport of gaseous iodine compared to the Mo-Cs-I-O–H system in steam. Nevertheless, such cadmium effect is observed for a very large Cd/I ratio.

The [Ag + MoCsI] test was performed with a large excess of silver relative to iodine (Ag/I ~ 55), thermo-hydraulic conditions close to the reference test and a low level of hydrogen (H2/H2O ~ 0.04) to limit possible silver oxidation. Contrarily to the tests performed with In and Cd, the "I2 line" turned out to be inefficient to trap molecular iodine (if any) in presence of metallic silver particles. Indeed, we experimentally checked that silver particles react readily and quantitatively with molecular iodine dissolved in toluene to form silver iodide. As a result, we retain only the data gained from the "Iaerosol&gas line" which shows a very low gaseous iodine fraction (<2%). One should keep in mind that this gaseous iodine fraction may be underestimated owing to possible gaseous iodine retention on the particles trapped on the inlet filter of the sampling line (similarly to the [Cd + MoCsI] test). Iodine-containing particles (expected to be AgI or CsI) turned out to be mainly soluble in aqueous media suggesting that formation of insoluble AgI is not the main reaction pathway leading to the release of iodine as aerosols. Indeed, only 10%-25% of iodine collected in the sampling lines could be identified as AgI, that is not consistent with thermochemical simulations predicting>75% of AgI. As a consequence, the most probable iodine form to be released at 150 °C is CsI.

Although the iodine nature at 150 °C (cold leg break conditions) cannot be fully described in presence of cadmium or silver, these control rod materials tend to lower the gaseous iodine fraction formed along the thermal gradient.

3.1.2. Element line distribution – Comparison with reference test [PL_MoCsI_3]

Distribution of elements in the CHIP line is too coarse to allow for the identification of species condensation peak. CHIP line was divided into two parts labelled as "main line": the alumina tube for a temperature range of 1600–600 °C and the stainless steel tube for 600–150 °C (see Table 2). Except for iodine, the other element found at the line outlet (at 150 °C) are attributed to transport in aerosol form owing to their low volatility. The following statements can be put forward based on the experimental results and compared with the [PL_MoCsI_3] reference test:

For iodine, no deposition is observed above 600 °C for all tests. Deposition below 600 °C is very low when iodine is mainly trans-

ported at the line outlet in gaseous form as for the [In + MoCsI] test (0.1% of total injection iodine found in the 600–150 °C temperature range) or the [PL_MoCsI_3] reference test. When iodine is found mainly transported in aerosol form at 150 °C, a significant iodine deposition is observed but only below 600 °C : 13% for the [Cd + MoCsI] test and 15% for the [Ag + MoCsI] test. Such iodine deposition in the CHIP line results from vapour condensation or aerosol deposition of iodine containing species as already observed in a previous CHIP test (Grégoire et al., 2015).

Mo distribution in the CHIP line for the [In + MoCsI] test shows 7% deposited above 600 °C, 21% deposited in the 600–150 °C temperature range and 72% transported as aerosols. These values are comparable to that obtained for the reference test. On the contrary, in presence of Cd or Ag, Mo high temperature deposition is enhanced up to 31% ([Cd + MoCsI] test) and 47% ([Ag + MoCsI] test) simultaneously to a strong decrease of the deposition in the stainless steel tube (10% of Mo deposited below 600 °C for both tests) and to a decrease of Mo found transported at 150 °C (59% for the [Cd + MoCsI] test and 43% for the [Ag + MoCsI] test). This distribution is comparable to that observed for the MoCsI test in steam/hydrogen (Grégoire et al., 2015), in which a significant reduction of Mo(VI) to the less volatile Mo(IV) and Mo(V) compounds was evidenced. Indeed reduction of Mo is not excluded as oxidation of Cd or Ag in the steam flow at high temperature results in the production of low amounts of hydrogen capable of reducing (even partly) the injected MoO_3 (in addition to the injected low hydrogen flow for the [Ag + MoCsI] test). As consequence Mo may be less reactive to form metallic molybdates and thus may contribute to the increased formation of metallic iodides (CsI, CdI_2 and to a less extent AgI).

Indium and silver are mainly found deposited in the high temperature zone above 600 °C (alumina tube) consistently with their strong refractive properties. For the [In + MoCsI] test, 42% of In is found in this zone, whereas deposition below 600 °C represents only 10% of initially injected In. For the [Ag + MoCsI] test, 57% of silver is found deposited above 600 °C and 6% below. On the contrary, cadmium which is more volatile is mainly found in the 600–150 °C temperature zone (41% for the [Cd + MoCsI] test and less at high temperature (3% above 600 °C).

Only caesium deposition pattern does not show significant changes in this test series: high temperature deposition (above 600 °C) represents 6–13% of initially injected caesium, deposition in the 600–150 °C temperature range 13–16% so that for all test, Cs is mainly transported to the line outlet in aerosol form (73–80%).

3.2. Characterization of condensed phase and aerosols in the 850–150 °C temperature range

A full understanding of iodine behaviour cannot be obtained alone from sampling line data and the element distribution in the line even if some first important information could be gained. In order to complement these data, a detailed characterization of aerosols and/or condensed material was undertaken. Both condensed deposits collected in the main line (in a temperature range from ~ 850 °C down to 350 °C) and aerosols collected at 150 °C were considered. Coupled analyses by SEM-EDX, RMS, XPS and XRD allowed to describe morphology, element composition and to identify the main species in collected condensed matter. In the following sections, analysis of deposits are detailed with decreasing deposit collection temperature.

3.2.1. Results for the [In + MoCsI] test

Deposit morphology evolution with decreasing temperature are observed by SEM in Back Scattering Electron imaging (BSE) as displayed on Fig. 2.

At high temperature (800–765 °C), both cubic like particles (2–3 μm) and large amorphous structures can be identified (Fig. 2.a). In dominates in cubic like structure whereas Si and O are found in amorphous structures. Mo and Cs are found in trace amount only. RMS allows to identify the cubic like particles (see Figure S2) as In_2O_3 by comparison with literature data (Kranert et al., 2014). The large amorphous structures observed in this temperature range are identified as melted silica with characteristics Raman bands at 230 and 416 cm^{-1} (see Figure S3). Traces of mixed Cs-In polymolybdates have been identified at 765 °C by their Raman characteristic bands at 786 and 935 cm^{-1} (Maczka, 1997).

Around 700–680 °C, large agglomerates of spherical or hexagonal like particles with diameter up to 10–30 μm are observed together with some isolated needle-like particles (5–20 μm, not shown here) (Fig. 2b). In addition to In, Cs and Mo are found as main components of the deposit with Mo/Cs elemental ratio close to 3; Mo/In ratio is close to 2. For the needle like particles, the higher Mo/In ratios (up to 5) indicates the possible presence of caesium molybdate species. Regarding elemental ratio and RMS identification (Figure S4), $CsIn(MoO_4)_2$ is the main species identified in this temperature range and appears as the large hexagonal and spherical particles 10–30 μm. Literature data predict the condensation of $CsIn(MoO_4)_2$ below 650 °C (Maczka, 1997) rather consistent with our experimental observations. The isolated needle like particles are identified by RMS as caesium molybdates ($Cs_2Mo_4O_{13}$ and $Cs_2Mo_7O_{22}$) (see Figure S5) in agreement with Hoekstra (1973) and the binary diagram of $CsMoO_4$-MoO_3 recently reported by Smith et al., (2021).

Around 600 °C, mixed Cs-In molybdates are still observed (not shown). In addition, indium molyddate as $In_2(MoO_4)_3$ is identified (Figure S6) by comparison with spectra reported by (Maczka et al., 2005). This new species dominates deposit composition at this temperature. Given data of the MoO_3-In_2O_3 binary diagram (Filipek et al., 2012), indium molybdates should have been observed at higher temperature (eutectic point at 780 °C) indicating possible competition with the formation of the mixed Cs-In molybdates (which are observed as of 765 °C).

Below 500 °C, micronic parallepipedic particles and very fine needles (<1μm) are observed together with larger stick like crystallites (~5–20 μm). The stick-like particle size increases as the temperature decreases (Fig. 2c and d). EDX analyses indicates a strong Mo enrichment in all particle types, suggesting that Mo compounds dominates deposition. Indeed, the large sticks are mainly identified by RMS as α-MoO_3 (Figure S7) (McEvoy and Stevenson, 2005; Ding et al., 2006) and more sparsely $Cs_2Mo_7O_{22}$. The aggregates of fine particles are tentatively attributed to molybdate species as their Raman spectra feature characteristic bands in the 900–1000 cm^{-1} range typical of Mo-O vibration modes. Around 500 °C, $In_2(MoO_4)_3$ is found in fine crystallised needles together with two other likely In/Cs molybdates but not fully attributed. At 400 °C, the fine particle agglomerates are mainly composed of a mixture of α-MoO_3 and $Cs_2Mo_7O_{22}$.

The submicronic aerosols transported at 150 °C are mainly composed of $CsIn(MoO_4)_2$ according to the Raman and XRD data (see Figure S8) but the presence of $Cs_2Mo_5O_{16}$ cannot be excluded.

Under the oxidative atmosphere of this test (injection of steam only and indium as indium oxide), mainly Mo(VI) species were transported in the line that is confirmed by XPS (Figure S9). At 150 °C, traces of reduced Mo species were observed in the aerosols (Figure S9). Similarly to the [PL_MoCsI_3] test, Mo-rich deposits are found below 600 °C. Iodine was not detected in the solid samples consistently with a transport almost only under gaseous form evidenced in the previous part. A summary of the main identified species is displayed in Table 3.

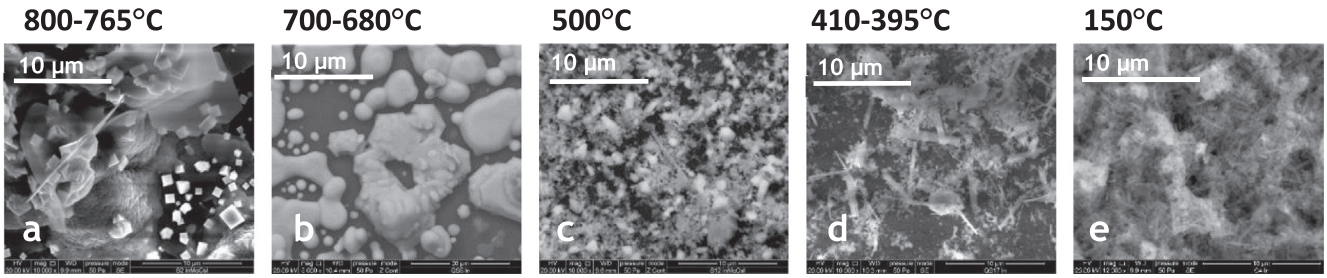

Fig. 2. [In + MoCsI] test – SEM – BSE images of deposits collected in the 800–150 °C temperature range (magnification × 5000 - ×12200).

Table 3
[In + MoCsI] test - Summary of the main identified species in the deposits and aerosols collected in the 800–150 °C temperature range. Dominant species are in bold characters.

Analyses	800–765 °C	700–680 °C	600–580 °C	500 °C	~410–395 °C	150 °C
SEM-EDX Morphology Elemental atomic composition and ratio Species	Cubic particles: In rich, In_2O_3. Amorphous structure: Si rich (fused silica), SiO_2	Large hexagonal and flattened drop like particles (10–30 µm): Cs and In rich, Mo/In ~ 2, Mo/Cs ~ 2, $CsIn(MoO_4)_2$	Not analysed	Micronic parallepipedic particles: Mo rich. Fine needles: In and Mo rich. Some large stick like crystallites : α-MoO_3 and possibly $(Cs/In)_xMo_yO_z$	Fine needles: Mo and In-rich. Numerous large stick like crystallites: Mo –rich, α-MoO_3 and possibly $(Cs/In)_xMo_yO_z$	Submicronic particles: mix where Mo dominates, Mo/In ~ 3, Mo/Cs ~ 4–5
RMS	**In_2O_3,** $CsIn(MoO_4)_2$, (Cs and/or $In)_xMo_yO_z$, Fused silica	In_2O_3, **$CsIn(MoO_4)_2$ trigonal,** Cs_2MoO_4, $Cs_2Mo_4O_{13}$(p), $Cs_2Mo_7O_{22}$	**$In_2(MoO_4)_3$, $CsIn(MoO_4)_2$ trigonal,** $Cs_2Mo_2O_7$	$In_2(MoO_4)_3$, Two distinct species of the type: **$(Cs/In)_xMo_yO_z$,** $Cs_2Mo_2O_7$, $Cs_2Mo_7O_{22}$ (trace), **α-MoO_3**	$In_xMo_yO_z$, $Cs_2Mo_2O_7$, $Cs_2Mo_7O_{22}$ (trace), **α-MoO_3**	**$CsIn(MoO_4)_2$ trigonal,** $CsIn(MoO_4)_2$ orthorhombic, $Cs_2Mo_5O_{16}$ (consistent with XRD)

3.2.2. Results for the [Cd + MoCsI] test

Condensed species were analysed in the 670 °C −150 °C temperature range. For temperature higher than 670 °C (alumina tube), very low amount of Cd-rich deposit are found (~3%, as reported in Table 3). Sizes of condensed material decrease with decreasing temperature. Large octahedrons - and rods-shaped particles are observed above 500 °C when submicronic needles and ball-shaped particles are found at lower temperatures (see Fig. 3a to e).

By comparison with Raman spectra referenced in the literature or in data bases (Ozkan et al., 1990; Phuruangrat et al., 2011; Xing et al., 2011; Tsyrenova and Pavlova, 2011), Raman spectra recorded from particles is assigned to several cadmium-rich species.

Cadmium molybdates (mainly $CdMoO_4$), and mixed Cs-Cd molybdates ($Cs_2Cd_2(MoO_4)_3$) are identified by RMS and XRD as main deposited species over all the 670–430 °C temperature range (Figures S10, S11 and S12). Additional particles composed of Cs-Cd mixed compounds as $Cs_{2x}Cd_y(MoO_4)_{x+y}$ are hypothesized regarding their typical Raman line shifts but these intermediates are not described in the literature. Cs-Cd molybdates may result from the reaction at high temperature between $MoO_{3(g)}$ and $Cd(OH)_{2(g)}$ and/or $Cd_{(g)}$ and $CsOH_{(g)}$. Above 600 °C, the morphology of $CdMoO_4$ is octahedral (Shahri et al., 2013) that is consistent with RMS results. With decreasing temperature, the overall particle size decreases and the particle shape changes from octahedral to spherical. Mixed Cs-Cd molybdates are observed in a cement like deposit (see Fig. 3b). Cadmium silicates are identified at lower temperatures (below 540 °C) by EDX and XRD (Figure S12) in plate-shaped particles or rods. Reaction between Cd with quartz plate substrate may account for the formation of such species.

The aerosols collected at 150 °C are composed of aggregates of submicron particles mixed with larger spherical particles (1–3 µm). $CdMoO_4$ and $Cs_2Cd_2(MoO_4)_3$ are the main compounds of aggregates. Besides spherical particles of Cd metal, part of Cd may be also oxidized in the steam flow as $Cd(OH)_2$ and CdO forms were detected by XRD (Figure S13). Additionally, traces of MoO_2 were also detected at 150 °C by RMS (Figure S14). As stated in section 3.1.2, the formation of molybdenum dioxide results indirectly from the oxidation of Cd metal exposed to the high temperature steam condition and producing hydrogen capable of reducing MoO_3 to MoO_2 (Grégoire et al., 2015). Although only evidenced at the line outlet, partial reduction of Mo(VI) to Mo(IV) is consistent with high amount of Mo found deposited in the high temperature zone consecutively to the formation of the less volatile Mo (IV)-oxide.

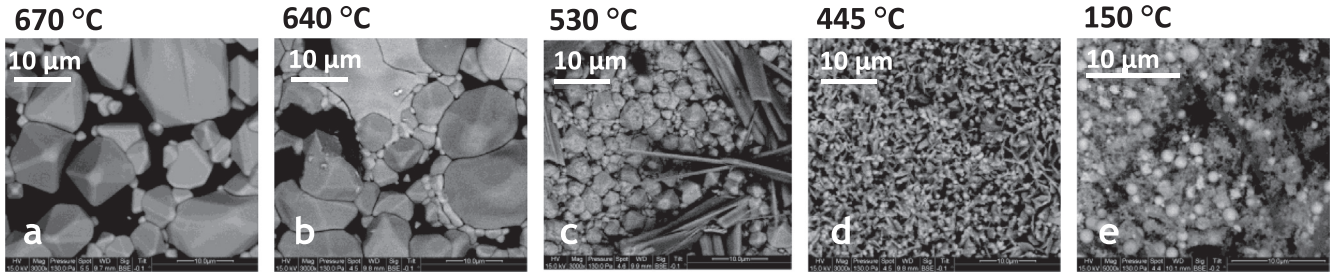

Fig. 3. [Cd + MoCsI] test – SEM-BSE images of deposits collected in the 670–150 °C temperature range (magnification at × 3000).

Table 4
[Cd + MoCsI] test - Summary of the main identified species in the deposits and aerosols collected in the 800–150 °C temperature range. Dominant species are in bold characters.

Analysis	~670 °C	~640 °C	~530 °C	~465 °C	~445 °C	150 °C
SEM-EDX *Morphology* Elemental atomic composition and ratio Species	***Octahedra:*** Mo/Cd = 1.0, **$CdMoO_4$**. ***"Cement"*** Mo/Cd = 1.9, Mo/Cs = 2.2, Cd/Cs = 1.5, **$Cs_{2x}Cd_y(MoO_4)_{x+y}$**.	***Octahedra:*** Mo/Cd = 0.9, **$CdMoO_4$**. ***"Cement":*** Mo/Cd = 1.5, Mo/Cs = 1.6, Cd/Cs = 1.0, **$Cs_2Cd_2(MoO_4)_3$**. ***"Cement":*** Mo/Cd = 2, Mo/Cs = 2.5, Cd/Cs = 1.2, **$Cs_{2x}Cd_y(MoO_4)_{x+y}$**.	***Sphere:*** Mo/Cd = 1.0, **$CdMoO_4$**. ***Rod:*** Cd/Si = 0.9, **$CdSiO_3$**. ***"Cement":*** Mo/Cd = 1.6, Mo/Cs = 1.6, Cd/Cs = 1.0, **$Cs_2Cd_2(MoO_4)_3$**.	***Sphere:*** Mo/Cd = 1.4, Mo/Cs = 1.3, Cd/Cs = 1.0, **$Cs_2Cd_2(MoO_4)_3$**. ***Plate:*** Cd/Si = 1.9, **Cd_2SiO_4**	***Sphere:*** Mo/Cd = 0.9, **$CdMoO_4$**. ***Plate:*** Cd/Si = 1.0, **$CdSiO_3$**. ***Sphere:*** Mo/Cd = 1.6, Mo/Cs = 1.6, Cd/Cs = 1.0, **$Cs_2Cd_2(MoO_4)_3$**.	***Sphere:*** Mo/Cd = 0.1, Mo/Cs = 1.6, Cd/Cs = 14–21, **Cd. *Aggregate:*** Mo/Cd = 0.2–0.4, Mo/Cs = 1.7–2.2, Cd/Cs = 4.2–17, **Mix**
RMS	$CdMoO_4$, $Cs_2Cd_2(MoO_4)_3$	$CdMoO_4$, $Cs_2Cd_2(MoO_4)_3$	$CdMoO_4$, $Cs_2Cd_2(MoO_4)_3$, $CdSiO_3$ or Cd_2SiO_4	$CdMoO_4$, $Cs_2Cd_2(MoO_4)_3$	$CdMoO_4$, $Cs_2Cd_2(MoO_4)_3$	$CdMoO_4$, $Cs_2Cd_2(MoO_4)_3$, MoO_2
XRD	$CdMoO_4$, $Cs_2Cd_2(MoO_4)_3$	$CdMoO_4$, $Cs_2Cd_2(MoO_4)_3$	$CdMoO_4$, $Cs_2Cd_2(MoO_4)_3$, $CdSiO_3$, Cd_2SiO_4	$CdMoO_4$, $Cs_2Cd_2(MoO_4)_3$, $CdSiO_3$, Cd_2SiO_4	$CdMoO_4$, $Cs_2Cd_2(MoO_4)_3$, $CdSiO_3$, Cd_2SiO_4	$CdMoO_4$, $Cs_2Cd_2(MoO_4)_3$, Cd, $CdCO_3$, $Cd(OH)_2$,

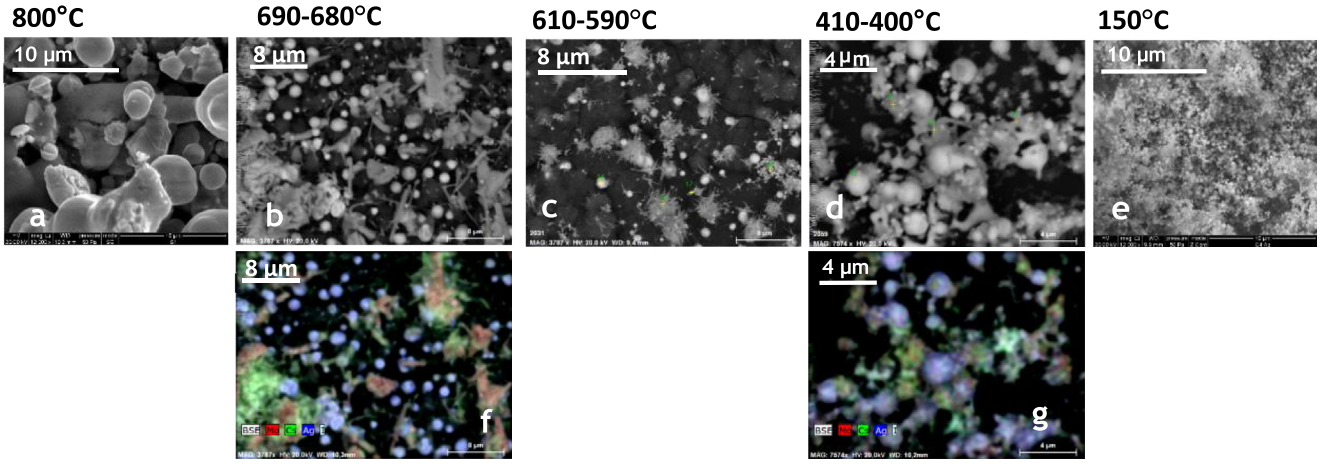

Fig. 4. [Ag + MoCsI] test - SEM-BSE (a-e) and EDX (f,g) images of deposits and aerosols collected in the 800–150 °C temperature range. (on elemental images f and g: red is Mo, blue is Ag and green is Cs). (For interpretation of the references to colour in this figure legend, the reader is referred to the web version of this article.)

No isolated caesium molybdate compounds are identified on any samples. The absence of such species in the deposits or in the transported aerosols can result from the competition between Cs and Cd when reacting with molybdenum which is in favour of the later one, since cadmium was injected in very large excess with respect to Cs and Mo. Indeed, cadmium molybdate is stable in the MoO_3-Cd system below 700 °C with a low formation standard enthalpy (-1034 kJ/mol at 25 °C - Ali (Basu) et al., 2005).

As far as iodine is concerned, no iodine containing species (such as CsI ou CdI_2) are evidenced in the 670 °C-430 °C temperature range. Low amounts of iodine are detected at 150 °C by XPS (Figure S15) with I $3d_{5/2}$ binding energy (BE) at 619.9 eV at 619.9 eV assigned to I-I bonds energy. Indeed, this BE is higher than the ones expected for Cs-I or Cd-I bonds. This last feature states for I_2 likely adsorbed on particles (Dillard et al., 1984). Nevertheless, in presence of large amounts of Cd, the I3d5/2 XPS peaks at 619 eV can be interfered by that of Cd3p3/2 (618.4 eV) so that chemical shift interpretation should be considered with caution; the I 3d3/2 peak (631.5 eV) remains free of interference but is less documented in the literature (NIST database). The characterization of the condensed material is consistent with results gained from gaseous phase (organic line) strengthening the fact that interaction between iodine and cadmium seems to be weaker than inferred from the Phébus FP tests (Girault and Haste, 2013), even for very large excess of Cd relative to I. Table 4 summarizes the main identified species in the [Cd + MoCsI] test.

3.2.3. Results for the [Ag + MoCsI] test

Various particle morphologies are identified by SEM (see Fig. 4) that are observed over almost all the temperature range (800–150 °C):

- Large Ag-rich spherical particles (>10 µm) are observed both partly coalesced at high temperature and then isolated with size decreasing along with sampling temperature to reach submicronic sizes (~100 nm) at 150 °C.
- Parallepipedic crystallites (not shown) with size decreasing from ~ 10 µm to<1 µm are seen from 800 °C to 150 °C. EDX analyses reveal that these particles are Mo-enriched above 600 °C and featured also Ag below 600 °C;
- Needle like particles are observed only when the temperature is below 700 °C. The particle size varies from initially 3–4 µm long at T = 700 °C to < 1 µm at the temperature sampling. The needles contain mostly Mo and Ag;

Table 5
[Ag + MoCsI] test - Summary of the main identified species in the deposits and aerosols collected in the 800–150 °C temperature range. Dominant species are in bold characters.

Analysis	800–765 °C	690–680 °C	610–590 °C	520–500 °C	410–400 °C	~350–340 °C	150 °C
SEM-EDX Morphology Elemental atomic Composition Species	Large spherical particles (>5–10 μm) : **Ag(0).**	Spherical particles (1–2 μm): **Ag (0). F**ine needles (~5 μm) and parallepipedic plates (2–10 μm) : Mo rich, MoO_3, MoO_2 and Ag_2MoO_4. Amorphous structure ("cement" like): Cs rich (CsxMoyOz?).	Spherical particles (1–2 μm) : **Ag(0).** Aggregates of fine particles around the spherical one's.	Not analysed	Spherical particles (1–2 μm): **Ag(0)** Aggregates of fine particles around the spherical one's Sparse AgI particles.	Same as 410–400 °C plate plus some Mo Rich large plates. Sparse AgI particles.	Submicronic spherical particles (100 nm) : **Ag(0).** Submicronic particles difficult to characterize.
RMS	**Ag_2MoO_4,** $Ag_2Mo_2O_7$, $Ag_2Mo_3O_{10}$, MoO_2	**Ag_2MoO_4,** $Ag_2Mo_2O_7$, $Cs_2Mo_2O_7$, $Cs_2Mo_3O_{10}$, **MoO_3,xH_2O, MoO_2**	**Ag_2MoO_4,** $Ag_2Mo_2O_7$/ $Cs_2Mo_2O_7$, $Ag_2Mo_3O_{10}$ / $Cs_2Mo_3O_{10}$, $(Cs/Ag)_x$ Mo_yO_z, **MoO_2, α-MoO_3**	**Ag_2MoO_4,** $(Cs/Ag)_x$ Mo_yO_z, $Cs_2Mo_2O_7$, $Cs_2Mo_3O_{10}$, **MoO_2,** MoO_3, xH_2O	Ag_2MoO_4, **$Cs_2Mo_2O_7$, $Cs_2Mo_3O_{10}$, $Cs_2Mo_5O_{16}$,** MoO_3 (p), MoO_2 (p)	Ag_2MoO_4, $Ag_2Mo_2O_7$ (p), **$Cs_2Mo_2O_7$, $Cs_2Mo_3O_{10}$, $Cs_2Mo_5O_{16}$,** MoO_3 (p), MoO_2 (p)	Ag_2MoO_4, $Ag_2Mo_2O_7$, Cs/Ag_x Mo_yO_z, **$Cs_2Mo_2O_7$, $Cs_2Mo_3O_{10}$,** $Cs_2Mo_4O_{13}$, $Cs_2Mo_5O_{16}$, Mo_xO_y

- Aggregates of very fine particles are seen below 700 °C, in which Cs is detected.

Table 5 summarizes the main identified species by combination of SEM-EDX and RMS analyses. Note that with decreasing temperature, fine particles agglomerate to form larger structures in which single components are difficult to identify. Consistently with its refractive properties, silver metal condenses early in the transport zone and is found as the main deposited species above 750 °C (EDX) in the large and partly coalesced droplets. Silver metal is then transported/deposited in the line as spherical particles as confirmed by EDX and XRD analyses (Figure S16).

In the 700–400 °C temperature region, molybdenum(VI) and (IV) oxides are found by RMS as predominant species. The presence of reduced forms of Mo is confirmed by XPS in the same temperature range (Figure S17). The formation of MoO_2 is consistent with the injection of a low amount of hydrogen and the presence of important amount of silver metal which can be considered as a reducing agent. The presence of the less volatile Mo(IV) species is also consistent with enhanced Mo deposition at high temperature (as stated in section 3.1). Silver molybdates (Ag_2MoO_4 as a major compound and $Ag_2Mo_2O_7$, $Ag_2Mo_3O_{10}$) are also identified by RMS (Beltran et al., 2014) in this temperature range (Figures S18 and S19). Molybdenum oxide and silver molybdates are mostly found in the needle and parallepipedic-shaped particles. In a lesser extent caesium molybdates are also identified and found as amorphous structure. Caesium molybdates account for the dominant species only below 500 °C. Competition between the formation of silver and caesium molybdates may explain the delayed deposition of caesium molybdate species when comparing with tests featuring only the Mo-Cs-I-O–H chemical system (Gouello, 2012). The distinction between silver and caesium molybdates remains challenging as Raman spectra of such compounds exhibit typical Raman bands related to Mo-O vibrational modes in the same spectral range (i.e. 800–100 cm^{-1}).

Only few single particles featuring either CsI or AgI are observed in deposits between 350 °C and 400 °C as seen on the SEM-EDX images (Figure S20). Because iodine is injected with an elemental flow rate ~ 50 times lower than silver one, metallic iodide (if formed) would account for a minor compound.

Table 6
Standard Enthalpy of formation of metallic iodide of interest taken from literature.

Chemical species	standard formation enthalpy for condensed species(kJ/mol) @298 K	standard formation enthalpy forgaseous species(kJ/mol) @298 K
CsI	−348.1(Cordfunke and Prins, 1985)	−153.3 ± 1.8(Roki et al., 2014)
CdI_2	−205(Konings et al., 1993)	−58.8 ± 2.5(Shugurov et al., 2021)
AgI	−61.8(Taylor and Anderson, 1921)	125.3(Barin, 1989)
InI	−102(Vasil'ev et al., 1987)	26.4(Gurvich et al. 1989)
InI_3	−223(Vasil'ev et al., 1987)	−105.4(Gurvich et al. 1989)

4. Discussion

In the presence of SIC control rods, the behaviour of iodine may be contrasted. Iodine is transported in the gaseous phase when indium is injected, but maintaining an excess of Mo with respect to Cs. Whereas silver and cadmium injection in large excess induce the formation of iodide aerosols. AgI formation seems to be limited despite a large excess of silver, with a formation rate lower than 10% with respect to iodine ([Ag + MoCsI] test). This point confirms that AgI is less stable than CsI and CdI_2 consistently with thermodynamic data (Table 6). More specifically, the three tests exhibited some significant differences as for iodine behaviour:

- For the [In + MoCsI] test, a part of the injected indium preferentially reacts with MoO_3 rather than iodine to form indium molybdates so that InI_x formation was not observed. As Mo was injected in excess of In and Cs, the molybdenum still acts as a Cs sink preventing CsI formation and thus allows the existence of gaseous iodine at 150 °C. It is not excluded that the injection of In_2O_3 in larger amounts (e.g. larger than Mo as for the tests with Cd and Ag) could result in an increased consumption of MoO_3 to form In-molybdate competing with Cs-molybdate formation and thus favouring cesium iodide formation, but in any case this is not very representative of the SA case (In is still in lower amount than Mo).
- For [Ag + MoCsI] and [Cd + MoCsI] tests, despite the injection of a huge excess of cadmium or silver relative to all the other elements, the formation of metallic iodide other than CsI seems not to be the main reaction pathway leading to the reduction of gaseous iodine release. Two reaction pathways are put forward. Firstly, the reactivity of cadmium and silver with molybdenum oxides may contribute to significantly reduce the Cs-scavenging role of Mo by preventing the formation of caesium molybdates with Mo(VI) oxidation state. Secondly, the oxidation of the injected metallic species (Cd, Ag) may indirectly promote the formation of less reactive MoO_2 oxide. This second reaction pathway should remain limited, however, as at most 10% of injected Mo(VI) could be reduced (XPS data, see section 3.2). As a result, the formation of CsI is favoured preferentially to AgI (observed) or CdI_2 (hypothesized) in agreement with the

Table 7
Standard Enthalpy of formation of molybdates of interest taken from literature.

Chemical species	standard formation enthalpy forcondensed species(kJ/mol)@298 K	standard formation enthalpy forgaseous species(kJ/mol)@298 K
α-MoO_3(s) and MoO_3(g)	−745.5(Crouch and Dickens, 1984)	−364.4 ± 20.0,(Cordfunke and Konings, 1990)
Cs_2MoO_4	−1514.4(Gamsjäger and Morishita, 2015)	−1179.2(Tangri et al., 1989)
In_2MoO_4	Not available	−855 ± 33(Lopatin et al., 2013)
Ag_2MoO_4	−838.2(Gamsjäger and Wiessner, 2018), (Gamsjäger and Morishita, 2015)	−459.6(CCSD(T)/CBS(TZ-QZ) value, method described in (Saab and Souvi, 2018))
$CdMoO_4$	−1034 ± 5.7 ; −1015.4 ± 14.5 (Ali (Basu) et al., 2005),(Mishra et al., 2006)	−606.0(CCSD(T)/CBS(TZ-QZ) value, method described in (Saab and Souvi, 2018))
$SnMoO_4$	Not available	−699 ± 29(Shugurov et al., 2015)

relative stability of these compounds. Indeed, available thermodynamic data tends to show that caesium iodide is the most stable metallic iodide to be considered here both in gaseous and condensed phases.

Characterization of the main compounds deposited in the CHIP line allowed for identifying several metallic polymolybdates in addition to the caesium molybdates already characterized in similar thermal hydraulic conditions (Lacoue-Nègre, 2010; Gouello et al., 2013; Grégoire et al., 2015). Such species were not mentioned for the VERCORS nor Phébus tests. Nevertheless, deposition profile of In, Cs and Mo obtained in a 800–200 °C thermal gradient for the VERCORS HT tests (deposition along Thermal Gradient Tube as reported by Pontillon and Ducros (2010)) showed concomitant deposition in the ∼ 800 °C (HT2 test), ∼675–725 °C (HT3 test) and ∼ 640 °C (HT2 test) temperature zones, so that deposition of metallic molybdates involving Cs and/or In cannot be excluded. Silver deposition is much more complex to discuss featuring a low homogeneous deposition detected below 700 °C (HT3 test) and 600 °C (HT2 test) and no data for Cd deposition is available. As only I and Cs deposition profiles were determined for the Phébus Thermal Gradient Tube (700–200 °C) during the FPT1 and FPT2 tests (Girault and Payot, 2013), it will be difficult to infer any comparison with our results.

The formation of various metallic polymolybdates entering in competition with the formation of caesium polymolybdates is clearly evidenced in the three tests. Indeed, deposits containing pure caesium molybdates were detected at a lower temperatures (below 600 °C for [In + MoCsI] and [Ag + MoCsI] tests) than observed when only Mo oxide and Cs species are reacting together (1000 °C, as reported in (Gouello et al., 2013). Cd and Ag are injected both in large excess relative to Mo and Cs, so that a direct comparison of the two tests in terms of molybdate formation can be put forward. Pure caesium molybdates are still observed in [Ag + MoCsI] test, as well as MoO_2 and MoO_3 species. On the contrary, cadmium-containing molybdates are the dominant species in the [Cd + MoCsI] test featuring only mixed CdCs molybdates and traces of MoO_2 (aerosols collected at the line outlet). These features indicate that the formation silver molybdates seem less favoured compared to that of cadmium molybdates in our test condition. Even if In_2O_3 was injected in lower amount (in default relative to Mo but in excess compared to Cs), the formation of indium molybdates seem favoured at high temperature, compared to that of pure caesium molybdates, as $CsIn(MoO_4)_3$ and $In_2(MoO_4)_3$ are the dominant species in the 500–750 °C temperature range. Caesium was found mainly as a mixed InCs molybdate compounds over all the temperature range, pure caesium molybdates appearing less abundant. In the oxidative atmosphere of this test (steam injection and no reducing species), the excess Mo was found mainly as α-MoO_3 from 500 °C down. It is nevertheless difficult to know exactly if the species are formed in the gas phase and/or in the solid phase after condensation of In, Mo and Cs species in oxide or hydroxide forms.

Formation enthalpies referenced in the literature show that caesium molybdates are most stable compared to cadmium, silver and indium molybdates even if the thermodynamic data are uncomplete with no mixed elements (see Table 7). In our conditions the large excess of Cd, Ag and In reagents compared to Cs may have displaced equilibrium in favour of Cd, Ag or In-molybdates in the high temperature zone. Consumption of these elements results in the formation of the more stable Cs molybdates at lower temperature as experimentally observed. In this discussion, possible kinetic limitations in the thermal–hydraulic transient are not taken into account and thermodynamic data are nevertheless not all available in the literature.

Even if trends could be inferred from a direct comparison of stability of the identified compounds, a full understanding of the main reactions which occurred in the CHIP line with these chemical systems will be gained by simulation of the experiments with severe accident calculation codes as ASTEC/SOPHAEROS (Cousin et al., 2008; Cantrel et al., 2013). Nevertheless, up to date, thermodynamic data of some metallic molybdates evidenced in these experiments are not available in the literature and cannot be accounted in the thermodynamic database of the simulation tools. Density Functional Theory calculations may help to provide some of the missing thermodynamic data for gaseous species.

5. Conclusion

A series of tests performed in the CHIP line with the Mo-Cs-I-O–H chemical system and CR elements revealed that the behaviour of each component (Ag, In and Cd) of the SIC control rod considered separately is much more complex than initially expected. Indeed, combined on-line sampling, elemental post-test analyses and an extended characterization of deposits allow for identifying most of formed compounds during the transport in the thermal gradient (1600–150 °C) of the CHIP line. These species could not be evidenced in the larger scale Phébus tests or VERCORS HT tests.

In the case of indium injection, a release of gaseous iodine similar to the [PL_MoCsI_3] reference test is observed. Indium iodide formation is not observed as expected from the low stability of InIx(g). The fully oxidative conditions contribute to maintain Mo in the + VI oxidation state and thus its capabilities to easily form metallic molybdates. Beside, significant deposition of In_2O_3 at high temperature (>750 °C) owing to the refractive behaviour of this species, the main contribution of In injection is the formation of indium and mixed In-Cs molybdates likely in the condensed phase. Owing to the large excess of Mo relative to both In and Cs, Mo still plays a Cs-sink role with a large fraction of gaseous iodine transported at low temperature.

In the case of both cadmium and silver injection, the formation of metallic iodide other than CsI seems not to be the main reaction pathways leading to a strong reduction of gaseous iodine release

despite the injection of a very large excess relative to all the other elements (I, Cs and Mo). The formation of various metallic silver or cadmium molybdates entering in competition with caesium molybdates contribute to significantly reduce the Cs-scavenging role of Mo.

It can be stated that due to the high stability of caesium iodide, only the absence of Cs can prevent its formation but if caesium molybdates are formed, as detailed before, caesium cannot be totally consumed by molybdenum in presence of control rod materials.

It is worth noting that all these results apply to the CHIP conditions where molybdenum is injected in slight excess and silver and cadmium in large excess with respect to representative conditions of a severe accident.

Efforts are ongoing to improve the ASTEC/SOPHAEROS modelling to reproduce as much as possible all the trends experimentally observed in terms of iodine chemical reactivity and also FPs deposits, to be at least capable to deepen the understanding of the FP's chemistry observed during the Phébus tests (Girault and Payot, 2013) and later on perform SA simulations.

CRediT authorship contribution statement

A.C. Grégoire: Investigation, Writing – original draft. **S. Sobanska:** Investigation, Writing – original draft. **C. Tornabene:** Investigation. **D. Talaga:** Investigation. **A.S. Mamede:** Investigation. **S. Morin:** Investigation. **L. Cantrel:** Writing – original draft.

Declaration of Competing Interest

The authors declare that they have no known competing financial interests or personal relationships that could have appeared to influence the work reported in this paper.

Acknowledgements

This work was performed in the frame of the experimental CHIP + programme with the financial support of EDF. The authors thank the Labex Cappa (ANR-11-LABX-0005-01) for funding XPS analyses performed at the 'plateforme d'analyses de surfaces' of the Lille University. The *Fonds Européen de Développement Régional* (FEDER), *CNRS*, *Région Nord Pas-de-Calais* and *Ministère de l'Education Nationale de l'Enseignement Supérieur et de la Recherche* are acknowledged for fundings of XPS/LEIS/ToF-SIMS spectrometers. Analyses performed at the Institute of Molecular Science of Bordeaux University were supported the IRSN/ADERA contract n °12033756. E. Assaf and G. Montaud are acknowledged for their participation in the RMS measurements of condensed phase samples. We thank P. Recourt from LOG UMR CNRS 8187 (Lille University) for SEM-EDX measurements of [Cd + MoCsI] test samples. LASIR UMR 8516 (Lille University) is acknowledged for making the RMS equipment available for measuring [Cd + MoCsI] test samples.

Appendix A. Supplementary data

Supplementary data to this article can be found online at https://doi.org/10.1016/j.anucene.2021.108900.

References

Ali (Basu), M., Bharadwaj, S.R., Das, D., 2005. The standard molar enthalpy of formation of $CdMoO_4$. J. Nucl. Mater. 336 (1), 110–112. https://doi.org/10.1016/j.jnucmat.2004.09.006.

Barin, I., 1989. Thermochemical Data of Pure Substances. VCH, Weinheim.

Beahm E. C., Weber C.F., Kress T. S., Parker, G. W. (1992). Iodine Chemical Forms in LWR Severe Accidents – Final Report, NUREG/CR-5732 – ORNL/TM-11861.

Beltran, A., Gracia, L., Longo, E., Andrés, J., 2014. First-principles study of pressure-induced phase transitions and electronic properties of Ag_2MoO_4. J. Phys. Chem. C 118 (7), 3724–3732. https://doi.org/10.1021/jp4118024.

Bowsher B.R. and Dickinson, S. (1986). The interaction of caesium iodide with boric acid: vapour phase and vapour condensed phase reactions, 1986, AEE-Winfrith R-2102.

Bowsher, B.R. and Nichols, A.L. (1985) High temperature studies of simulant fission products: Part IV, Interaction of caesium iodide with boric acid over the temperature range 400 to 1000 °C, AEE-Winfrith R-1973.

Cantrel, L., Louis, F., Cousin, F., 2013. Advances in mechanistic understanding of iodine behaviour in Phebus-FP tests with the help of ab-initio calculations. Ann. Nucl. Energy 61, 170–178. https://doi.org/10.1016/j.anucene.2013.02.034.

Chino, M., Nakayama, H., Nagai, H., Terada, H., Gatata, G., Yamazawa, H., 2011. Preliminary estimation of release amounts of I-131 and Cs-137 accidentally discharged from the fukushima daiichi nuclear power plant into the atmosphere. J. Nucl. Sci. Technol. 48, 1129–1134. https://doi.org/10.1080/18811248.2011.9711799.

Clément B. and Zeyen R. (2005). The Phébus Fission Product and Source Term International Programs. Proc. Int. Conf. on Nuclear Energy for New Europe, Bled, Slovenia, 5-8 September, Nuclear Society of Slovenia.

Clément B. Cantrel L., Ducros G., Funke F., Herranz L., Rydl A., Weber G., Wren C. (2007). State of the art report on iodine chemistry, NEA/CSNI/R(2007)1.

Cordfunke, E.H.P., Prins, G., 1985. The thermochemical properties of caesium iodide. I thermodynamic functions of solid CsI. Thermochim. Acta 90, 169–176. https://doi.org/10.1016/0040-6031(85)87094-5.

Cordfunke, E.H.P., Konings, R.J.M., 1990. Thermochemical Data for Reactor Materials and Fission Products. Elsevier, Amsterdam.

Cousin, F., Dieschbourg, K., Jacq, F., 2008. New capabilities of simulating fission product transport in circuits with Astec/Sophaeros vol 1.3. Nucl. Eng. Des. 238 (9), 2430–2438. https://doi.org/10.1016/j.nucengdes.2008.03.018.

Crouch, B.S., Dickens, P.G., 1984. Standard molar enthalpy of formation of a-MoO_3-H_2O by solution calorimetry. J. Chem. Thermodyn. 16, 301–302. https://doi.org/10.1016/0021-9614(84)90093-4.

de Boer, R., Cordfunke, E.H.P., 1995. On the Caesium rich part of the Cs-Te phase diagram. J. Alloy. Compd. 228 (1), 75–78. https://doi.org/10.1016/0925-8388(95)01666-X.

Dillard, G., Moers, H., Klewe-Nebenius, H., Kirch, G., And, P.G., Ache, H.J., 1984. The absorption of methyl iodide on uranium and uranium dioxide: surface characterisation using X-ray photoelectron spectroscopy. Surf. Sci. 145, 62–86. https://doi.org/10.1016/0039-6028(84)90766-0.

Ding, Q.P., Huang, H.B., et al., 2006. Molybdenum trioxide nanostructures prepared by thermal oxidation of molybdenum. J. Cryst. Growth 294 (2), 304–308. https://doi.org/10.1016/j.jcrysgro.2006.07.004.

Elrick R.M., *et al.* (1987). Boron Carbide – Steam Reactions with Cesium hydroxide and with Cesium Iodide at 1270 K in an Inconel 600 system, NUREG CR-4963, SAN87-1491.

Filipek, E., Rychlowska-Himmel, I., Paczesna, A., 2012. Thermal stability of $In_2(MoO_4)_3$ and phase equilibria in the MoO_3-In_2O_3 system. J. Therm. Anal. Calorim. 109 (2), 711–716. https://doi.org/10.1007/s10973-012-2224-7.

Gamsjäger, E., Wiessner, M., 2018. Low temperature heat capacities and thermodynamic functions described by Debye-Einstein integrals. Monatsh. Chem. 149 (2), 357–368. https://doi.org/10.1007/s00706-017-2117-3.

Gamsjäger, H., Morishita, M., 2015. Thermodynamic properties of molybdate ion: reaction cycles and experiments. Pure Applied Chemistry 87 (5), 461–476. https://doi.org/10.1515/pac-2014-1105.

Geng, X., Xie, Z., Zhang, L., 2017. Influence of emission rate on atmospheric dispersion modeling of the Fukushima Daiichi Nuclear Power Plant accident. Atmos. Pollut. Res. 8, 439–445. https://doi.org/10.1016/j.jenvrad.2016.01.011.

Girault, N., Payot, F., 2013. Insights into iodine behaviour and speciation in the Phébus primary circuit. Ann. Nucl. Energy 61, 143–156. https://doi.org/10.1016/j.anucene.2013.03.038.

Girault, N., Bosland, L., Dickinson, S., Funke, F., Güntay, S., Herranz, L.E., Powers, D., 2012. LWR severe accident simulation: iodine behaviour in FPT2 experiment and advances on containment iodine chemistry. Nucl. Eng. Des. 243, 371–392. https://doi.org/10.1016/j.nucengdes.2011.11.011.

Girault, N., Bosland, L., Dienstbier, J., Dubourg, R., Fiche, C., 2010. LWR severe accident simulation fission product behavior in FPT2 experiment. Nucl. Technol. 169 (3), 218–238. https://doi.org/10.13182/NT10-A9375.

Gouello M. (2012). Chemistry of iodine and aerosol composition in the primary circuit of a nuclear plant in severe accident conditions, Ph-D, University J. Fourier, Grenoble (in French).

Gouello, M., Mutelle, H., Cousin, F., Sobanska, S., Blanquet, E., 2013. Analysis of the iodine gas phase produced by interaction of CsI and MoO_3vapours in flowing steam. Nucl. Eng. Des. 263, 462–472. https://doi.org/10.1016/j.anucene.2013.06.016.

Grégoire, A.C., Délicat, Y., Tornabene, C., Cousin, F., Gasnot, L., Lamoureux, N., Cantrel, L., 2017. Study of the iodine kinetics in thermal conditions of a RCS in nuclear severe accident. Ann. Nucl. Energy 101, 69–82. https://doi.org/10.1016/j.anucene.2016.10.013.

Grégoire, A.C., Haste, T., 2013. Material release from the bundle in Phébus FP. Ann. Nucl. Energy 61, 63–74. https://doi.org/10.1016/j.anucene.2012.02.037.

Grégoire, A.-C., Kalinainen, J., Cousin, F., Mutelle, H., Cantrel, L., Auvinen, A., Haste, T., Sobanska, S., 2015. Studies on the role of molybdenum on iodine transport in the RCS in nuclear severe accident conditions. Ann. Nucl. Energy 78, 117–129. https://doi.org/10.1016/j.anucene.2014.11.026.

Grégoire A.C., March P., Payot F., Zabiego M., De Bremaecker A, Biard B., Schlutig S., Grégoire G. (2008). FPT2 Final report, (IPSN) - PH-PF report IP/08/579.
Grégoire A.C., Morin S., Cantrel L. (2018). Main outcomes of the IRSN experimental CHIP and CHIP+ *programmes* in Proc. of Conference Nuclear Energy for New Europe, 2018, Portoros 10-13 September (Slovenia). Communication.
Grégoire A.C., Mutelle H. (2012). Experimental Study of the [B, CS, I, O, H] and [Mo, Cs, I, O, H] Systems in the Primary Circuit of a PWR in Conditions Representative of a Severe Accident in Proc. Of Conference Nuclear Energy for New Europe, Ljubljana 5-7 September (Slovenia).
Gurvich L.V., Veyts I.V.,Alcock C.B. (1989). Thermodynamic Properties of Individual Substances - 4th edition.
Haste, T., Payot, F., Bottomley, P.D.W., 2013. Transport and deposition in the Phébus FP circuit. Ann. Nucl. Energy 61, 102–121. https://doi.org/10.1016/j.anucene.2012.10.032.
Hoekstra, H.R., 1973. The Cs_2MoO_4-MoO_3 system. Inorg. Nucl. Chem. Lett. 9 (12), 1291–1301. https://doi.org/10.1016/0020-1650(73)80013-3.
Hoeve, J.E.T., Jacobson, M.Z., 2012. Worldwide health effects of the Fukushima Daiichi nuclear accident. Energy Environ. Sci. 5, 8743–8757. https://doi.org/10.1039/C2EE22019A.
Huh, C., Hsu, S., Lin, C., 2012. Fukushima-derived fission nuclides monitored around Taiwan: free tropospheric versus boundary layer transport. Earth Planet. Sci. Lett. 319, 9–14. https://doi.org/10.1016/j.epsl.2011.12.004.
Jacquemain D., Bourdon S., De Bremaecker A., Barrachin M., (2000). FPT1 Final report, (IPSN) - PH-PF report IP/00/479.
Jacquemain, D., 2015. Nuclear Power Reactor Core Melt Accident, Current state of knowledge. EDP Science https://www.edp-open.org/images/stories/books/fulldl/Nuclear_Power_Reactor_Core_Melt_Accidents.pdf.
Konings, R.J.M., Cordfunke, E.H.P., Ouweltjes, W., 1993. The standard molar enthalpies of formation of CdI2(s) and Cs2Cd2I4(s). J. Chem. Thermodyn. 25, 271–276. https://doi.org/10.1006/jcht.1993.1026.
Kranert, C., Schmidt-Grund, R., Grundmann, M., 2014. Raman Active Phonon modes of cubic In2O3. Phys Status Solidii RRI 8 (6), 554–559. https://doi.org/10.1002/pssr.201409004.
Lacoue Nègre M. (2010). Iodine chemistry in the reactor coolant system of a nuclear power plant in case of a severe accident – study of CsI/MoO_3 mixture under steam, Ph-D, university USTL, Lille (in French).
Lebel, L.S., Dickson, R.S., Glowa, G.A., 2016. Radioiodine in the atmosphere after the Fukushima Dai-ichi nuclear accident. J. Environ. Radioact. 151, 82–93. https://doi.org/10.1016/j.jenvrad.2015.06.001.
Lopatin, S.I., Panin, A.I., Shugurov, S.M., 2013. Stability and structures of gaseous In_2MoO_4, In_2WO_4 and $In_2W_2O_7$. Dalton Trans. 42, 8339–8346. https://doi.org/10.1039/c3dt32719a.
Maczka, M., 1997. Vibrational Characteristics of the alkali metal-indium double molybdate M-$In(MoO_4)_2$ and tungstate M-$In(WO_4)_2$ (M=Li, Na, K, Cs). J. Solid State Chem. 129, 287–297. https://doi.org/10.1006/jssc.1996.7248.
McFarlane J., Leblanc, J.L. (1996). Fission product Tellurium and Cesium telluride. Chemistry revisited. AECL report 11333 COG 95-L76-I.
Masson O., Tschiersch J., Lebel L.S., Wershofen H., Mietelski J.W., Steinhauser G., Blanchardon E., Cantrel L., Grégoire A.C., Quélo D. (2019), Radio-iodine release in : Nuclear Emergencies (Book) , Chap 15, Ed G. Steinhauser, A. Koizumi, K. Shozugawa, ISSN 2364-8333 ISSN 2364-8341. doi: 10.1007/978-981-13-8327-4.
Maczka, M, Hermanowicz, K, Hanuza, J, 2005. Phase transition and vibrational properties of A2(BO4)3 compounds (A=Sc, In; B=Mo, W). Journal of Molecular Structure (744–747), 283–288. https://doi.org/10.1016/j.molstruct.2004.10.049.
Masson, O., Baeza, A., Bieringer, J., Brudecki, K., Bucci, S., Cappai, M., Carvalho, F.P., Connan, O., Cosma, C., Dalheimer, A., Didier, D., Depuydt, G., De Geer, L.E., De Vismes, A., Gini, L., Groppi, F., Gudnason, K., Gurriaran, R., Hainz, D., Halldórsson, Ó., Hammond, D., Hanley, O., Holeý, K., Homoki, Z.s., Ioannidou, A., Isajenko, K., Jankovic, M., Katzlberger, C., Kettunen, M., Kierepko, R., Kontro, R., Kwakman, P. J.M., Lecomte, M., Leon Vintro, L., Leppänen, A.-P., Lind, B., Lujaniene, G., Mc Ginnity, P., Mahon, C.M., Malá, H., Manenti, S., Manolopoulou, M., Mattila, A., Mauring, A., Mietelski, J.W., Møller, B., Nielsen, S.P., Nikolic, J., Overwater, R.M. W., Pálsson, S.E., Papastefanou, C., Penev, I., Pham, M.K., Povinec, P.P., Ramebäck, H., Reis, M.C., Ringer, W., Rodriguez, A., Rulík, P., Saey, P.R.J., Samsonov, V., Schlosser, C., Sgorbati, G., Silobritiene, B.V., Söderström, C., Sogni, R., Solier, L., Sonck, M., Steinhauser, G., Steinkopff, T., Steinmann, P., Stoulos, S., Sýkora, I., Todorovic, D., Tooloutalaie, N., Tositti, L., Tschiersch, J., Ugron, A., Vagena, E., Vargas, A., Wershofen, H., Zhukova, O., 2011. Tracking of airborne radionuclides from the damaged Fukushima Dai-Ichi nuclear reactors by European Networks. Environ. Sci. Technol. 45 (18), 7670–7677. https://doi.org/10.1021/es2017158.
McEvoy, T.M., Stevenson, K.J., 2005. Spatially resolved imaging of inhomogeneous charge transfer behavior in polymorphous molybdenum oxide. I. Correlation of localized structural, electronic, and chemical properties using conductive probe atomic force microscopy and Raman microprobe spectroscopy. Langmuir 21 (8), 3521–3528. https://doi.org/10.1021/la047276v.
McFarlane, J., Wren, J.C., Lemire, R.J., 2002. Chemical speciation of iodine source term to containment. Nucl. Technol. 138 (2), 162–178. https://doi.org/10.13182/NT138-162.
Mishra, R., Bharadwaj, S.R., Das, D., 2006. DETERMINATION OF THERMODYNAMIC STABILITY OF $CdMoO_4$ BY KNUDSEN EFFUSION VAPOR PRESSURE MEASUREMENT METHOD. J. Therm. Anal. Calorim. 86 (2), 547–552. https://doi.org/10.1007/s10973-005-7285-4.
Miyahara, N., Miwa, S., Horiguchi, N., Sato, I., Masahiko, O., 2019. Chemical reaction kinetics dataset of Cs-I-B-Mo-O-H system for evaluation of fission product chemistry under LWR severe accident conditions. J. Nucl. Sci. Technol. 56 (2), 228–240.
Ozkan, U.S., Gill, R.C., Smith, M.R., 1990. Synergy in $CdMoO_4/MoO_3$ catalysts in partial oxidation reactions of C4 hydrocarbons. Appl. Catal. 62 (1), 105–117. https://doi.org/10.1016/S0166-9834(00)82240-X.
Phuruangrat, A., Ekthammathat, E., Thongtem, T., Thongtem, S., 2011. Microwave-assisted synthesis and optical property of $CdMoO_4$ nanoparticles. J. Phys. Chem. Solids 72 (3), 176–180. https://doi.org/10.1016/j.pcs.2010.12.003.
Pontillon, Y., Ducros, G., 2010. Behaviour of fission products under severe PWR accident conditions The VERCORS experimental programme—Part 2: release and transport of fission gases and volatile fission products. Nucl. Eng. Des. 240 (2010), 1853–1866. https://doi.org/10.1016/j.nucengdes.2009.06.024.
Roki, F.-Z., Ohnet, M.-N., Fillet, S., Chatillon, C., Nuta, I., 2014. Critical assessment of thermodynamic properties of CsI solid, liquid and gas phases. J. Chem. Thermodyn. 70, 46–72. https://doi.org/10.1016/j.jct.2013.09.038.
Saab, M., Souvi, S., 2018. Quantum modelling of $AgHMoO_4$, $CsHMoO_4$ and $AgCsMoO_4$ chemistry in the field of nuclear power plant safety. Int. J. Chem. Mol. Eng. 12 (5), 244–248. https://doi.org/10.5281/zenodo.1317244.
Shahri, Z., Sobhani, A., Salavati-Niasari, M., 2013. Controllable synthesis and characterization of cadmium molybdate octahedral nanocrystals by coprecipitation method. Mater. Res. Bull. 48 (10), 3901–3909. https://doi.org/10.1016/j.materresbull.2013.05.100.
Smith, A.L., Vlieland, J., Pignié, M.-C., Abbink, M., Mikaelian, G., Benigni, P., 2021. New insights into the Cs-Mo-O system: experimental studies of the $Cs2MoO_4$-MoO_3 pseudo-binary system. Thermochim. Acta 696, 178825. https://doi.org/10.1016/j.tca.2020.178825.
Spies J.R.(1936). Process for obtaining free silver and iodine from silver iodide, Patented n°2,060,539.
Shugurov, S.M., Panin, A.I., Lopatin, S.I., Emelyanova, K.A., 2015. Thermodynamic study of gaseous tin molybdates by high-temperature mass spectrometry. Rapid Commun. Mass Spectrom. 29 (5), 1427–1436. https://doi.org/10.1002/rcm.7237.
Shugurov, S.M., Panin, A.I., Lopatin, S.I., Panaeva, M.A., 2021. Vapor pressures and thermodynamic properties of simple and complexe iodides. Thermochim Acta 703,. https://doi.org/10.1016/j.tca.2021.178996 178996.
Stohl, A., Seibert, P., Wotawa, G., Arnold, D., Burkhart, J.F., Eckhardt, S., Tapia, C., Vargas, A., Yasunari, T.J., 2012. Xenon-133 and caesium-137 releases into the atmosphere from the Fukushima Dai-ichi nuclear power plant: determination of the source term, atmospheric dispersion, and deposition. Atmos. Chem. Phys. 12 (5), 2313–2343. https://doi.org/10.5194/acp-12-2313-2012.
Tangri, R.P., Venugopal, V., Bose, D.K., Sundaresan, M., 1989. Thermodynamics of vaporisation of caesium molybdate. J. Nucl. Mater. 167, 127–130. https://doi.org/10.1016/0022-3115(89)90433-9.
Taylor, H.S., Anderson, W.T., 1921. The heat of formation of silver iodide. J. Am. Chem. Soc. 43 (9), 2014–2017. https://doi.org/10.1021/ja01442a004.
Tsyrenova, G.D., Pavlova, N.N., 2011. Synthesis, structure, and electrical and acoustic properties of $Cs_2Cd_2(MoO_4)_3$. Inorg. Mater. 47 (7), 786–790. https://doi.org/10.1134/S0020168511070235.
Vasil'ev, Ya.V., Matskevich, N.I., Stenin, Yu. G. (1987). New determination of enthalpies of indium tri- and monoiodide formation. Massive adiabatic calorimeter, Izvestiya Sibirskogo Otdeleniya Akademii Nauk SSSR, Seriya Khimicheskikh Nauk; ISSN 0002-3426; CODEN IZSKA; (no.2); p. 3-8.
Wang, Y.L., Nagy, J.C., Margerum, D.W., 1989. Kinetics of hydrolysis of iodine monochloride measured by the pulsed-accelerated-flow method. J. Am. Chem. Soc. 111, 7838–7844. https://doi.org/10.1021/ja00202a026.
William D.A. (1994). OECD International Standard Problem Number34 Falcon Code Comparison Report, NEA/CNSI/R(94)27.
Xing G. Xu y., Zhao C., Wang Y. Li Y., Wu Z., Liu T. Wu G. (2011). Photoluminescence properties of CdMoO4 disk and hollow microsphere-like crystals synthetized by hydrothermal conventional method. Powder Technol. 213, 109–115. doi: 10.1016/j.powtec.2011.07.012.

Journal of Hazardous Materials 409 (2021) 124519

Contents lists available at ScienceDirect

Journal of Hazardous Materials

journal homepage: www.elsevier.com/locate/jhazmat

Research paper

Chemical stability of caesium iodide deposits in air/steam atmosphere

D. Obada [a,b], H. Hijazi [a,b], J.-F. Paul [b,*], L. Gasnot [c], A.-C. Grégoire [a], A.-S. Mamede [b], L. Cantrel [a]

[a] Institut de Radioprotection et de Sûreté Nucléaire, Pôle Sûreté Nucléaire, CEN Cadarache, Saint Paul lez Durance F-13115, France
[b] Univ. Lille, CNRS, Centrale Lille, Univ. Artois, UMR 8181 - UCCS - Unité de Catalyse et Chimie du Solide, F-59000 Lille, France
[c] Univ. Lille, CNRS, UMR 8522 - PC2A - Physicochimie des Processus de Combustion et de l'Atmosphère, F-59000 Lille, France

ARTICLE INFO

Editor: Dr. H. Zaher

Keywords:
Fission products
Re-vaporization
Severe nuclear accident
DFT calculations

ABSTRACT

Iodine compounds that may be released in case of severe nuclear accident will have important radiotoxicity if they are disseminated in air. One of the most important iodine species is CsI that is deposited on the surfaces of the reactor coolant system. However, depending on the conditions, CsI can volatilize or react with oxidants to produce $I_{2(g)}$. Theoretical and experimental studies demonstrate that the oxidation of iodide depends on the temperature and in the presence of oxidants in the gas. It is also slightly influenced by the crystallinity of the CsI particles and the nature of the support. In case of a high temperature deposition, the iodine release started at temperature lower than 300 °C. For the CsI vapour and aerosol depositions, the iodine is detected only at temperature above 450 °C and become very important above 550 °C.

1. Introduction

In case of a severe accident (SA) occurring in a Pressurized Water Reactor (PWR), volatile radioactive fission products (FPs), such as caesium and iodine, are released from the degraded fuel. They are transported through the reactor coolant system (RCS) and the containment building and can be released into the environment via direct leakages of the nuclear containment and/or by the containment venting process in case of overpressure. As a result, these FPs can contribute to the radiological consequences for the population in the short term for iodine and the long-term for caesium.

In order to simulate an accidental scenario and predict the release of FPs, the ASTEC (Accident Source Term Evaluation Code) calculation code has been developed by the French Institute for Radiological Protection and Nuclear Safety (IRSN). In order to get predictive simulations (Cantrel et al., 2014), a comprehensive knowledge of all the phenomena occurring in a PWR during a severe accident situation is necessary. Considerable advances have been made in the field of understanding the behaviour of volatile FPs such as iodine after their release from the damaged core, thanks to experimental programs such as Phébus-FP (Haste et al., 2013) and other experimental works devoted to FP behavior (Cantrel et al., 2018) and subsequent modelling works.

Nevertheless, some phenomena are not accounted for yet by the simulation tools and it is difficult to predict their outcome, mostly because of a lack of experimental and/or theoretical data. It is the case with the re-vaporization of FPs deposits from the surface of the RCS. FPs will form deposits on the surface of the RCS by different mechanisms, the most important of which are vapour condensation and thermophoresis as predicted by Hidaka et al. (1995) and Maruyama et al. (1999), as well as gravity deposition. The Phébus-FP experimental program has shown that Cs and I can significantly deposits in the RCS (Girault and Payot, 2013). The main identified iodine compounds is CsI – resulting from condensation of CsI vapours in the 600–650 °C temperature range (as expected from thermodynamic calculations and simulation with severe accident software as the ASTEC code (Cantrel et al., 2014)). Other condensed iodine form were identified too, but their nature could not be fully unravelled – they are expected to be metallic iodide of control rod material (Cd or Ag). Moreover, it was determined from Phébus tests, that Cs remobilization can reach up to 75% of the initial deposit in certain conditions (Haste et al., 2013). More recently, in the aftermath of the Fukushima Daiichi accident, delayed releases for iodine and caesium have been detected several days after the accident (Katata et al., 2015; Terada et al., 2012), and are believed to be related to the chemical re-vaporization of caesium and iodine containing deposits.

In the past several attempts have been made to understand the phenomenon of FPs remobilization. As a follow-up of the Phebus-FP tests, a series of research programs have been launched by several institutions. The studies focused mainly on the re-vaporization of caesium in a wide range of temperature and carrier gas conditions; iodine behaviour, for its part, was less studied. The studied precursor was

* Corresponding author.
E-mail address: jean-francois.paul@univ-lille.fr (J.-F. Paul).

https://doi.org/10.1016/j.jhazmat.2020.124519
Received 30 July 2020; Received in revised form 10 October 2020; Accepted 23 October 2020
Available online 9 November 2020

mostly CsOH (Terada et al., 2012; Anderson et al., 2000; Auvinen et al., 2000; Bottomley et al., 2014; Knebel et al., 2014), less frequently CsI (Auvinen et al., 2000; Kalilainen et al., 2014; Shibazaki et al., 2001; Berdonosov and Sitova, 1997; Berdonosov and Baronov, 1999).

As for caesium, AEA-T Anderson et al. (2000) studied the re-vaporization of synthetic CsOH deposits in a flow reactor at temperatures reaching up to 1100 °C, analysing the mass balance and surface interaction between caesium and the substrate made of 304 SS steel. Auvinen et al. (2000) have studied the vaporization of CsOH and CsI powders from stainless steel crucibles. The samples were traced with radioactive Cs (^{134}Cs or ^{137}Cs), which allowed establishing a release kinetics thanks to γ-spectrometry measurements. The two studies used steam as carrier gas and it was established that the Cs re-vaporization starts at ≈ 500 °C. Bottomley et al. (2014) and Knebel et al. (2014) performed online γ-spectrometry measurements of ^{137}Cs from deposits issued from the Phebus-FP tests (vapour deposition at temperatures up to 700 °C), which are as realistic as possible. However the initial composition of the deposits, as well as the surface state of the stainless steel substrate is not well defined. The results show that in steam Cs is released starting from 550 °C, whereas in air atmosphere the release occurs at a lower temperature, as low as 300 °C.

The studies dealing with CsI were aimed at investigating conditions leading to CsI decomposition and subsequent gaseous iodine releases. Experiments performed by Kalilainen et al. (2014) allowed a better understanding of the re-vaporized Cs and I distribution between gaseous and aerosol forms, thanks to the use of liquid scrubbers and filters adapted for each type of material. It was found that up to 27% of initial iodine content is released in gaseous form in an argon/steam atmosphere, and that it decreases with the introduction of hydrogen in the carrier gas. Shibazaki et al. (2001) performed tests with CsI in steam and concluded that it starts re-vaporizing at ≈ 490 °C and is released mainly as CsI. Berdonosov and Sitova (1997) and Berdonosov and Baronov (1999) conducted small-scale tests to further study the chemical nature of the released gaseous iodine. By heating CsI in air up to 1250 °C, the formation of gaseous molecular iodine I_2 has been observed, the higher the temperature the larger the amount. Kulyukhin et al. (2004) studied the hydrolysis of CsI in presence of molecular oxygen in the 630–1300 °C range and the formation of I_2 has been also confirmed, indirectly. However, some key parameters were not fully investigated in those studies. For instance, the FP deposit-substrate interaction was not always taken into account. Indeed, if some studies featured stainless steel substrates (Auvinen et al., 2000; Kalilainen et al., 2014) the initial surface state is not documented. Some studies featured even substrates not representative of the RCS (glass or platinum (Shibazaki et al., 2001; Berdonosov and Sitova, 1997; Berdonosov and Baronov, 1999), alumina (Auvinen et al., 2000)). Secondly, the process of CsI deposition was not always examined as most of studies were performed with commercial CsI powder; CsI vapour and aerosol deposition were only considered in (Kalilainen et al., 2014). Finally, the influence of carrier gas composition and thermal conditions on re-vaporization were not fully investigated: most of studies considered steam or steam/hydrogen atmospheres which are more representative of early degradation phase during SA, whereas air was only considered in (Shibazaki et al., 2001; Berdonosov and Sitova, 1997; Berdonosov and Baronov, 1999), but in the latter case, the thermal treatment (flash heating up to 1250 °C) seems unrealistic regarding late phase SA conditions.

From the theoretical point of view, to the best of our knowledge, the revaporisation and the chemical reactivity of CsI aerosols had only been studied by Hijazi (2017). The other theoretical studies in a nuclear frame focused on the gas reactivity of iodine species or on chemical stability/reactivity of caesium species (Khanniche et al., 2016a, 2016b, 2016c, 2017a, 2017b; Villard et al., 2019; Khiri et al., 2019; Sudolská et al., 2014a, 2014b). Severe accident simulations in the RCS are based on chemical equilibrium in gas phase thus ab initio computations were performed on the speciation at the equilibrium of the compound containing iodide or caesium. The gas inorganic chemistry involves mainly molecular iodine (I_2), monoatomic iodine radicals ($I^{\bullet}$) and iodine oxides (IO_x). The conversion between the species are fast and are favoured by oxidants such as nitrogen oxide and by visible light or radiation. The interaction with water occurs through the formation of hydrogen bonds and hydrogen transfer between acidic and radical species. The reactivity of caesium species in the gas phase has not been studied extensively. The reaction between CsO and H_2 have been investigated by Šulková et al. (2015). Based on all these studies, it is possible to estimate the concentrations of some iodine and caesium species in the gas phase depending on the experimental conditions (Taamalli et al., 2020).

In conclusion, data on caesium and more particularly on gaseous iodine re-vaporization are too scarce and remain to be confirmed in more representative conditions to build an appropriate modelling.

The work presented here was aimed at fill in the gap in knowledge on CsI re-vaporization in conditions as representative as possible of a late phase of a SA scenario, in terms of: i/ substrate nature (pre-oxidized 304 L and 316 L stainless steel which correspond to RCS steel composition) ii/ deposit generation (reproducing the different temperature deposition processes as in (Kalilainen et al., 2014): high temperature deposition, vapour condensation and finally aerosol impaction with realistic deposited amounts ~i.e. few mg/cm^2) iii/ re-vaporization thermal conditions (with heating up to 750 °C), iv/ presence of air (steam/air mixtures), since air is susceptible to penetrate in the RCS in case of an air-ingress accidental scenario (Giordano et al., 2010). We aimed at a better assessment of gaseous iodine release with the identification of re-vaporized species and their kinetics.

Preliminary results of the study have been published before (Obada et al., 2017; Mamede et al., 2016) and were focused mainly on the re-vaporization of CsI aerosol deposits in pure atmosphere (air or steam). This paper expands on the previous results and presents the re-vaporization of different types of CsI deposits in a mixed air/steam carrier gas as well as investigates the release kinetics for gaseous molecular iodine Special attention was brought to the substrate nature, and its preparation in order to obtain a surface state as similar as possible of RCS inner parts after several hours of oxidation in steam conditions (Mamede et al., 2016; Obada et al., 2018) at high temperature. The surfaces before and after deposit re-vaporization process were carefully determined by combining X-Ray Photoelectron Spectroscopy (XPS) and Time-of-Flight Secondary Ion Mass Spectrometry (ToF-SIMS). The release rate was monitored by thermogravimetric analysis (TGA) and the nature of released vapours was determined. Also, the release kinetics for molecular iodine has been studied by a novel spectroscopic technique, Incoherent Broadband Cavity Enhanced Absorption Spectroscopy (IBB-CEAS) (Johansson et al., 2014).

Hereafter the article is composed of an experimental section which describes the equipment used and the analytical techniques employed. The following section presents the experimental results concerning the re-vaporization CsI deposits. Finally, a theoretical modelling of the experiments is done, in order to improve the understanding of the reaction mechanisms.

2. Materials and methods

The experimental study is based on a multistep approach including:

- Substrate pre-oxidation;
- CsI deposits generation;
- CsI deposits thermal treatment.

After each step the samples are characterized in order to establish the surface state of the substrate (XPS, ToF-SIMS), deposit quantity (ICP-MS), mass balance for caesium and iodine after re-vaporization (ICP-MS, TGA, UV-Visible spectroscopy).

2.1. Substrate pre-oxidation

304 L stainless steel coupons (8 ×15 ×2 mm), whose composition is presented in Table 1, underwent a thermal treatment in a controlled atmosphere in a flow reactor to reproduce as close as possible the surface state of the RCS inner part in SA conditions. The thermal treatment consisted in exposing the coupons to a flow of argon/steam (% vol. 50/50) at 750 °C during 24 h. The heating rate was 5 °C/min and steam was injected at 150 °C. The total gas flow rate was fixed at 1 L_n/min[1] at standard conditions. 316 L foils (100 × 500 ×0.075 mm, see composition in Table 1) were pre-oxidized in the same thermal conditions and process gas composition, except that the total gas flow was 4 L_n/min at standard conditions. In both case, the carrier gas flow was laminar and steam proportion in the flow (50%) is large enough to allow equivalent oxidation conditions of the stainless steel surfaces.

2.2. CsI deposits generation

In this study three types of CsI deposits were considered: aerosols impaction at room temperature by Room temperature (RT) aerosol impaction, high-temperature vapour deposition/condensation and temperature aerosol deposition.

The CsI impacted aerosols were obtained following the procedure described by Obada et al. (2018) which consists in nebulizing a concentrated CsI aqueous solution. The obtained wet aerosols are then dried in a strong argon flow (10 L/min) and afterwards impacted on the pre-oxidized 304 L coupons placed in an exposition chamber (8 coupons per batch).

The high-temperature CsI deposits were generated using a high-temperature furnace. The thermal profile of the heated alumina tube is bell-shaped, with a 5 cm isotherm zone at the centre. An alumina crucible (5 cm) containing CsI powder (Acros Organics, 99.9%) was placed inside a 1 m long alumina tube (30 mm inner diameter), inserted in the furnace. The crucible was placed in the isothermal zone. Downstream the alumina tube wall was lined by a 316 L pre-oxidized foil. The crucible was heated up to 750 °C (5 °C/min rate) and the temperature was maintained at 750 °C for 6 h. The carrier gas was a mixture of argon and steam (% vol. 20/80) at total gas flow of 0.62 L_n/min. The 316 L foil was placed in a strong thermal gradient as such vaporized CsI was transported by the carrier gas and was deposited along the pre-oxidized 316 L foil in a wide temperature range (from 750° to 150 °C)_ covering thus all deposition processes from a high temperature vapour deposition (above 620 °C), vapour condensation (between 620 and 400 °C) and aerosol deposition (below 440 °C). Downstream of the alumina tube was a series of two liquid scrubbers containing an alkaline solution (NaOH 0.1 M) dedicated for steam condensation and trapping any non-deposited material. The line was terminated by an integral filter. After the test, the 316 L foil is recovered and divided into several sections (~2–3 cm long and 1–2 cm large) based on a visual inspection of the deposit.

The deposited mass is determined after leaching one of the 304 L coupons (wet deposition) and a selection of small 316 L samples, cut from the foil (high temperature deposit generation) in selected area, in alkaline media (NaOH 0.1 M) for I and Cs recovery in solution followed by elemental I and Cs determination by Inductively Coupled Plasma – Mass Spectrometry (ICP MS –Varian 810 MS).

2.2.1. CsI deposits thermal treatment

The re-vaporization of CsI deposits from pre-oxidized stainless steel surfaces were carried out in a thermogravimetric analysis (TGA) device as described by Obada et al. (2017). Given the TGA furnace geometrical constraints (inner diameter of less than 1 cm), only the 304 L coupons could be thermally treated in this device. The thermal treatment consisted in heating the samples up to 750 °C (except for some tests, where samples were heated up to 970 °C or 550 °C only) at a rate of 5 °C/min and hold for 1 h, before cooling down by natural convection. The rate of the heating ramp is a compromise between chemical equilibrium conditions and test duration (2–3 h) (Obada, 2017). During the thermal cycle, the sample is swept by a low carrier gas flow either composed of synthetic air (30 mL_n/min) or air/argon/steam mixtures (air/steam mixture featuring a total flow rate of 30 mL_n/min; argon flow rate set at 70 mL_n/min). Air/steam mixtures were injected at temperature above 150 °C and switched off during the cooling phase (below 400 °C).

The main outcome of the TGA tests is the onset temperature of the mass loss linked to the start of the re-vaporization process. The overall mass change (loss) cannot be considered as a measure of CsI re-vaporization as the oxidation of the substrate during the thermal treatment may counterbalance the mass loss linked to re-vaporization. On the more, the inner alumina liner of the TGA device presents an important reduction in diameter (from 1 cm to 0.4 cm (Obada, 2017)) just downstream of the sample, probably inducing at its vicinity some perturbation in the fluid flow which may enhance deposit retention on the sample.

To complement the results obtained by TGA, the RIGolo (Re-vaporization of Iodine in Gaseous form and “piccolo”=”small” in Italian) experimental device has been developed with a double purpose:

- Establish the nature and quantity of released iodine-containing species;
- Determine the release kinetics for gaseous molecular iodine.

It is an open flow reactor (Fig. 1) composed of a tubular furnace (WATLOW ceramic heater CF-964255, 15 cm) in which an alumina tube (45 cm long, 20 mm inner diameter) is inserted. The sample is placed at the centre of the furnace and the carrier gas is fed up at the inlet of the test line. The vaporized vapour and/or generated aerosols from the heated sample are transported by the carrier gas to the line outlet. Based on the type of information searched in the experiment, the downstream part of the RIGolo device has two configurations: “integral measurement” for determining the nature and quantity of released iodine-containing species and “online measurement” for establishing the gaseous I_2 release kinetics.

The “integral measurement” configuration is described by Obada et al. (2017) and consists in connecting the alumina tube outlet to a series of selective liquid scrubbers, containing a mix of toluene/acidic water. It has been shown that in these conditions molecular iodine will be selectively trapped in the organic phase, while inorganic iodine compounds (CsI, HI) will be trapped in the aqueous phase (Gouello et al., 2013; Grégoire et al., 2015). Since the detection limit of I_2 in toluene by UV-Visible spectroscopy is between 2×10^{-8} and 6×10^{-7} mol/L (for the absorption wavelengths of 309 nm and 496 nm respectively), it is necessary to accumulate I_2 over a long period of time (2 h), hence the experiment was called “integral”.

The “online measurement” configuration consists in connecting the alumina tube outlet to an Incoherent Broadband Cavity Enhanced Absorption Spectroscopy (IBB-CEAS) device dedicated to monitor online the gaseous molecular iodine concentration, transported up to the optical cell, by absorption spectroscopy in the 510–570 nm range (Johansson et al., 2014; Bahrini et al., 2018). In this case the re-vaporization products (gaseous species, aerosols) are diluted in an argon flow before being injected in the optical cell. The technique has a low detection limit (1 ppb volumic in the gas phase) and a good temporal resolution (10 s), which makes possible a kinetic study in our experimental conditions (1–2 mg of iodine re-vaporized for ≈1 h in a 200 mL_n/min gas flow).

The thermal treatment in the RIGolo device is similar to the one applied in the TGA device: heating up to 750 °C (rate 5 °C/min) and hold for 1 h, before cooling by natural convection. The carrier gas during

[1] The gas flow rates are given for the reference conditions: 273 K, 101,325 Pa and are thus noted L_n/min.

Table 1
General composition (wt%) of the 304 L and 316 L stainless steels (Mamede et al., 2016).

	C	Cr	Fe	Mn	Mo	Ni	Si	Other
304 L	0.03	18.0–20.0	Base	2.0		8.0–12.0	1.0	P,S< 0.045
316 L	0.03	16.0–18.0	Base	2.0	2.0–3.0	10.0–14.0	0.75	P,S< 0.025

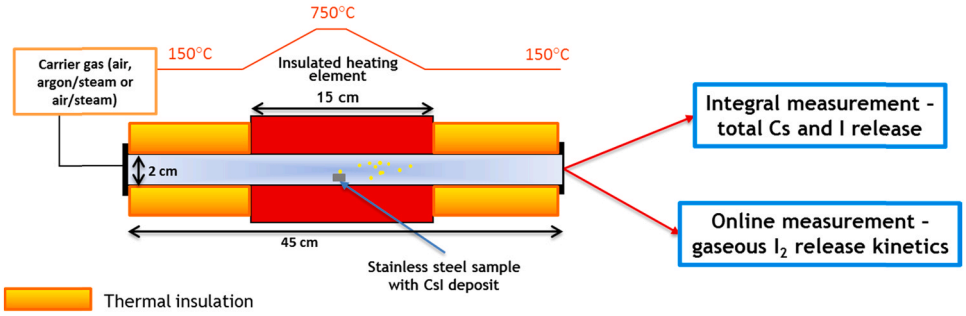

Fig. 1. General design of the RIGolo experimental device.

the tests was either air (53 mL_n/min) or a mixture of air/steam (200 mL_n/min) of variable composition. The gas flow rates have been adjusted to the new alumina tube inner diameter, in order to have the same gas velocity above the sample as in the TGA tests.

2.3. Post-test analysis

2.3.1. Elemental mass balance determination

After each test, the entire facility, including the stainless steel and gold coupons, was leached in alkaline media for iodine and caesium deposits recovery and elemental determination. As in (Obada et al., 2017), the solutions were analysed by ICP-MS for elemental quantification with an uncertainty of +/- 8% (at 95% confidence level). The organic phase of the liquid scrubbers has been also recovered and analysed by UV-Visible spectroscopy for quantification of I_2 in toluene, which was performed with an Agilent Cary 8454 spectrometer at 309 nm and 496 nm with an uncertainty of +/- 6% (at 95% confidence level).

2.3.2. Surface characterization techniques

The sample surface was characterized by combination of X-ray Photoelectron Spectroscopy (XPS) and Time-of-Flight Secondary Ion Mass Spectrometry (ToF-SIMS). XPS provides chemical composition of less than 10 nm depth scale of the surface while the ToF-SIMS was used in depth profiling mode to reach composition up to several micrometres in depth. The morphology of the surface before and after re-vaporization was investigated by Scanning Electron Microscopy (SEM).

XPS measurements were carried out on a Kratos AXIS $Ultra^{DLD}$ spectrometer equipped with a monochromatic Al Kα source (1486.6 eV). Calibration was done by using the C 1s component of adventitious at BE (binding energy) = 285.0 eV. Binding energy value uncertainty is +/−0.1 eV and uncertainty on quantitative elemental analysis is +/- 10%.

ToF-SIMS analyses were carried out using a ToF-SIMS 5 instrument (ION-TOF GmbH). Pulsed Bi^+ primary ions have been used for analysis (25 keV, ≈1 pA) and O_2^+ for sputtering (2 keV, ≈500 nA). Given the sputter parameters, estimated sputter speed is 1.6 nm/s. Mass spectra were recorded in positive (for each sample) and negative for one sample polarity from an analysis area of 100 µm x 100 µm centred into a 300 µm x 300 µm sputtered area. Charging effects, due to analysis and erosion ion beam, were compensated using low energy electrons (20 eV).

Scanning Electron Microscopy (SEM) images were obtained using a LEO-435 VP microscope. A 20 kV accelerating voltage was used giving an interaction depth above 2.5 μm^3.

2.3.3. IBB-CEAS signal interpretation and presentation

The IBB-CEAS configuration and characteristics are extensively discussed in (Bahrini et al., 2018) and (Johansson et al., 2014). It is based on the I_2 fine resolved spectrum in the 510–570 nm spectral range owing to the numerous rovibronic transitions in the I_2 B←X electronic absorption spectrum (Bahrini et al., 2018). The light source is a LED emitting in the 480–580 nm and the detector is a CCD camera (Andor iDus).

As explained by Bahrini et al. (2018) and Johansson et al. (2014), the I_2 spectra registered by the CCD detector require mathematical processing in order to separate the spectral contribution of gaseous molecular iodine from the continuous component of the spectra. Moreover, for practical reasons (Bahrini et al., 2018), a calibrated source of I_2 is analysed by the IBB-CEAS at the beginning of each experiment. Iodine concentration in the sample is then displayed as the adimensional N_{rel} value which is the ratio of I_2 sample concentration to the calibration source concentration. Absolute concentration in the samples requires to be adjusted for the sampling, calibration and dilution flow rates. In our case, as the main objective is to determine the release kinetic, it was decided to stay with relative concentration. For comparison purpose, the kinetic curves were rescaled based on the overall fractional release of molecular iodine, whenever possible (data from integral RIGolo experiments). Hereafter the figures displaying I_2 release kinetics present the rescaled N_{rel} evolution as a function of time and temperature.

2.3.4. DFT calculations

All DFT (density functional theory) calculations were carried out with VASP (Vienna Ab initio Simulation Package (vasp.5.4.1; Hafner, 2008; Kresse and Furthmüller, 1996). Plane waves are used to describe the wave functions and the PAW (Projector Augmented Wave) (Kresse and Joubert, 1999) method for electron-ion interactions. The energy is calculated using GGA as parametrized by Perdew et al. (1996) and with a Methfessel and Paxton (1989) smearing parameter sigma set to 0.1 eV. The Kohn−Sham equations are solved self-consistently until the energy difference between two successive steps is lower than 10^{-5} eV. The atomic positions were optimized without symmetry constraints until the forces being less than 0.03 eV/Å. The electron configurations [Xe] 6s1, [Kr] 4d10 5s2 5p5, [He] 2s2 2p4 and 1s1 were used for caesium, iodine, oxygen and hydrogen respectively. The cut of energy was set to 450 eV and 3 × 3x 1 or larger K-point meshes (Monkhorst and Pack, 1976) have been used for all the surface calculations (distance between K point smaller than 0.035 $Å^{-1}$). Van der Waals interactions are included in the

calculation through the TSHI formalism (Tkatchenko and Scheffler, 2009) that take into account the charges on the atoms.

The adsorption energy (E_{ads}) is defined as the opposite of the adsorption reaction energy. A positive adsorption energy is associated to an exothermic adsorption.

$$A_{(g)} + \text{Surface} = A - \text{Surface} \quad E_{ads} = E(A_{(g)}) + E(\text{Surface}) - E(A - \text{Surface}).$$

3. Experimental matrix

The first tests concerning the re-vaporization of CsI aerosols (Room temperature aerosol impaction) from pre-oxidized 304 L or 316 L substrate in presence of argon/steam have shown an integral release of Cs and I (Obada et al., 2017). As such these test conditions will serve as reference. The goal of this research was to assess gaseous iodine release during re-vaporization of CsI deposits, through small-scale analytical tests.

Stainless steels of different grades (304 L or 316 L) were used to represent the inner surface of the RCS in general. The coupons were pretreated (pre-oxidation at 750 °C in steam conditions) so as to feature a surface state representative of the RCS in case of a SA. As reported in (Mamede et al., 2016), the structure of surface oxide is similar for both stainless steels grades and has no influence on the CsI re-vaporization behaviour. In the case of 316 L foils, oxide structure is slightly different, presenting an outer Fe-rich layer (as opposed to a Mn-rich layer) and an inner Cr-rich layer. Nevertheless, taking into account the thickness of the deposit (estimated to be in the range of 2–7 μm for 1–3 mg/cm^2 for deposited CsI), we expected a low contribution of deposit/surface interaction on re-vaporized species. Indeed, for such thick deposits, the fraction of CsI in contact with the substrate surface is low.

Except for one test, the same thermal cycle was applied: heating at 5 °C/min up to 750 °C. This final temperature is high enough to be able to catch every release events concerning CsI re-vaporization and remains within the expected temperature range which could prevail in the RCS during a late SA phase.

The study was focused on the two main following parameters (see Table 2):

- The CsI deposition process, to be able to reproduce the different deposition zones in the RCS: RT temperature aerosol impaction (simulating CsI deposition in the cold leg of the RCS), high temperature vapour deposition (above 620 °C, simulating a deposition in the hot leg of the RCS and SG inlet), vapour condensation (620–400 °C, simulating SG deposition) and temperature aerosol deposition (around 400 °C, SG deposition).
- The atmosphere composition featuring either air, air/steam mixtures and argon/steam. Air and steam atmospheres are not representative of SA scenario but may help in understanding the CsI re-vaporization behaviour and gaseous iodine production. Realistic atmospheres are mixture of air/steam with a low air content. Re-vaporization of CsI aerosols (RT aerosol impaction) on 304 L coupons featured the largest atmosphere compositions (5 different compositions as reported in Table 2, from pure air contents to argon/steam). Tests were performed in both TGA and RIGolo devices. Based on the results of this test series, the number of tested atmospheres has been reduced for the CsI vapour deposition and vapour condensation: one test in steam, one in air and one in a 20/80 air/steam atmosphere. Finally, for the deposit obtained by temperature aerosol deposition (400 °C), only the pure air and steam atmospheres have been retained for the re-vaporization tests, to check for consistency with CsI aerosol impaction at room temperature. The tests have been performed in the RIGolo device only, as the 316 L foil samples were not suited for the TGA device (see Table 2).

Two complementary tests were performed:

On test with an inert substrate to assess the contribution of deposit/surface interaction in terms of nature of re-vaporized species (especially for iodine). CsI aerosols were deposited on gold coupons by the room temperature aerosol impaction process. Tests conditions featured air atmosphere and a thermal cycle (5 °C/min up to 750 °C) similar to conditions 1. Tests were performed in both devices (TGA and RIGolo) to allow a complete comparison with condition 1, Table 2.

One test with a lower final test temperature (550 °C), dedicated to the observation of iodine re-vaporization kinetics at low temperature. This test was conducted with initial CsI RT aerosol deposits on a stainless steel coupon ad a mixed steam/air atmosphere was applied (instead of pure air) to be more representative of a reactor case. This test was performed in the RIGolo device in the I_2 on-line monitoring configuration. The sample was initially heated up to 420 °C in argon (rate 5 °C/min), then the carrier gas was switched for a mixture of air/steam (% vol. 50/50). After that the sample was heated up to 550 °C (rate 5 °C/min) and held for 4 h before cooling by natural convection. The upper limit for temperature was chosen based on the results of Bottomley et al. (2014), where it has been observed that Cs re-vaporization is much slower and less significant after 750–800 °C.

Table 2
CsI re-vaporization - Experimental matrix for test performed with thermal cycle up to 750 °C at 5 °C/min.

Substrate	Deposition process	Re-vaporization carrier gas (% vol)	Experiment type (repeat)			Condition n°
			Integral	Kinetic	TGA	
Pre-oxidized 304 L	Aerosols impaction at room temperature	Air (100%)	x (Obada et al., 2017) (3)	x	x (Obada et al., 2017)	1
		Air/steam (50/50)	x	x		2
		Air/steam (20/80)	X (2)	x	x	3
		Air/steam (3/97)	x	x	x	4
		Argon/steam (50/50)	x (Taamalli et al., 2020)		x (Taamalli et al., 2020)	5
Pre-oxidized 316 L	High-temperature vapour deposition (720–620 °C)	Air (100%)	x	x		6
		Air/steam (20/80)	x			7
		Argon/steam (50/50)	x			8
	Vapour condensation (620–440 °C)	Air (100%)	X (2)	x		9
		Air/steam (20/80)	X	x		10
		Argon/steam (50/50)	X			11
	Aerosols deposits (< 400 °C)	Air (100%)	X			12
		Argon/steam (50/50)	x			13
Gold (Au)	RT aerosol impaction	Air (100%)	x	x	x	14

4. Results

4.1. Deposit characterization

After the pre-oxidation of 304 L and 316 L stainless steel coupons and foil, CsI is deposited as described in Section 2.2. Afterwards the size and the morphology of the deposits are characterized by SEM and the amount of deposited CsI is determined by ICP-MS after lixiviation.

The CsI aerosols deposits obtained by impaction at room temperature have been described by Obada et al. (2018). SEM analysis has revealed the presence of particles with irregular shapes and particle agglomerates with sizes from 5 to 20 μm. After several weeks, the particles also appear to hydrate, given the hygroscopic nature of CsI (Riggs et al., 2007). ICP-MS analysis has revealed similar CsI quantity among all the 304 L coupons of the same batch, with values ranging from 0.8 to 4.2 mg/cm^2 of CsI from one experiment to another.

The Cs and I deposits obtained at high temperature, on the other hand, exhibit different sizes and morphologies based on the deposition temperature. For instance, in the 720–620 °C temperature range, SEM analysis has revealed an amorphous deposit, homogeneously spread across the entire surface of the 316 L foil (Fig. 2a) – corresponding to the deposition of liquid droplets. The average amount of caesium and iodine per surface unit in this temperature range is about 2.9 mg/cm^2, as determined by ICP-MS analysis. Also, the Cs/I mass ratio of 0.94 is consistent with to the theoretical value (1.05) taking into account uncertainties measurement, which strongly suggests that caesium and iodine were deposited as CsI. In the 620–440 °C temperature range, the deposit is composed of polyhedrons that range between 10 and 30 μm in size, as well as acicular particles with lateral dendrites that reach several hundred microns in size (Fig. 2b). The deposit in this temperature range is the most important in terms of quantity, up to 8.3 mg/cm^2, and the Cs/I mass ratio (0.96) suggests that the chemical species is CsI. Below 440 °C, the deposit consists of spherical particles that reach up to 4 μm in diameter (not presented here). The amount of deposit decreases progressively from 4.3 mg/cm^2 at 440 °C to 0.7 mg/cm^2 at 150 °C. Given the Cs/I mass ratio (0.89–0.99), it is highly likely that the deposit is composed of CsI.

4.2. Re-vaporization: identification of released and residual species and release kinetics

In this chapter are presented the results of RIGolo and TGA tests in different conditions (Table 2) as well as the results of the kinetics tests. Since the goal is to investigate the separate effect of different parameters, the results are presented following the listed parameters: carrier gas composition, deposition process, substrate nature (stainless steel vs gold) and finally low temperature re-vaporization. Here the main trends will be discussed depending on the test parameters. Variability in test results may occur for equivalent test conditions (and for repeats) due to inhomogenities of CsI deposits.

4.2.1. Influence of carrier gas composition: air vs. mixed air/steam (conditions 1–5)

As previously reported (Obada et al., 2017, 2018), the carrier gas composition during the re-vaporization phase is one of the key parameters regarding the nature of re-vaporized and residual species. As such, in an argon/steam carrier gas, caesium and iodine are released integrally from the surface of stainless steel coupons (condition 5). The absence of gaseous iodine species at the line outlet and Cs/I ratios measured downstream of the steel coupon close to ~ 1.1 (main line data), suggest a re-vaporization as CsI only (Obada et al., 2017).

With the addition of air in the carrier gas (in increasing amounts following conditions 4, 3, 2 up to pure air, condition 1), we can observe that the overall fraction of released molecular iodine (RIGolo test in integral configuration) is roughly the same (~ 23–33% of total iodine) as soon as air is present in the gas phase, except for pure air conditions featuring much higher gaseous iodine releases (up 75% of total iodine amount). Indeed, oxygen is always present in sufficient amount to react with iodine taking into account the oxygen flow (from ~0.02 up to 0.7 mg/s), the test duration (2 h of heating and one hour at 750 °C) and the initial iodine mass (1–2 mg) – so that the role of oxygen is expected to be the same in all the cases as soon as it is present (see Section 5 for theoretical part). In pure air, TGA tests have shown that the release starts at 420 °C on average, releases seems to be delayed as soon as steam is present with onset temperatures in the 450–470 °C range. These observations (lower gaseous iodine releases and higher re-vaporization onset temperature) in air/steam conditions compared to pure air condition may be owed to possible limiting effects of steam which are not yet understood.

Concerning the residue (RIGolo tests in integral configuration), the ICP-MS analysis of the leaching solutions of the stainless steel coupons has consistently revealed the absence of iodine, which implies its total re-vaporization, and the presence of a residual amount of caesium. In pure air (Table 3, condition n°1), Cs retention amounts up to 10% of the total measured amount at the end of the test. The ICP-MS analysis of the alumina tube leachate shows a Cs/I mass ratio in between ≈ 5–11. This feature indicates that beside CsI, Cs is mainly deposited in other chemical forms – expected to be CsO as this species is the most stable from a thermodynamic point of view in the absence of steam. In air/steam, Cs retention on the coupon represents up to 9% of total Cs collected mass (Table 3, conditions n°2 & 3). The integral experiment in conditions n°4, which featured the smallest ratio of air to steam (% vol. 3/97), has resulted in a residual amount of Cs of only 1.5%. The Cs/I mass ratio in the alumina tube does not vary a lot when considering all the mixed air steam conditions (1.4–1.6). This value is still above the Cs/I mass ratio of CsI (1.05) and support the hypothesis that beside CsI, other Cs compounds may have deposited in the main line (though in a lesser extent compared to pure air condition). In presence of steam, the other expected Cs compound is CsOH.

A detailed surface characterization by XPS and ToF-SIMS of 304 L samples after re-vaporization in air or argon/steam has been discussed

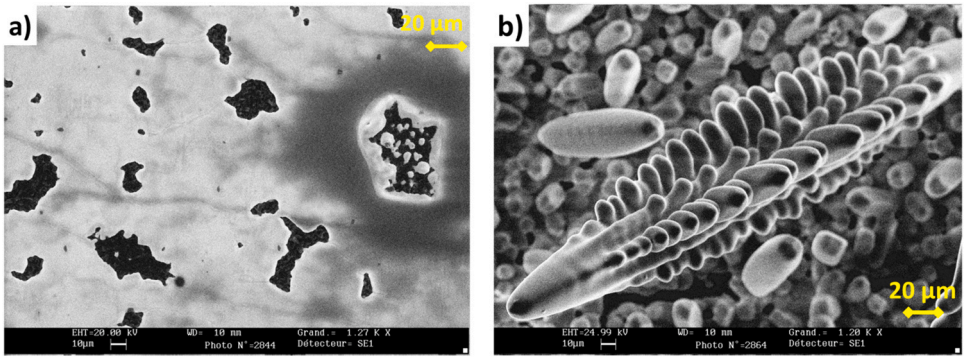

Fig. 2. SEM images of high-temperature CsI deposit on pre-oxidized 316 L foil: a) between 720 and 620 °C and b) between 620 and 440 °C.

Table 3
Summary table of main experimental results.

Substrate	CsI deposit	Re-vaporization carrier gas (% vol)	Main results					Cond n°
			Temp. of release initiation (°C)[1]	I_2 released[2,3]	Cs residual[2,4]	I residual[2,4]	Cs/I line1	
Pre-oxidized 304 L	Aerosols impaction at room temperature	Air (100%)	420	50–75%	<10%	<1%	5–11	1
		Air/steam (50/50)	460	26%	6.5%	< l.d.	1.5	2
		Air/steam (20/80)	470	23–33%	7–9%	< l.d.	1.6	3
		Air/steam (3/97)	450	26%	2%	< l.d.	1.4	4
		Argon/steam (70/30)	480	0%	3.4%	< l.d.	1.1	5 (Taamalli et al., 2020)
Pre-oxidized 316 L	High-temperature vapour deposition (720–620 °C)	Air (100%)		53%	3.4%	< l.d.	10	6
		Air/steam (20/80)		13%	9.7%	8.6%	1.6	7
		Argon/steam (70/30)		0%	1.9%	< l.d.	3.8	8
	Vapour condensation (620–440 °C)	Air (100%)		7–15%	2.4–4.5%	<1%	1.3	9
		Air/steam (20/80)		12%	2.0%	<1%	1.1	10
		Argon/steam (70/30)		0%	0.5%	0.6%	3.1	11
	Aerosols deposits (< 400 °C)	Air (100%)		45%	2.4%	< l.d.	12	12
		Argon/steam (70/30)		0%	2.9%	1.0%	1.2	13
Gold (Au)	Aerosols Impaction (RT)	Air (100%)		28%	0.4%	< l.d.	1.6	14

[1] As measured by TGA.
[2] wt% wrt the total collected Cs and I at the end of test.
[3] As measured by UV-Visible spectroscopy.
[4] As measured by ICP-MS.

by Obada et al. (2018). The same process has been applied to the 304 L samples obtained after re-vaporization in air/steam atmosphere and the results show evidence of the formation of mixed Cs-Cr oxides, specifically Cs_2CrO_4 and $Cs_2Cr_2O_7$. This observation is supported by XPS analysis which revealed the presence of two chemical forms of chromium: Cr(III) and Cr(VI) oxides. Also, ToF-SIMS analysis has revealed the presence of secondary ion clusters $Cs_2CrO_3^+$ and $Cs_2Cr_2O_9H^+$, which is a strong indication that the said oxides have been formed during the re-vaporization process. These results demonstrate that the nature of the support affect the behaviour of residual Cs+ but not that the same support participate to the iodine oxidation but that in oxidizing condition, the chromium of the support can react with the air (Souvi et al., 2017).

This test series (conditions 1–5) was complemented by RIGolo tests performed with the on-line configuration in order to monitor I_{2g} release during the thermal treatment. Based on TGA tests results (no release event below 400 °C), the I_2 release kinetics was monitored from ~ 330 °C on.

A first test has been performed in an argon/steam atmosphere (condition 5), serving as reference (Fig. 3, red curve). There is no signal increase up to 640 °C, indicating the lack of gaseous I_2. The weak signal detected in the 640–680 °C temperature range and interpreted as N_{rel} ‡ 0 is nevertheless not representative of any I_2 release kinetics. Indeed, the raw spectra in this temperature range lack the fine structure of the I_2 spectrum (Bahrini et al., 2018; Johansson et al., 2014) and thus the signal is attributed to the light extinction due to the presence of aerosols (probably CsI) transported up to the optical cell. This online measurement experiment with a sensitive technique confirmed the absence of gaseous molecular iodine released in steam conditions.

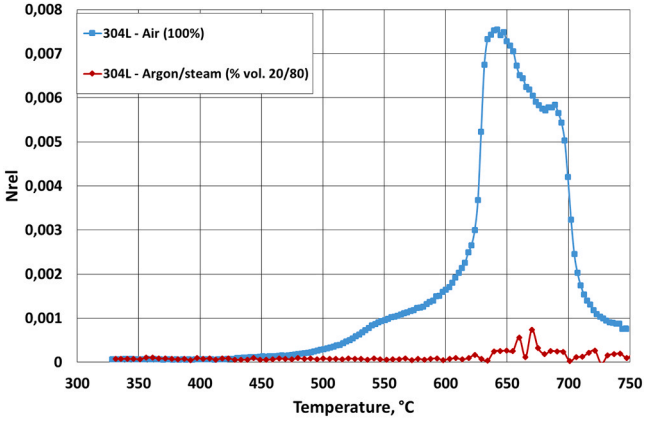

Fig. 3. Release and transport kinetics of I_2 during re-vaporization of CsI aerosols (RT aerosol impaction) with a heating rate of 5 °C/min up to 750 °C; blue curve: pure air with a flow rate of 53 mL_n/min (condition 1); red curve: argon/steam (70/30) with flow rate of 200 mL_n/min (condition 5).(For interpretation of the references to colour in this figure legend, the reader is referred to the web version of this article.)

In pure air (Table 2, condition 1), I_2 release starts at approx. 440 °C, which is coherent with the TGA tests, and occurs in two steps (Fig. 3, blue curve):

1) Between ≈ 440–550 °C a first slow and low release is observed;
2) Above 550 °C the majority of iodine is rapidly released (exponentially). Reproducibility tests have been performed in these conditions and the results were similar.

Further on, the re-vaporization tests in air/steam atmosphere (Table 2, conditions 2, 3 and 4) showed that I_2 release is initiated at a higher temperature, ≈ 480–500 °C (Fig. 4), compared to air re-vaporization, which is coherent to the TGA results of similar tests. While the release of I_2 in two steps is still noticeable for the % vol. 50/50 (condition 2), it is less pronounced for the other two carrier gas compositions (conditions 3 and 4). It is also interesting to note that the release curves present "spikes" (above ≈520 °C), which resemble those in the case of argon/steam re-vaporization. This suggests the presence of a larger amount of aerosols, which in turn prevent a reliable measurement of I_2.

4.2.2. Influence of CsI deposition process: high-temperature (conditions 6–13) vs. aerosol impaction at room temperature

As a general rule, the re-vaporization of CsI deposits obtained by different routes follows the same trend if the same experimental conditions are applied.

Compared to RT aerosol impaction, CsI aerosols deposited in the 400–150 °C temperature range present a similar re-vaporization behaviour with atmosphere composition (Table 3, air and argon/steam conditions only): similar gaseous iodine releases and overall deposition trends were observed for the RIGolo integral tests. It is thus assumed that CsI re-vaporization behaviour is very close when

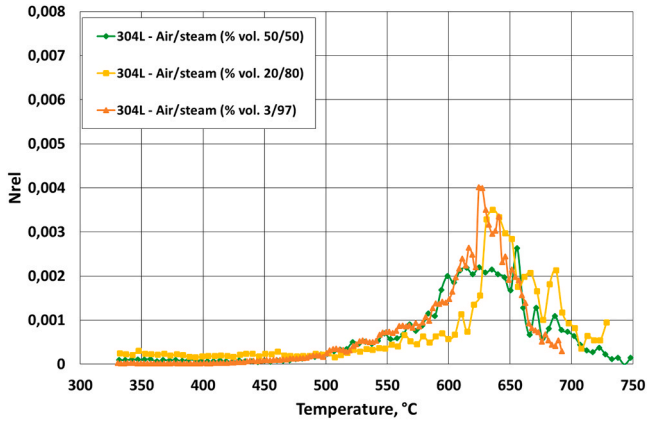

Fig. 4. Release and transport kinetics of I_2 during re-vaporization of CsI aerosols (RT aerosol impaction) with a heating rate of 5 °C/min up to 750 °C. green curve: air/steam % vol. 50/50 (condition 2); yellow curve:, air/steam % vol. 20/80 (condition 3); orange curve: air/steam % vol. 3/97 (condition 4). Gas flow: 200 mL_n/min for all conditions.(For interpretation of the references to colour in this figure legend, the reader is referred to the web version of this article.)

considering deposited aerosols.

For the two other deposition routes (high temperature vapour deposition 720–620 °C and vapour condensation 620–440 °C), re-vaporization in argon/steam (conditions 8 and 11) did not lead to the release of I_2; those results are comparable to the re-vaporization of CsI aerosols (conditions 5 and 12). Nevertheless, the Cs/I mass ratio in the RIGolo line is much higher (3.8 and 3.1 for conditions 8 and 11 respectively) compared to condition 5 (1.1). This observation indicates that besides CsI, other species can be involved during steam re-vaporization of such CsI deposits. CsOH is a possible candidate for the other Cs compounds, the iodine transported species could not be clearly identified.

Re-vaporization in air of the high-temperature deposits (condition n°6) and the aerosols deposits in has resulted in the release of 53% of iodine as I_2. The ICP-MS analysis of the alumina tube leachate shows a Cs/I mass ratio ~ 10. Both results are consistent with the re-vaporization behaviour of CsI aerosols as described in Section 4.2.1. Only one mixed air/steam carrier gas composition (% vol. 20/80) was tested with the high-temperature (720–620 °C, condition 7) and vapour condensation (620–440 °C, condition 10) deposits. The results show that 12–13% of iodine is released as I_2 and that the Cs/I ≈ 1.1 – 1.6 in the alumina tube, which is again consistent with the results presented in Section 4.2.1. However, there was a noticeable difference in the amount of released molecular iodine for condition 9. The re-vaporization in pure air of a CsI deposit obtained by vapour condensation (620–440 °C) resulted in the release of only 7–15% of I_2, which is much lower when compared to the amount of released I_2 in other experiments in the same re-vaporization conditions. The residual amount of Cs on the steel coupon is 2.4 – 4.5% and the Cs/I ≈ 1.3 in the alumina tube, suggesting the re-vaporization of Cs as several different species. The possible reasons, which may be linked to the organized crystalline structure of the deposit, are discussed further.

Surface characterizations by XPS and ToF-SIMS have been performed on the 316 L foils after CsI re-vaporization of high temperature deposits and condensed vapour (as displayed in Fig. 6). The presence of the mixed Cs-Cr-O compounds described above (see Section 4.2.1) is confirmed (Fig. 6b, depth profiles in negative polarity), as soon as air is present in the carrier gas. Also, in both cases, the Cs depth profile indicates that Cs had migrated in the oxide layer during the thermal treatment – or that the oxide layer may have growth up to the CsI deposit. Indeed the Cs_2^+ and Cs_2I^+ signals are very low at the surface and in the first oxide layer (composed of Fe and Mn) and increase strongly in the second Cr-Mn oxide layer (Fig. 6, depth profile in positive polarity). Migration of CsI inside the oxide layer may explain the significantly more important residual mass of Cs (9.7%) and I (8.6%) observed on the 316 L foil after re-vaporization of high-temperature vapour deposit in steam/air (Table 3, condition 7).

Based on the results of the integral tests, online measurement tests have been performed with CsI high-temperature (720–620 °C) and vapour condensation (620–440 °C) deposits with the same thermal cycle as for conditions 6 and 9. The carrier gas was pure air. The I_2 release kinetics from CsI deposits obtained by vapour condensation (condition n°9) presents a similar pattern as from CsI deposits obtained by RT aerosol impaction (condition n°1) (Fig. 6). The process occurred in two steps: 1) a slow and low release between ≈ 350–500 °C, and 2) a more rapid re-vaporization above 500 °C, which results in the total release of iodine from the surface of the pre-oxidized 316 L foil.

The kinetic study of I_2 release in case of a high-temperature CsI deposit (720–620 °C), on the contrary, has highlighted a new phenomenon. While the cumulated amount of released I_2 is consistent with the release observed in condition 1 (RT aerosol impaction), the I_2 release and transport kinetics is slightly different (Fig. 5). There is a two-step molecular iodine release between ≈ 400–550 °C (slow) and above 550 °C (rapid), which is consistent with previous results. However, there is an additional release peak between ≈ 200–350 °C, which has been reproduced in another test, hinting at a different re-vaporization process, probably linked to the nature of the deposit in this temperature range (720–620 °C). This new release mechanism may be owed to the CsI deposition temperature which resulted in a non-uniform amorphous like layer of deposits (see Section 4.1) which is quite different to aerosol impaction (Taamalli et al., 2020) so that one can expect strong evolution at the molecular level too (for instance in the structure of the CsI outermost surface), inducing differences in the reaction mechanism – as will be seen with the DFT calculations (Section 5).

The kinetic test results have shown the absence of any release below 200 °C, hence the I_2 release kinetics for this series of tests is shown starting at ≈ 170–250 °C.

4.2.3. Influence of substrate nature: stainless steel vs. gold inert surface (condition 14)

A previous study (Sasaki et al., 2013) has linked the formation of gaseous molecular iodine to the interaction between CsI and Cr_2O_3 in presence of dioxygen. This assumption is supported by the fact that the reaction cited by Sasaki et al. (2013) is thermodynamically favoured in the temperature range of our conditions. In air conditions, our observations (release of I_2 and formation of caesium chromate species) allowed us to propose a similar reactivity with the surface (Obada et al., 2017). For the further understanding of the phenomenon, it was decided to perform additional tests whose goals were to determine whether there are other mechanisms involved in the formation of I_2, besides CsI-substrate interaction.

Consequently, CsI aerosol deposits (aerosol impaction at room temperature) have been generated on a chemically inert surface – gold coupons, and a series of re-vaporization tests in pure air have been performed afterwards (condition n°14). Integral tests in the RIGolo device have led to the total release of caesium (0.4% detected on the coupon after re-vaporization by ICP-MS) and iodine from the surface of the gold coupon. The Cs/I ≈ 1.6 in the alumina tube, suggesting again the re-vaporization of Cs under other species besides CsI compounds. Up to 28% of iodine has been released as I_2 (relative to the total measured amount of iodine at the end of test), which is lower compared to the re-vaporization from the pre-oxidized 304 L coupons and 316 L foils in the same conditions (conditions 1 and 12 respectively). Nevertheless, this lower release may be owed to deposit inhomogeneities. These results suggest that the formation of I_2 is not due only to the interaction of CsI with the oxide substrate, but that the oxidation of iodide by the gas phase plays an important role in iodine vaporization.

From a kinetic point of view, TGA analysis has shown that the

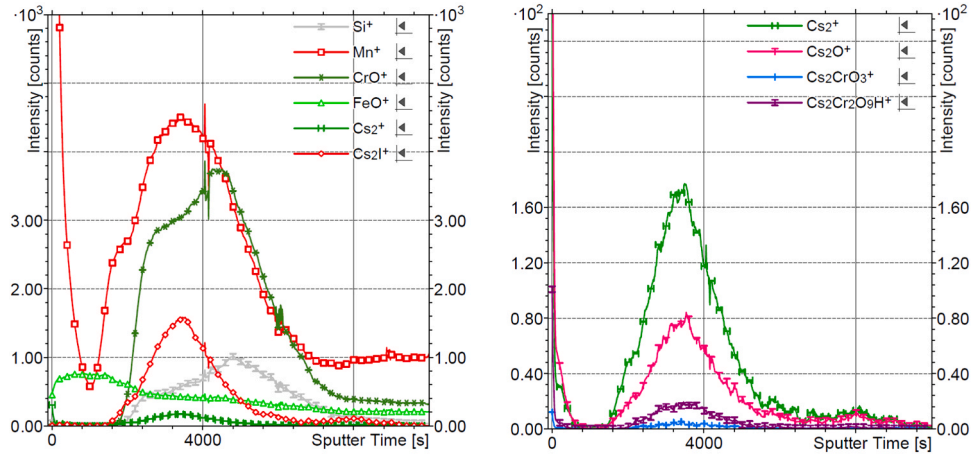

Fig. 5. TOF-SIMS profile of CsI vapour condensation deposition 316 L pre-oxidized foil and re-vaporized in air/steam atmosphere (condition 10, Table 3). Secondary ions in positive polarity a) major fragments and b) minor fragments.

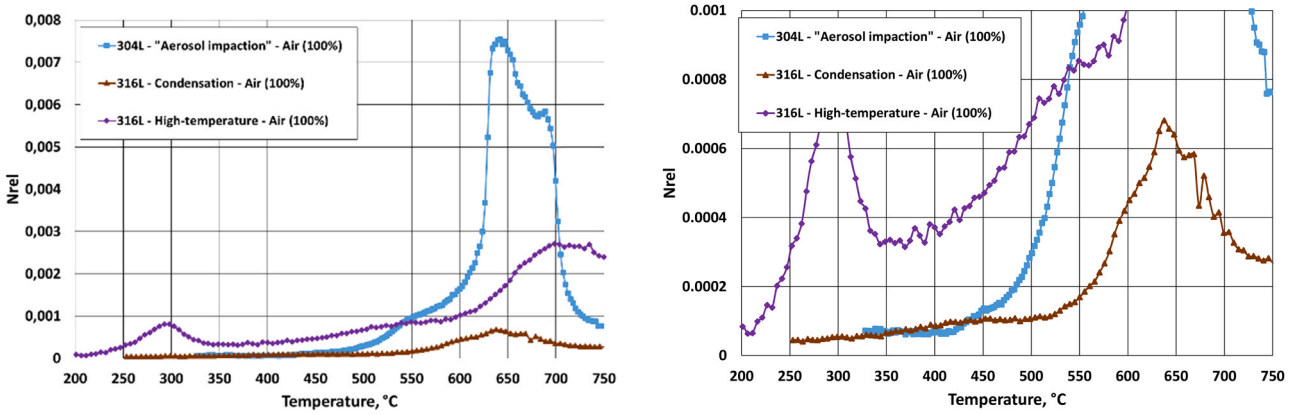

Fig. 6. Release and transport kinetics of I_2 during re-vaporization of CsI deposits in pure air with a heating rate of 5 °C/min up to 750 °C; blue curve: CsI RT aerosol impaction" (condition 1, air flow rate 53 mL_n/min), brown curve: CsI vapour condensation (condition 9, air flow rate 200 mL_n/min); purple curve: CsI high-temperature vapour deposition (condition 6, air flow 200 mL_n/min).(For interpretation of the references to colour in this figure legend, the reader is referred to the web version of this article.)

process is initiated at a higher temperature (526 °C) compared to CsI re-vaporization onset on 304 L coupons (see Section 4.2.1). Fig. 7 shows the gaseous molecular iodine release kinetics and the pattern clearly resembles that of CsI re-vaporization from pre-oxidized stainless steel surface (condition n°1):

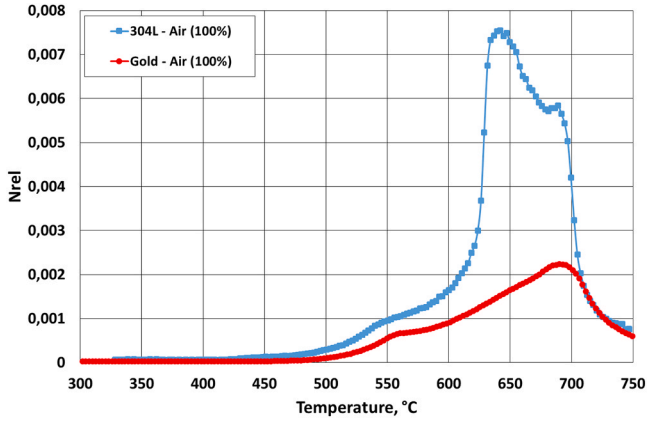

Fig. 7. Release and transport kinetics of I_2 during re-vaporization of CsI aerosols (RT aerosol impaction) in pure air (53 53 mLn/min) and with a heating rate of 5 °C/min up to 750 °C; blue curve: pre-oxidized 304 L surface; red curve: gold surface.(For interpretation of the references to colour in this figure legend, the reader is referred to the web version of this article.)

1) A low release between ≈ 450–560 °C;
2) A more important release (up to the depletion of the iodine source) above 560 °C. It is worth noting that this release is slower compared to the release in condition n°1.

This suggests that the mechanisms governing the formation of I_2 are very close, regardless of the substrate. As a consequence, the role of pre-oxidized stainless steel in the production of gaseous iodine species is less important than initially expected.

Nevertheless, the differences observed between kinetic of I_2 productions when considering an inert surface and pre-oxidized stainless steel, indicates that some substrate effect cannot be excluded at high temperature.

4.2.4. *Thermal cycle boundaries: kinetic of I_2 release up to 550 °C*

Based on the results of previous online measurement tests, it was decided to conduct another one with a limited maximum temperature of ≈ 550 °C, which is the upper limit for the first step of I_2 release. The goal was to study the release phenomenon in the 450–550 °C range. In order to reduce the carrier gas interference at low temperature, the sample was heated under argon up to ≈ 420 °C, and then the carrier gas was

switched to a mixture of air/steam (% vol. 50/50). Fig. 7 shows the I_2 release and transport kinetics and it can be noticed that the release starts at ≈ 440 °C and ends just after the final temperature of ≈ 550 °C is reached, with a subsequent decrease in signal, which is probably due to the depletion of the source involved in this first mechanism. The fine peak at 420 °C is an artifact in the IBBCEAS response due to a transient overpressure in the IBB CEAS cell when switching the carrier gas composition from argon to the air/steam mix. This transient induced a shit in the baseline which could not be corrected during the test. The I_2 spectral fingerprint is indeed clearly observed from 450 °C on.

No integral test in the RIGolo device has been performed in these conditions, but surface characterization by ToF-SIMS of the sample has been done. The depth profile analysis in positive polarity revealed an intense Cs^+ signal (Fig. 8a), while the analysis in negative polarity has revealed the presence of relatively intense I^- secondary ions (Fig. 8b). Also, the secondary ion clusters $Cs_2CrO_3^+$ and $Cs_2Cr_2O_9H^+$ have been detected, which indicates the formation of Cs–Cr–O compounds. All these results suggest that a part of iodine has been released from the surface as I_2 and that caesium mainly remained on the surface, both as CsI and mixed Cs–Cr oxides. Furthermore, it would seem that up to 550 °C the formation of I_2 is based on the reaction between the CsI deposit and carrier gas components in a heterogeneous phase. The most intense release observed above 550 °C (Fig. 3, blue curve) could then be explained by the vaporization of CsI deposits (which starts between 550 and 600 °C) followed by a reaction in gaseous (homogeneous) phase, which would favour the contact between CsI and carrier gas molecules. In this latter case, the residual quantity of Cs on the surface would be low as observed in condition 1 (see Table 3). (Figs. 9–12).

5. Theoretical modelling

In order to get insight in the molecular mechanism of the CsI revaporisation for small aerosols, we performed DFT modelling of the possible oxygen interaction and reaction on the surface of the CsI Aerosol. The size of the particle deposited in the experiment is large (larger than 1 μm). The larger part of the CsI particles will not be directly in interaction with the support. Furthermore, the evolution at relatively low temperatures (500 – 650 °C) is mostly independent of the nature of the support. A theoretical model that does not include explicitly the support will be valid to investigate the CsI surface oxidation mechanism. Furthermore, the reactivity of the deposited CsI depends on the preparation conditions which will modify both the size of the particles and the nature of the exposed surfaces and sites. By defining various models of the CsI surfaces, it will be possible to explain the differences observed experimentally as well as the effect of O_2 and water on the surfaces.

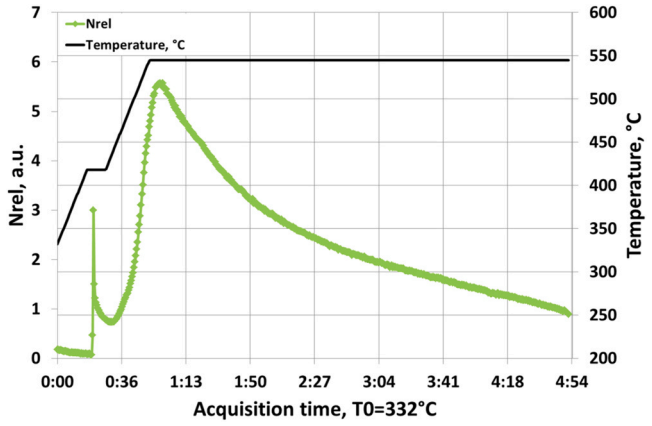

Fig. 8. Release and transport kinetics of I_2 during re-vaporization of CsI aerosols (RT aerosol impaction) from pre-oxidized 304 L coupon. Thermal cycle and carrier gas composition: 1) heating up to 420 °C in argon; 2) maintain for 10 min at 420 °C, switching to air/steam (% vol. 50/50); 3) heating up to 550 °C and 4) maintain at 550 °C for 6 h. Gas flow 200 mL_n/min. Heating up at 5 °C/min.

5.1. Model

CsI crystal has a simple cubic structure which belongs to the Pm3m group, with two atoms in the unit cell, caesium at (0, 0, 0) and iodine at (a/2) (1, 1, 1) while 'a' being the lattice constant (456.67 pm) (Satpathy, 1986) kept fixed in the calculation at the experimental. The nature of the exposed surface is defined by the surface energy of low index surfaces. In order to compute them, we define super-cell composed of at least 8 layer of CsI and added 15 Å of vacuum to avoid any interaction between the slab. The four outermost layers have been relaxed. The surface energies of low index surfaces are summarized in Table 4.

The (011) surface is the most stable one and considering the large surface energy difference, it will be the only surface exposed by dehydrated CsI particles. The (011) surface is composed of alternating rows of Cs and I anions.

5.2. H_2O and O_2 interaction with perfect (011) surfaces

The reactive molecules in the gas phase during the experiments are water and dioxygen. We studied theoretically the interaction of these two molecules with the CsI surfaces to determine the reaction that may occur on the surface and may explain the iodine revaporisation.

The water absorption on the surface is molecular. One hydrogen atom of the water molecule forms a hydrogen bond with the surface iodine while the negatively charged oxygen atom interacts with the Cs cation. The Cs–O and H–I distances are 3.16 and 2.45 Å respectively. The adsorption energy is 0.52 eV. The adsorption is exothermic but as the main interaction is a weak hydrogen bond, the water molecule adsorption will not be favoured at high temperature. We tested the dissociative adsorption of the water molecule on the surface to form both Cs-OH and HI groups. This adsorption is very endothermic (−3,54 eV). The formation of IH groups on the perfect surface is not possible and such we can exclude the departure of HI(g) molecule from the surface.

The oxygen molecule adsorption on the surface is also a molecular one. The O_2 molecule is located in a η2 geometry, on top of one Cs cation. The O–Cs distances are 3.04 A and the O–O one is 1.24 very close to the O–O distance in the gas phase (. The adsorption is endothermic (Eads = −0.18 eV). We study the dissociative adsorption. The oxygen atoms are located in the first surface plane, between Cs and I ion. This adsorption mode is even more endothermic (Eads = −0.88 eV) than the molecular one. The oxygen adsorption and reaction with a perfect surface is not probable at high temperature.

5.3. O_2 interaction with defective surfaces

The presence of defects on the surface increases their reactivity. To model these defects, we study the O_2 interaction with a step (0 1 1) surface: i.e. the (0 1 4) surface, composed a step and a (0 1 1) terrace (Fig. 13). The iodine ions located on the step are under-coordinated which would increase their reactivity.

On the opposite to the perfect surface, the oxygen molecular adsorption on the iodine ion located on the step is an exothermic process (ΔE = −0,57 eV/Eads = 0.57 eV) (b step, Fig. 14). The oxygen molecule is located between two iodine anions of the edge. The I–O distance is 2.86 Å and the O–O one is 1.27 Å, 0.04 Å larger than the distance for the gas phase molecule. The oxygen molecule is activated when adsorbed on a defect. The dissociative adsorption is favoured on the edge. The adsorption energy is then 1,07 eV (c step, Fig. 14). One the oxygen molecule is dissociated on the surface, the desorption of $IO^\bullet$ radical is possible. This final step is endothermic (d step, Fig. 14) but will be favoured by a very concentration of iodine in the gas and by the continuous gas flow above the surface. $IO^\bullet$ being a strong oxidant it will

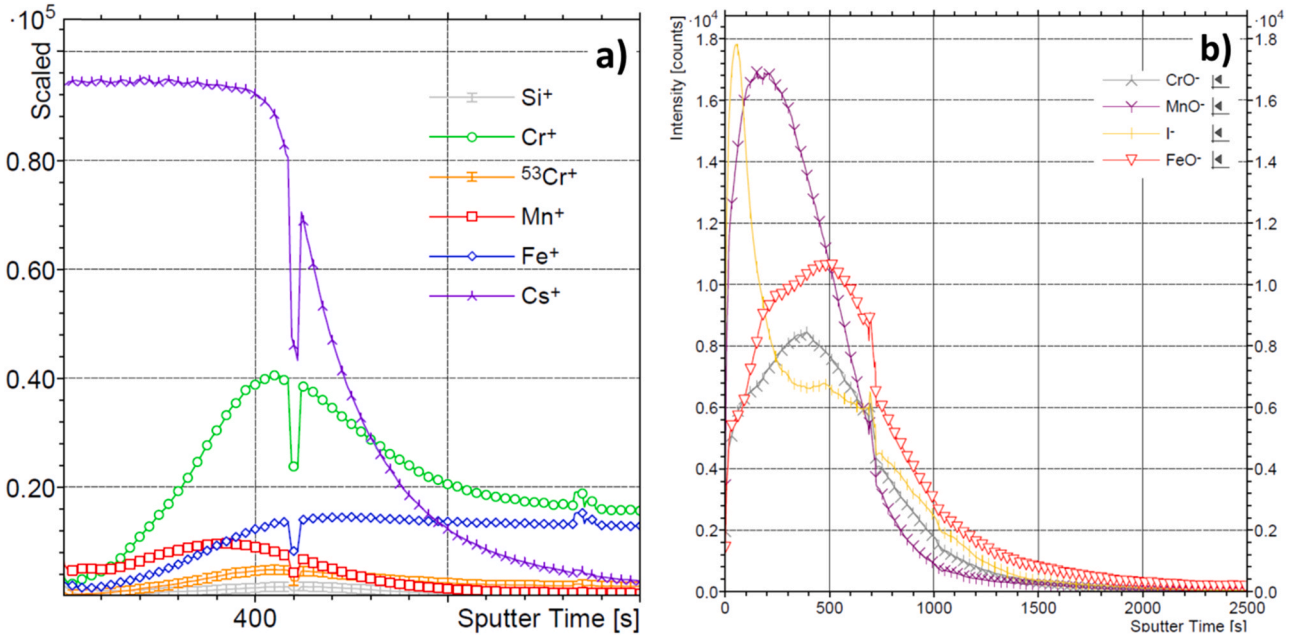

Fig. 9. ToF-SIMS depth profile of a CsI aerosol deposit re-vaporized from pre-oxidized 304 L coupon: a) secondary ions in positive polarity and b) secondary ions in negative polarity.

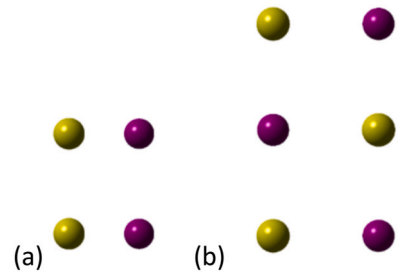

Fig. 10. Top (a) and side (b) view of the (011) surface (most stable surface)(Cs in yellow, I in purple).(For interpretation of the references to colour in this figure legend, the reader is referred to the web version of this article.)

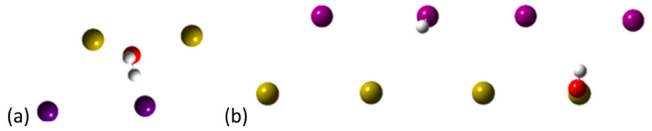

Fig. 11. Water adsorption on the perfect (011) surface (a) molecular adsorption (b) dissociative adsorption (Cs in yellow, I in purple, O in red, H in white). (For interpretation of the references to colour in this figure legend, the reader is referred to the web version of this article.)

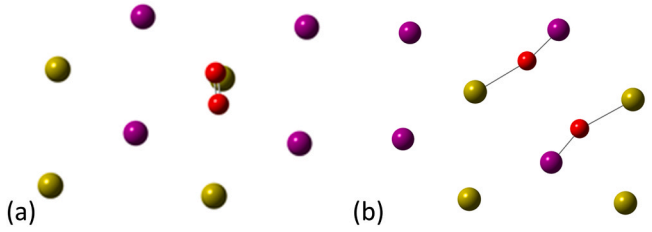

Fig. 12. O_2 adsorption on the perfect (011) surface (a) molecular adsorption (b) dissociative adsorption (Cs in yellow, I in purple, O in red).(For interpretation of the references to colour in this figure legend, the reader is referred to the web version of this article.)

Table 4
Surface energy ($mJ.m^{-2}$) after relaxation of low index surfaces.

Surface index	(011)	(111)	(210)	(211)	(001)
Surface energy ($mJ.m^{-2}$)	193	520	365	417	615

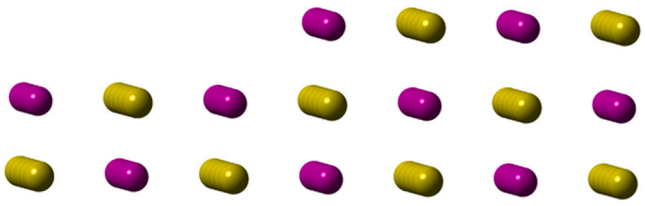

Fig. 13. Side view of the stepped (014) surface (Cs in yellow, I in purple).(For interpretation of the references to colour in this figure legend, the reader is referred to the web version of this article.)

react with the iodide to produce $I_{2(g)}$ as demonstrated in liquid (Sakamoto et al., 2009) and in the gas phase (Fortin et al., 2019).

In order to get insight in the kinetic of the oxygen molecule dissociation on the surface, we computed the activation energy of the reaction (Fig. 15). The activation energy is small (E_{act} = 0,64 eV), which indicate that the surface oxidation will be fast on defects. The O–O distance on the transition state is 1.77 Å.

From the DFT calculation, we can conclude that the water molecule will not be involved directly in the CsI oxidation reactions and in the I_2 formation. However, when the quantity of water in the feed is much larger than the oxygen one, the water will have a competitive adsorption on the surface.

On the opposite to water, the O2 molecules can react on the CsI particles to form in the first step the radical species $IO^{\bullet}$, but this process will mainly occur on the surface defects. The oxygen reactivity depends then of the nature of the surface and on the numbers of defects. However, once the $IO^{\bullet}$ radical have been formed, this reactive species may react with the surface and such create defects on the particle surface. This mechanism may be responsible for the very fast increase of the reaction rate with temperature that is observed experimentally. It may

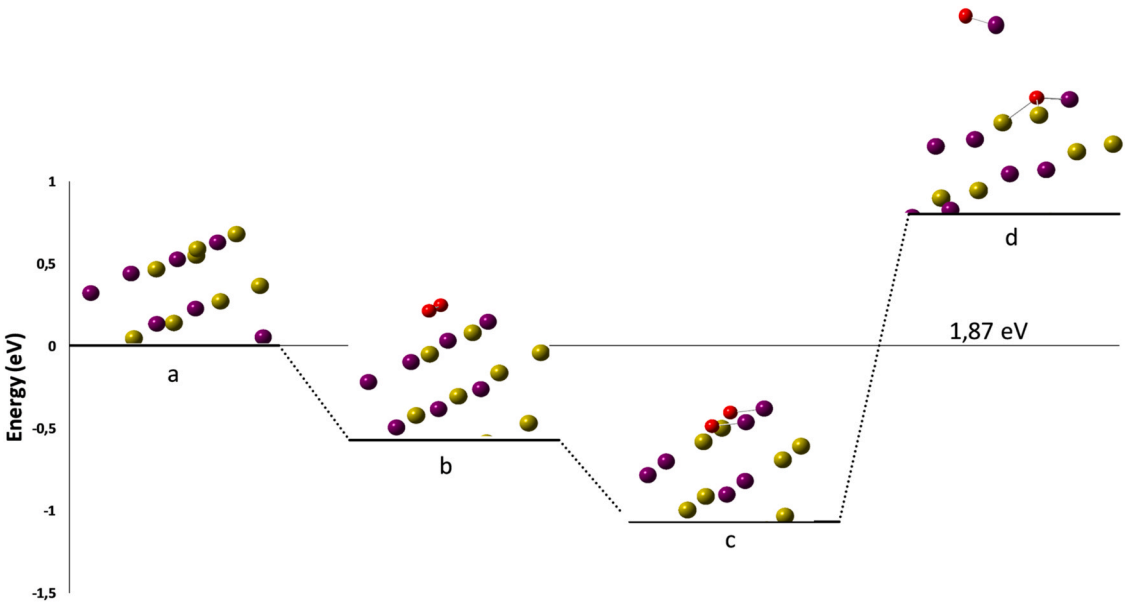

Fig. 14. Adsorption and dissociation of O2 on stepped surface (Cs in yellow, I in purple, O in red).(For interpretation of the references to colour in this figure legend, the reader is referred to the web version of this article.)

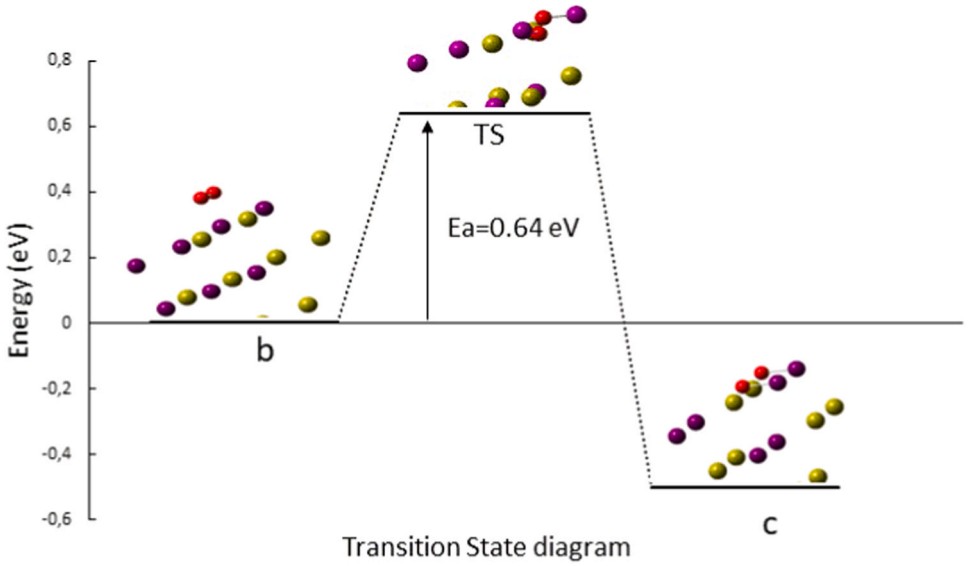

Fig. 15. O_2 activation mechanism on the step surface ((Cs in yellow, I in purple, O in red).(For interpretation of the references to colour in this figure legend, the reader is referred to the web version of this article.)

be mentioned that the CsI reactivity at low temperature (around 400 °C according to the experiments) will depend on the exact nature of the surface and on the deposition method. A fast cooling of hot particles on the surface will favour the formation of defects and increased its reactivity.

6. Conclusion

From the experimental study, the following trends can be summarized as follows:

- In presence of air, the re-vaporization of CsI deposits from pre-oxidized stainless steel surfaces leads to the release of 45–75% of I_2 from initial iodine inventory – except for CsI deposit by vapour condensation. A part of Cs is retained on the surface (2.5–10% of initial amount) and forms mixed Cs–Cr–O compounds;
- In a mixed air/steam atmosphere, between 12% and 33% of iodine is released as I_2, regardless of the air content in the carrier gas, the molecular iodine fraction probably depends temperature deposits;
- The deposit nature (aerosol, high temperature vapour deposition and vapour condensation) does not seem to influence the amount of released molecular iodine strongly or retained caesium. An exception is the CsI deposit by vapour condensation (620–440 °C) which is crystalline and thus has an organized structure;
- The re-vaporization of CsI aerosols from an inert surface (gold) in air leads to the formation of 28% of molecular iodine (relative to I initial amount), which is lower compared to the re-vaporization from a stainless steel surface;
- The gaseous molecular iodine release kinetic pattern is generally the same, regardless of carrier gas composition, deposit or substrate nature and consists of two steps: an initial reduced release between ≈ 440–550 °C and a second rapid release above 550 °C. In the case of

CsI high-temperature deposits (720–620 °C) there is an additional I_2 release peak between 200 and 350 °C.

The analysis of these results allows us to make the following conclusions and hypotheses:

- There seem to be several mechanisms responsible for I_2 formation, depending on the temperature. Below 550 °C the results suggest a solid-gas (heterogeneous) phase interaction between the deposit and the carrier gas. Above 550 °C, the CsI starts to vaporize and the interaction is in gas (homogeneous) phase, which would explain the increased rate of I_2 release;
- The iodine formation is favoured on the CsI surface defects, and such is influenced by the CsI deposition process. The I_2 formation start at higher temperature on well crystallized particles. However, the formation of the first I_2 molecules will induce the formation of defects on the surface which will increase the surface oxidation rate.

To develop some models and cover severe accident boundary conditions, additional experimental investigations are needed to explore other fission products and other gas composition.

CRediT authorship contribution statement

D. Obada: Investigation, Writing - original draft, Writing - review & editing; **H. Hijazi**: Investigation; **J.-F. Paul**: Investigation, Writing - original draft, Writing - review & editing; **L. Gasnot**: Investigation; **A.-C. Grégoire**: Investigation, Writing - original draft, Writing - review & editing; **A.-S. Mamede**: Investigation, Writing - original draft, Writing - review & editing **L. Cantrel**: Writing - original draft, Writing - review & editing.

Declaration of Competing Interest

The authors declare that they have no known competing financial interests or personal relationships that could have appeared to influence the work reported in this paper.

Acknowledgements

This work was performed in the frame of the French Research Program ANR-11-RSNR-0013-01 called MiRE (Mitigation of outside releases in case of nuclear accident), with the financial support of EDF and Framatome. The authors thank the HPC centre of the Lille University for providing CPU resources. Surface analysis have been performed at the 'plateforme d'analyses de surfaces' of the Lille University.

References

Anderson, A., Auvinen, A., Bottomley, P., Bryan, C., Freemantle, N., Hieraut, J., Jokiniemi, J., Kingsbury, A., & Tuson, A. (2000). Revaporisation tests on samples from Phebus fission products: Final report. (Issue 2 ed.) AEA Technology Report, No. AEAT/R/NS/0124.

Auvinen, A., Lehtinen, K.E.J., Enriquez, J., Jokiniemi, J.K., Zilliacus, R., 2000. Vaporisation rates of csoh and csi in conditions simulating a severe nuclear accident. J. Aerosol Sci. 31, 1029–1043. https://doi.org/10.1016/S0021-8502(00)00027-6.

Bahrini, C., Grégoire, A.-C., Obada, D., Mun, C., Fittschen, C., 2018. Incoherent broadband cavity enhanced absorption spectroscopy for sensitive and rapid molecular iodine detection in the presence of aerosols and water vapour. Opt. Laser Technol. 108, 466–479. https://doi.org/10.1016/j.optlastec.2018.06.050.

Berdonosov, S.S, Baronov, S.B, 1999. Interaction of caesium Iodide with an air flow at high temperatures. Radiochemistry 41, 63–66.

Berdonosov, S.S., Sitova, M.A., 1997. Chemical forms of iodine occurring at evaporation and condensation of cesium iodide in air. Radiochemistry 39, 341–342.

Bottomley, P.D.W., Knebel, K., Van Winckel, S., Haste, T., Souvi, S.M.O., Auvinen, A., Kalilainen, J., Kärkelä, T., 2014. Revaporisation of fission product deposits in the primary circuit and its impact on accident source term. Ann. Nucl. Energy 74, 208–223. https://doi.org/10.1016/j.anucene.2014.05.011.

Cantrel, L., Albiol, T., Bosland, L., Colombani, J., Cousin, F., Grégoire, A.C., Leroy, O., Morin, S., Mun, C., Ohnet, M.N., Souvi, S., Monsanglant-Louvet, C., Louis, F., Azambre, B., Volkringer, C., 2018. Research works on iodine and ruthenium behavior in severe accident conditions. J. Nucl. Eng. Radiat. Sci. 4, 020903 https://doi.org/10.1115/1.4038223.

Cantrel, L., Cousin, F., Bosland, L., Chevalier-Jabet, K., Marchetto, C., 2014. ASTEC V2 severe accident integral code: fission product modelling and validation. Nucl. Eng. Des. 272, 195–206. https://doi.org/10.1016/j.nucengdes.2014.01.011.

Fortin, C., Fèvre-Nollet, V., Cousin, F., Lebègue, P., Louis, F., 2019. Box modelling of gas-phase atmospheric iodine chemical reactivity in case of a nuclear accident. Atmos. Environ. 214, 116838 https://doi.org/10.1016/j.atmosenv.2019.116838.

Giordano, P., Auvinen, A., Brillant, G., Colombani, J., Davidovich, N., Dickson, R., Haste, T., Kärkelä, T., Lamy, J.S., Mun, C., Ohai, D., Pontillon, Y., Steinbrück, M., Vér, N., 2010. Recent advances in understanding ruthenium behaviour under air-ingress conditions during a PWR severe accident. Prog. Nucl. Energy 52, 109–119. https://doi.org/10.1016/j.pnucene.2009.09.011.

Girault, N., Payot, F., 2013. Insights into iodine behaviour and speciation in the Phébus primary circuit. Ann. Nucl. Energy 61, 143–156. https://doi.org/10.1016/j.anucene.2013.03.038.

Gouello, M., Mutelle, H., Cousin, F., Sobanska, S., Blanquet, E., 2013. Analysis of the iodine gas phase produced by interaction of CsI and MoO3 vapours in flowing steam. Nucl. Eng. Des. 263, 462–472. https://doi.org/10.1016/j.nucengdes.2013.06.016.

Grégoire, A.-C., Kalilainen, J., Cousin, F., Mutelle, H., Cantrel, L., Auvinen, A., Haste, T., Sobanska, S., 2015. Studies on the role of molybdenum on iodine transport in the RCS in nuclear severe accident conditions. Ann. Nucl. Energy 78, 117–129. https://doi.org/10.1016/j.anucene.2014.11.026.

Hafner, J., 2008. *Ab-initio* simulations of materials using VASP: density-functional theory and beyond. J. Comput. Chem. 29, 2044–2078. https://doi.org/10.1002/jcc.21057.

Haste, T., Payot, F., Bottomley, P.D.W., 2013. Transport and deposition in the Phébus FP circuit. Ann. Nucl. Energy 61, 102–121. https://doi.org/10.1016/j.anucene.2012.10.032.

Hidaka, A., Igarashi, M., Hashimoto, K., Sato, H., Yoshino, T., Sugimoto, J., 1995. Experimental and analytical study on the behavior of cesium iodide aerosol/vapor deposition onto inner surface of pipe wall under severe accident conditions. J. Nucl. Sci. Technol. 32, 1047–1053. https://doi.org/10.1080/18811248.1995.9731813.

Hijazi, H., 2017. Réactivité chimique des aérosols d'iode en conditions accidentelles dans un réacteur nucléaiRE. Université de Lille.

Johansson, O., Mutelle, H., Parker, A.E., Batut, S., Demaux, P., Schoemaecker, C., Fittschen, C., 2014. Quantitative IBBCEAS measurements of I2 in the presence of aerosols. Appl. Phys. B 114, 421–432. https://doi.org/10.1007/s00340-013-5536-9.

Kalilainen, J., Kärkelä, T., Zilliacus, R., Tapper, U., Auvinen, A., Jokiniemi, J., 2014. Chemical reactions of fission product deposits and iodine transport in primary circuit conditions. Nucl. Eng. Des. 267, 140–147. https://doi.org/10.1016/j.nucengdes.2013.11.078.

Katata, G., Chino, M., Kobayashi, T., Terada, H., Ota, M., Nagai, H., Kajino, M., Draxler, R., Hort, M.C., Malo, A., Torii, T., Sanada, Y., 2015. Detailed source term estimation of the atmospheric release for the Fukushima Daiichi Nuclear Power Station accident by coupling simulations of an atmospheric dispersion model with an improved deposition scheme and oceanic dispersion model. Atmos. Chem. Phys. 15, 1029–1070. https://doi.org/10.5194/acp-15-1029-2015.

Khanniche, S., Louis, F., Cantrel, L., Černušák, I., 2017a. Investigation of the reaction mechanism and kinetics of iodic acid with OH radical using quantum chemistry. ACS Earth Space Chem. 1, 227–235. https://doi.org/10.1021/acsearthspacechem.7b00038.

Khanniche, S., Louis, F., Cantrel, L., Černušák, I., 2017b. Thermochemistry of HIO_2 species and reactivity of iodous acid with oh radical: a computational study. ACS Earth Space Chem. 1, 39–49. https://doi.org/10.1021/acsearthspacechem.6b00010.

Khanniche, S., Louis, F., Cantrel, L., Černušák, I., 2016a. Computational study of the I2O5+ H2O = 2 HOIO2 gas-phase reaction. Chem. Phys. Lett. 662, 114–119. https://doi.org/10.1016/j.cplett.2016.09.023.

Khanniche, S., Louis, F., Cantrel, L., Černušák, I., 2016b. A theoretical study of the microhydration of iodic acid (HOIO2). Comput. Theor. Chem. 1094, 98–107. https://doi.org/10.1016/j.comptc.2016.09.010.

Khanniche, S., Louis, F., Cantrel, L., Černušák, I., 2016c. A density functional theory and *ab Initio* investigation of the oxidation reaction of CO by IO radicals. J. Phys. Chem. A 120, 1737–1749. https://doi.org/10.1021/acs.jpca.6b00047.

Khiri, D., Vandeputte, R., Taamalli, S., Cantrel, L., Louis, F., 2019. Microhydration of caesium metaborate: structural and thermochemical properties of CsBO2 + n H2O (n = 1–4) aggregates. J. Mol. Model. 25, 207 https://doi.org/10.1007/s00894-019-4094-4.

Knebel, K., Bottomley, P.D.W., Rondinella, V.V., Auvinen, A., Jokiniemi, J., 2014. An experimental device to study the revaporisation behaviour of fission product deposits under severe accident conditions. Prog. Nucl. Energy 72, 77–82. https://doi.org/10.1016/j.pnucene.2013.07.022.

Kresse, G., Furthmüller, J., 1996. Efficiency of ab-initio total energy calculations for metals and semiconductors using a plane-wave basis set. Comput. Mater. Sci. 6, 15–50. https://doi.org/10.1016/0927-0256(96)00008-0.

Kresse, G., Joubert, D., 1999. From ultrasoft pseudopotentials to the projector augmented-wave method. Phys. Rev. B 59, 1758–1775. https://doi.org/10.1103/PhysRevB.59.1758.

Kulyukhin, S.A., Mikheev, N.B., Kamenskaya, A.N., Rumer, I.A., Konovalova, N.A., Novichenko†, V.L., 2004. Oxidative hydrolysis in water vapor-air phase of CsI radioaerosols produced by CsI sublimation from metallic surface. Radiochemistry 46, 63–66. https://doi.org/10.1023/B:RACH.0000024639.33411.68.

Mamede, A.-S., Nuns, N., Cristol, A.-L., Cantrel, L., Souvi, S., Cristol, S., Paul, J.F., 2016. Multitechnique characterisation of 304L surface states oxidized at high temperature in steam and air atmospheres. Appl. Surf. Sci. 369, 510–519. https://doi.org/10.1016/j.apsusc.2016.01.185.

Maruyama, Y., Shibazaki, H., Igarashi, M., Maeda, A., Harada, Y., Hidaka, A., Sugimoto, J., Hashimoto, K., Nakamura, N., 1999. Vapor condensation and thermophoretic aerosol deposition of cesium iodide in horizontal thermal gradient pipes. J. Nucl. Sci. Technol. 36, 433–442. https://doi.org/10.1080/18811248.1999.9726226.

Methfessel, M., Paxton, A.T., 1989. High-precision sampling for Brillouin-zone integration in metals. Phys. Rev. B 40, 3616–3621. https://doi.org/10.1103/PhysRevB.40.3616.

Monkhorst, H.J., Pack, J.D., 1976. Special points for Brillouin-zone integrations. Phys. Rev. B 13, 5188–5192. https://doi.org/10.1103/PhysRevB.13.5188.

Obada, D., Gasnot, L., Mamede, A.-S., Grégoire, A.-C., 2017. Assessment of Medium-Term Radioactive Releases in Case of a Severe Nuclear Accident on a Pressurized Water Reactor: Experimental Study of Fission Products Re-Vaporization from Deposits (Cs,I). In: Proceedings of ICAPP 2017. Atomic Energy Society of Japan, Fukui and Kyoto (Japan), p. 17328. In: Proceedings of ICAPP 2017.

Obada, D., Mamede, A.-S., Nuns, N., Grégoire, A.C., Gasnot, L., 2018. Combined ToF-SIMS and XPS characterization of 304L surface after interaction with caesium iodide under PWR severe accident conditions. Appl. Surf. Sci. 459, 23–31. https://doi.org/10.1016/j.apsusc.2018.07.212.

Obada, D., 2017. Evaluation de rejets moyen-terme en situation accidentelle grave d'un Réacteur à Eau Pressurisée: étude expérimentale de la re-vaporisation de dépôts de produits de fission (Cs, I). Université de Lille.

Perdew, J.P., Burke, K., Ernzerhof, M., 1996. Generalized gradient approximation made simple. Phys. Rev. Lett. 77, 3865–3868. https://doi.org/10.1103/PhysRevLett.77.3865.

Riggs, C.A., Tompson, R.V., Ghosh, T.K., Loyalka, S.K., Viswanath, D.S., 2007. Water adsorption isotherms for charged and uncharged cesium iodide aerosol particles. Nucl. Technol. 157, 74–86. https://doi.org/10.13182/NT07-A3803.

Sakamoto, Y., Yabushita, A., Kawasaki, M., Enami, S., 2009. Direct emission of I_2 Molecule and IO radical from the heterogeneous reactions of gaseous ozone with aqueous potassium iodide solution. J. Phys. Chem. A 113, 7707–7713. https://doi.org/10.1021/jp903486u.

Sasaki, K., Tanigaki, T., Tomohiro, O., et al., 2013. Microstructure analysis for chemical interaction between cesium and SUS316 steel in fast breeder reactor application. J. Energy Power Eng. 7, 716–725. https://doi.org/10.17265/1934-8975/2013.04.014.

Satpathy, S., 1986. Electron energy bands and cohesive properties of CsCl, CsBr, and CsI. Phys. Rev. B 33, 8706–8715. https://doi.org/10.1103/PhysRevB.33.8706.

Shibazaki, H., Maruyama, Y., Kudo, T., Hashimoto, K., Maeda, A., Harada, Y., Hidaka, A., Sugimoto, J., 2001. Revaporization of a CsI Aerosol in a horizontal straight pipe in a severe accident condition. Nucl. Technol. 134, 62–70. https://doi.org/10.13182/NT01-A3186.

Souvi, S.M.O., Badawi, M., Virot, F., Cristol, S., Cantrel, L., Paul, J.F., 2017. Influence of water, dihydrogen and dioxygen on the stability of the Cr2O3 surface: a first-principles investigation. Surf. Sci. 666, 44–52. https://doi.org/10.1016/j.susc.2017.08.005.

Sudolská, M., Cantrel, L., Budzák, Š., Černušák, I., 2014a. Molecular structures and thermodynamic properties of monohydrated gaseous iodine compounds: modelling for severe accident simulation. J. Nucl. Mater. 446, 73–80. https://doi.org/10.1016/j.jnucmat.2013.11.029.

Sudolská, M., Cantrel, L., Černušák, I., 2014b. Microhydration of caesium compounds: Cs, CsOH, CsI and Cs2I2 complexes with one to three H2O molecules of nuclear safety interest. J. Mol. Model. 20, 2218. https://doi.org/10.1007/s00894-014-2218-4.

Šulková, K., Cantrel, L., Louis, F., 2015. Gas-phase reactivity of cesium-containing species by quantum chemistry. J. Phys. Chem. A 119, 9373–9384. https://doi.org/10.1021/acs.jpca.5b05548.

Taamalli, S., Khiri, D., Suliman, S., Khanniche, S., Černušák, I., Cantrel, L., Ribaucour, M., Louis, F., 2020. Unraveling the tropospheric microhydration processes of iodous acid HOIO. ACS Earth Space Chem. 4, 92–100. https://doi.org/10.1021/acsearthspacechem.9b00257.

Terada, H., Katata, G., Chino, M., Nagai, H., 2012. Atmospheric discharge and dispersion of radionuclides during the Fukushima Dai-ichi Nuclear Power Plant accident. Part II: verification of the source term and analysis of regional-scale atmospheric dispersion. J. Environ. Radioact. 112, 141–154. https://doi.org/10.1016/j.jenvrad.2012.05.023.

Tkatchenko, A., Scheffler, M., 2009. Accurate molecular van der waals interactions from ground-state electron density and free-atom reference data. Phys. Rev. Lett. 102, 073005 https://doi.org/10.1103/PhysRevLett.102.073005.

vasp.5.4.1.

Villard, A., Khanniche, S., Fortin, C., Cantrel, L., Černušák, I., Louis, F., 2019. A theoretical study of the microhydration processes of iodine nitrogen oxides. Int. J. Quantum Chem. 119, e25792 https://doi.org/10.1002/qua.25792.

Environmental Science Processes & Impacts

ROYAL SOCIETY OF CHEMISTRY

PAPER

Cite this: *Environ. Sci.: Processes Impacts*, 2021, **23**, 1771

Interaction process between gaseous CH_3I and NaCl particles: implication for iodine dispersion in the atmosphere†

Hanaa Houjeij,[ab] Anne-Cécile Gregoire,*[b] Gwenaëlle Le Bourdon,[a] Laurent Cantrel[b] and Sophie Sobanska *[a]

Received 6th July 2021
Accepted 8th September 2021

DOI: 10.1039/d1em00266j

rsc.li/espi

Gaseous iodomethane (CH_3I) is naturally emitted into the atmosphere by biological activity in oceans and during severe accidents (SAs) in nuclear power plants. In this latter case, a part of radioactive iodine such as ^{131}I may be released. Improving the knowledge of CH_3I transport and reactivity in the atmosphere is important since they are strongly linked to first the cycle of ozone and second to the dispersion of radioactive CH_3I with potential radiological consequences on both the environment and human health. Here, the interaction process of CH_3I with NaCl as a surrogate of atmospheric aerosols was investigated under ambient air conditions by using Diffuse Reflectance Fourier Transform Spectroscopy (DRIFTS). The DRIFTS spectra of NaCl clearly evidenced CH_3I adsorption on the NaCl particle surface. A part of CH_3I ($(1.68 \pm 0.85) \times 10^{14}$ molecule per mg_{NaCl}) was found to be strongly bonded to NaCl since no desorption was observed. The CH_3I adsorption on the NaCl surface presented a 1st order kinetics relative to its gas phase concentration. The uptake coefficient was determined to be in the order of 10^{-11}. These results show a low probability of CH_3I to be taken up by halide-containing aerosols. These data are crucial for completing the iodine atmospheric chemical scheme.

Environmental significance

Methyl iodine once either emitted by natural sources or released in case of severe nuclear accidents may interact with atmospheric aerosol particles. Studying interactions between CH_3I and sea salt aerosols is relevant since sea salt particles are known as reactive surfaces for heterogeneous and multiphase chemical reactions for both inorganic and organic gases. A low probability of CH_3I to be taken up by sea salt aerosol particles is demonstrated through the low uptake coefficient values. However, though in a small amount, the irreversible characteristics of adsorption make it particularly important for the dispersion of CH_3I in the atmosphere. These data are crucial for completing the iodine atmospheric chemical scheme and helpful to implement the dispersion model to evaluate environmental contamination.

1. Introduction

Gaseous organic iodine species (CH_3I, ^{127}I) are naturally emitted at trace levels (maximum at 2000 ppt) into the atmosphere over oceans through algae and phytoplankton activities.[1,2] Iodine has attracted strong interest in the atmospheric chemistry field. Over the last four decades, numerous experimental and theoretical studies have been carried out on the quantification of iodine forms (gaseous or particulate) in the troposphere, the identification of natural sources of iodine and finally its reactivity, with the aim of better understanding the iodine cycle and its interaction with other compounds present in the troposphere.[3,4] In this atmospheric context, many gas phase mechanisms of iodine have been developed and a large database of the iodine cycle data is now available.[1–6] However, the interaction of gaseous iodine compounds with atmospheric aerosols and its resulting speciation have not been well documented, yet. Indeed, only a few laboratory studies have investigated the interaction of iodinated species with atmospheric aerosol surrogates. For instance, it was found that HOI can react with NaCl and NaBr to form ICl or IBr in the gaseous phase in the 5–25 °C temperature range.[7] The measured steady state uptake coefficient was determined to be in the order of 10^{-2}. Similarly, the uptake of CH_3I[8] and C_2H_5I[9] by commercial soot films and carbon thin films, respectively, was determined to be in the order of 10^{-2} at 25 °C. Most of the studies imply that iodine species are highly reactive and may interact with the other species (gas or particles) present in the atmosphere to evolve in a gaseous or particulate form. However, neither the

[a]Institut des Sciences Moléculaires, Université de Bordeaux, UMR CNRS 5255, Talence Cedex 33405, France. E-mail: sophie.sobanska@u-bordeaux.fr

[b]Institut de Radioprotection et de Sûreté Nucléaire (IRSN), PSN-RES, SEREX, Laboratoire Expérimentation Environnement et Chimie (L2EC), St Paul Lez Durance 13115, France. E-mail: anne-cecile.gregoire@irsn.fr

† Electronic supplementary information (ESI) available. See DOI: 10.1039/d1em00266j

uptake processes nor influence of the condensed phase on gaseous iodine reactivity was unravelled.

Following a severe accident in nuclear reactors such as Three Mile Island (USA, 1978), Chernobyl (Ukraine, 1986), and more recently Fukushima (Japan, 2011), iodine radioactive -isotopes (such as ^{131}I, half-life of 8.02 days) produced by the fuel fission may be released into the atmosphere mainly under gaseous (mainly I_2 and RI–R = alkyl group/chain type CH_3I) or aerosol (CsI) forms.[10,11] Particularly, gaseous CH_3I is mainly a product of the reaction between I_2 and carbon-based materials such as epoxy paints existing in the nuclear reactor building. Among released iodine species, CH_3I is the most challenging to be filtered by the current mitigation systems (such as metallic filters, aqueous scrubbers, or sand bed filters).[12–14] Radioactive isotopes of iodine (such as ^{131}I) are highly toxic to human health due to their easy and almost irreversible transport to the human thyroid gland, where it can locally induce cancer.[15,16] Indeed, after the accident of Chernobyl and Fukushima, near field activity concentrations of ^{131}I in air were found to be 750 000 Bq. m^3 (~0.03 ppt) and 5600 Bq. m^3 (~0.0002 ppt), respectively.[17] A previous study showed that ^{131}I was dispersed to long distances *i.e.*, >3000 km in the atmosphere after Chernobyl and Fukushima severe nuclear accidents.[17] Moreover, it should be noted that local meteorological conditions can cause a great variability in activity concentrations in environmental media and can result in locations further away being higher in concentration than closer locations.[17–20] With this intention, the French Institute of Radioprotection and Nuclear Safety (IRSN) developed specific simulation software (C^3X platform) which is capable of reproducing the release and dispersion of the radionuclides in the atmosphere.[21–23] However, one potential problem with such a simulation tool is that the transport of ^{131}iodine products following an accident is currently modelled without considering the physical/chemical evolution of iodine in the atmosphere, *i.e.* the gas phase evolution or interaction with atmospheric aerosols even if recent studies[24] focused on organic reactivity in the field of a nuclear accident.

To the best of our knowledge, there is no literature report on the uptake coefficient of methyl halides (CH_3Br, CH_3Cl, and CH_3I) by atmospheric aerosols. Hence, to date, the heterogeneous reactivity of CH_3I in the atmosphere has been fully accounted neither by the atmospheric community, nor in the field of nuclear safety. This is worrisome because the simulated atmospheric dispersion of radioactive isotopes of iodine[20,25,26] may be quite different from the actual one due to the different possible fates of iodine within the earth's atmosphere.

Thus, this study focused on gaseous CH_3I interactions with atmospheric aerosols, which may affect the chemical forms of iodine in the atmosphere and thus, their atmospheric fate and dispersion. Studying sea salt aerosols is particularly significant since first CH_3I is naturally emitted by the ocean surface and second sea salt particles are well known as reactive surfaces for heterogeneous and multiphase chemical reactions for both inorganic and organic gases.[27,28]

In this work, the adsorption of CH_3I on sea salt particle surrogates (NaCl, KBr and NaI) was investigated by using the diffuse reflectance infrared Fourier transform spectroscopy (DRIFTS) technique. Solid sodium chloride as the main sea salt component was firstly considered (NaCl). Then after potassium bromide (KBr) and sodium iodide (NaI) were used in view of investigating the influence of halide atoms on the interaction process. The evolution of the FTIR spectra of CH_3I in interactions with solids was followed as a function of time. The capability of desorption of CH_3I from salts was also explored. Considering the importance of this interaction to the dispersion of gaseous CH_3I in the atmosphere, the uptake coefficient was determined. Owing to the adsorption process of CH_3I on sea salt particle surrogates investigated here, knowledge on the fate and dispersion of CH_3I in the atmosphere could be further gained.

2. Materials and methods

2.1 Chemicals

Methyl iodide 1000 ppm (0.1% CH_3I, 99.9% Ar) and argon (99.99% pure) gas bottles were obtained from commercial cylinder air products and air liquids, respectively. The gases were used without any further purification. For the experiments, commercial powdered solids were used: sodium chloride (NaCl, 99.99%, ALFA AESAR), potassium bromide (KBr, 99+%, SIGMA ALDRICH) and sodium iodide (NaI, 99+%, ACROS).

Before each experiment, the salt sample was manually ground and then preheated for a minimum of 4 hours at 600 °C to remove water and pre-adsorbed species (impurities) on the powder surface. The granulometry of the ground powders was estimated by mechanical sieving on a series of 4 grids allowing sorting out the granulometry from 300 μm down to less than 50 μm. For NaCl, the particles with size ranges 300–100 μm, 100–60 μm, 60–50 μm, and <50 μm accounted for 32%, 26%, 39% and 3% in mass, respectively. A similar granulometry distribution was found for NaI and KBr ground salt powders.

The specific surface area of ground NaCl was determined on a nitrogen sorption Micromeritics ASAP 2010 analyzer by using the Brunauer–Emmett–Teller (BET) method. The BET surface area was found to be low (0.26 m^2 g^{-1}), in the same order of magnitude as the BET surface area previously determined for NaCl powder (0.68 m^2 g^{-1}).[29] The BET surface areas of NaI and KBr were assumed to be close to that of NaCl. The low BET surface area indicated that these solids were non-porous and that the available surface area was very low for colliding with trace gas phase species.

2.2 *In situ* diffuse reflectance Fourier transform spectroscopy (DRIFTS) experiments

The continuous, *in situ* monitoring of solids was performed in a DRIFTS cell (Harrick, Praying Mantis™ High Temperature Reaction Chambers, 24 V, HVC-DRP-4) with an interior volume of 15.78 mL equipped with zinc selenide (ZnSe) windows. The DRIFTS cell was housed in an FTIR-spectrometer (Nicolet 6700 – Thermo Optek) equipped with a high sensitivity deuterated triglycine sulfate (DTGS) detector. The cell can be temperature controlled in the 23–400 °C range. The cell temperature was monitored using a K-type thermocouple. The relative humidity

(RH) and temperature were continuously measured using a RH/$T°$ sensor (SHT75 Sensirion) placed on the line before the DRIFTS cell.

For each experiment, a known mass of powdered salts (close to 145 mg for each experiment) was placed in a crucible (6.3 mm internal diameter and 3.18 mm height) of the DRIFTS cell without using a packing device. The DRIFTS cell was purged with argon at 23 °C for 10 minutes to remove as much as possible H_2O and gaseous impurities. Solid powder was taken as the background spectrum under an Ar flow of 108 mL min^{-1}.

Four series of experiments were conducted as described below:

(1) NaCl was exposed continuously to an argon/CH_3I flow (108 mL min^{-1}) with a CH_3I concentration of 1000 ppm during 5 hours (named the exposure phase). Then after, the Ar/CH_3I flow was stopped, the DRIFTS cell was closed and desorption of sorbed species was monitored for 1 hour (named the spontaneous desorption phase). An additional step in dynamic condition involved flowing pure Ar (108 mL min^{-1}) up to 1 hour (named the induced desorption phase). Experiments were performed under ambient conditions (% RH = 20%) at 23 °C and 1 atm. Each experiment was repeated three times.

Although not atmospherically relevant, the excess of CH_3I in the solid *i.e.* the concentration of 1000 ppm was chosen in the first approach for our experiments in order to ensure the detection of reaction species if any. The influence of CH_3I concentration on the uptake coefficient is explored in the following sections.

(2) The desorption process was thermally activated by increasing the temperature up to 350 °C under an Ar flow (named the activated desorption phase). In view of this, NaCl was firstly exposed to an Ar/CH_3I flow (108 mL min^{-1}, CH_3I 1000 ppm) for 1 hour under % RH = 20% at 23 °C and 1 atm (exposure phase). In the second step, the DRIFTS cell was closed and spontaneous desorption was monitored for 4 hours. In the last step, desorption was monitored under dynamic conditions under an Ar flow (108 mL min^{-1}) for 1 hour still at 23 °C (induced desorption phase). Finally, the temperature was gradually increased up to 100, 200 and finally 350 °C under the same Ar flow (named the activated desorption phase). A heating rate of 3 K min^{-1} was applied with a dwell of 15 minutes at each target temperature.

(3) The third series of experiments aimed to investigate the influence of the CH_3I gas phase concentration on the CH_3I sorption process on NaCl under % RH = 20% at 23 °C and 1 atm. Similar to the first series of experiments, NaCl was exposed to a continuous flow of CH_3I of 500 and 200 ppm maintained at 108 mL min^{-1} for 5 hours. No spontaneous, induced or activated desorption phases were applied in this scenario.

(4) Finally, the four series of experiments considered the nature of the halide salts (NaI and KBr) on CH_3I sorption compared to NaCl. Experiments were limited to the exposure phase (CH_3I at 1000 ppm in argon for a total flow of 108 mL min^{-1} at 23 °C) and for a test duration of 1 hour.

Experimental conditions of the series of experiments performed in this study are summarized in Table S1 in the ESI.†

For the whole experiments, the infrared spectra were recorded as a function of time in the spectral range from 4000 to 600 cm^{-1} with a resolution of 8 cm^{-1}. Each spectrum was an average of 200 scans featuring a spectral sampling frequency of 7–8 spectra per hour. Note that the C–I stretching mode at 572 cm^{-1} cannot be observed because the ZnSe window cuts the spectrum between 16 000 and 600 cm^{-1}. The background subtraction was achieved by the Omnic software for each spectrum. The baseline was corrected using a linear interpolation model using Omnic software. The DRIFTS spectra were reported as $\log(1/R_\infty)$ (pseudo-absorbance), where R is the diffuse reflected signal. Note that this pseudo-absorbance gives a better linear representation of DRIFTS band intensity against the adsorbate surface concentrations than that given by the Kubelka–Munk function for poorly absorbing adsorbates.[30] A band decomposition of the overlapped bands was accomplished by the Gaussian function multiple band with the Levenberg–Marquardt mathematical model using FityK software.[31] Absolute uncertainty of the band area in 1400–1000 cm^{-1} was found between ~0.03 and 0.37 arbitrary units at the 95% confidence level.

2.3 Analysis of solids

After each DRIFT experiment, the total amount of iodine(I) adsorbed on NaCl was determined using an inductively coupled plasma mass spectrometer (ICP-MS, 810 MS VARIAN). The detection limit of 3 μg L^{-1} was determined for iodine element.[32] Two thirds of the NaCl powder samples were dissolved instantly after exposure to 5 hours of continuous CH_3I flow (1000 ppm, 108 mL min^{-1}), by NaOH (0.1 mol L^{-1}) for analysis. The total amount of iodine(I) adsorbed on NaCl could be thus determined.

3. Results and discussion

To investigate the influence of the interaction of CH_3I with sea salt surrogates on the dispersion of CH_3I in the atmosphere, the following sections examine: (1) the sorption process of CH_3I on NaCl, (2) the evolution of adsorbed CH_3I on NaCl over time, (3) the kinetics of the adsorption process of CH_3I on NaCl and the influence of temperature, concentration and nature of halide salts on this process and finally (4) the uptake coefficient determination.

3.1 Spectroscopic evaluation of the adsorption of CH_3I on NaCl at 23 °C and % RH = 20%

A representative spectrum of NaCl exposed to CH_3I for 5 hours and recorded in the mid IR region (4000–600 cm^{-1}) is shown in Fig. 1. Three typical regions assigned to CH_3 stretching, CH_3 deformation and CH_3 rocking were observed (Fig. 1). The detailed description of the CH_3 stretching (3050–2800 cm^{-1}) and CH_3 deformation (1500–900 cm^{-1}) for appropriate assignment is given below. In the CH_3 rocking (900–700 cm^{-1}) spectral region the bands observed were not resolved enough to be properly assigned.

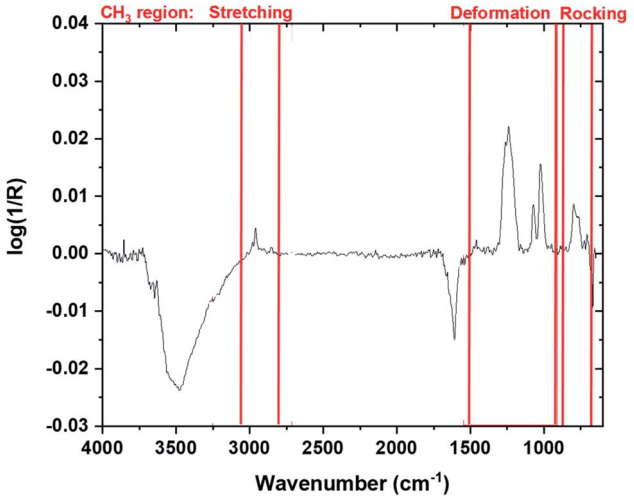

Fig. 1 Typical DRIFTS spectrum in the mid IR spectral range [4000–600 cm^{-1}] of NaCl exposed to 5 hours of CH_3I flow (108 mL min^{-1}, 1000 ppm) at 23 °C and 1 atm (the two negative broad bands around 3500 cm^{-1} and 1600 cm^{-1} are related to H_2O peaks derived from the baseline correction).

In the CH_3 stretching region (3050–2800 cm^{-1}) shown in Fig. 2(a), bands at 3018, 2993, 2981, 2961, 2855 and 2847 cm^{-1} were observed. Overlapped bands in the 2961 cm^{-1} region were decomposed using the Gaussian function into two bands at 2961 and 2953 cm^{-1} (Fig. 2(c)). The IR bands observed at 2981, 2953, and 2847 cm^{-1} were assigned to the characteristic bands of CH_3I in the gas phase (see bands marked in green in Fig. 2(a)) as described in the literature.[33,34] The bands at 2981, 2953 and 2847 cm^{-1} were attributed to the CH_3 asymmetric stretching, CH_3 symmetric stretching and overtone modes of CH_3I in the gas phase, respectively. Gaseous CH_3I remaining near the NaCl surface was detected by DRIFTS measurements. Based on the IR bands observed for CH_3I adsorbed on titanium oxide[33] and silver zeolites,[34] the bands observed at 3018, 2961 and 2855 cm^{-1} (marked in blue in Fig. 2(a)) were assigned as characteristic bands for CH_3I adsorbed on NaCl. The frequencies were attributed to CH_3 asymmetric stretching, symmetric and overtones modes of adsorbed CH_3I, respectively. This is consistent with a blue shift of the CH_3 asymmetric stretching (37 cm^{-1}), symmetric stretching (8 cm^{-1}) and asymmetric overtone (8 cm^{-1}) modes of CH_3I related to gaseous species. Additionally, a low intensity band at 2993 cm^{-1} was observed and can be also attributed to the interaction of CH_3I with NaCl. Actually, compared to CH_3I adsorbed on Si[35] and Cu[36] surfaces, the stretching mode of CH_3 varied between 3080 and 2909 cm^{-1}. Thus, 2993 cm^{-1} can be tentatively attributed to the CH_3 stretching of adsorbed CH_3I. The observation of two bands *i.e.* at 2993 and 2961 cm^{-1} for the same CH_3 stretching mode might be explained with different geometrical adsorbed structures of CH_3I on the NaCl surface.

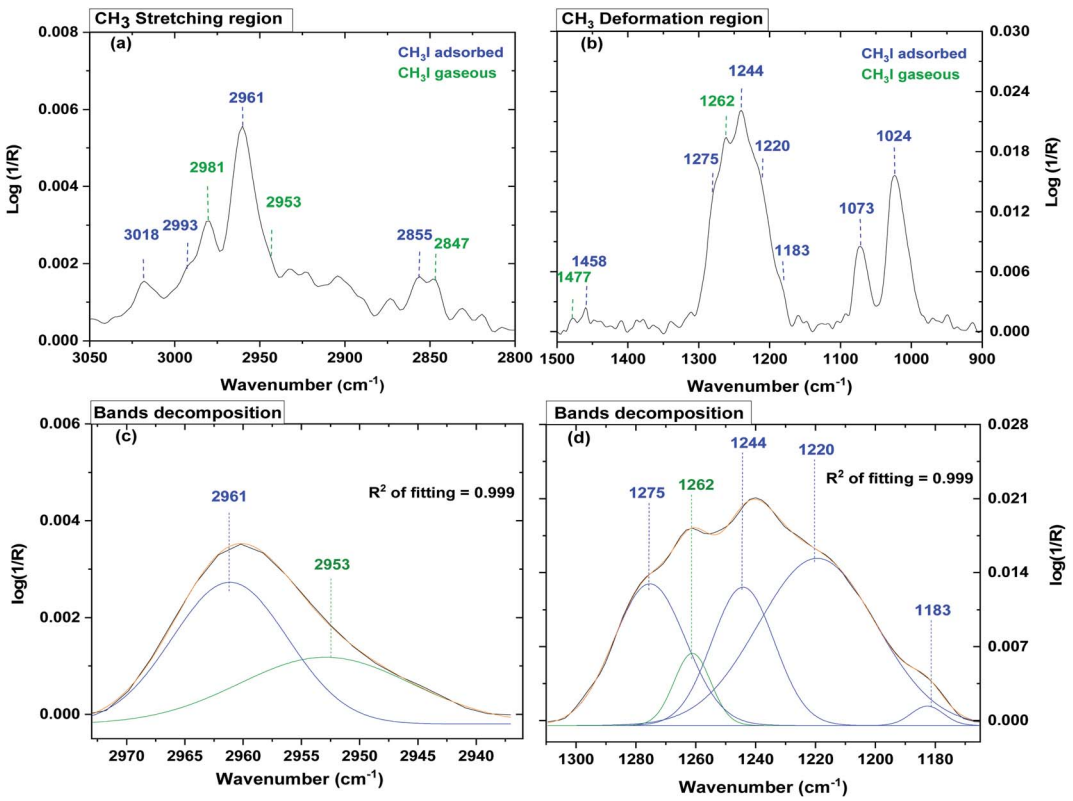

Fig. 2 DRIFTS spectra of NaCl exposed to 5 h of CH_3I (108 mL min^{-1}, 1000 ppm) continuous flow at 23 °C and 1 atm (a) in the 3050–2800 cm^{-1} (b), 1500–900 cm^{-1} (c) 2963–2935 cm^{-1} and (d) 1305–1160 cm^{-1} IR spectral ranges. Bands were decomposed with the Gaussian function using FityK software. Blue bands are CH_3I adsorbed on NaCl and green bands are CH_3I in the gas phase near the NaCl surface.

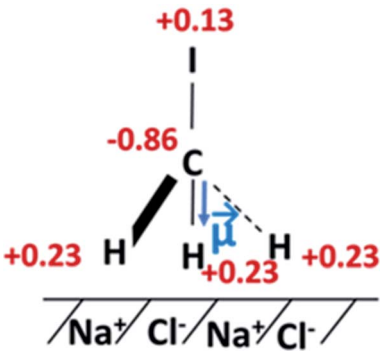

Fig. 3 Scheme of CH_3I monomer adsorption on NaCl and Mulliken charge distribution calculated with DFT performed using the ωB97XD/aug-cc-pVTZ-PP level of theory.

In the CH_3 deformation region (1500–900 cm^{-1}), bands at 1477, 1458, 1262, 1244, 1073 and 1024 cm^{-1} were observed (Fig. 2(b)). Based on the literature[33,34] the bands at 1477 and 1262 cm^{-1} were assigned to the CH_3 asymmetric and symmetric deformations of gaseous CH_3I which was consistent with the frequencies reported for the CH_3 stretching region of gaseous CH_3I. Based on a previous study,[33] the band at 1458 cm^{-1} (Fig. 2(b)) was attributed to the CH_3 asymmetric deformation of adsorbed CH_3I. In this spectral region, the band centered at 1244 cm^{-1} evidenced some shoulders; the decomposition of this band and the fitting procedure using the Gaussian function allowed the extraction of the additional bands at 1275, 1220 and 1183 cm^{-1} (see Fig. 2(d)). Similar shoulders were clearly observed in previous studies although they were not assigned.[33,34] As previously reported,[33–39] the CH_3 symmetric deformation of the CH_3I can shift (red and blue shift) from 1190 cm^{-1} to 1250 cm^{-1} depending on the type of solid or on the orientation of the crystallographic planes of single metallic solids. This strongly suggests that the bond geometries of the adsorbed CH_3I on NaCl are key for understanding the adsorption of CH_3I on salts and their subsequent reactivity which can highly affect the observed vibrational modes.

In addition, two intense bands at 1073 and 1024 cm^{-1} were observed (Fig. 2(b)). These bands were not reported in the literature for CH_3I molecules adsorbed on surfaces. Based on their band wavenumbers they can be assigned to CH_2I_2,[40–42] CH_3OH[34] or CH_3Cl.[43–45] The hypothesis of formation of such species on NaCl was discarded because experimental conditions required to form such species were drastically different in terms of temperature or surfaces, compared to the conditions used in our experiments. The SN_2 halide substitution at the NaCl surface suggested by Gu *et al.*,[45] in a theoretical study, was not consistent with our results obtained with the NaI surface. Indeed, the exposure of NaI to CH_3I conducted with similar experimental conditions yielded the same FTIR spectrum with new bands at 1073 and 1024 cm^{-1} (Fig. S1†). In consequence, a non-described adsorption geometry of CH_3I at the surface was hypothesized.

These intense bands in the CH_3 deformation region at 1073 and 1024 cm^{-1} (Fig. 2(b)) were strongly red shifted compared to the CH_3 deformation band of free CH_3 at 1262 cm^{-1} with values at −189 and −238 cm^{-1}, respectively. The latter suggests a strong interaction of CH_3I with the NaCl surface. It was reported,[37–39] that with low coverage, CH_3I adsorbed on the single metallic surface was of C_3 symmetry. However, with higher coverages geometrical rearrangement occurs until the C–I bond becomes aligned with the surface maintaining C_{3v} symmetry in binding to the surface. In contrary to the powdered sample, a single crystal sample has a continuous, unbroken and free of defects lattice. Additional density functional theory calculations (see the ESI†) of the CH_3I monomer have shown that the iodomethane dipole moment was oriented toward the carbon atom, which leads to a partial negative Mulliken's charge for the carbon atom and a partial positive Mulliken's charge for hydrogen and iodine atoms as shown in Fig. 3. Assuming that CH_3I was adsorbed on NaCl with a C_{3v} configuration as shown

Table 1 Tentative assignment of the observed IR absorption bands in cm^{-1} of CH_3I in the gas (g) and adsorbed (ads) on the surface of halide salts (NaCl, NaI and KBr) under % RH = 20% at 23 °C and 1 atm

Experimental wavenumber (cm^{-1})	Assignment	Corresponding species
3018	CH_3 asymmetric stretching	$CH_3I_{(ads)}$
2993	CH_3 symmetric stretching	$CH_3I_{(ads)}$
2981	CH_3 asymmetric stretching	$CH_3I_{(g)}$
2961	CH_3 symmetric stretching	$CH_3I_{(ads)}$
2953	CH_3 symmetric stretching	$CH_3I_{(g)}$
2855	CH_3 overtone	$CH_3I_{(ads)}$
2847	CH_3 overtone	$CH_3I_{(g)}$
1477	CH_3 symmetric deformation	$CH_3I_{(g)}$
1458	CH_3 asymmetric deformation	$CH_3I_{(ads)}$
1275	CH_3 asymmetric deformation	$CH_3I_{(ads)}$
1262	CH_3 symmetric deformation	$CH_3I_{(g)}$
1244	CH_3 symmetric deformation	$CH_3I_{(ads)}$
1220	CH_3 symmetric deformation	$CH_3I_{(ads)}$
1183	CH_3 symmetric deformation	$CH_3I_{(ads)}$
1073	CH_3 symmetric deformation	$CH_3I_{(ads)}$
1024	CH_3 symmetric deformation	$CH_3I_{(ads)}$

in Fig. 3, we may expect an attraction of hydrogen atoms toward chloride atoms at the surface of NaCl due to the charge difference. The observation of two bands for this configuration probably reflects the non-equivalent hydrogen atoms attached to the Cl on the NaCl surface. Moreover, the electronegativity of the chloride atom is higher than that of the iodine atom, which might reveal the strongest interaction of the hydrogen atom with the iodine ion (weakest ionic bonding). Thus, one would expect more than one geometrical orientation of adsorbed CH_3I with the powdered NaCl sample. This highly reflects the observation of more than one band for CH_3 symmetric deformation and symmetric stretching modes of adsorbed CH_3I on halide salts. Thus, the new intense bands were assigned to the unique C_{3v} geometrical adsorption of CH_3I that occurs specifically with halide salt surfaces. This geometry was not described in the literature.

Experimental wavenumbers observed from the interaction of CH_3I on halide salts (NaCl, NaI and KBr) and respective assignments are summarized in Table 1.

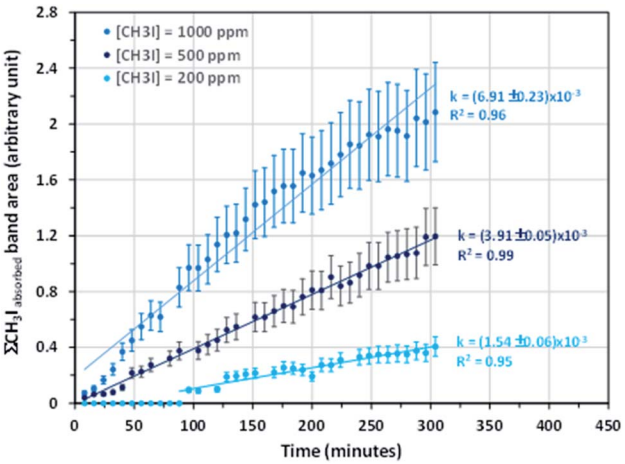

Fig. 5 Area of the $\sum CH_3I_{adsorbed}$ bands as a function of time during the exposure phase of CH_3I on NaCl. The exposure phase denotes the continuous flow of 108 mL min^{-1} of 1000, 500 ppm and 200 ppm of CH_3I in the gas phase. k = rate constant (experiment series (4)).

3.2 Time evolution of CH_3I adsorption and desorption on NaCl

The time evolution of the CH_3I amount adsorbed or desorbed on the NaCl surface was evaluated by following the sum of the band areas related to $CH_3I_{(ads)}$ (*i.e.* bands at 1275, 1244, 1220, 1183, 1073 and 1024 cm^{-1} labelled as $\sum CH_3I_{adsorbed}$ in the following sections). Time evolution in the CH_3I deformation region (1400–900 cm^{-1}) is reported in Fig. S2† for the CH_3I exposure phase and in Fig. S3† for the spontaneous and induced desorption phases for experiment series (1).

The evolution of the band area of the band at 1262 cm^{-1} related to the gaseous phase is stable over time in both CH_3I exposure and spontaneous desorption phases (Fig. 4). The complete disappearance of the IR bands related to gaseous CH_3I under an Ar flow (Fig. 4(a)) indicates the presence of gaseous CH_3I near the NaCl surface. The evolution of the bands related to adsorbed CH_3I ($\sum CH_3I_{adsorbed}$) is reported in Fig. 4(b). The $\sum CH_3I_{adsorbed}$ bands increase during the CH_3I exposure phase to reach an apparent plateau with no apparent desorption in both spontaneous and induced desorption phases.

In order to activate the desorption process (if any) of adsorbed CH_3I, the NaCl sample was heated up to 350 °C, at a rate of 3 K min^{-1}, under an argon flow (experiment series (2)). The heating step occurred at 23 °C after CH_3I exposure, spontaneous and induced desorption phases which lasted for 1, 4 and 1 hours, respectively. Spectra were recorded at 100, 200 and 350 °C. The evolution of deformation band intensity during the heating steps did not show significant changes (see Fig. S4 in the ESI†). This result would indicate the non-desorbing capability of CH_3I under different static, Ar flow and temperature conditions when adsorbed on the NaCl surface.

3.3 Kinetic adsorption of CH_3I on halide salts and the influence of the CH_3I concentration

During the CH_3I exposure phase, the evolution of the adsorption *versus* time is interpolated by a linear function and the rate

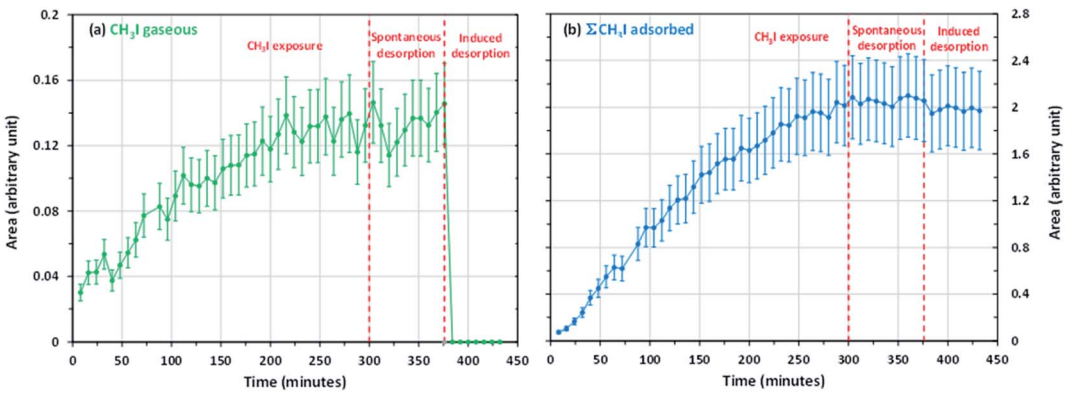

Fig. 4 Areas of the (a) CH_3I gaseous band and (b) $\sum CH_3I_{adsorbed}$ bands as a function of time during CH_3I exposure, spontaneous and induced desorption phases. The exposure phase denotes the continuous flow of 108 mL min^{-1} of CH_3I (1000 ppm) on NaCl. The spontaneous desorption phase denotes the static conditions after 5 h of CH_3I flow and the induced desorption phase denotes the continuous pure Ar flow after the static condition.

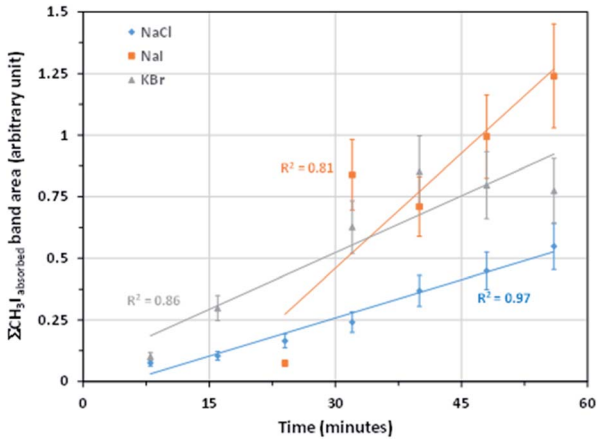

Fig. 6 Area of the $\sum CH_3I_{adsorbed}$ bands as a function of time during the exposure phase of CH_3I on NaCl, NaI and KBr. The exposure phase denotes the continuous flow of 108 mL min^{-1} of CH_3I (1000 ppm).

(k) of methyl iodide adsorption can then be determined from the linear interpolation of the adsorption band area curve *versus* time. The average rate of adsorption (k) was determined for various concentrations of CH_3I (experiment series 3) and is presented in Fig. 5. The average rates of adsorptions were repeatable with values of $k = (6.91 \pm 0.23) \times 10^{-3}$ arbitrary unit per min, $(3.91 \pm 0.05) \times 10^{-3}$ arbitrary unit per min and $(1.54 \pm 0.06) \times 10^{-3}$ arbitrary unit per min for initial concentrations of 1000 ppm, 500 ppm, 200 ppm, respectively. These values clearly show that the adsorption rate depends on the initial concentration with a decrease by factors 2 and 5 when the concentration decreases from 1000 ppm to 500 and 200 ppm, respectively. Assuming that this relationship can be extrapolated to low CH_3I concentrations found in the atmosphere (*i.e.* the atmospheric $[CH_3I]_g$ maximum is 2000 ppt (ref. 46)), very low CH_3I adsorption may be expected with an adsorption rate expected to be diminished by a factor 5×105.

The rate order of adsorbed CH_3I on NaCl determined from the slope of the bi-logarithmic plot of the k rate *versus* the concentration of CH_3I in the gas phase[47,48] (see Fig. S5 in the ESI†) was estimated to be 0.84 ± 0.05 indicating a first order rate for CH_3I adsorption on NaCl.

Experiments with NaI and KBr salts were conducted by a continuous flow of CH_3I (108 mL min^{-1}, 1000 ppm) for 1 hour and compared to the adsorption on NaCl salt (experiment series (4)). The adsorption rate was determined for one hour test duration (Fig. 6). The k rates of adsorption of CH_3I on NaI and KBr are $(3.10 \pm 0.87) \times 10^{-2}$ arbitrary unit per min and $(1.53 \pm 0.31) \times 10^{-2}$ arbitrary unit per min, respectively. Although k values estimated for NaCl and KBr are similar, the adsorption is enhanced for NaI. Seemingly, the adsorption rate increased in the following order: NaCl ≈ KBr < NaI. The change of adsorption rate with halide solid type indicates the influence of electronegativity on the adsorption of CH_3I on halide particles. Indeed, regarding the Mulliken's charge distribution calculated for the CH_3I monomer (see Section 3.1), the strongest interaction is expected with iodine compared to chlorine and bromine.

3.4 Determination of uptake coefficients

The CH_3I concentration on the solid was determined by ICP-MS assuming that the overall amount of adsorbed iodine is in the CH_3I form. The average concentration of iodine found in NaCl exposed to CH_3I (1000 ppm) for 5 h (test series (1)) amounts up to $(1.68 \pm 0.86) \times 1014$ molecule per mg_{NaCl} (Table S3†). Taking into account the total mass of NaCl involved in the experiment, the total amount of adsorbed CH_3I (denoted as $\{CH_3I_{ads}\}$) can thus be determined. Comparing the total amount of injected gaseous CH_3I_g during the exposure phase to the total amount of adsorbed CH_3I_{ads} on NaCl, it is found that only 3×10^{-3}% of initially injected methyl iodide was adsorbed on NaCl as shown in Table 2, indicating a very low residual amount of CH_3I on NaCl.

For a quantitative interpretation of the observed IR bands in terms of amount of methyl iodide taken up by NaCl, the area of the bands assigned to adsorbed methyl iodide was assumed to be proportional to the total amount of iodine taken up by NaCl (pseudo absorbance equation[30]). Typical FTIR bands of adsorbed iodine were assumed to represent the overall amount of adsorbed CH_3I determined by ICP-MS analysis (see the ESI†).

Table 2 Calculations of % $\{CH_3I\}$ residue on NaCl for experiment series (1) 5 h exposition of NaCl to 1000 ppm CH_3I corresponds to 8.03×10^{20} injected gaseous CH_3I molecules

Test repeat	Total amount of adsorbed CH_3I $\{CH_3I_{ads}\}$ in molecules	% of CH_3I residual on NaCl = $\{CH_3I_{ads}\}/(CH_3I)_g \times 100$
Repeat 1	$(2.05 \pm 0.16) \times 10^{16}$	2.55×10^{-3}%
Repeat 2	$(2.36 \pm 0.19) \times 10^{16}$	2.94×10^{-3}%
Repeat 3	$(3.00 \pm 0.24) \times 10^{16}$	3.74×10^{-3}%

Table 3 Average uptake coefficient of CH_3I on NaCl for an exposure phase duration of 5 hours and under % RH = 20% at 23 °C and 1 atm

$[CH_3I]$ in ppm	$[CH_3I]$ in molecule per m^3	Rate of collision in molecule per s	Adsorption rate in molecule per s	γ_{ss}
1000	2.48×10^{22}	4.74×10^{22}	1.31×10^{12}	$(2.76 \pm 0.93) \times 10^{-11}$
500	1.24×10^{22}	2.37×10^{22}	7.40×10^{11}	$(3.17 \pm 1.05) \times 10^{-11}$
200	4.96×10^{21}	9.49×10^{21}	2.92×10^{11}	$(3.07 \pm 1.04) \times 10^{-11}$

Table 4 Initial uptake coefficient of CH_3I (1000 ppm) on NaCl, NaI and KBr for an exposure phase duration of 1 hour and under % RH = 20% at 23 °C and 1 atm. 1000 ppm = 2.48×10^{22} molecule per m^3

Salt	$[CH_3I]$ in molecule per m^3	Adsorption rate in molecule per s	γ_{ss}
NaCl	2.48×10^{22}	1.31×10^{12}	$(2.76 \pm 0.93) \times 10^{-11}$
NaI	2.48×10^{22}	5.89×10^{12}	$(1.24 \pm 0.81) \times 10^{-10}$
KBr	2.48×10^{22}	2.91×10^{12}	$(6.13 \pm 3.18) \times 10^{-11}$

The band area of the $\sum CH_3I_{adsorbed}$ bands was therefore translated from the arbitrary unit absorbance of the spectrum to the total amount of iodine taken up by NaCl by a conversion factor (eqn (1)). Based on the experiment series (1), an average conversion factor (F) of $(1.14 \pm 0.37) \times 10^{16}$ at the 95% confidence level could be determined (Table S3†).

$$F = \frac{\text{Total amount of iodine taken by total solid}}{\text{Band area}} \quad (1)$$

The uptake coefficient, γ, is defined as the ratio of the gas-surface collision rate to the total gas-surface collision rate.[31,48,49] Thde saturation effect phase has been hardly reached after 5 hours of continuous CH_3I exposure time (see Fig. 4). Thus, the uptake in this work can be assumed as an average uptake during the 5 hours of CH_3I exposure and was determined as follows:

$$\gamma = \frac{d\{CH_3I\}}{dt} \times \frac{1}{Z} \quad (2)$$

$$Z = \frac{1}{4}\omega A[CH_3I]_g \quad (3)$$

$$\omega = [8RT/(\pi M)]^{1/2} \quad (4)$$

where $d\{CH_3I\}/dt$ is the surface adsorption rate of CH_3I on NaCl, $[CH_3I]_g$ denoted the concentration of CH_3I (molecule per m^3) in the gas phase under 5 hours of constant flow, ω is the mean thermal velocity of CH_3I (210 m s^{-1}) and A is the effective surface area (BET surface area × mass of NaCl).

The uptake values in the range of 10^{-11} were obtained at CH_3I gaseous concentrations of 1000, 500 and 200 ppm (Table 3). These values were much lower than those reported previously for the uptake coefficients of HOI, $HOI/IONO_2$, and ICl on halide salts[50] and of CH_3I on soot films[8] which were found to be in the order of 10^{-2}. This reflects the low colliding probability of CH_3I with NaCl compared to the high affinity of CH_3I for soot particles and to the reactivity of gaseous inorganic iodinated species (HOI, $HOI/IONO_2$, and ICl) with halide particles. Assuming that the uptake coefficient is independent of gaseous methyl iodide concentration, we can expect a very low methyl iodide uptake ($\sim 10^{-11}$) on NaCl under atmospheric conditions *i.e.* $[CH_3I]_g = 2000$ ppt or nuclear severe accident conditions.

The uptake coefficients calculated for KBr and NaI are reported in Table 4. Obviously, the initial adsorption rate of CH_3I was enhanced with NaI and its uptake coefficient increases by ~30 in comparison to NaCl and KBr. Once again, this trend (*i.e.* NaCl ≈ KBr < NaI) reflects the influence of electronegativity on the CH_3I–halide salt interaction process.

4. Conclusion and environmental implications

The interaction of gaseous CH_3I with NaCl as a surrogate of atmospheric sea salt aerosols has been investigated at 23 °C and 1 atm. CH_3I adsorption was clearly observed at low humidity level NaCl (% RH = 20% at 23 °C). In addition to the adsorbed CH_3I bands already referenced in the literature, the DRIFTS spectra revealed the presence of new strong vibrational bands at 1073 and 1024 cm^{-1}. Owing to the inhomogeneity of the NaCl surface and to the time evolution of these bands, we assumed that these new bands were attributable to the additional geometrical form of CH_3I as C_{3v} on the NaCl surface described here for the first time. Further, CH_3I molecules seem to be strongly bonded on the NaCl solid since no desorption was observed even after heating the system. We have found that the interaction is strongly related to the electronegativity of the halide. The adsorption does not depend on the initial concentration of CH_3I and the uptake coefficient reflecting that the colliding probability with the surface is very low compared to inorganic iodine species. Indeed, the % $\{CH_3I\}_{residual}$ sticks on solid NaCl were found to be 0.003%.

Though atmospheric and severe nuclear accident CH_3I concentrations are 10^{-5}–10^{-9} lower than the concentrations used in this study experiment, a very low uptake on NaCl can be expected – at least of the same order (10^{-11}). Thus, the influence of NaCl aerosols on the behaviour of gaseous CH_3I can be considered as negligible. However, though in a low amount, the irreversible characteristics of adsorption makes it of particular importance for the dispersion of CH_3I in the atmosphere. Considering the total concentration of atmospheric iodine measured in the case of SA, *e.g.* 75×10^{-2} ppt and 50×10^{-4} ppt for Chernobyl and Fukushima,[11,17,25] respectively, a corresponding estimated amount of about 2.2×10^{-5} ppt and 1.5×10^{-7} ppt of CH_3I would be expected to be transported by sea salt aerosols. Although these concentrations seem low, this point should be deeper examined to evaluate any influence on the atmosphere and environment contamination.

Author contributions

The manuscript was written through the contributions of all authors. All authors have given approval to the final version of the manuscript. HH, and GLB performed the experiments. LC,

ACG and SS designed the experiments, drafted, revised, and edited the manuscripts.

Conflicts of interest

Authors declare no conflicts of interest.

Acknowledgements

The authors acknowledge funding from the Region Nouvelle Aquitaine and IRSN to the SPECAERO project (grant no. 2017-1R10108-00013011). The authors wish to thank Sonia Taamali and Dr Florent Louis for the discussion on performing theoretical calculations. Theoretical calculations were kindly performed by the Centre de Ressources Informatiques (CRI) of the University of Lille and the Centre Régional Informatique et d'Applications Numériques de Normandie (CRIANN).

References

1 L. J. Carpenter, S. M. Macdonald, M. D. Shaw, R. Kumar, R. W. Saunders, R. Parthipan, J. Wilson and J. M. C. Plane, Atmospheric iodine levels influenced by sea surface emissions of inorganic iodine, *Nat. Geosci.*, 2013, **6**, 108–111, DOI: 10.1038/ngeo1687.

2 A. Saiz-lopez, J. M. C. Plane, A. R. Baker, L. J. Carpenter, R. Von Glasow, C. G. Juan, G. Mcfiggans and R. W. Saunders, Atmospheric Chemistry of Iodine, *Chem. Rev.*, 2012, **112**, 1773–1804, DOI: 10.1021/cr200029u.

3 A. Saiz-Lopez, R. P. Fernandez, C. Ordóñez, D. E. Kinnison, J. C. G. Martín, J. F. Lamarque and S. Tilmes, Iodine chemistry in the troposphere and its effect on ozone, *Atmos. Chem. Phys.*, 2014, **14**, 13119–13143, DOI: 10.5194/acp-14-13119-2014.

4 W. R. Simpson, R. Von Glasow, K. Riedel, P. Anderson, P. Ariya, J. Bottenheim, J. Burrows, L. Carpenter, U. Frieß, M. E. Goodsite, D. Heard, M. Hutterli, H.-W. Jacobi, L. Kaleschke, B. Neff, J. Plane, U. Platt, A. Richter, H. Roscoe, R. Sander, P. Shepson, J. Sodeau, A. Steffen, T. Wagner and E. Wolf, Halogens and their role in polar boundary-layer ozone depletion, *Atmos. Chem. Phys.*, 2007, **7**, 4285–4403, DOI: 10.5194/acp-7-4375-2007.

5 A. Saiz-Lopez, J. M. C. Plane, C. A. Cuevas, A. S. Mahajan, J. F. Lamarque and D. E. Kinnison, Nighttime atmospheric chemistry of iodine, *Atmos. Chem. Phys.*, 2016, **16**, 15593–15604, DOI: 10.5194/acp-16-15593-2016.

6 L. J. Carpenter, Iodine in the Marine Boundary Layer, *Chem. Rev.*, 2003, **103**, 4953–4962.

7 J. C. Mossinger and R. A. Cox, Heterogeneous Reaction of HOI with Sodium Halide Salts, *Phys. Chem. Chem. Phys.*, 2001, **105**, 5165–5177, DOI: 10.1021/jp0044678.

8 W. Wang, M. Ge, Y. Tian and L. Yao, A flow tube study of methyl iodine uptake on soot surface, *Chem. Phys. Lett.*, 2007, **440**, 348–351, DOI: 10.1016/j.cplett.2007.04.053.

9 Y. Shi, W. Weigang and G. MaoFa, The uptake of ethyl iodide on black carbon surface, *Chin. Sci. Bull.*, 2008, **53**, 733–738, DOI: 10.1007/s11434-007-0488-2.

10 S. Dickinson, A. Auvinen, Y. Ammar, L. Bosland, B. Clément, F. Funke, G. Glowa, T. Kärkelä, D. A. Powers, S. Tietze, G. Weber and S. Zhang, Experimental and modelling studies of iodine oxide formation and aerosol behaviour relevant to nuclear reactor accidents, *Ann. Nucl. Energy*, 2014, **74**, 200–207, DOI: 10.1016/j.anucene.2014.05.012.

11 L. S. Lebel, R. S. Dickson and G. A. Glowa, Radioiodine in the atmosphere after the Fukushima Dai-ichi nuclear accident, *J. Environ. Radioact.*, 2016, **151**, 82–93, DOI: 10.1016/j.jenvrad.2015.06.001.

12 L. Bosland, L. Cantrel, N. Girault, B. Clement, L. Bosland, L. Cantrel, N. Girault and B. Clement, Modeling of Iodine Radiochemistry in the ASTEC Severe Accident Code: Description and Application to FPT-2 PHEBUS Test, *Nucl. Technol.*, 2010, **171**, 99–107, DOI: 10.13182/NT10-A10774.

13 L. Bosland, S. Dickinson, H. C. Glowa, G. A. Herranz, L. E. Kim, D. A. Powers, M. Salay and S. Tietze, Iodine-paint interactions during nuclear reactor severe accidents, *Ann. Nucl. Energy*, 2014, **74**, 184–199, DOI: 10.1016/j.anucene.2014.07.016.

14 M. Chebbi, B. Azambre, C. Volkringer and T. Loiseau, Dynamic sorption properties of Metal-Organic Frameworks for the capture of methyl iodide, *Microporous Mesoporous Mater.*, 2018, **259**, 244–254, DOI: 10.1016/j.micromeso.2017.10.018.

15 A. V. Brenner, M. D. Tronko, M. Hatch, T. I. Bogdanova, V. A. Oliynik, J. H. Lubin, L. B. Zablotska, V. P. Tereschenko, R. J. Mcconnell, G. A. Zamotaeva, P. O. Kane, A. C. Bouville, L. V. Chaykovskaya, E. Greenebaum, I. P. Paster, V. M. Shpak and E. Ron, I - 131 Dose Response for Incident Thyroid Cancers in Ukraine Related to the Chernobyl Accident, *Environ. Health Perspect.*, 2011, **119**, 933–939, DOI: 10.1289/ehp.1002674.

16 T. Ohba, T. Ishikawa, H. Nagai, S. Tokonami and A. Hasegawa, Reconstruction of residents' thyroid equivalent doses from internal radionuclides after the Fukushima Daiichi nuclear power station accident, *Nat. Sci. reports*, 2020, **10**, 3639, DOI: 10.1038/s41598-020-60453-0.

17 G. Steinhauser, A. Brandl and T. E. Johnson, Comparison of the Chernobyl and Fukushima nuclear accidents: a review of the environmental impacts, *Sci. Total Environ.*, 2014, **470–471**, 800–817, DOI: 10.1016/j.scitotenv.2013.10.029.

18 T. Imanaka, G. Hayashi and S. Endo, Comparison of the accident process, radioactivity release and ground contamination between Chernobyl and Fukushima-1, *J. Radiat. Res.*, 2015, **56**, 56–61, DOI: 10.1093/jrr/rrv074.

19 T. Christoudias and J. Lelieveld, Modelling the global atmospheric transport and deposition of radionuclides from the Fukushima Dai-ichi nuclear accident, *Atmos. Chem. Phys.*, 2013, **13**, 1425–1438, DOI: 10.5194/acp-13-1425-2013.

20 O. Masson, G. Steinhauser, H. Wershofen, H. W. Fischer, L. Pourcelot, O. Saunier, J. Bieringer, T. Steinkopff, M. Hýža, A. Dalheimer, A. de Vismes-Ott, K. Eleftheriadis, M. Forte, C. G. Leonarte, B. Møller, T. W. Bowyer and E. Dalaka, Potential Source Apportionment and

Meteorological Conditions Involved in Airborne 131 I Detections in January/February 2017 in Europe, *Environ. Sci. Technol.*, 2018, **52**, 8488–8500, DOI: 10.1021/acs.est.8b01810.

21 M. Tombette, E. Quentric, D. Quélo, J. Benoit, A. Mathieu, I. Korsakissok and D. Didier, *C3X: A Software Platform for Assessing the Consequences of an Accidental Release of Radioactivity into the Atmosphere*, Poster, France, 2014, http://venus.iis.u-tokyo.ac.jp/English/workshop/Poster/3rdMarch/DamienDidier.pdf.

22 Y. Ando, K. Nishihara and H. Takano, Estimation of spent fuel compositions from light water reactors, *J. Nucl. Sci. Technol.*, 2000, **37**, 924–933, DOI: 10.1080/18811248.2000.9714974.

23 O. Saunier, I. Korsakissok, D. Didier, T. Doursout and A. Mathieu, Real-time use of inverse modeling techniques to assess the atmospheric accidental release from a nuclear power plant, *Radioprotection*, 2020, **55**, 107–115, DOI: 10.1051/radiopro/2020044.

24 C. Fortin, V. Fèvre-Nollet, F. Cousin, P. Lebègue and F. Louis, Box modelling of gas-phase atmospheric iodine chemical reactivity in case of a nuclear accident, *Atmos. Environ.*, 2019, **214**, 116838, DOI: 10.1016/j.atmosenv.2019.116838.

25 V. Winiarek, M. Bocquet, O. Saunier and A. Mathieu, Estimation of errors in the inverse modeling of accidental release of atmospheric pollutant: application to the reconstruction of the cesium-137 and iodine-131 source terms from the Fukushima Daiichi power plant, *J. Geophys. Res.: Atmos.*, 2012, **117**, D05122, DOI: 10.1029/2011JD016932.

26 O. Masson, A. Baeza, J. Bieringer, K. Brudecki, S. Bucci, M. Cappai, F. P. Carvalho, O. Connan, C. Cosma, A. Dalheimer, D. Didier, G. Depuydt, L. E. De Geer, A. De Vismes, L. Gini, F. Groppi, K. Gudnason, R. Gurriaran, D. Hainz, Ó. Halldórsson, D. Hammond, O. Hanley, K. Holeý, Z. Homoki, A. Ioannidou, K. Isajenko, M. Jankovic, C. Katzlberger, M. Kettunen, R. Kierepko, R. Kontro, P. J. M. Kwakman, M. Lecomte, L. Leon Vintro, A. P. Leppänen, B. Lind, G. Lujaniene, P. Mc Ginnity, C. M. Mahon, H. Malá, S. Manenti, M. Manolopoulou, A. Mattila, A. Mauring, J. W. Mietelski, B. Møller, S. P. Nielsen, J. Nikolic, R. M. W. Overwater, S. E. Pálsson, C. Papastefanou, I. Penev, M. K. Pham, P. P. Povinec, H. Ramebäck, M. C. Reis, W. Ringer, A. Rodriguez, P. Rulík, P. R. J. Saey, V. Samsonov, C. Schlosser, G. Sgorbati, B. V. Silobritiene, C. Söderström, R. Sogni, L. Solier, M. Sonck, G. Steinhauser, T. Steinkopff, P. Steinmann, S. Stoulos, I. Sýkora, D. Todorovic, N. Tooloutalaie, L. Tositti, J. Tschiersch, A. Ugron, E. Vagena, A. Vargas, H. Wershofen and O. Zhukova, Tracking of airborne radionuclides from the damaged Fukushima Dai-Ichi nuclear reactors by European Networks, *Environ. Sci. Technol.*, 2011, **45**, 7670–7677, DOI: 10.1021/es2017158.

27 A. Laskin, R. C. Moffet, M. K. Gilles, J. D. Fast, R. A. Zaveri, B. Wang, P. Nigge and J. Shutthanandan, Tropospheric chemistry of internally mixed sea salt and organic particles: surprising reactivity of NaCl with weak organic acids, *J. Geophys. Res.: Atmos.*, 2012, **117**, D15302, DOI: 10.1029/2012JD017743.

28 J. W. Chi, W. J. Li, D. Z. Zhang, J. C. Zhang, Y. T. Lin, X. J. Shen, J. Y. Sun, J. M. Chen, X. Y. Zhang, Y. M. Zhang and W. X. Wang, Sea salt aerosols as a reactive surface for inorganic and organic acidic gases in the Arctic troposphere, *Atmos. Chem. Phys.*, 2015, **15**, 11341–11353, DOI: 10.5194/acp-15-11341-2015.

29 R. Vogt and B. J. Finlayson-Pitts, A Diffuse Reflectance Infrared Fourier Transform Spectroscopic (DRIFTS) study of the surface reaction of NaCl with gaseous NO_2 and HNO_3, *J. Phys. Chem.*, 1994, **98**, 3747–3755, DOI: 10.1021/j100065a033.

30 J. Sirita, S. Phanichphant and F. C. Meunier, Quantitative analysis of adsorbate concentrations by diffuse reflectance FT-IR, *Anal. Chem.*, 2007, **79**, 3912–3918, DOI: 10.1021/ac0702802.

31 C. Lentz, S. P. Jand, J. Melke, C. Roth and P. Kaghazchi, DRIFTS study of CO adsorption on Pt nanoparticles supported by DFT calculations, *J. Mol. Catal. A: Chem.*, 2017, **426**, 1–9, DOI: 10.1021/ac0702802.

32 M. Gouello, *Chimie de l'iode et composition des aérosols dans le circuit primaire d'un réacteur nucléaire en situation d'accident grave*, Thèse de doctorat, Université de Grenoble, 2013.

33 C. Su, J. C. Yeh, C. C. Chen, J. C. Lin and J. L. Lin, Study of adsorption and reactions of methyl iodide on TiO_2, *J. Catal.*, 2000, **194**, 45–54, DOI: 10.1006/jcat.2000.2909.

34 M. Chebbi, B. Azambre, L. Cantrel and A. Koch, A Combined DRIFTS and DR-UV-Vis Spectroscopic *in situ* Study on the Trapping of CH_3I by Silver-Exchanged Faujasite Zeolite, *J. Phys. Chem. C*, 2016, **120**, 18694–18706, DOI: 10.1021/acs.jpcc.6b07112.

35 M. L. Colaianni, P. J. Chen, H. Gutleben and J. T. Yates, Vibrational studies of CH_3I on Si(100)-(2×1): adsorption and decomposition of the methyl species, *Chem. Phys. Lett.*, 1992, **191**, 561–568, DOI: 10.1016/0009-2614(92)85589-3.

36 C. J. Jenks, B. E. Bent, N. Bernstein and F. Zaera, The Chemistry of Alkyl Iodides on Copper Surfaces, *J. Phys. Chem. B*, 2000, **104**, 3008–3016, DOI: 10.1021/jp993021s.

37 M. A. Henderson, G. E. Mitchell and J. M. White, The chemisorption of methyl halides (Cl, Br and I) on Pt(111), *Surf. Sci. Lett.*, 1987, **184**, 325–331, DOI: 10.1016/0167-2584(87)90754-7.

38 F. Solymosi and G. Klivényi, HREELS study of CH_3I and CH_3 adsorbed on Rh(111) surface, *J. Electron Spectrosc. Relat. Phenom.*, 1993, **64/65**, 499–506, DOI: 10.1016/0368-2048(93)80115-3.

39 J. Lin and B. E. Bent, Iodomethane dissociation on Cu(111): bonding and chemistry of adsorbed methyl groups, *J. Vac. Sci. Technol., A*, 1992, **10**, 2202–2209, DOI: 10.1116/1.578005.

40 G. Klivényi and F. Solymosi, Generation of CH_2 species: thermal and photo-induced dissociation of CH_2I_2 on Rh(111) surface, *Surf. Sci.*, 1995, **342**, 168–184, DOI: 10.1016/0039-6028(95)00767-9.

41 M. K. Weldon and C. M. Friend, Spectroscopic characterization of surface methylene on Mo(110), *Surf. Sci.*, 1994, **321**, L202–L208, DOI: 10.1016/0039-6028(94)90175-9.

42 C. Scheer, A. Kis, J. Kiss and J. M. White, Adsorption and reactions of CH_2I_2 on clean and oxygen-modified Ag (111): a RAIRS and TPD study, *Top. Catal.*, 2002, **20**, 43–51, DOI: 10.1023/A:1016395214602.

43 T. Makino, S. Zulaehah, J. S. Gueriba, W. A. Diño and M. Okada, CH_3Cl/Cu(410): Interaction and Adsorption Geometry, *J. Phys. Chem. C*, 2018, **122**(1), 1825–11831, DOI: 10.1021/acs.jpcc.8b01296.

44 J. Cserenyi, L. Ovari, T. Bansagi and F. Solymosi, Adsorption and reactions of CH_3Cl on Mo_2C based catalyst, *J. Mol. Catal. A: Chem.*, 2000, **162**, 335–352, DOI: 10.1016/S1381-1169(00)00301-0.

45 M. Gu, X. Liu, L. Yang, S. Sun and J. Zhang, Dynamics of $Cl^-(H_2O)$ + CH_3I Substitution Reaction: The Influences of Solvent and Nucleophile, *J. Phys. Chem. A*, 2019, **123**, 2203–2210, DOI: 10.1021/acs.jpca.9b00348.

46 A. Saiz-Lopez, J. M. C. Plane, A. S. Mahajan, P. S. Anderson, A. E. Jones, H. K. Roscoe, R. A. Salmon, W. J. Bloss and J. D. Lee, On the vertical distribution of boundary layer halogens over coastal Antarctica: implications for O_3, HO_x, NO_x and the Hg lifetime, *Atmos. Chem. Phys.*, 2008, **8**, 887–900, DOI: 10.5194/acp-8-887-2008.

47 L. D. Kong, X. Zhao, Z. Y. Sun, Y. W. Yang, H. B. Fu, S. C. Zhang, T. T. Cheng, X. Yang, L. Wang and J. M. Chen, The effects of nitrate on the heterogeneous uptake of sulfur dioxide on hematite, *Atmos. Chem. Phys.*, 2014, **14**, 9451–9467, DOI: 10.5194/acp-14-9451-2014.

48 H. J. Li, T. Zhu, D. F. Zhao, Z. F. Zhang and Z. M. Chen, Kinetics and mechanisms of heterogeneous reaction of NO_2 on $CaCO_3$ surfaces under dry and wet conditions, *Atmos. Chem. Phys.*, 2010, **10**, 463–474, DOI: 10.5194/acp-10-463-2010.

49 M. Ullerstam, M. S. Johnson, R. Vogt and E. Ljungström, DRIFTS and Knudsen cell study of the heterogeneous reactivity of SO_2 and NO_2 on mineral dust, *Atmos. Chem. Phys.*, 2003, **3**, 4069–4096, DOI: 10.5194/acp-3-2043-2003.

50 A. Allanic and M. J. Rossi, Heterogeneous reactions of HOI on substrates of atmospheric importance, *Geophys. Res. Lett.*, 1999, **104**, 18689–18696, DOI: 10.1029/1999JD900285.